UNIVERSITÉ DE STRASBOURG

ÉCOLE DOCTORALE DE PHYSIQUE ET CHIMIE-PHYSIQUE
Institut Pluridisciplinaire Hubert Curien (IPHC) – UMR 7178

THÈSE

présentée par :

Kenny KALE SAYI

soutenue le : **9 Juillet 2018**

pour obtenir le grade de : **Docteur de l'Université de Strasbourg**
Discipline/ Spécialité : **Physique des particules**

Study of the cosmic muon-induced background in the Double Chooz neutrino oscillation experiment

THÈSE dirigée par :	
Mme. JOLLET Cécile	Enseignant-chercheur, CENBG-Bordeaux
RAPPORTEURS :	
M. PIQUEMAL Fabrice	Chercheur, CENBG-Bordeaux
M. GIGANTI Claudio	Chercheur, LPNHE-Paris

AUTRES MEMBRES DU JURY :	
Mme. TONAZZO Alessandra	Chercheur, APC-Paris
M. BAUDOT Jérôme	Enseignant-chercheur, Université de Strasbourg-IPHC

A mon Pasteur Job Esongo regretté
Pour cette vie dont tu m'as appris les préceptes
Pour celle d'après où désormais tu me précèdes
Pour tout, pour tant, pour l'éternité.

Remerciements

On doit tellement de choses à tellement de gens. Toutes ces bonnes âmes disposées favorablement sur nos chemins d'infortune pour nous faire accomplir quelque peu de notre destin, quelques uns de nos rêves d'enfant.

Et combien sont déjà sans vie, des yeux qui nous ont vus grandir ! Ce fut d'abord Nana Kale puis vint le tour de Job Esongo. D'où je viens on commence par ceux-là. Car la mort est la plus éloquente des lécons de la vie. Le plus beau voyage de la vie est peut-être celui dont on ne revient jamais sans avoir jamais quitté les cœurs de ceux qu'on n'a tant soit peu aimés. Je pense à vous comme pensaient alors aux villages de leur enfance, nos ancêtres, entravés, voguant courageux malheureux vers les tristes terres d'Amérique. Je pense à vous comme un ange déchu qui se souvient des cieux. Larmes de gratitude.

Tant de choses à tant de gens; sans doute encore un peu plus quand on relève de cette catégorie des hommes, au nombre desquels je me range, ceux qui au marathon de la vie sont partis haletant, le front baissé mais le coeur dressé, sans nulle autre promesse que la foi d'y croire toujours, la furieuse espérance d'y arriver un jour, à leur tour.

Je dois ici dire ma reconnaissance à Cécile et Anselmo, pour avoir daigné accepter de diriger cette thèse. De la formulation critique des hypothèses à la validation des résultats maintes fois éprouvés, j'aurais appris de vous la nature même de la démarche scientifique.

A l'heure d'écrire ces quelques mots j'ai une pensée amicale pour les équipes Neutrino de l'institut Pluridisciplinaire Hubert Curien et du Centre Nucléaire Bordeaux Gradignan, pour tous ces inspirants échanges scientifiques et ces mini pauses d'après-midi où nous refaisions le monde, le café dans une main, la physique dans l'autre.

A Papa et à Maman, pour l'amour inconditionnel, l'abnégation infinie et ces sacrifices inombrables au prix desquels je suis arrivé là. J'aurais aimé être l'enfant dont vous êtes les parents, si je ne l'étais déjà. Merci Papa et Maman. Au-delà des mots.

Lettre d'amour à mes sœurs et à mes frères, pour tant de soutien et d'affection. Cet amour inextinguible que partagent en commun des âmes habitant des

corps drainés par le même sang: Donnelle, Blanche, Orly, Verfel dit Bobo, Briane, tous Kale. Je n'aurais été qu'à moitié heureux si je n'avais pas été l'oncle aux neuveux: Sabrina et Freddo, tous Kale.

Je suis particulièrement reconnaissant à Ulrich Goerlach, à Jerome Baudot et à Monique Petitdidier. Si j'ai pu arriver là, vous y êtes pour beaucoup. Trouvez ici la gratitude d'un homme que vos mots, et bien plus, ont soutenu.

Je pense à toi mon ami, le Dr. Philippe Esongo. Pour la simple raison qu'il n'y a pas de raison. Le cœur j'imagine.

Cette thèse a été rendue possible grâce au soutien conjoint de l'ambassade de France en République Démocratique et du département de physique de la faculté de sciences de l'Université de Kinshasa.

A ma Jordane chérie, que dire que tu ne saches déjà. Je te dois mon bonheur.

Abstract

The Double Chooz experiment is a reactor antineutrino disappearance experiment located on the site of the Chooz nuclear power plant in the Ardennes region in France. The principal aim of the experiment is a high precision measurement of the oscillation amplitude $\sin^2 2\theta_{13}$ of the antineutrinos emitted from the two reactor cores of the Chooz power plant. The robustness and accuracy of this measurement depends strongly on a precise knowledge of the rates and spectral shapes of the backgrounds that contaminate the antineutrinos selection over the neutrino oscillation expected region. We have studied in the present thesis the muon induced background in the Double Chooz experiment. Indeed, cosmic muons crossing the detectors or interacting in the neighborhood constitute the main source of background events encountered in Double Chooz. Two distinct backgrounds analysis are presented in this thesis: fast neutrons (FN) and double capture of neutrons (DnC). Dedicated identification techniques have been developed for each of these backgrounds and, consequently, the associated spectral shapes and rates have been determined. The values obtained in this work serve as inputs in the final fit whence the θ_{13} value is extracted. The latest measurement released by the Double Chooz collaboration is $\sin^2 2\theta_{13} = 0.119 \pm 0.016$.

Résumé

L'expérience Double Chooz, située sur le site de la centrale nucléaire de Chooz dans la région des Ardennes en France, étudie la disparition des antineutrinos. Le but principal de l'expérience est de mesurer avec une grande précision l'amplitude d'oscillation $\sin^2 2\theta_{13}$ des antineutrinos émis par le deux réacteurs de la centrale de Chooz. La précision de cette mesure dépend fortement d'une connaissance précise des taux et de la forme des spectres des bruits de fond qui contaminent la sélection finale des antineutrinos en particulier dans la gamme d'énergie où l'oscillation des neutrinos est attendue. Nous avons étudié dans la présente thèse le bruit de fond d'origine cosmique dans l'expérience Double Chooz. En effet, les muons cosmiques traversant les détecteurs ou interagissant dans le voisinage immédiat sont la principale source du bruit de fonds observé dans Double Chooz. Deux types de bruits de fonds sont analysés et présentés dans cette thèse: les neutrons rapides (FN) et la double capture de neutrons (DnC). Des techniques d'identification dédiées ont été développées pour chacun de ces bruits de fond et, par conséquent, les formes spectrales et les taux associés ont été déterminés. Les valeurs obtenues dans le cadre de ce travail servent de paramètres d'entrée dans le fit final d'où la valeur de θ_{13} est extraite. La dernière mesure publiée par la collaboration Double Chooz est $\sin^2 2\theta_{13} = 0.119 \pm 0.016$.

Contents

Introduction

Neutrinos stand as the most intriguing particles encountered out of the numerous particles that constitute the invisible building blocks of the visible universe. It is known now that neutrinos are weakly interacting neutral fermions existing, at least, in three leptonic flavours or families: the electron neutrino, the muon neutrino and the tau neutrino (ν_e, ν_μ and ν_τ). Postulated in 1930 by W. Pauli as the solution to the non-conservation of energy observed in beta decay processes, neutrinos have since evidenced many outstanding properties that have been studied or revealed by several experiments around the world. These observations have established, inter alia, that neutrinos have a small but non-zero mass contrary to the null mass hypothesis of the standard model; this suggests that an extension of the standard model, or a model beyond it, is needed in order to provide a full theoretical description of neutrinos interactions and properties.

However, many questions about neutrinos still remain unanswered. Indeed, it is not known yet whether neutrinos are distinct from their antiparticles (Dirac neutrinos) or their own antiparticles (Majorana neutrinos). Besides, one still ignores what is the absolute mass of neutrinos and why this mass is expected to be, by far, lighter than the masses of the other fermions. The list of unanswered questions is even longer since; it is not known neither, at present, if neutrinos are related to leptogenesis, if there exists more than three flavours and if the CP symetry is conserved or not in the lepton sector. All these fundamental questions justify the great interest to neutrino physics observed in last decades by the multiplication of experiments and theoretical attempts in order to find responses to these crucial open questions.

Neutrinos undergo a particular phenomenon directly related to their mass, referred to as *neutrino oscillation* whereby a neutrino created with a specific leptonic flavor has a non-zero probability to be later measured to have a different flavor. The oscillation probability varies periodically as a function of the neutrino energy and the distance traveled from the creation source to the detection point. Oscillations, consequent of the non-zero mass of neutrinos, arise from the non-identity of the neutrino flavor and mass eigenstates and are governed by six independent parameters: three mixing angles, two mass squared differences, and a CP-violation phase. At present the mixing angles have been measured with more or less accuracy while the sign of one mass square difference and the CP-violation phase, despite of some recent hints, are still not known.

The Double Chooz experiment (DC) observes the disappearance of electron anti-neutrinos, as they oscillate into different flavours, in order to measure specially the mixing parameter θ_{13} which has been for long the last unknown angle of the mixing matrix of neutrinos oscillation. For this purpose, Double Chooz uses the neutrino flux originating from the two reactor cores of the Chooz nuclear power plant located in the Ardennes region in the East of France. The experiment consists of two identically designed liquid scintillator detectors: a near detector (ND), located at 400 meters from the reactors designed to quantify the initial flux of neutrinos and a far detector (FD), located at 1050 meters measuring the oscillation itself. A rate and shape analysis are performed to search for distortion in the measured energy spectrum due to $\overline{\nu}_e$ disappearance. The latest measurement released by the Double Chooz collaboration is $\sin^2 2\theta_{13} = 0.119 \pm 0.016$. The precision and accuracy of this measurement relies on precise knowledge of the rates and spectral shapes of the backgrounds contaminating the $\overline{\nu}_e$ selection over the neutrino oscillation expected region as these two informations, the backgrounds rate and the spectral shape, constitute inputs of the final fit from which emerges the θ_{13} angle value. The Double Chooz detectors consist in three optically isolated sub-detectors: the Inner Detector (ID), the Inner Veto (IV) and the Outer Veto (OV). The ID consists of 3 cylindrical volumes namely, from inside to outside, Target (doped with Gd), Gamma Catcher and Buffer. The IV is a cylindrical volume surrounding the ID having as principal function to detect and tag the muons, source of background, entering the detector. The OV installed on the top of the detectors is, both for electronics and read-out point of views, independent from the ID and the IV.

This thesis presents, in five chapters, the study of the cosmic muon induced background in the DC neutrino oscillation experiment. Indeed, the cosmic muons crossing the detectors or interacting in the near neighborhood constitute the main source of the background encountered in DC. The first chapter of this volume reviews, in a nutshell, the physics of neutrinos, the oscillation phenomenon, the current knowledge of neutrinos and some of the open questions. The second chapter describes in details the DC experiment design while the subsequent chapters are devoted to the analysis work undertaken in this thesis. The third chapter studies the correlated background, especially the fast neutrons (FN) from the identification technique to the rates measurements and the spectral shapes determination. An other muon induced background, the Double neutron capture (DnC) is evidenced in the data and presented in the fourth chapter. Here as well, the identification technique developed and the rate measurements are described in details.

The last chapter is devoted to the a special subject that is the accidental leak of Gd in the Gamma Catcher observed in the ND. The work done has allowed to evidence the leak, to give an estimation of the leak and to study its evolution overtime.

Chapter 1

Neutrino physics

> *"All truths are easy to understand once discovered; the point is to discover them"*
>
> Galileo Galilei

1.1 The missing energy and the neutrino hypothesis

The history of neutrinos is first of all a history of ideas and originates in a problem that the scientific community faced. Early observations revealed that a nucleus could decay from one state with additional unit of positive charge by emitting a single electron, this process is known at present as the beta decay. The amount of energy released is several times much greater than the rest mass energy of the electron (0.511 MeV). Now, if a nucleus at rest decays into two bodies, the final nucleus and the electron, the laws of momentum and energy conservations imply that the two must separate with equal and opposite momentum while the electron is emitted with a constant energy.

Moreover, since a nucleus is thousands of times heavier than an electron, its recoil velocity would be negligible compared to that of the electron, and of the constant electron energy would carry off about all the energy released by the decay.

The figure 1.1 shows the unexpected results obtained from the experiment. The electrons from beta decay were not emitted with a constant energy. Instead, they were emitted with a continuous spectrum of energies up to the expected value. In most instances, some of the energy released in the decay appeared to be lost. The crisis had grown so severe that N. Bohr had

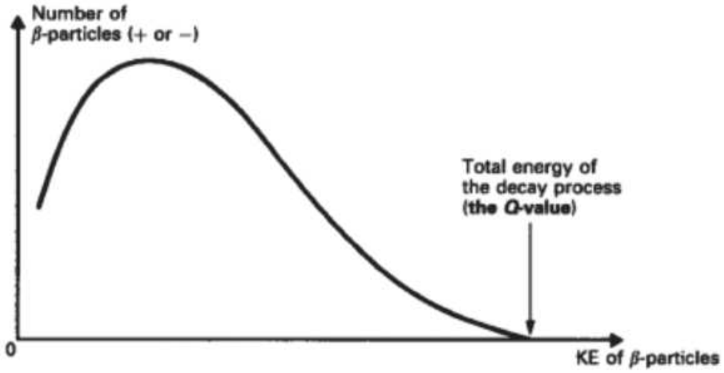

Figure 1.1: *Energy spectrum of electrons in a beta decay process as observed in experiments.*

even begun to contemplate abandoning the law of energy conservation in physical processes.

The solution to this "energy crisis" will be found finally by W. Pauli in his famous letter of 4th December 1930 [1] [1] in which he proposes that in a beta decay process the nucleus was transformed not into two but three distinct bodies: the final nucleus, the electron and a new type of particle electrically neutral, half spin and at least as light as the electron. This particle is the one we call nowadays the neutrino[2]. Thus, the continuous energy spectrum observed so far finds its explanation: the constant energy expected for the electron alone is in reality shared between these two light particles, and the electron was being emitted with the observed spectrum of energies without violating the energy conservation law.

1.2 Detection of neutrinos

The direct detection of neutrinos has been achieved more than two decades after they have been postulated by W. Pauli. Meantime, several measurements provided indirect proofs of the neutrinos reality. Early experiments in Wilson cloud chambers indicated that substantial energy was missing in sensitive measurements of energy of beta decay electrons as of their recoiling nucleus [2]. James S. Allen studied nuclear recoils following K-shell

---

[1] An open letter to a physics conference at Tubingen addressed, with humour, to "Dear Radioactive Ladies and Gentlemen".

[2] This particle was named, in a first time "neutron" by Pauli. When J. Chadwick discovered in 1932 the neutron as we know it today, E. Fermi renamed the Pauli's particle the *neutrino*.

electrons captures in Beryllium and observed that these electrons were absorbed by nuclei without the emission of any particle [3]. The measured recoil energy was consistent with the expected energy that would have been produced by the emission of a neutrino during the process. Also, in 1936, with the discovery of the muon (μ), the existence of a second neutrino is postulated. The first has a clear link with the electron and the second has a link with the muon. The quest for neutrino discovery was then opened.

In 1953, C. Cowan and F. Reines decided to install a neutrino detector at the Hanford nuclear reactor using a 300 l of a liquid scintillator [4], but the signal was not satisfactory in particular because of a rather poor shielding against the background. They repeat their experience more meticulously with the reactor Savannah River (California) in 1956. This time, it is a success: they obtain the manifest signature of an electronic antineutrino. F. Reines and C. Cowan opted to search the reaction:

$$\nu + p \rightarrow n + e^{+} \tag{1.1}$$

which should yield in a prompt light signal in the organic scintillator due to the positron's annihilation followed by a second light flash due to neutron capture. This interaction is the inverse beta decay whose double coincidence in a scintillator provides an unambiguous signature of an antineutrino interaction. In June 1956, C. Cowan and F. Reines inform Pauli via a telegram message the discovery. F. Reines alone will be awarded the Nobel Prize 40 years later, Cowan unfortunately passed away meantime.

In 1962, L. Lederman, M. Schwartz and J. Steinberger show that there are at least two kinds of neutrinos [5], one attached to the electron, the other to the muon. The experiment uses the Brookhaven National Laboratory synchrotron. Collisions on target nuclei of accelerated protons produce secondary beams of charged π mesons which, later, disintegrate into muons and neutrinos. By observing the subsequent interactions of these neutrinos in a spark chamber, a long rectilinear trace on each of the photographs of the rare neutrino interactions with the detection device is identified, characteristic of the muons that are the charged particles interacting the least with matter. The neutrinos produced during the decay of the π mesons are therefore very different from those which accompany the beta decays. The Nobel Prize in physics will reward this discovery in 1988.

An important milestone in history of neutrino is the formulation in 1967 of the theory of electroweak interactions by S.L. Glashow, S. Weinberg and A.Salam. This model in addition of the charged mediators bosons W^{+} and W^{-} predicted the existence of weak neutral currents and the Z boson. In 1973, this prediction is confirmed by the discovery of neutral-current neutrino interactions (interaction of a neutrino with matter without the neutrino being transformed into another particle such as the muon or the electron) consecutively in the Gargamelle experiment at CERN and the Fermi Lab [6].

A series of experiments conducted between 1974 and 1977 with the SPEAR collider of SLAC, allows the discovery of the tau lepton τ and suggests the existence of a third family of neutrino: the tau neutrino ν_τ. But it is only in 2000 that this new neutrino is discovered thanks to the DONUT (Direct Observation of the NU Tau) experiment [7].

Following the discovery of the tau neutrino family, the question of the number of neutrino families arose. The answer was found in the late 1990s, early 2000s at LEP [8] by measuring the total decay width Γ_z of the Z boson. The number N_ν of light neutrinos (neutrinos sensitive to electroweak interaction, with $m_\nu < m_z/2$) provided by the most recent fit of LEP data [9] is $N_\nu = 2.9841 \pm 0.0083$ in excellent agreement with $N_\nu = 3$ predicted by the theory.

1.3 Neutrinos in the Standard Model

The Standard Model (SM) is the theoretical frame that describes all known particles and their interactions. Developed in the 1970s, the SM has been successfully tested in several experiments over the past 35 years. According to this model, matter is composed of fermions : quarks and leptons and their corresponding antiparticles; these fermions interact by exchanging force carrier particles, the bosons. A chart of the SM particles can be seen in figure 1.2.

The properties of neutrinos in the SM can be summarized as follows

- Neutrinos are electrically neutral and exist in three different families or flavours, one for each charged lepton; as illustrated in figure 1.2.
- Neutrinos and antineutrinos are distinct particles and, respectively, left-handed and right-handed.
- Neutrinos are massless.

While the helicity of neutrinos has been established by Goldhaber [10] in a famous experiment, the null mass, on contrary, is simply assumed. This assertion does not fully reflect reality as seen in nature since, as it will be discussed later, many experiments have shown that neutrinos have a small but non-zero mass. Hence, even though the SM is the most successful modern theory in physics and has been able to describe all particle interactions observed so far with very high precision, the model is no more valid when it comes to describe neutrinos.

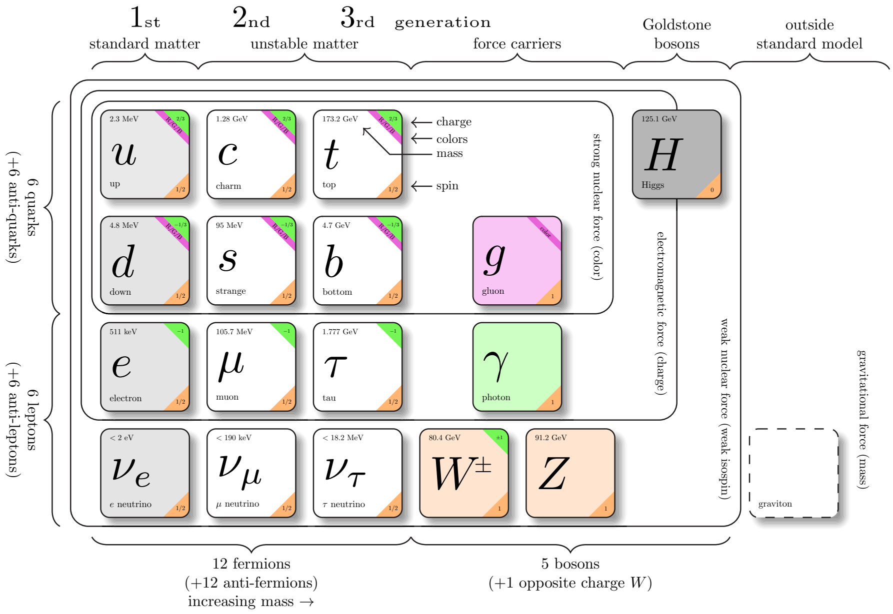

Figure 1.2: *The particles of the Standard Model.*

1.4 Neutrino oscillation

The Standard Model of particles is certainly the most tested theory in physics. Almost all its predictions have been confirmed experimentally with a relatively high precision. However, many other phenomena remain unexplained or insufficiently described in the framework of the SM, revealing its incompleteness in the description of the subatomic universe. Neutrinos nature happens to be one of the limits of the SM. Indeed, in the SM the interaction of the Higgs field with the leptons through the Yukawa interaction leaves neutrino massless [11] whereas we know now, thanks to many repeated experiments, that neutrinos oscillate, which implies that they have at least a small but non-zero mass. Hence, a modification or an extension of the Standard Model of particle physics is required.

Neutrino oscillation is the quantum phenomenon in which a neutrino created with a specific lepton flavour (electron, muon or tau) can be later detected as of a different flavour. While the current neutrino oscillation formalism dates from 1967, historically the phenomenon has been, first, suggested in 1957 by B. Pontecorvo as the transformation of a neutrino into an antineutrino [12, 13]. This idea was based on the observations of kaons oscillations evidenced a few years earlier [14].

In 1985, S. Mikheyev and A. Smirnov inspired by the work of the L. Wolfenstein claimed that the oscillations were amplified in the presence of matter

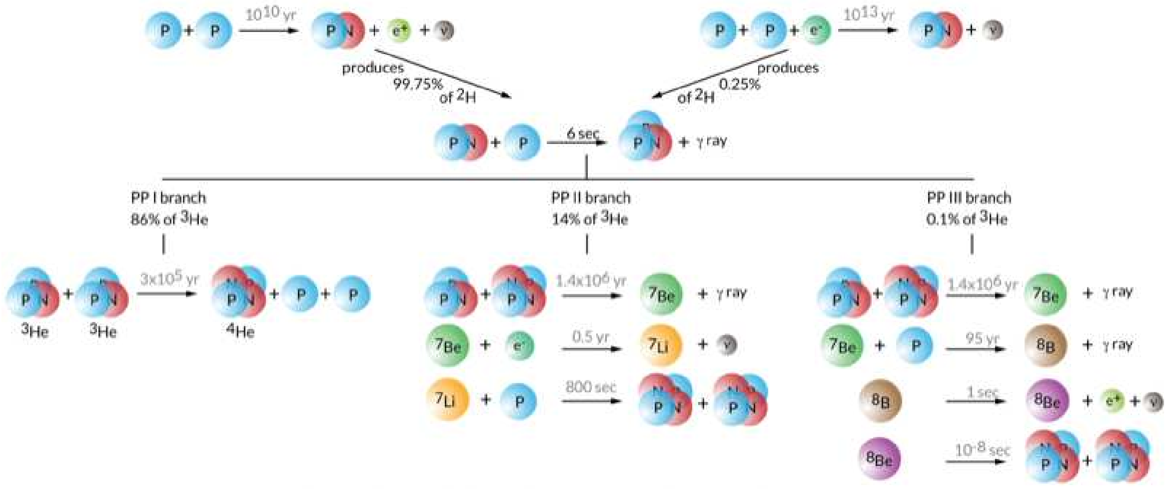

The weights of the branches are for conditions in the Sun.

Figure 1.3: *The pp chain of stellar thermonuclear reactions. The three main branches (ppI, ppII and ppIII) are indicated as well as the lifetimes of the reactions involved. In grey balls are indicated the produced neutrinos.*

[15, 16]. According to their so-called MSW theory, the density in the center of the Sun was sufficient for two-thirds of the electron neutrinos produced to be able to change into muon neutrinos in the half-second spent in the heart of the star.

1.4.1 Evidences of the oscillation

The solar neutrino anomaly

The theory that proton-proton reactions are at the base of the burning of stars and more particularly of the Sun has emerged in the 1920s mainly by A. Eddington. In these chain reactions stars convert their hydrogen into helium by means of a fusion reaction of two protons followed by a β^+ decay of the deuterium as illustrated in figure 1.3. In addition to this set of fusion reactions, C. Weizsaker and H. Bethe proposed in 1938 and 1939 respectively and independently of each other [17, 18], a new theory called the CNO cycle (for Carbon-Nitrogen-Oxygen)[3]. One can notice that only electronic neutrinos are created in both p-p and CNO reactions.

The Sun is mainly composed of hydrogen ($\simeq 75\%$) and helium ($\simeq 25\%$). The temperature varies from a few thousand Kelvin on the surface to a few million Kelvin at its center. The pressure of the gas creates a force that compensates the gravitational force; hence the Sun is in hydrostatic equilib-

---

[3] The CNO cycle consists in the fusion of four protons that produce in fine two positrons, one alpha particle and two electron neutrinos

rium. The temperature at its radiative heart is sufficient to initiate nuclear fusion reactions. Solar energy originates from thermonuclear reactions: 98 % comes from pp cycles and 2% from the CNO cycle according to the Solar Standard Model (SSM)[19].

By analyzing the pp cycle and taking into account that it is from this cycle that the solar energy comes, the thermal energy of the Sun can be summarized as due to the reaction

$$4p + 2e^- \rightarrow 4He + 2\nu_e \tag{1.2}$$

So, neglecting the mass of the neutrino, the energy Q of the reaction is (c = 1) :

$$Q = \Sigma(m_{inital}) - \Sigma(m_{final}) = 4m_p + 2m_e - m_{He} = 26.73 \quad MeV \tag{1.3}$$

We can then estimate the neutrino flux arriving on Earth :

$$\phi \simeq \frac{2L}{4\pi d^2(Q - < E_\nu >)} \simeq 6.38 \times 10^{10} \quad cm^{-2}s^{-1} \tag{1.4}$$

where $L \simeq 3.84 \times 10^{26}$ Watts the solar luminosity, $d \simeq 1.495 \times 10^{15}$ m the Earth-Sun distance and $\langle E_\nu \rangle = 0.3$ MeV. Hence, although helioseismological measurements[20] have made the SSM model credible, the precise measurement of this neutrino flux would provide an additional proof of the SSM validity. Several experiments focused on detecting these neutrinos from the Sun.

The first type of detection that has been proposed is the radiochemical detection which will be used in the Homestake experiment conducted by Davis Jr and Bahcall in the Homestake gold mine in South Dakota [21]. The first results were published in 1968 and the measurements were taken until the closure of the mine in 2002. For the purpose 400 m^3 of tetrachloroethylene have been used as cible under 1600 m of depth . The size of the target as well as the great depth allowed to reduce backgrounds from high-energy cosmic ray muons and to increase the probabilities of capture of neutrinos.

The experiment is based on the reaction:

$$\nu_e +^{37} Cl^- \rightarrow^{37} Ar + e^- \tag{1.5}$$

The number of neutrinos interacting with the chlorine can be deduced from the proportion of the radioactive isotopes of Argon that can be extracted by chemical processes. The result is a capture rate of 2.56 ± 0.23 SNU[4], three

---

[4] 1 SNU = 10^{36} captures/target atom /second

times lower than that predicted by the Standard Model of the Sun. This discrepancy inaugurated the solar anomaly problem.

Morevover, two other experiments, GALLEX (1991-1997) and Sage (1990-1993), similar in conception to the Homestake experiment have come to the same conclusion i.e a noticeable difference between predictions and observations. The detection principle was the reaction:

$$\nu_e +^{71} Ga \rightarrow^{71} Ge + e^- \tag{1.6}$$

The results for capture rates are 67 ± 5 SNU for Sage [22] and 69 ± 5 SNU for GALLEX [23] while the SSM predicts about 128 SNU.

These two experiments combined to the results provided by Davis Jr and Bachall have highlighted what will be commonly called the solar neutrino anomaly. Experiments based on the Cherenkov radiation, in their turn will confirm the anomaly.

Unlike previous experiments that can only detect neutrinos as a flux, experiments based on the Cherenkov effect detect neutrinos "one by one". This is the case of Kamiokande and Super-Kamiokande (Super-K) experiments. Created initially to determine the proton decay existence, The Kamiokande experiment used a detector built in 1983 consisted of 3000 tons of pure water and about 1000 photomultiplier tubes. The Super-K detector, the improved version of Kamiokande, consists of 50,000 tonnes of ultra pure water and approximately 11,100 photomultiplier tubes to detect the Cherenkov effect [24]. The principle is the neutrino-electron scattering:

$$\nu_a + e^- \rightarrow \nu_a + e^- \tag{1.7}$$

Kamiokande could detect neutrinos at energies above 7.5 MeV and 5.5 MeV for Super-K. The advantage of these detectors is that they allow to determine from which direction the neutrino comes. Indeed, the electron, in this case moves faster than light and creates, by Cherenkov effect, a cone of light which allows to determine the opening angle from its energy and back to the original direction of the neutrino. The maximum angular distribution obtained corresponds to a neutrino coming from the Sun confirming the theory of neutrino production by the Sun. Two major results have been obtained by Kamiokande and Super K [25, 26]:

- Observation of a reduction of solar neutrinos by more than 50 % compared to the predictions.
- Absence of a day/night asymmetry for the neutrino flux:
    - $\phi_{day} = (2.70 \pm 0.27) \times 10^6$ cm^{-2} s^{-1}

  - $\phi_{night} = (2.87 \pm 0.26) \times 10^6 \text{ cm}^{-2} \text{ s}^{-1}$.

The Sudbury Neutrino Observatory (SNO) was the first to experimentally link the observed solar neutrino deficit to the oscillation phenomenon by comparing the different observed neutrino fluxes[27, 28]. Located at about 2 km underground in Ontario (Canada), the SNO detector consists of a sphere of acrylic containing 1000 tones of heavy water (D_2O). The sphere is surrounded by 9600 photomultipliers and the whole is immersed in 7000 tons of ultra pure water acting as shielding. The choice of Deuterium has been made in order to detect all neutrino flavours through the following possible reactions:

- The charged current (CC) sensitive only to electron neutrinos: $\nu_e + d \rightarrow p + p + e^-$
- The elastic electron scattering (ES): $\nu_\alpha + e^- \rightarrow \nu_\alpha + e^-$
- The neutral current (NC): $\nu_\alpha(\overline{\nu}_\alpha) + d \rightarrow \nu_\alpha(\overline{\nu}_\alpha) + p + n$

where $\alpha = e, \mu, \tau$. In the first reaction, the neutrino must have a minimum energy of 1.44 MeV. Moreover, as the oscillation phenomenon decreases the number of electron neutrinos reaching earth, it occurs less often.

The second is sensitive mainly to the electron neutrino because of larger cross sections.

$$\phi_{ES} = \phi_e + 0.154(\phi_\mu + \phi_\tau). \tag{1.8}$$

The third and last reaction can be observed by adding sodium chloride (NaCl) in heavy water. In this case, 8.6 MeV photons produced during the capture of the final neutron by ^{35}Cl are detected. In addition, the detector is sensitive to the three flavours equally thanks to the sensibility of the neutral current sensibility:

$$\phi_{NC} = \phi_e + \phi_\mu + \phi_\tau. \tag{1.9}$$

The neutrino must have a minimum energy of 2.23 MeV. The measured flows are:

$$\phi_{CC} = (1.76^{+0.06}_{-0.05}(stat) \pm 0.09(syst)) \times 10^6 \quad cm^{-2}s^{-1} \tag{1.10}$$
$$\phi_{ES} = (2.39^{+0.24}_{-0.23}(stat) \pm 0.12(syst)) \times 10^6 \quad cm^{-2}s^{-1} \tag{1.11}$$
$$\phi_{NC} = (5.09^{+0.44}_{-0.43}(stat) \pm 0.43(syst)) \times 10^6 \quad cm^{-2}s^{-1} \tag{1.12}$$

The flux of electron neutrinos found is:

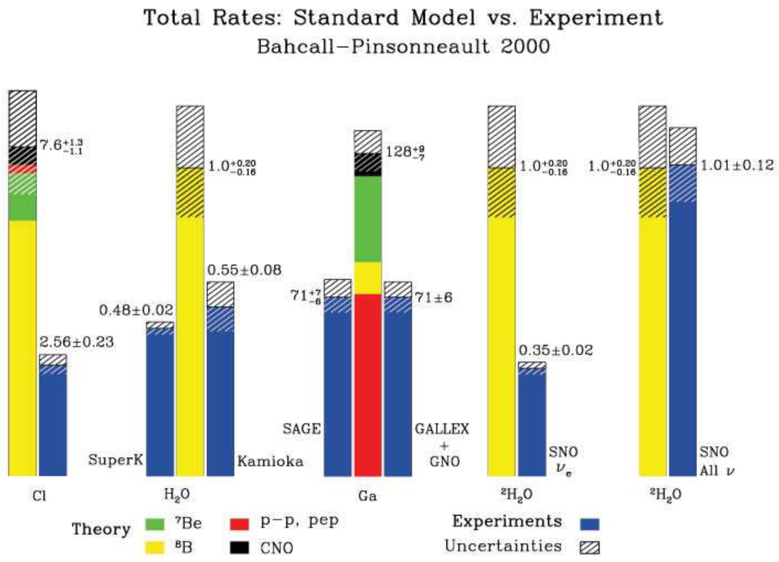

Figure 1.4: *Observed and predicted rates of solar neutrinos. Group of bars represent different detection techniques. For each group, the central bar represents the SSM prediction in which contribution of different flux component are featured with different colours, while the side bars (blue) show results from different solar neutrino experiments. Uncertainties are represented in grey.*

$$\phi_e = (1.76 \pm 0.05(stat) \pm 0.09(syst)) \times 10^6 \quad cm^{-2}s^{-1} \tag{1.13}$$

against

$$\phi^{\nu_e}_{SSM} = 5.05^{+1.01}_{-0.81} \times 10^6 cm^{-2}s^{-1}. \tag{1.14}$$

Once again the observed fluxes of electronic neutrinos (ν_e) from the Sun are lower than the predictions and the different results do not seem to match. Several explanations from particle physics have been suggested among which the idea that the SSM could be inaccurate and therefore leading to incorrect predictions. This assertion is strongly contradicted by the helioseismology measurements, based on SSM, which had previously confirmed the accuracy of the SSM. Thus, one physically coherent explanation could stand: the neutrino is massive and can change its flavour, by interaction in the solar plasma or in the vacuum, and consequently detectors sensitive only to electronic neutrinos, the case of Homestake, Sage and GALLEX previously described, do not detect all but only the fraction of solar neutrinos that have not oscillated during the journey from the Sun to the Earth.

Indeed, in view of results 1.13 and 1.14 and knowing that the total flux of muon and tau neutrinos has been provided :

$$\phi_{\mu,\tau} = (3.41 \pm 0.45(stat) - 0.45 + 0.48(syst)) \times 10^6 \quad cm^{-2}s^{-1} \tag{1.15}$$

One can easily notice that

$$\phi_e + \phi_{\mu,\tau} \simeq \phi_{SSM} \tag{1.16}$$

With SNO, as it can be seen in figure 1.4 neutrino oscillations contemplated by the Super-K collaboration only as an hypothesis in 1998 is definitely established.

Atmospheric neutrinos anomaly

Cosmic rays, mainly composed of protons, collide with the nuclei in the upper atmosphere creating a shower of hadrons (mostly pions and kaons) whose primary and secondary decays produce neutrinos of all flavours.

$$p + Air \to p, n, \pi^{\pm}, \pi^0, K^{\pm}... \tag{1.17}$$
$$\pi^{\pm} \to \mu^{\pm}\nu_\mu(\overline{\nu}_\mu) \tag{1.18}$$
$$K^{\pm} \to \mu^{\pm}\nu_\mu(\overline{\nu}_\mu) \tag{1.19}$$
$$K_L \to \pi^{\pm}e^{\pm}\nu_e(\overline{\nu}_e) \tag{1.20}$$
$$\mu^+ \to e^+\nu_e\overline{\nu}_\mu \quad and \quad \mu^- \to e^-\overline{\nu}_e\nu_\mu \tag{1.21}$$

A prediction of a flux ratio of muon neutrinos to electron neutrinos is possible based on this kinematic chain. The final estimated uncertainty in the flux ratio is about 5%. Atmospheric neutrinos are produced in an area ranging from about 15 km ($\cos\theta = 1$, with θ the zenith angle of the neutrino) to 13000 km ($\cos\theta = -1$) above the detectors and can be detected by large underground detectors like Super-K.

The ratio ν_μ/ν_e depends on the energy of the neutrino and its trajectory (zenith angle). Theoretical calculations predict that it is close to 2 for low energy neutrinos with a horizontal trajectory and higher for more energetic neutrinos that have vertical trajectories. Due to uncertainties affecting the simple ratio ν_μ/ν_e an other ratio is rather considered

$$r_{\mu/e} = \frac{\nu_\mu + \overline{\nu}_\mu}{\nu_e + \overline{\nu}_e} \tag{1.22}$$

For low energy neutrinos (<1 GeV), $r_{\mu/e} \simeq 0.45$.

The ratio experiment-theory:

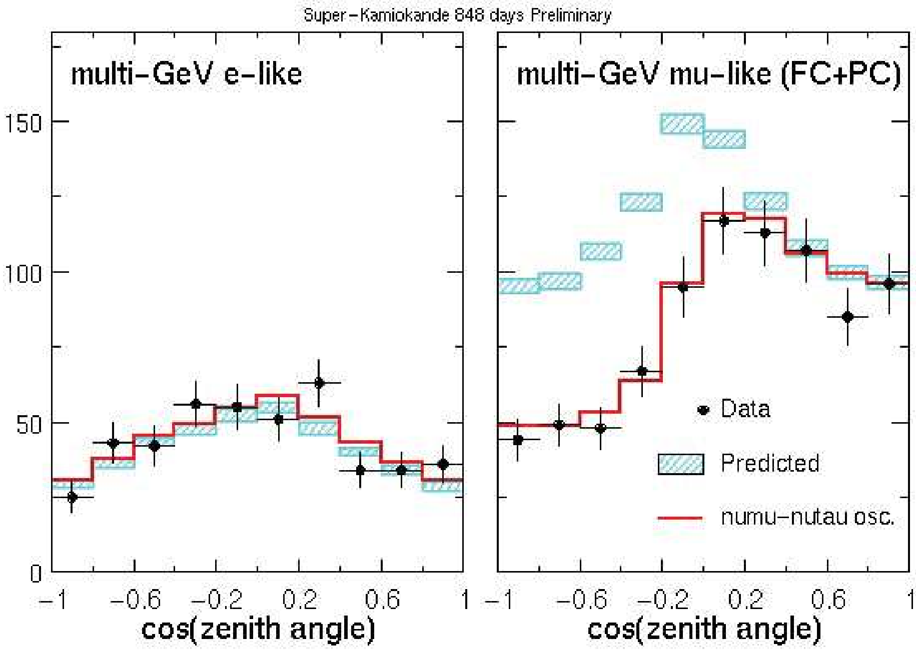

Figure 1.5: *Zenith angle distributions of atmospheric* ν_e *(Left) and* ν_μ *(right) in Super-K experiment. Upward-going particles have* $\cos\theta < 0$ *and downward-going particles have* $\cos\theta > 0$*. Observed distributions are compared with two predictions : with and without oscillation, respectively in green and red.*

$$R(\mu/e) = \frac{[(\nu_\mu + \overline{\nu}_\mu)/(\nu_e + \overline{\nu}_e)]_{exp}}{[(\nu_\mu + \overline{\nu}_\mu)/(\nu_e + \overline{\nu}_e)]_{th}} \tag{1.23}$$

is expected to be equal to 1 in absence of oscillation. However, Super-K provided results much smaller than the predictions:

- $R = 0.68 \pm 0.02(stat) \pm 0.05(syst)$ (visible energy < 1.33 GeV)
- $R = 0.68 \pm 0.04(stat) \pm 0.08(syst)$ (visible energy > 1.33 GeV)

The difference between predictions and observations, as shown here in figure 1.5, called the anomaly of atmospheric neutrinos, can be explained by the phenomenon of 3 flavour oscillations.

1.4.2 Neutrino oscillation phenomenology

The neutrino oscillation evidenced in the previous section implies that neutrinos must have mass. Thus, as in the quark sector, there is a mixing matrix relating the mass eigenstates and the flavour states:

$$|\nu_\alpha\rangle = U^*_{\alpha j}\,|\nu_j\rangle \tag{1.24}$$

where $\nu_\alpha = (\nu_e, \nu_\mu, \nu_\tau)$ are the flavour states and $\nu_j = (\nu_1, \nu_2, \nu_3)$ the mass eigenstates of masse m_j. The mixing matrix U also called the PMNS matrix is named after Pontecorvo-Maki-Nakagawa-Sakata[5].

Since $|\nu_j\rangle$ are mass eigenstates, their propagation after a time t can be described by plane wave solutions of the form :

$$|\nu_i(t)\rangle = e^{-i(E_i t - \vec{p}_i \cdot \vec{x})} \mid \nu_i(0)\rangle, \tag{1.25}$$

where E_i is the energy of mass eigenstates i, $\vec{p_i}$ is the three-dimensional momentum and $\vec{x}$ is the current position of the particle. For ultrarelativistic neutrinos $|\vec{p_i}|= p_i \gg m_i$. Thus the energies E_i

$$E_i = \sqrt{p^2 + m_k^2} \tag{1.26}$$

can be approximated by :

$$E_i \simeq E + \frac{m^2}{2E} \tag{1.27}$$

---

[5] This matrix was introduced in 1962 by Ziro Maki, Masami Nakagawa and Shoichi Sakata to explain the neutrino oscillations predicted by Bruno Pontecorvo.

with E being the total energy of the particle.

In this case

$$E_i - E_j \simeq \frac{\Delta m_{ij}^2}{2E} \tag{1.28}$$

where Δm_{ij}^2 is the squared-mass difference $m_i^2 - m_j^2$.

The probability amplitude of finding a neutrino of initial flavor ν_α in the flavor state ν_β as a function of time t is

$$A(\nu_\alpha \to \nu_\beta) = \langle \nu_\alpha | \nu_\beta \rangle = \sum_k U_{\alpha k}^* U_{\beta k} e^{-iE_k t} \tag{1.29}$$

The transition probability, usually called oscillation probability, is the square of the absolute value of the amplitude :

$$P_{\alpha\to\beta} = |\langle \nu_\beta(t) | \nu_\alpha \rangle|^2 = \sum_{i,j} U_{\alpha i}^* U_{\beta i} U_{\alpha j} U_{\beta j}^* exp(- i\frac{\Delta m_{ij}^2 t}{2E}) \tag{1.30}$$

$$\tag{1.31}$$

In neutrino oscillation experiments the time t is not measured. What is known is the distance L between the source and the detector. Thus, since ultrarelativistic neutrinos travel almost at the speed of light the approximation $t = L$ (with c=1) is possible, leading to :

$$P_{\alpha\to\beta} = \sum_{i,j} U_{\alpha i}^* U_{\beta i} U_{\alpha j} U_{\beta j}^* exp(- i\frac{\Delta m_{ij}^2 L}{2E}) \tag{1.32}$$

The survival probability defined as the probability for a neutrino to conserve its flavour derives simply from 1.32 as a consequence of the rule of conservation of probability

$$P_{\alpha\to\alpha} = 1 - P_{\alpha\to\beta} \tag{1.33}$$

In view of expression 1.32, it can be seen that in addition of the squared mass differences which are physical constants, the source-detector distance L and the energy E, two quantities depending on the experiment, enter also in the determination of the phase of neutrino oscillations:

$$\varphi_{ij} = -\frac{\Delta m_{ij}^2 L}{2E} \tag{1.34}$$

The amplitude of the oscillation is determined by the elements of the mixing matrix U. Therefore, neutrino oscillation experiments allow the measurements of both the squared-mass difference Δm_{ij}^2 and the PMNS matrix elements.

Quasi all neutrinos experiments results obtained so far can be explained by the following neutrino model[6]:

- 3 light neutrinos ($m_i < 1eV$)
- Three active neutrino flavours : ν_e, ν_μ, ν_τ
- The unitary matrix U with 5 distinct parameters : 3 mixing angles ($\theta_{13}, \theta_{23}, \theta_{12}$), 1 CP violation phase δ and 2 Majorana phases (α and β).

The most commonly used parametrization of PMNS matrix allows a decomposition into terms that can be associated with different regimes of mixing that have been explored by different classes of experiments[29]. This parametrization is

$$U = \begin{bmatrix} 1 & 0 & 0 \\ 0 & c_{23} & s_{23} \\ 0 & -s_{23} & c_{23} \end{bmatrix} \begin{bmatrix} c_{13} & 0 & s_{13}e^{-i\delta_{CP}} \\ 0 & 1 & 0 \\ -s_{13}e^{i\delta_{CP}} & 0 & c_{13} \end{bmatrix} \begin{bmatrix} c_{12} & s_{12} & 0 \\ -s_{12} & c_{12} & 0 \\ 0 & 0 & 1 \end{bmatrix} \begin{bmatrix} e^{i\alpha_1/2} & 0 & 0 \\ 0 & e^{i\alpha_2/2} & 0 \\ 0 & 0 & 1 \end{bmatrix} \tag{1.35}$$

where $s_{ij} = \sin\theta_{ij}$ and $c_{ij} = \cos\theta_{ij}$. In this representation the (23) sector is identified with the atmospheric neutrinos while the (12) sector corresponds to the solar neutrinos. The (13) sector, as it will be seen in section 1.5 describes oscillations in the interference reactor sector.

The expression 1.32 represents the oscillation probability of neutrinos. For antineutrinos the U matrix has to be replaced by its complex conjugate U^*. Thus, if the CP-violating phase δ in 1.35 is not zero,U differs from U^*. In consequence, CP violation could manifest in a different oscillation behaviour of neutrinos and antineutrinos. However, this is only possible if $\theta_{13} \neq 0$ due to the connection between θ_{13} and δ as it can be seen in 1.35. Fortunately, reactor neutrino experiments (Double Chooz, Daya Bay and RENO) have found a non-zero θ_{13} value, opening the possibility to investigate the CP violation phase.

In the short baseline reactor experiments a two neutrino mixing model can be a good approximation. From equation 1.32 the derivation of the oscillation probability in the two-neutrino mixing [29] yields to

---

[6] Except, maybe, the results of LSND experiment as described further in section 1.8.4

$$P_{\nu_\alpha \to \nu_\beta}(L,E) = \sin^2 2\theta \sin^2 \frac{\Delta m^2 L}{4E} \qquad (\alpha \neq \beta) \tag{1.36}$$

In SI units, the formula 1.36 becomes

$$P_{\alpha \to \beta, \alpha \neq \beta} = \sin^2(2\theta)\sin^2\left(1.27\frac{\Delta m^2 L}{E}\frac{[\mathrm{eV}^2]\,[\mathrm{km}]}{[\mathrm{GeV}]}\right). \tag{1.37}$$

Whence the oscillation length

$$L_{osc}[km] = 2.47\frac{E[MeV]}{\Delta m^2[eV^2]} \tag{1.38}$$

which corresponds to the location of the maximal oscillation, that is the first dip of the oscillation probability curve. Hence, in experiments based on terrestrial neutrino sources, namely accelerators or nuclear reactors, it is possible to choose a L/E ratio that is the most suitable for observing the oscillation.

1.4.3 Oscillation in matter and the MSW effect

Since neutrinos interact very weakly with matter, oscillation calculations are usually made for propagation in a vacuum as done so far in this volume. However, as they interact via the weak interaction, a high electron density can influence sensibly their propagation. In 1978, Wolfenstein discovered that neutrinos, as they propagate through matter, are subject to the potential due to the coherent forward elastic scattering with the electrons and nucleons present in the medium [30].

This potential depends on the density of the medium. Indeed,

$$V = \sqrt{2}G_F N_e \tag{1.39}$$

where G_F and N_e are respectively the Fermi coupling constant and the electrons density of the medium.

In 1985, S.P Mikheev and A. Yu Smirnov discover a resonance in the transition of flavors during propagation in a non-constant density medium [16], allowing the effective missing angle to reach the maximal mixing value, $\pi/4$, in a region along the neutrino path. This is known as the *MSW effect*[7].

Similarly to the vacuum case, the mixing angle in matter, θ_m, determines relations between the eigenstates in matter and the flavor states ν_{1m} and ν_{2m} as:

---

[7] To the honor of Mikheev, Smirnov and Wolfenstein

$$\nu_e = \cos\theta_m \nu_{1m} + \sin\theta_m \nu_{2m} \tag{1.40}$$

In matter, both the eigenstates and eigenvalues, and consequently, the mixing angle depend on matter density and neutrino energy. Theoretical calculations lead to the expression of the mixing angle in matter as follows

$$\sin 2\theta_m = \frac{\sin 2\theta}{\sqrt{(V/\Delta m^2 - \cos 2\theta)^2 + \sin^2 2\theta}} \tag{1.41}$$

Hence, if $V = \Delta m^2 \cos 2\theta$ the matter oscillation amplitude θ_m is maximal; this condition realizes the MSW resonance.

1.5 The way to θ_{13}

1.5.1 Introduction

Unknown until 2012, θ_{13} has been the last of the three mixing angles to be determined. Indeed, $\theta_{12} \approx 33°$ has been determined by KamLAND [31] and solar neutrino experiments while the $\theta_{23} \approx 45°$ arised from atmospheric neutrino experiments, namely Super-K [24] and some long baseline disappearance experiments such as MINOS [32], NOVA [33], T2K [34] and K2K [35].

In the standard parametrization of the mixing matrix of equation 1.35, the CP violation phase δ_{CP} appears attached to θ_{13} in the form $\sin\theta_{13}e^{-i\delta_{CP}}$. Hence, as already mentioned, if θ_{13} was zero the PMNS matrix would be purely real and there would be no way to access the CP violation phase δ_{CP} in the neutrino sector. This is one of the reasons why measuring θ_{13} happened to be of great importance in particle physics.

The θ_{13} value can be accessed through, at least, two different ways. The first is through reactor antineutrino disappearance experiments by measuring the survival probability of electron antineutrinos $P(\overline{\nu}_e \rightarrow \overline{\nu}_e)$. In this case, as it can be seen in figure 1.7 , a detector is suitably located at a distance L near the first maximum of $\sin^2\Delta_{31}$, the amplitude of the oscillation is then given by $\sin^2 2\theta_{13}$. The second way to probe θ_{13} is in appearance experiments by looking, for instance, the oscillation of muon neutrinos into electron neutrinos. However, in this method the amplitude of the oscillation depends not only on θ_{13}, but also on several parameters including θ_{23}, and the unknown CP phase δ_{CP} and neutrino mass hierarchy.

Hence, the direct and unambiguous measurement for θ_{13} is through the first method described above i.e through the survival probability $P_{\overline{\nu}_e \rightarrow \overline{\nu}_e}$ of electron antineutrinos produced abundantly in beta decays of fissile nuclei present in nuclear reactor. This has been done in the 1990s by CHOOZ [36] and Palo Verde [37] experiments and recently in Double Chooz, Daya Bay and RENO experiments. The Double Chooz (DC) experiment on which is based this thesis is described in great details in the next chapter. More details on Daya bay can be found in [38]; RENO is described extensively in [39].

1.5.2 Historical measurements

In 2011, almost a decade after CHOOZ and Palo Verde experiments, several hints collectively suggested a non-zero θ_{13}. Indeed, accelerator neutrino experiments MINOS and T2K reported their search for ν_μ to ν_e appearance to be also sensitive to θ_{13}. In particular, T2K disfavored the $\theta_{13} = 0$ hypothesis at 2.5σ [40]. In early 2012, the Double Chooz reactor experiment reported that the $\theta_{13} = 0$ hypothesis was disfavored at 1.6σ based on their far detector measurement [41]. These hints of non-zero θ_{13} culminated in March 2012 when Daya Bay reactor neutrino experiment claimed the discovery of non-zero θ_{13} with a 5.1σ significance [42]. About one month later, RENO confirmed the Daya Bay finding of a non-zero θ_{13} with a 4.9σ significance [43]. The same year 2012, Daya Bay increased the significance to 7.7σ with a larger data set [44]. Non-zero θ_{13} was firmly established with observation of reactor antineutrino oscillation at baselines of kilometers.

In the following, we review in a nutshell in one hand the CHOOZ and Palo Verde experiments and in the other hand the more recent experiments that are Daya Bay, RENO and Double Chooz.

1.5.3 CHOOZ and Palo Verde

Historically, the first attempts in the determination of θ_{13} have been made in the late 1990s to early 2000s by CHOOZ and Palo Verde, two reactor neutrino experiments built in a single-detector configuration at a baseline of about 1 kilometer.

CHOOZ, the ancestor of the current Double Chooz experiment, located in the Ardennes region in France, used a detector mass of about 5 tons and the distance to reactor cores was about 1050 m. The data-taking started in April 1997 and ended in July 1998.

The Palo Verde experiment was located in the United States at the Palo Verde Nuclear Generating Station in the Arizona desert. The Palo Verde detector mass was about 12 tons and the distances to three reactor cores were 750, 890, and 890 m. The data-taking started in October 1998 and ended in

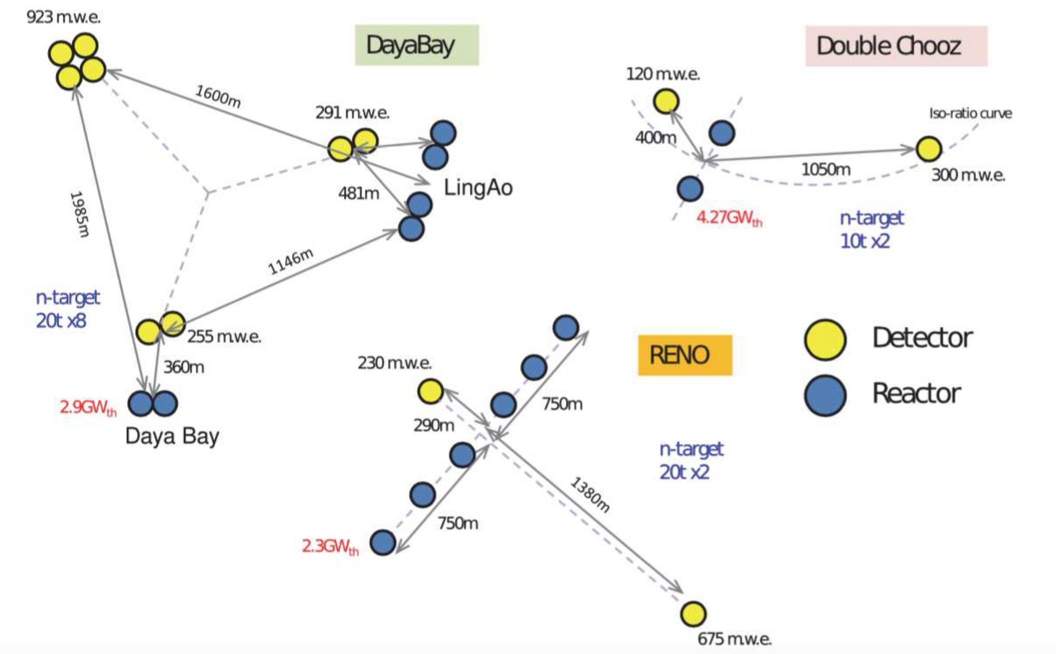

Figure 1.6: *Configuration for three kind of reactor experiments: Daya Bay (China), RENO (Korea) and Double Chooz (France).*

July 2000 [37].

The two experiments did not observe any oscillation; nevertheless, an upper limit of $\sin^2 2\theta_{13} < 0.12$ was set at 90% confidence level by CHOOZ.

1.5.4 Double Chooz, Daya Bay and RENO

Very similar in their design and operation mode, the three experiments look for the disappearance of the electron antineutrinos emitted from the nuclear reactors. Double Chooz, Daya Bay and RENO being reactor experiments have the peculiarity to provide a relatively clean measurement of the θ_{13} mixing angle; this thanks to two majors reasons:

- The disappearance probability (cf. equation 1.37) does not depend on the CP phase δ_{CP}.
- The low-energy range of the reactor electron antineutrinos, of about 3-4 MeV in average, combined to the short baseline (1-2 km) allow to neglect, in first approximation, the matter effect described in the previous section.

Some of the specific differences between the three experiments are gathered in table 1.1 while their distinct configurations are depicted in figure 1.6. The

Features	**Double Chooz**	**RENO**	**Daya Bay**
Power [GW_{th}]	8.5	16.5	17.4
Overburden [m.w.e] Near/Far	120 / 300	120 / 450	250 / 860
Baseline [m]	400 /1050	290 / 1380	360 /500/1580
Target Material Gd-doped Liquid scintillator	PXE-based	LAB	LAB
Mass [tons]	8/8	16 / 16	2×20 4 ×20 4×20
$\sin^2 2\theta_{13}$	0.119 ± 0.016	0.082 ± 0.011	0.084 ± 0.005

Table 1.1: *Specific differences between Double Chooz, RENO and Daya Bay experiments. The latest measurement of* $\sin^2 \theta_{13}$*, and its associated uncertainty, for each experiment is added in the last row.*

antineutrino energy spectrum is obtained as the convolution between the reactor flux and the inverse beta decay cross section. The use of a near detector, which monitors the neutrino flux and spectrum before any significant oscillation, in addition of a far detector that measures the oscillation allows a significant reduction of the uncertainties due to the reactor flux. This two detectors scheme is illustrated in figure 1.7. The θ_{13} value is extracted from the observed energy spectra and ratios to expectations.

Another important detail is the way neutrinos are detected in these three experiments: the inverse beta decay $\overline{\nu}_e + p \rightarrow n + e^+$. The prompt signal comes from the positron scintillation light plus the eventual annihilation photons. The delayed coincidence comes from neutron capture on the gadolinium. Indeed, detectors in Double Chooz, Daya Bay and RENO are functionally similar and designed with an inner volume viewed by a series of photomultipliers tubes and containing a liquid scintillator doped with Gadolinium. For use Gd-doped liquid scintillator, the neutron capture time

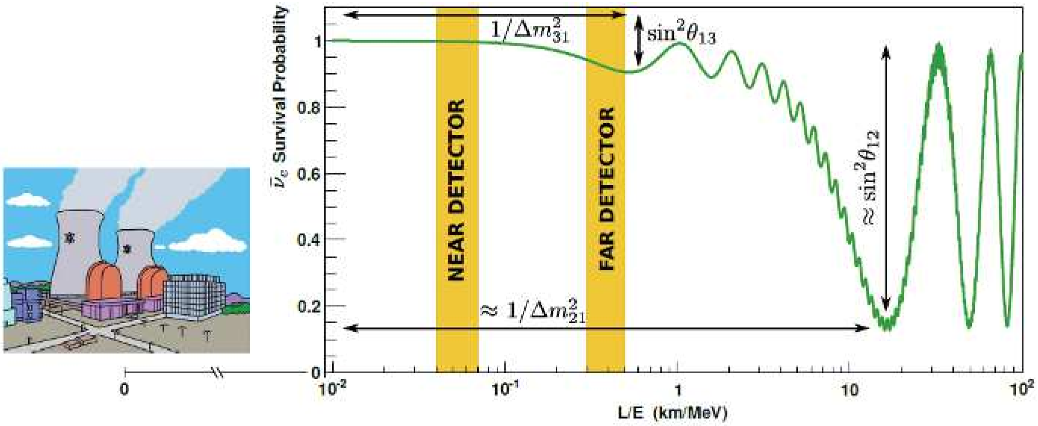

Figure 1.7: *Survival probability of electron antineutrinos as a function of distance from reactors. The coloured bands indicate the detectors locations in the particular case of DC.*

is much reduced. This lowers to about 200 μs the cut on the time difference between the prompt and delayed signals; a significant reduction, compared for instance to the 1 ms of KamLand, that leads to a much reduced accidental background. The two-fold coincidence signature of the signal permits to reduce backgrounds. To reach an high events rate and in order to be located at the maximun oscillation distance, the experiments are built on the site of multi-cores power plants.

The figure 1.10 shows the measured $\overline{\nu}_e$ disappearance probability as a function of L/E in Daya Bay. The best fit curve corresponds to $\sin^2 2\theta_{13} = 0.0841 \pm 0.0027(stat.) \pm 0.0019(syst.)$. The latest Double Chooz result with both near and far detector yielded $\sin^2 2\theta_{13} = 0.119 \pm 0.016$ while RENO has provided a measurement of $\sin^2 2\theta_{13} = 0.082 \pm 0.011$. These values are gathered in the last row of table 1.1 and shown in a comparative way in figure 1.8.

The precision of $\sin^2 2\theta_{13}$ from Daya Bay is better than 4% making it the best measured mixing angle. Given the relatively large value of θ_{13}, the $|\Delta m^2_{32}|$ can be measured using reactor antineutrinos, given the well-controlled systematics regarding detector and the antineutrino flux. In particular, the precision of $|\Delta m^2_{32}|$ from Daya Bay has surpassed the measurements from those from accelerator neutrino and atmospheric neutrino experiments, as shown in figure 1.9.

1.5.5 MINOS and T2K

In MINOS and T2K a proton beam targeted on graphite is used to produce firstly pions which, later on, decay in flight inside a helium-filled pipe to produce predominantly μ^+ and ν_μ. After passing through about 100 m of

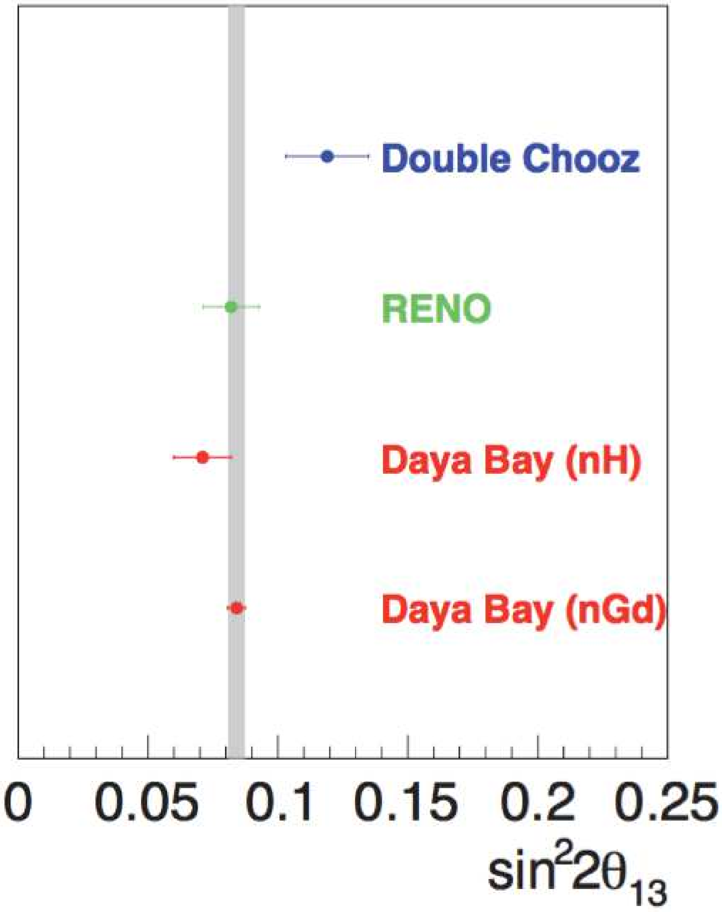

Figure 1.8: *Global results on* θ_{13} *based. From [9] updated.*

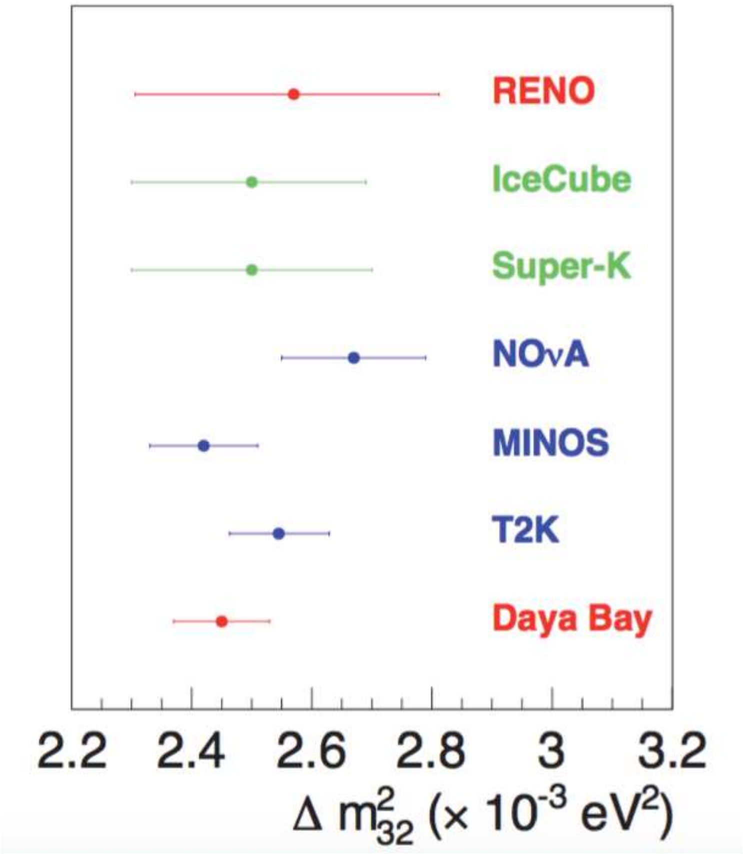

Figure 1.9: *Global results on* Δm_{32}*. From* [40].

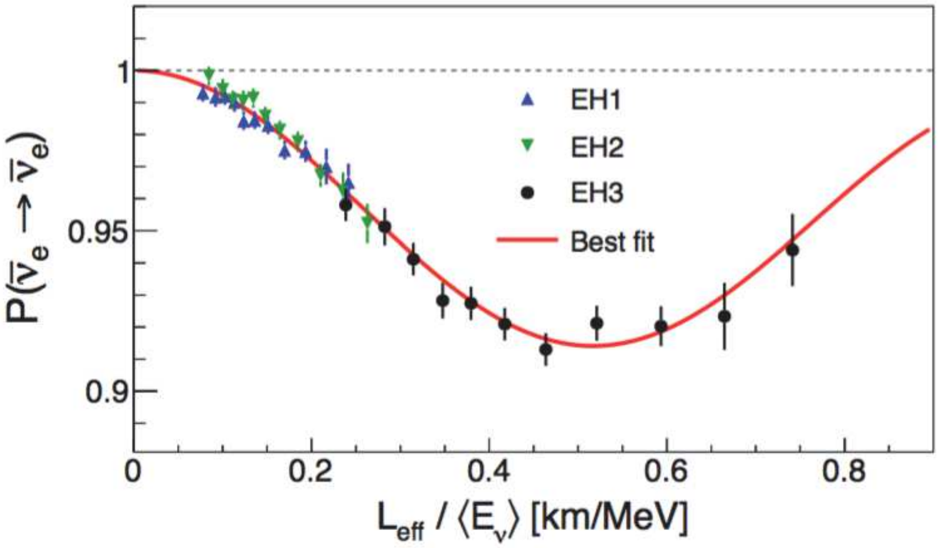

Figure 1.10: *The measured* $\overline{\nu}_e$ *disappearance probability as a function of L/E from Daya Bay* [45]*. The oscillation probability corresponds to* $\sin^2 2\theta_{13} = 0.0841 \pm 0.0027(stat) \pm 0.0019(syst.)$*. The oscillation frequency corresponds to* $|\Delta m^2_{ee}| = 2.50 \pm 0.06(stat) \pm 0.06(syst) \times 10^{-3}\, eV^2$ [40].

ground only neutrinos remain. A few percent of antineutrinos and ν_e nevertheless contaminate the ν_μ beam. Hence, these two experiments use the $\nu_\mu \to \nu_e$ oscillation channel, and search for appearance of ν_e in a detector located further.

The results from MINOS [32] and T2K [34] disfavour a null value of $\sin^2 2\theta_{13}$ at 89% and 99.3% of confidence level respectively.

1.6 Current knowledge on neutrino oscillations

More than 70 years after the "conceptual birth", our knowledge about neutrinos and their properties has increased significantly. This was made possible thanks to several and various neutrino experiments around the world. The table 1.2 from [9] gathers the best-fit values of the 3-neutrino oscillation parameters, derived from a global fit of the current neutrino oscillation data.

Parameter	Best-fit	3σ
Δm^2_{21} $[10^{-5}]$ eV^2	7.37	6.93 - 7.97
$\mid \Delta m^2 \mid$ $[10^{-5}]$ eV^2	2.50 (2.46)	2.37 - 2.63 (2.33 - 2.60)
$\sin^2\theta_{12}$	0.297	0.250 - 0.354
$\sin^2\theta_{23}, \Delta m^2 > 0$	0.437	0.379 - 0.616
$\sin^2\theta_{23}, \Delta m^2 < 0$	0.569	0.383 - 0.637
$\sin^2\theta_{13}, \Delta m^2 > 0$	0.569	0.0185 - 0.0246
$\sin^2\theta_{13}, \Delta m^2 < 0$	0.0214	0.0186 - 0.0248
δ/π	1.35 (1.32)	(0.92 - 1.99) ((0.83 - 1.99))

Table 1.2: *The best-fit values and 3σ allowed ranges of the 3-neutrino oscillation parameters, derived from a global fit of the current neutrino oscillation data (from [9]) . For the Dirac phase δ we give the best fit value and the 2σ allowed ranges; at 3σ no physical values of δ are disfavored. The values (values in brackets) correspond to $m_1 < m_2 < m_3$ $(m_3 < m_1 < m_2)$. The definition of Δm^2 used is: $\Delta m^2 = m_3^2 - (m_2^2 + m_1^2)/2$. Thus , $\Delta m^2 = \Delta m^2_{31} - \Delta m^2_{21}/2 > 0$, if $m_1 < m_2 < m_3$, and $\Delta m^2 = \Delta m^2_{32} + \Delta m^2_{21}/2 < 0$ for $m_3 < m_1 < m_2$.*

The oscillation parameters Δm^2_{12} and $\sin^2\theta_{12}$ have been measured by KamLAND and solar neutrino experiments whereas Δm^2_{23} and $\sin^2\theta_{23}$ values are due to Super-K, together with MINOS and T2K; which are long baseline experiments.

For a long time θ_{13} has been unknown, with respect to the other two mixing angles; the reason why it is also referred to as "the last missing angle". The

$\sin^2\theta_{13}$ value will be finally provided by reactor neutrinos experiments that are Double Chooz, RENO and Daya Bay as already presented in section 1.5.

Despite the progress reported in this section, many others questions about neutrinos, as well as theoretical than experimental, still miss suitable and quantified answers. These open questions are the subject of the next section.

1.7 Open questions

Despite the progress accomplished so far in neutrino physics as much in the theoretical field as in the experimental measurements, many other questions remain nevertheless unanswered today. The first group of these interrogations are related to the mass of neutrinos.

- Although the squared mass differences have now been measured, the absolute mass of neutrinos is still unknown.
- The sign of squared mass differences, except Δm^2_{12}, are not known. Thus, the heavier neutrino, equivalently the lightest neutrino, out the three is not known yet. This is referred as the mass hierarchy problem.
- Apart from the hint that the CP phase $\delta_{CP} \simeq 3\pi/2$ [46], no other experimental information on the CP violation phase in the neutrino mixing matrix is available at present. Thus, the status of CP symmetry in the lepton sector is essentially unknown.
- The theoretical question about the mechanism that attributes to neutrinos their mass particularly low, with respect to other SM particles, is not fully answered. It is natural to relate the smallness of neutrino mass to the existence of a new physics beyond or in the extension of the Standard Model.

An other important interrogation concerns the nature of these particles. Indeed, since they do not carry any electric charge neutrinos can either be Dirac or Majorana particles. In the first case they would have distinct antiparticles while in the second case they would be their own antiparticles.

In astrophysics, cosmic background neutrinos are contemplated to potentially influence the formation of large-scale structures and to contribute to dark matter. However, direct experimental attempts to measure background neutrinos have failed by many orders of magnitude to reach the expected density.

The importance and the number of these questions ensure to neutrino physics a key role in the comprehension of the universe, and for the years to come, a privileged place in scientific research.

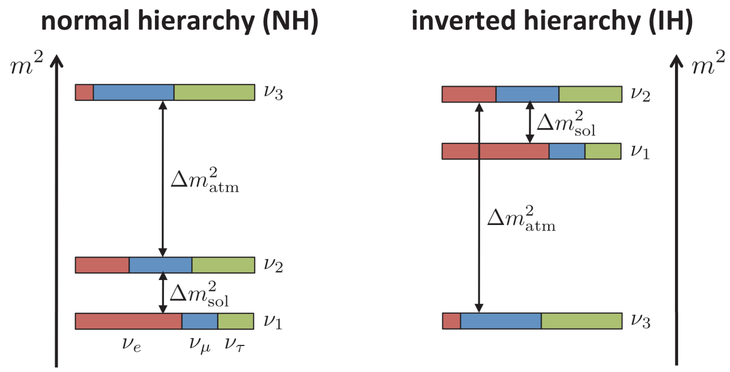

Figure 1.11: *The two neutrino mass hierarchies. An Arbitrary labelling numbers of the massive neutrinos has been used in order to have* $\Delta m^2_{SOL} = \Delta m^2_{21}$ *and* $\Delta m^2_{ATM} = \Delta m^2_{31}$

1.8 Future of research

The future of neutrino research is guided by the open questions mentioned above. A non-exhaustive list of these experiments of the future is presented below.

1.8.1 Mass hierarchy

At the present time, we do not know whether ν_3 neutrino mass eigenstate is heavier or lighter than the ν_1 and ν_2 neutrino mass eigenstates in nature. The scenario in which the ν_3 is heavier, is referred to as the normal hierarchy (NH). The opposite scenario, in which the ν_3 is lighter, is referred to as the inverted mass hierarchy (IH). The two scenarios are illustrated in figure 1.11.

In summary, the mass hierarchy (MH) is as follows

- Normal hierarchy (NH) : $m_1 < m_2 \ll m_3$ and $\Delta m^2 > 0$
- Inverted hierarchy (IH) : $m_3 \ll m_1 < m_2$ and $\Delta m^2 < 0$

with $\Delta m^2 = m_3^2 - (m_1^2 + m_2^2)/2$.

The precise measurement of $\sin^2\theta_{13}$ by the current generation of short baseline reactor neutrino experiments has provided a unique opportunity to determine the MH in a medium baseline ($\sim$ 55 km) reactor neutrino experiment [40].

The MH is the main subject of the JUNO (Jiangmen Underground Neutrino Observatory) experiment[47] in which will be employed a 20×10^3 tons liquid scintillator detector located in a laboratory 700 meters underground. JUNO aims to determine the MH at 3σ sensitivity. This goal relies on a unprecedented $3\%\sqrt{E(MeV)}$ energy resolution, which requires a $\simeq 80$ % photo-cathode coverage, an increase in both liquid scintillator photon yield and attenuation length, and an increase in PMT quantum efficiency in addition of an excellent control of the energy scale uncertainty.

JUNO will detect reactor electron antineutrinos, emitted from two nuclear power plants (Yangjiang and Taishan), via inverse beta decay (IBD). The site location, which is at 53 km from both Yangjiang and Taishan, is optimized to have the best sensitivity for the mass hierarchy determination. The sensitivity aimed is of at least 3σ on the mass hierarchy within 6 years of data taking. The laboratory is under construction in the south of China while the beginning of data taking is expected for 2020.

JUNO is designed to resolve the neutrino MH using precision spectral measurements of reactor antineutrino oscillations[48]. The electron antineutrino survival probability in vacuum can be written as

$$\begin{aligned} P_{\overline{\nu}_e \to \overline{\nu}_e} &= 1 - \cos^4\theta_{13}\sin^2 2\theta_{12}\Delta_{21} \\ &- \sin^2 2\theta_{13}\sin^2|\Delta_{31}| \\ &- \sin^2\theta_{12}\sin^2 2\theta_{13}\sin\Delta_{21}\cos(2|\Delta_{31}|) \\ &\pm \frac{\sin^2\theta_{12}}{2}\sin^2 2\theta_{13}\sin 2\Delta_{21}\sin^2|\Delta_{31}| \end{aligned} \tag{1.42}$$

In equation 1.42 above the ± sign is either + or − according to whether the MH is normal or inverted. Hence, the spectral distortion contains the MH information as it can be noticed on figure 1.12.

Besides the mass hierarchy, the JUNO experiment should be able to provide improved measurements of three mixing parameters Δm^2_{21}, Δm^2_{31}, and $\sin^2\theta_{12}$ with a precision better than 1%.

In addition of the sub-percent precision measurements of solar sector oscillation parameters and atmospheric mass-squared splitting and the MH determination, the 20 kt target mass in JUNO offers a rich physics program of proton decay, geo-neutrinos, superniva neutrinos, and many exotic neutrino physics [40].

A proposal similar to JUNO physics research in Korea, the RENO-50 project [49], is at the design study step. RENO-50 is proposed to employ a 18 kt liquid scintillator detector in South Korea, at a distance of 47 km from the nuclear reactors. Potentially, it can give comparable MH sensitivities to the JUNO experiment [50].

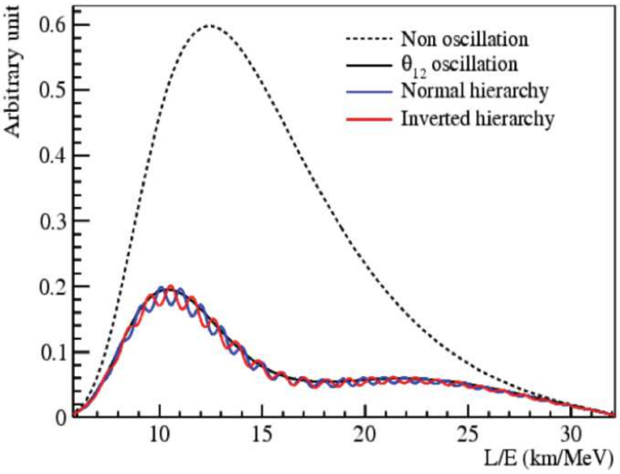

Figure 1.12: *The relative difference of energy spectrum shapes of the reactor antineutrino for different MHs.*

Besides reactor neutrino experiments mentioned here, determination of MH is also expected from future large detectors that fall mainly into three categories: water Cherenkov (PINGU [51], ORCA [52], Hyper-K [53]), magnetized iron tracker (ICal [54]), and liquid argon TPC (DUNE [55]). A time ordered status and prospects summary on MH determinantion can be given as follows [56]

- Today: Super-K, MINOS, and T2K have proof-of-principle results that constrain the mass hierarchy at an insignificant level.
- By 2020: NOvA will have most of its planned data set and can make a statement at $2-3\sigma$ for favorable values of δ_{CP}. For unfavorable values, NOvA's hierarchy measurement will be correlated with its δ_{CP} measurement, and an unambiguous hierarchy determination will not yet be possible. In these cases, combining with T2K will help marginally.
- By 2025: PINGU and ORCA could provide $3-6\sigma$ sensitivity if the experiment is deployed in a timely manner. If the JUNO detector performs as required, a partial JUNO exposure could provide $2-3\sigma$ sensitivity by this date.
- By 2030: some uncertain fraction (<50%) of DUNE's 340-kton-year exposure could be available, yielding sensitivities of $\geq 3\sigma$. Similarly, Hyper-K could provide $2-4\sigma$, and JUNO's sensitivity would reach its design 4σ. Input from cosmology would be firmly in hand. ICAL could reach 3σ by this time.
- By 2035: if DUNE proceeds in a timely manner, a large fraction of its full exposure would be available, and the hierarchy would be defini-

tively established at $> 5\sigma$. Hyper-K would be at or beyond its design $3-6\sigma$.

1.8.2 Nature and absolute mass of neutrino

Beta decay

The current state of knowledge allows to affirm that there are at least two massive neutrinos, one with a mass larger than about $\sqrt{\Delta m^2_{21}} \simeq 9 \times 10^{-3} eV$ and another with a mass larger than about $\sqrt{\Delta m^2_{31}} \simeq 5 \times 10^{-2} eV$ [29]. The most sensitive known method to measure the electron neutrino mass is by observing the electron spectrum in nuclear beta decays

$$N(A,Z) \rightarrow N(A,Z+1) + e^- + \overline{\nu}_e \tag{1.43}$$

where A and Z are respectively the mass and atomic numbers of the parent nucleus. The reaction energy Q_β is defined as the mass difference of the initial and the final states

$$Q_\beta = M_i - M_f - m_e - m_\nu \tag{1.44}$$

M_i and M_f are here, respectively, the masses of the parent and the daughter nuclei. If we neglect the recoil of daughter nuclei in 1.1, then the electron and the antineutrino share the available energy Q_β of the reaction by conservation of the energy. Thus, if antineutrino has zero mass then the maximal kinetic energy T^e_{max}, as it could be seen in figure 1.1 will be Q_β. On the contrary, if this is not the case

$$T^e_{max} = Q_\beta - m_{\nu_e} \tag{1.45}$$

Hence, one could measure the neutrino mass by measuring the shift of the end-point of the electron spectrum even though the frequency of events in this region falls drastically close to zero. Information on the neutrino mass is obtained, in practice, by looking for a distortion of the end point in figure 1.13.

However, the mass of the antineutrino is considered very low compared to the reaction energy Q_β of most nuclei. Also, to expect an acceptable number of events in the region of the spectrum close to the Q_β value, the chosen nucleus must have not only a low β decay transition energy but, as well, a sufficiently short lifetime and therefore a significant activity. The Tritium nucleus with its relatively short half-life ($\tau_{1/2} = 12.3$ years) and a relatively low $Q_\beta = 18.6$ keV has been used in Mainz and Troitzk experiments with, as results, stringent upper bounds on the electron neutrino mass:

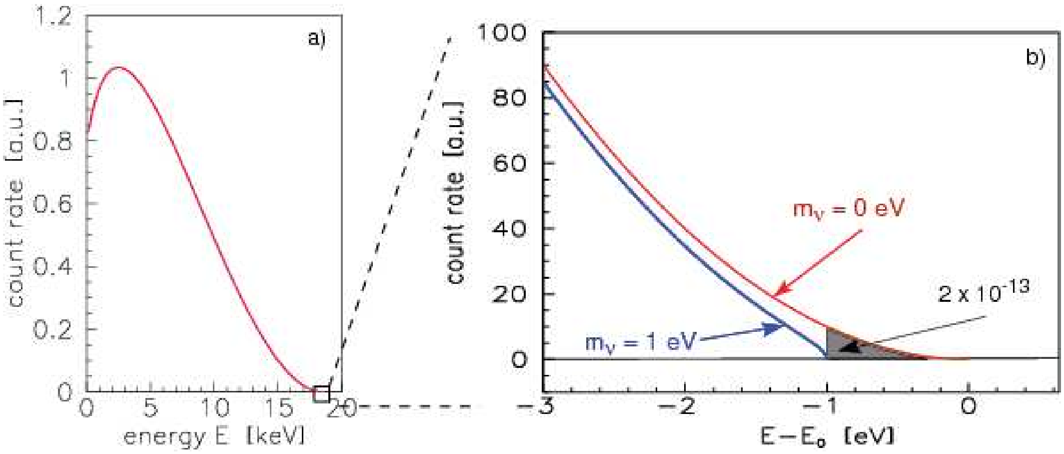

Figure 1.13: *(a) Typical beta decay spectrum. (b) Expanded beta spectrum endpoint for* m_{ν_e} *(red line) and for an arbitrary chosen neutrino mass of 1 eV (blue line). In the case of tritium, the area shaded in grey corresponds to a fraction of* 2×10^{-33} *of all tritium* β *decays.*

- $m_{\nu_e} < 2.3$ eV (95% CL) for Mainz [57].
- $m_{\nu_e} < 2.05$ eV (95% CL) for Troitzk [58].

The Mainz and Troitzk collaborations have merged in a improved experiment called KATRIN[59] that aims a sensitivity of about 0.2 eV. Results are expected within the next 5 years at the time of writing of this volume.

Neutrinoless double beta decay

The most direct way to establish if neutrinos are Dirac or Majorana particles is the observation of neutrinoless double beta decay. Indeed, the double beta decay with two neutrinos

$$N(A,Z) \to N(A,Z-2) + 2e^+ + 2\nu_e \tag{1.46}$$
$$N(A,Z) \to N(A,Z+2) + 2e^- + 2\overline{\nu}_e \tag{1.47}$$

suggested by M. Goeppert-Mayer in 1935 is the radioactive decay in which two protons are simultaneously transformed into two neutrons, or vice versa in the same nucleus [60]. So far, experiments have evidenced 35 isotopes capable naturally of double beta decay. On the contrary, neutrinoless double beta decay proposed in 1939 by W.H. Furry as

$$\begin{aligned} N(A,Z) &\to N(A,Z-2) + 2e^+ \\ N(A,Z) &\to N(A,Z+2) + 2e^- \end{aligned} \tag{1.48}$$

is forbidden in the SM since they do not conserve the lepton number.

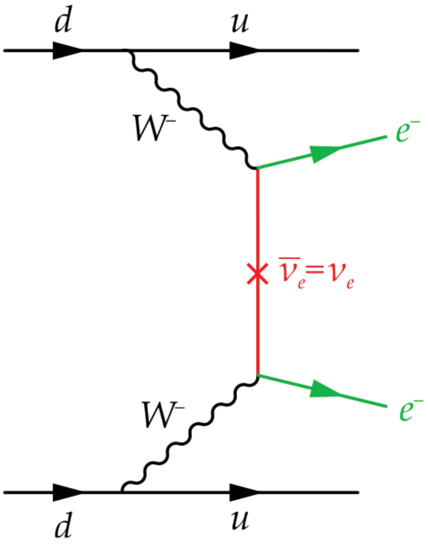

Figure 1.14: *Feymann diagram of the neutrinoless double beta decay process. The total lepton number is violated by two units. The two antineutrino lines join to form a virtual neutrino that propagates between the two leptonic weak interaction vertices. This process is not allowed in the Standard Model.*

However, the neutrinoless beta decay is possible only if neutrinos are massive Majorana particles. In this case, as shown in the Feymann diagram 1.14, there is an exchange of a virtual neutrino which must be of Majorana type for reasons of orthogonality between the eigenstates and the weak interaction [29].

One of the extensions of the Standard Model proposes the existence of a Goldstone boson making double decay a three-body process characterized by the energy spectrum of the electrons produced. This boson is called Majoron and noted χ. In theories of supersymmetry, the exchange of a gluino or a massive neutralino allows the double beta desintegration. These mechanisms imply the existence of a Majorana neutrino.

At present, several experiments, some listed here in table 1.3 have been launched to observe the double β decay without neutrino emission. However, no signal has been detected indisputably yet.

1.8.3 CP phase

As reported in the conclusion of section 1.4.2, since θ_{13} is not null, the Dirac phase δ can generate CP violating effects in neutrino oscillations. The magnitude of CP violation in the lepton sector is related to the determination of the rephasing invariant J_{CP} defined as

Experiment	Isotope	Detector	Status
COBRA	^{116}Cd, ^{130}Te	10 kg CdTe semiconductor	R&D
Super Nemo	^{82}Se	10 kg foils with TPC	On-going
nEXO	^{136}Xe	1 ton enrichided Xe TPC	R&D
GENIUS	^{76}Ge	1 ton enriched Ge in LN_2	R&D
MAJORANA	^{76}Ge	0.5 ton enriched Ge diodes	On-going
XMASS	^{136}Xe	10 t of liquid Xe	Under construction

Table 1.3: *Non exhaustive list of planned and on-going experiments on neutrinoless Double beta decay.*

$$J_{CP} = Im(U_{\mu 3}U^*_{e3}U_{e2}U^*_{\mu 2}) = \frac{1}{8}\cos\theta_{13}\sin 2\theta_{12}\sin 2\theta_{23}\sin 2\theta_{13}\sin\delta \tag{1.49}$$

Inserting the current data from table 1.2 implies

$$J_{CP} = 0.035\sin\delta \tag{1.50}$$

In August 2017, a preliminary analysis of T2K latest data rejects the hypothesis that neutrinos and antineutrinos oscillate with the same probability at 95% confidence (2σ) level by observing a ν_e appearance rate significantly higher than would be expected if CP symmetry were conserved. This result is presented in figure 1.15. As a reminder, in T2K experiment a beam of muon neutrinos is directed towards the Super-K detector, which is 295 km away. T2K measures the oscillation of ν_μ to ν_e. From now on, T2K proposes an extended program to collect more data and achieve 3σ sensitivity to exclude CP conserving values for favorable true values of δ_{CP}.

Besides, several long baseline experiments have been proposed for a direct measure of δ_{CP} via oscillation in matter. One of them is the Deep Underground Neutrino Experiment (DUNE) which will observe neutrinos at the Sanford Lab in South Dakota with a liquid argon detector; these neutrinos produced at Fermilab will travel over a distance of 1,300 km. The experiment sites and the detectors are under construction. The data taking is planned to begin in 2027.

1.8.4 Sterile neutrino

The hypothesis of sterile neutrinos was raised following the observation of what is known now as the *reactor antineutrino anomaly* [61]. These hypothetical particles do not interact via any of the fundamental interactions except gravity.

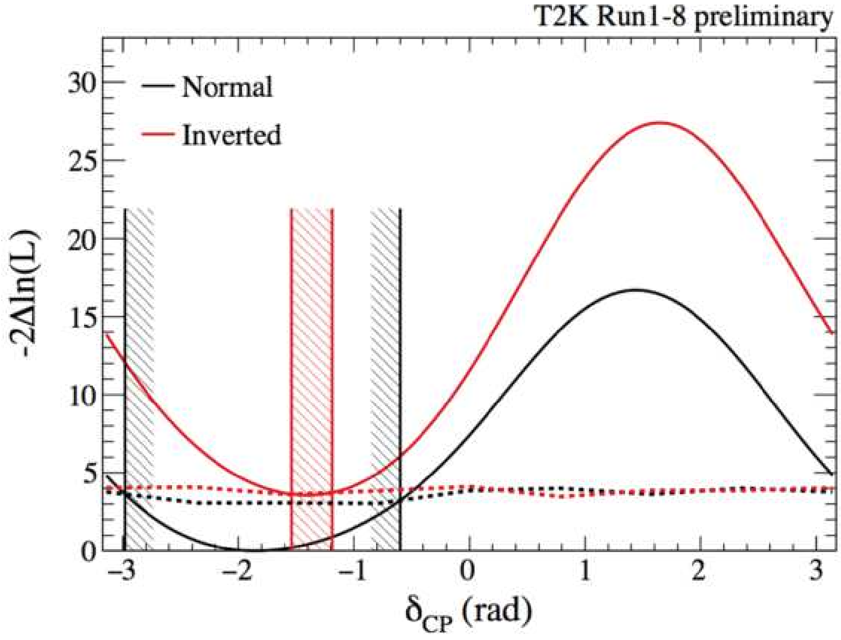

Figure 1.15: $-2\Delta lnL$ *(equivalent of* $\Delta\chi^2$*) as a function of* δ_{CP} *for the normal (black) and inverted (red) mass ordering. The vertical lines show the corresponding allowed 95% confidence interval [34].*

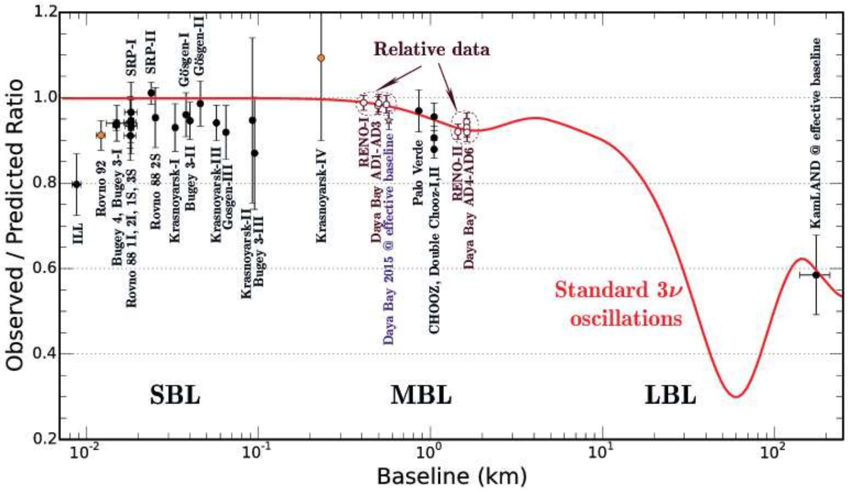

Figure 1.16: *Short baseline reactor antineutrino anomaly. The different experimental results are compared to the theoretical prediction (red line) based on 3-flavours oscillation. A mean averaged deficit of events (≈ 7%) is clearly observed in the short baseline (SBL) sector. From [62]*

Indeed, the anomaly of reactor neutrino was observed by reactor neutrino experiments, after a re-evaluation of the predicted reactor spectra. In a nuclear reactor the main neutrino flux ($0 < E_{\nu_e} < 10$ MeV) is produced by the fission fragments of the four isotopes ^{235}U, ^{239}Pu, ^{238}U and ^{241}Pu. High-precision measurements of the electron spectra of fissioning ^{235}U, ^{239}Pu and ^{241}Pu were collected. From these, the neutrino spectra can be deduced following the laws of energy conservation and under application of a set of energy dependent corrections. Until 2011, a set of reference spectra computed by Schreckenbach et al. were used (for ^{238}U the spectrum was built based on nuclear data bases). The errors on these spectra, however, were with 3 % on average a significant uncertainty in the analysis of the upcoming generation of neutrino experiments, trying to measure the smallest neutrino mixing angle θ_{13}. Hence, a re-evaluation of the neutrino spectra by two independent groups has been performed, using updated nuclear data bases and refined approaches in the application of the correction factors. Both groups found a $\sim 4\%$ increase in the absolute neutrino flux and an increase of about 1.5 % in neutrino detection cross section, which was linked to a change of the measured neutron lifetime, the predicted neutrino flux detected by reactor experiments went up by almost 6 % [63].

Meantime, several reactor experiments with different baselines, as they can be seem gathered in figure 1.16, have measured a neutrino flux systematically lower than the theoretical prediction flux of about 7% on average a deficit: the observed-to-predicted mean ratio of the absolute neutrino rate was found to be $R = 0.936 \pm 0.024$. It is precisely this deficit of 2.7 σ significance is known as the *Reactor Antineutrino Anomaly (RAA)*.

In 1996, the LSND experiment claimed the observation of $\overline{\nu}_e$ appearance in a $\overline{\nu}_\mu$ beam at short baseline (SBL) [64]. The results obtained suppose the existence of an additional mass splitting $\Delta_m^2 \simeq 1eV^2$. Thereby, one or more additional sterile neutrinos should exist in nature.

However, in March 2007, the MiniBoone experiment showed no evidence for ν_μ to ν_e neutrino oscillations in the low energy region as claimed by LSND [65]. Currently, the MicroBoone experiment [66], an upgraded version of the MiniBoone, has been proposed to investigate this controversy. MicroBoone is taking data since 2015. First results are to come in a near future.

Reactor neutrino experiments performed so far, although designed to probe the neutrino oscillation parameters of the three known active neutrinos, measure the neutrino flux but also the energy spectrum and therefore could investigate the sterile neutrino existence (e.g Double Chooz, Daya Bay, etc.). However, the baselines are too long to be sensitive to the Δm$^2 \simeq$ 1eV^2 expected for sterile neutrinos. A new generation of experiments is hence built at shorter baselines of about 20 meters and less. Ideally an oscillation signal is observed as distortion of the measured neutrino spectrum, which changes

Experiment	Technology	M_t	P_{th}	L[m]	R_ν [Day^{-1}]	S/B	$\sigma_{E,Ph}/E$
DANSS	Gd-PS	0.9	3000	10.7-12.7	5000	20	0.18
NEOS	Gd-LS	1	2800	24	1976	22	0.05
Neutrino-4	Gd-LS	1.4	90	6-12	1800	≥ 1	-
STEREO	Gd-LS	1.8	57.8	9-11	300	~ 1	0.05
Solid	^{6}Li-PS	1.6	60-80	6-8	1200	~ 1	0.14
Prospect	^{6}Li-LS	3	85	7-12	660	3	0.045

Table 1.4: *Non exhaustive list of sterile neutrino experiments. Listed are the detector technology (PS: plastic scintillator, LS: liquid scintillator), the target mass M_t, the thermal power of the reactor P_{th}, the reactor to detector baseline L and the signal-to-background ratio S/B. R_ν is the measured (or expected) neutrino rate at reactor on and shortest baseline. The photon statistical part of the energy resolution $\sigma_{E,Ph}/E$ is given at 1 MeV visible energy. From [63].*

with respect to the measurement baseline. In order to observe such a dependence and gain sensitivity, most of these new detectors are segmented, movable or both at the same time. Among these sterile neutrino experiments there are, inter alia, NEOS [67] and STEREO [62]. Table 1.4 summarises the key characteristics of a selection of current very short baseline projects located at nuclear reactors.

NEOS is a non-segmented 1 ton detector, deployed at 23 meters distance from one of the six reactor cores of the Hanbit power plant (Korea), where also the RENO experiment is located. The detector measured about 2000 IBD events per day with a remarkable signal-to-background ratio of 20. It took data for eight months. In the shape-only analysis, for which NEOS compared their measured spectrum to the Daya Bay spectrum as reference, they found no strong evidence to favour a 3+1 scenario over a model with only three neutrinos. In the Δm^2 new range from 0.2 to 2.3 eV^2 they could limit $\sin^2(2\theta_{new})$ to be below 0.1 at a confidence level larger than 90%. The minimal χ^2 value was found for the parameter set $(\sin^2(2\theta_{new}), \Delta m^2_{new}) = (0.05, 1.73 eV^2)$ [63].

In France, the STEREO experiment has designed a 6-cells segmented volume of Gd-loaded liquid scintillator to track the electron anti-neutrino energy spectrum distortion from 3 to 8 MeV due to such a new L/E oscillation, and should therefore confirm or reject the light sterile neutrino hypothesis [62]. The analysis is going on.

Another anomaly was observed in the spectral shape of neutrinos produced at nuclear reactors. Indeed, the monitoring of the neutrino flux from nearby nuclear power plants has revealed an unexpected bump around 5 MeV with 4.1σ significance [68]. This problem known as the *"The 5 MeV excess"* which can be seen on figure 1.17 was first reported by the Double Chooz experiment in 2014 and later confirmed subsequently by RENO and Daya Bay. This anomaly is seen by detectors with different baselines to the reactor core and hence not considered as possible hint of a light sterile neutrino signal. [63]

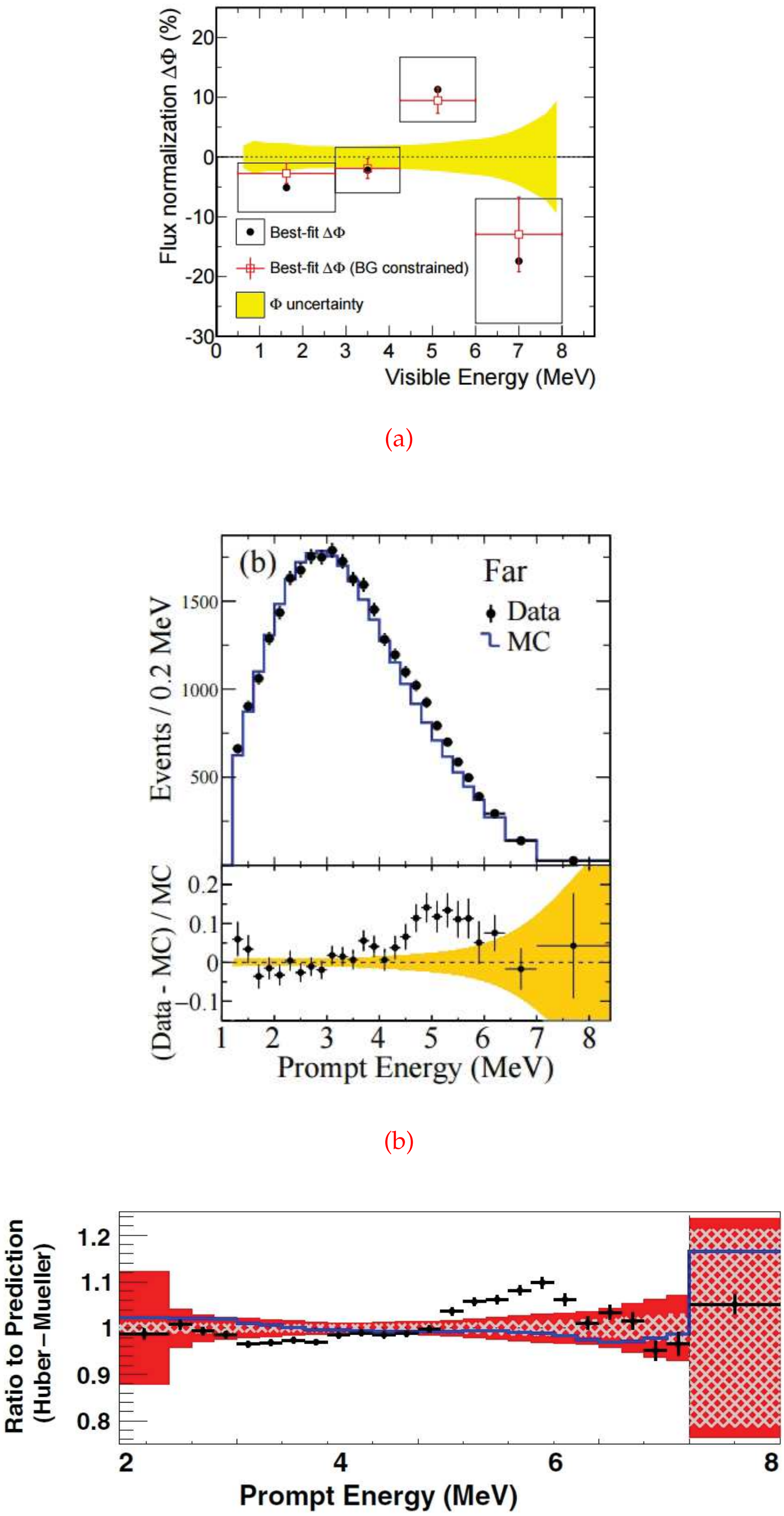

(a)

(b)

(c)

Figure 1.17: *The 5 MeV excess in the reactor neutrinos flux as observed by Double Chooz (a), RENO (b) and Daya Bay (c). Reported first by Double Chooz, the excess was originally not statistically significant. The latest measurement by Daya Bay provides to the excess a local significance of 4.1 σ i.e a probability of less than one in ten thousand for the signal being due to pure chance.*

Chapter 2

The Double Chooz experiment

> *"Pure logical thinking cannot yield us any knowledge of the empirical world; all knowledge of reality starts from experience and ends in it. "*
>
> A. Einstein

2.1 Introduction

The Double Chooz (DC) experiment, as already introduced in the previous chapter, has as principal objective a precise measurement of the θ_{13} mixing angle. In this race, DC has been the first, in November 2011, to release a remarkable result that excluded with 99.73 % of confidence level a null value of θ_{13} after the upper limit of $\sin^2\theta_{13} < 0.02$ set by the CHOOZ experiment [1] in 1997 [69, 70]. The main results of DC can be found in [41] , [71] and [72].

The experiment site is located in the region of Ardennes in France, precisely on the EDF [2] power plant site in the village which gives its name to the experiment, the Chooz village.

2.2 Experimental concept

DC consists in two identical detectors: a near and a far detector (ND and FD) located respectively at an average distance of 400 m and 1050m from

---

[1] The Double Chooz site hosted a previous θ_{13} sensitive experiment, the CHOOZ experiment. The use of two identical detectors is the main improvement that has been brought by Double Chooz.

[2] The French national electricity company.

the two reactor cores as illustrated in figure 7.2. The two detectors, ND and FD, have respectively 300 and 120 meters water equivalent (m.w.e.) rock overburden to shield cosmic muons which constitue, by far, the main source of background in an experiment like this one. The two detectors present two different topologies: flat for the ND and a hill one for the FD.

In this configuration, the Near Detector monitors the flux of electron antineutrinos prior to a significant oscillation while the flux measured in the far detector 1km further allows the comparison from which emerges the oscillation parameter that is θ_{13}. This double detector set-up provides a great improvement in the search of minimisation of the systematic uncertainties due to the relatively low precision with which is known theoretically both the flux and the energy spectrum of the reactor antineutrinos.

The Far Detector was built between 2009 and 2010 and it is taking data since April 2011 while the Near Detector, built between 2011 and 2014, is taking data since January 2015. The FD in the single detector period (2011-2015) is commonly designed as FD-I in DC analysis literature; FD-2 refers to FD in the multi detector period (2015-2018) where data are taken simultaneously in the ND and FD. These two denominations of FD are used in the present text as well.

The electron neutrinos that are detected in DC are produced in the two fission reactors cores of the Chooz power plant during the chain of beta decays of neutron rich nuclei[3]. For each Giga-Watt of thermal power, a typical pressurized water reactor power plant as it is the case in Chooz releases about 2×10^{20} neutrinos per second [29].

2.3 Detector design

For the reactor antineutrinos detection two similar liquid scintillator detectors are used in DC. Indeed, both detectors have an identical design in order to reduce systematic uncertainties as much as possible. As schematized in figure 7.1 each detector can be divided in 3 parts that are the Inner Detector (ID), the Inner Veto (IV) and the Outer Veto(OV).

The whole Far Detector is covered and surrounded by 15 cm of demagnetized steel to suppress external gamma rays. In the Near Detector this role is played by a 15 cm layer of of pure water.

---

[3] The power of a reactor is mainly due to the fission of four isotopes that are ^{235}U, ^{238}U, ^{239}Pu, and ^{241}Pu.

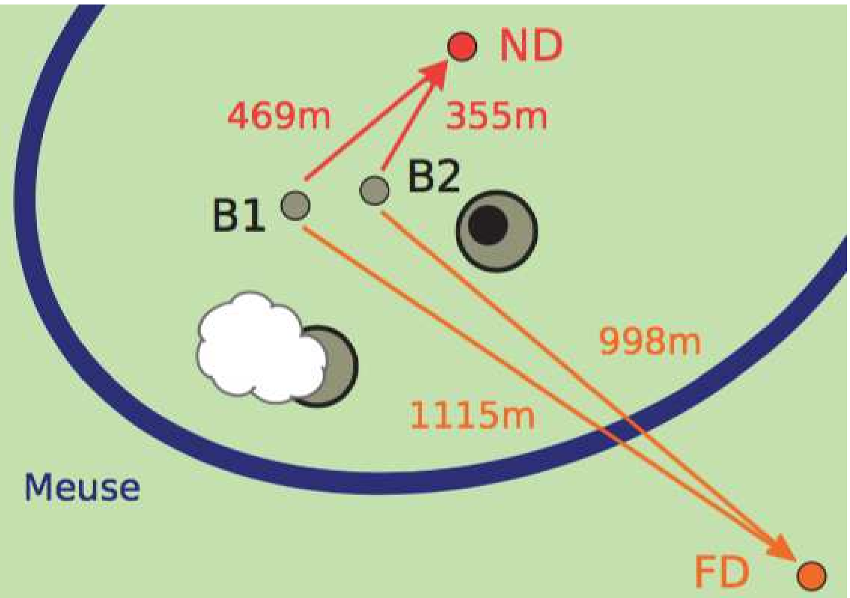

Figure 2.1: *Layout of the Double Chooz experiment. The reactor cores B1 and B2 are indicated in black. From the cooling towers, which make use of the water from the Meuse river, we can see that reactor B2 is off in this schematic, thereby temporarily turning the near detector (ND, red) into a perfect flux monitor of the far detector (FD, orange), at the cost of lower statistics. The distances between the reactor cores and the near and far detectors are next to the arrows representing the direction of the relevant part of the* $\overline{\nu}_e$ *flux, when both reactors are on. From [73]*

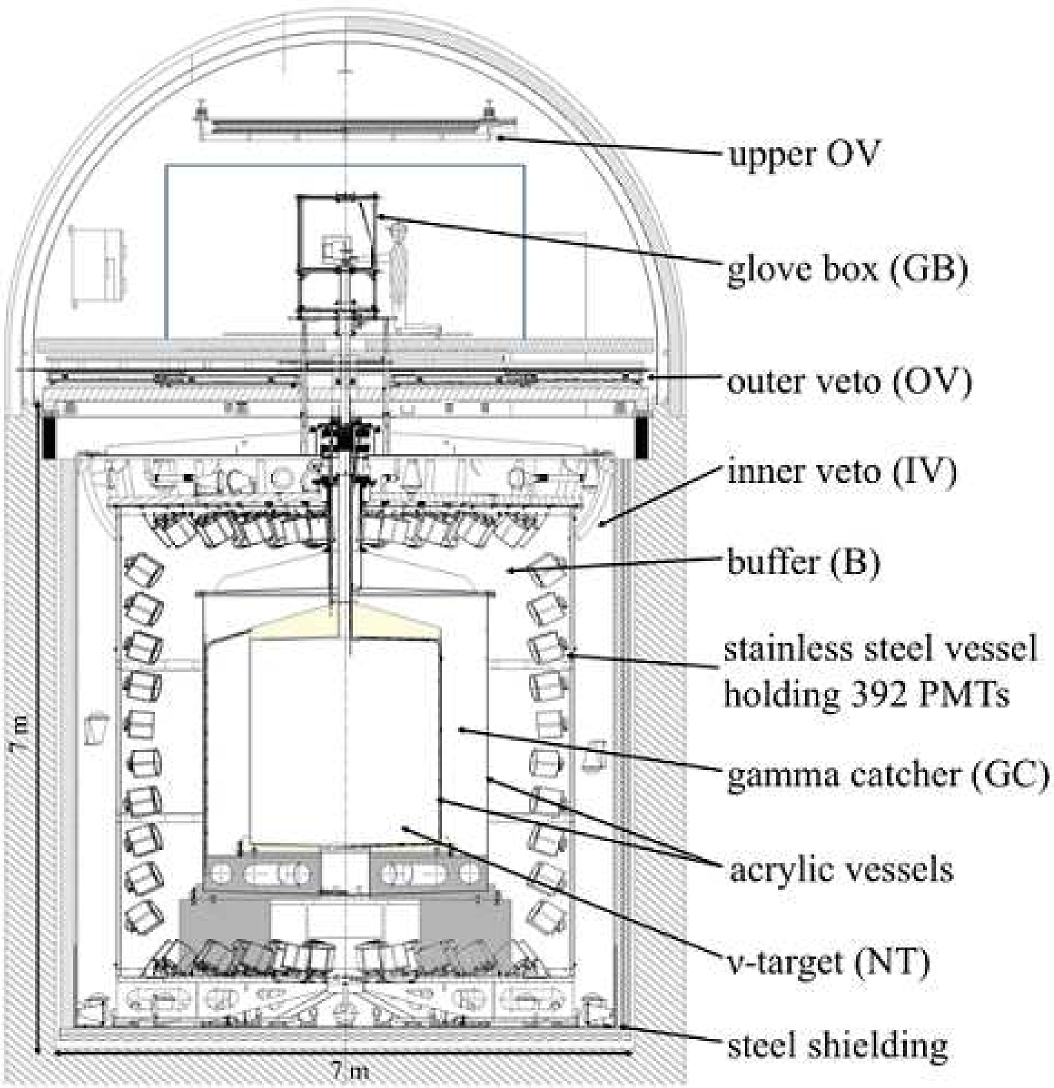

Figure 2.2: *The Double Chooz detector.*

2.3.1 The Inner Detector

The ID consists in a set of 3 concentric cylinders that are the Target (T), the Gamma-Catcher (GC) and the Buffer(B).

- **The Target**, which is the innermost and the main antineutrinos detection volume, is a 8 mm thick transparent acrylic vessel filled with 10.3 m^3 of a novel Gadolinium- loaded organic liquid scintillator. The composition of this liquid scintillator is 80% dodecane ($C_{12}H_26$), 20% PXE (C_6H_18), 7g/L of PPO ($C_{15}H_{11}NO$), 20g/L of bis-MSB ($C_{24}H_22$), and of 1g/L of Gadolinium (Gd). This Gd fraction is enough to capture, in probability, about 85% of neutrons thermalizing in the target.

- **The Gamma Gatcher (GC)** is a 2 mm thick acrylic vessel containing, unlike the target, 22.3 m^3 of Gadolinium-free liquid scintillator. The role of this volume is to detect deexcitation gammas from the neutron capture on Gadolinium which escape from the Target volume. This is important for an accurate reconstruction of the event energy, especially for events occuring near the Target edges. Moreover, for the Gd-analysis[4], the Gamma Catcher acts as an additional shielding protecting the Target from fast neutrons.

  The composition of the GC liquid scintillator was chosen to match the density and light yield of the target liquid, in order to assure the safety of acrylic vessels and increase the uniformity of the detector response. This composition is 30% dodecane, 66% mineral oil (Shell Ondina909), 4% PXE, 2g/L of PPO and 20 mg/L of bis-MSB.

- **The Buffer**, which surrounds the Gamma Catcher, is a 105 cm thick vessel filled with 114m^3 of a highly transparent and non-scintillating oil composed of 47.2% n-alkanes and 52.8% On-dina917 oil. This composition has been chosen to ensure material compatibility with the Gamma Catcher acrylic vessel and with PMTs, and an high transparency in the scintillator emission wavelengths.

  The Buffer liquid is accommodated in a 3 mm steel tank, which also supports the 390 Hamamatsu 10 inches-photomultiplier tubes (PMTs) that covers about 13 % of the surface. The scintillation light produced in the inner two volumes described previously traverses the Buffer liquid and is detected by the PMTs. The buffer volume shields the Target and the Gamma Catcher volumes from radioactivity gammas coming mainly from PMTs. The side walls of the buffer vessel are covered with reflective VM2000 sheets to maximize the light collection.

---

[4] Analysis in which only are considered events whose delayed signal is a capture on Gd

It is the occasion here to say that the Inner Detector composition as described above has encountered two shortcomings at the running time of the detectors. Indeed, unlike the initial design, the analysis of data has revealed the presence of some scintillating liquid in the ND Buffer while the data have evidenced, always in the ND, a leak of Gd from the Target into the Gamma Catcher. The scintillation of the Buffer liquid is detailed in section 2.10.1 and the question of the ND leak is the topic of chapter 5.

2.3.2 The Inner Veto

The Inner Veto (IV) is a 50 cm thick scintillator layer that surrounds the ID and equipped with 78 8-inch PMTs, among which 24 PMTs are arranged on the top, 12 PMTs at mid-height on the side walls and 42 PMTs on the bottom. This PMT spatial configuration has been optimized through MC simulation in order to obtain an homogeneous detector response.

The IV is filled with 90 m^3 of a liquid scintillator, composed of 50% n-alkanes and 50% linear alkyl benzene (LAB) with 2g/L of PPO and 20mg/L of bis-MSB [41]. Optically separated form the ID, the IV is designed to work as an active veto to cosmic muons, to external radioactivity and to fast neutrons from outside of the detector. The IV is contained in a 6.8 m high stainless steel cylinder whose inner surface is painted with highly reflective white coating (AR100/CL) in order to maximize the light collection.

2.3.3 The Outer Veto

The Outer Veto consists of two panels of plastic scintillator strips, one (the lower OV) that covers directly the top of the detector tank and the other hanging on the ceiling of the hall (the upper OV). The OV aims at detecting the passage of cosmic muons. Due to its coverage range larger than the IV diameter, the OV allows also the detection of muons not entering the detector as these muons can interact with the surrounding rock and generate, through spallation reaction, fast neutrons which can later enter the detector.

Each OV panel is made up of two orthogonal layers of modules, an X layer and a Y layer, so that precise coordinate information about the muon can be obtained on both axes.

2.3.4 The chimney

The DC detector is not a fully covered structure. Indeed, as depicted in figure 7.1, a narrow passage linking the ID and the outside, the chimney, is disposed on the top of the detector. The existence reason of the chimney is

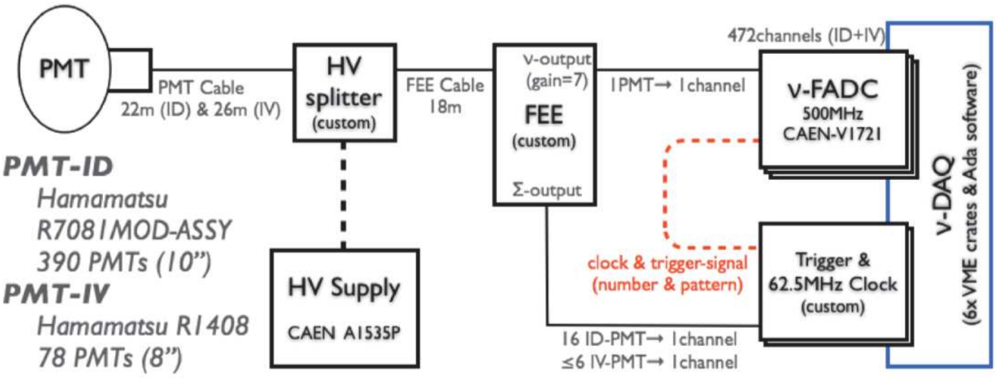

Figure 2.3: *Diagram of the DC readout and ν-DAQ system shared by the ID and the IV. From [76]*

to allow the introduction of liquids and, during the calibration campaigns, the insertion of radioactive sources inside the ID.

The upper OV has been installed to compensate this inefficiency zone created by the chimney since the lower OV leaves this chimney region uncovered.

2.4 The Data Acquisition System

The Double Chooz data acquisition system (DAQ) and readout are composed of two separated sub-systems: the ν-DAQ, shared between the ID and the IV, and the OV dedicated system (OV-DAQ).

2.4.1 ν-DAQ

The DC readout and ν-DAQ system are depicted in the diagram of figure 2.3. PMT signals are processed by custom front-end electronics (FEE) where the signals are optimized for digitization (amplified, clipped, baseline-restored, and filtered for coherent noise) and sent to the flash-ADC digitizing system (ν-FADC). The FEE also sums sets of 8 PMT channels and feeds the summed charge signals to a custom trigger system. To prevent overshoot in the trigger system, the summed signal is truncated after 100 ns by re-adding a delayed signal; this also has the effect of suppressing signals of larger frequency than $\sim$ 1MHz. [74, 75].

The trigger system is designed to be deadtime-free and applied to three groups of PMTs : two groups of 195 PMTs each distributed uniformly around the ID, denoted A and B; and one grouping of the IV PMTs. If the sum of any group is above a specified threshold, all waveforms of all PMTs in the ID and IV are recorded for 256 ns. This threshold is approximately 350 keV of visible energy for the ID, and 10 MeV for the IV which is equivalent to a track of about 8 cm for a minimum ionizing muon. This low threshold of the ID trigger yields an efficiency of 100% with negligible uncertainty at the analysis threshold of 0.7 MeV.

Waveform digitization is carried out by 64 waveform digitizers. Each unit reads eight channels with 8-bit flash-ADCs at a sampling rate of 500 Hz. Each channel has memory composed of 1024 circular buffers, which can each hold a $4 \mu s$ waveform. The 256 ns readout length for each waveform was chosen based on MC studies to sample at least $\sim$ 90% of the scintillation light from the single energy deposition. The dynamic range of the flash-ADC units leads to nonlinear response above 100 MeV visible energy, with significant ($\sim$ 40%) non-linearity estimated above 500 MeV. Periodic monitoring of FADC baselines shows them to be stable to within a single ADC unit, though power-cycling of the units has been observed to induce instabilities in the baselines. This instability induces nonlinearities in single-channel response at low energies, below 2 photoelectrons. However, the effect has been measured using light injection calibration data, and is corrected for in offline processing [75].

2.4.2 OV-DAQ

The OV Data Acquisition System (OV-DAQ), independent from the ID and the IV readout, is responsible for receiving the scintillation light coming from the Outer Veto strips as collected by optical fibers which are connected at one end to a PMT. At the other end of the optical fiber is positioned a mirror in order to reflect the light.

The OV PMT is connected to a custom FEE board allowing adjustment for each channel gain. The signals are converted into electrical impulses with the 64-channel multi-anode PMTs, digitizing the pulse heights. If the signals exceed a common threshold, the trigger is generated and the signals are written and stored in a disk, in a portable format.

2.5 Reactor model

Especially during the first phase of the Double Chooz experiment when only the FD was operational, a precise knowledge of the reactor $\overline{\nu}_e$ flux is mandatory in order to obtain the unoscillated $\overline{\nu}_e$ flux. Indeed, as described in details section 2.13.1, the θ_{13} value is obtained through the ratio of the oscillated and the unoscillated flux. Hence, the simulation of the reactor $\overline{\nu}_e$

flux is a crucial point in reactor neutrino experiments.

Nuclear reactors are intense, isotropic sources of $\overline{\nu}_e$ that are produced in beta decays resulting from fission fragments of the main fuel isotopes: ^{235}U, ^{238}U, ^{239}Pu, and ^{241}Pu. These four isotopes provide the majority of the neutrinos, with $< 0.3\%$ coming from other sources [41]. The instantaneous rate and spectrum of $\overline{\nu}_e$ produced in such decays depends on the total thermal power at which the reactor is operating, the mean cross section per fission, and the mean energy per fission. The modelling of these reactor parameters used to generate the predicted spectrum.

2.5.1 Thermal power

The instantaneous thermal power of each reactor is provided to DC by EDF in time steps of one minute. The thermal power is estimated via measurements of water temperature and flow rate in the primary loop i.e the closed coolant loop in direct contact with the core. This measurement is calibrated once weekly, by measurement of the heat balance at the secondary (steam-generating) loop. The final result has an uncertainty of 0.5% for reactors running at full power (a condition that is true for the majority of our data), and increases at lower power [75].

2.5.2 The mean cross section per fission

The mean cross section per fission indicates the spectrum-averaged cross section for neutrinos interacting in DC, for given relative abundances of the 4 main reactor fuel isotopes. Hence, it is a combination of several factors: the IBD cross section, the neutrino energy spectrum for each fuel isotope decay, and the fractional fission rates of the isotopes [74].

The mean cross section per fission is given by:

$$\langle\sigma_f\rangle = \sum_k \alpha_k \langle\sigma_f\rangle_k = \sum_k \alpha_k \int_0^{\mathrm{inf}} dE D_k(E)\sigma_{IBD}(E) \tag{2.1}$$

where α_k and S$_k$ are the fractional fission rates and neutrino energy spectra for the kth isotope, and σ_{IBD} is the IBD cross section discussed in details in section 2.6 below.

The S$_k$ are derived using beta spectra from the Institute Laue-Langevin reactor (ILL), in conjunction with an updated procedure for conversion from the beta spectrum to the $\overline{\nu}_e$ spectrum. A separate measurement and analysis was performed for ^{238}U. [77]

2.5.3 Fractional Fission Rates

The Chooz reactors are initially loaded with uranium fuel enriched in ^{235}U. The fission of ^{235}U and resultant beta decays produce the majority of the $\overline{\nu}_e$ detected by DC. However, the composition of the fuel evolves in time, with ^{235}U being depleted as it fissions, this process is known as "*burnup*". Meantime, the contribution of other isotopes increases as, for example, ^{238}U captures fast neutrons and beta decays to become ^{239}Pu, which will fission upon absorption of neutrons.

Istope	$\langle\alpha\rangle_k$	$\langle E\rangle_k$ MeV
^{235}U	0.496± 0.016	201.92 ± 0.46
^{239}Pu	0.351±0.013	209.99 ± 0.60
^{238}U	0.087±0.006	205.52 ± 0.96
^{241}Pu	0.066±0.007	209.99 ± 0.60

Table 2.1: *Fractional fission rates and mean energy per fission for the 4 main isotopes in the reactor.*

Therefore, the fractional fission rates (α_k) vary with time, as does the neutrino rate. In order to determine the α_k variation with time and therefore the expected $\overline{\nu}_e$ rate and spectrum it is necessary to perform careful reactor simulations to study the fuel evolution with time.

2.5.4 The Bugey4 normalization

The sensitivity to θ_{13} is limited by the large uncertainties in the reference spectra ($\sim 3\%$) in a single detector configuration. These uncertainties can be reduced using the Bugey4 rate measurement as an effective Near Detector. The Bugey4 measurement was made 15 m from a 2.8 GWth PWR at the Bugey nuclear power plant, and obtained a cross section of $\langle\alpha\rangle_{Bugey} = 5.750 \times 10^{-43}$ cm^2/fission [78]. The normalization of the mean cross section per fission to this rate measurement is done as follows

$$\langle\alpha_k\rangle_{DC} = \langle\alpha_f\rangle_{Bugey} + \sigma_k(\alpha_k^{DC} - \alpha_k^{Bugey})\,\langle\alpha_f\rangle_k \tag{2.2}$$

where the second term reduces the errors due to the uncertainties on the predicted mean cross sections. The obtained correction is small ($0.9 \pm 1.3\%$), allowing to suppress the uncertainties on the reference spectra and letting the main uncertainty to come from the Bugey4 measurement, of about 1.7%.

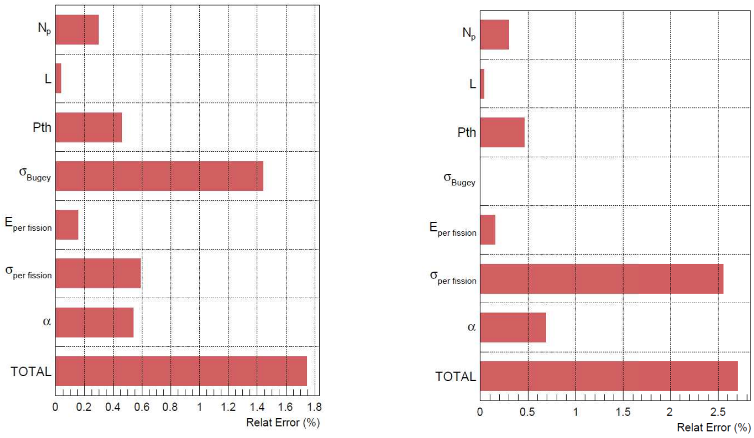

Figure 2.4: *Reactor $\overline{\nu}_e$ rate prediction uncertainty. On the left with Bugey4 normalization, where the main contribution comes from this normalization, of about 1.4%. On the right without the Bugey4 normalization, where the main contribution comes from the mean cross section perfission, of about 2.5%, due to the uncertainties related to the reference spectra.*

The use of Bugey4 correction allows the decrease of the reactor related systematics from 2.7% to 1.7% as shown in figure 2.4.

2.5.5 Reactor $\overline{\nu}_e$ flux simulation

Based on the ingredients mentioned above (thermal power, the mean cross section per fission, fractional fission rates), a precise modelling of the reactor cores has been developed in DC using the MURE framework (MCNP Utility for Reactor Evolution). The main aim of the MURE package is to perform nuclear reactor time-evolution. This framework provides an interface to MCNP using Object-Oriented programming and the ability to calculate nuclear fuel depletion. Neutron transport is performed by Monte-Carlo (MC) transport and depletion is calculated using numerical integration. Successive MC runs and Bateman equation resolutions are performed until the end of the evolution time. Interactions during the evolution calculation allow the user to impose conditions such as power levels, flux, etc. [79].

The Bateman equation allows to compute the nuclei activities (λ) and abundances (N) in a decay chain as a function of time [80]. Equation 2.3 describes the computation of the ith nucleus depletion:

$$\frac{\delta N_i}{\delta t} = -\lambda_i N_i + \sum_j \lambda_j^{j\to i} + \sum_{j'} N_{j'} \langle \sigma_{j'} \rangle^{j'\to i} \langle \phi \rangle - \sum_r N_i \langle \sigma_i \rangle^{(r)} \langle \phi \rangle \tag{2.3}$$

Where N$_i$ is the initial abundance of the ith nucleus, and λ_i its initial decay rate. j is the jth nuclei in the material, with $\lambda_j^{j\to i}$ the rate of its decays on the ith nucleus and N$_j$ its initial abundance.

This computation is done after each MCNP execution: particle transport is simulated via MCNP and then the nuclear fission rate is computed by MURE. The result on the fission rates is normalized by the reactor thermal power and the boron concentration in the reactor. The boron concentration has a great influence over the fission rate as the boron is used as a neutron absorber inside the reactor, due to its high thermal capture cross-section. These data are provided by EDF via the EXALT database. Due to the confidentiality of these data, the database access is allowed only onsite. In order to use these data, in-charge experts have to download the data from the onsite access and to fix the potential issues in these data. Indeed, these data can be unavailable in some cases (detector failure, data corruption, etc.) and have to be corrected before being used by the collaboration. The time periods without data are not used to measure θ_{13}, yet it is difficult to exclude time periods from the reactor simulation. Then these data correction are critical to not bias the reactor simulation and so the fission rate prediction [77].

2.6 Neutrino detection

Neutrinos are detected in DC, as in their first time by Reines and Cowan, through the inverse beta decay (IBD):

$$\overline{\nu}_e + p \rightarrow e^+ + n \tag{2.4}$$

in which the interaction of $\overline{\nu}_e$ with a proton produces a positron and a neutron. In this reaction the positron annihilates immediately with one electron of the complex after having, or not, ionized an atom in his path. This constitutes the prompt signal that will be viewed by the detector. Later on, the neutron, after thermalisation, is captured either by a Hydrogen or a Gd nucleus whose deexcitation produces the delayed signal. According to the nucleus capturing the neutron the energy released and the mean capture time are not the same; these different values are presented in table 2.2 below. This prompt-delayed coincidence is the first signal selection criteria that allows to distinguish the antineutrino events from a certain number of backgrounds.

Hydrogen	Energy released : 2.2 MeV Mean neutron capture time : $\Delta t \simeq 200$ μs
Gadolinium	Energy released : 8 MeV Mean neutron capture time : $\Delta t \simeq 30$ μs

Table 2.2: *Characteristics of neutron capture in DC exeperiment.*

By energy conservation, the equation 2.4 allows to relate the neutrino and the positron energies as follows

$$E_\nu = E_e + T_n + m_n - m_p \tag{2.5}$$

where T$_n$ is recoil energy of the neutron.

In general, the threshold for a scattering process of type [29]

$$\nu + A \rightarrow \Sigma X \tag{2.6}$$

is given by

$$E_\nu^{th} = \frac{(\Sigma m_x X)^2}{2m_A} - \frac{m_A}{2} \tag{2.7}$$

From this and neglecting the small recoil of the neutron, the neutrino energy threshold in an IBD process is straightforward

$$E_\nu = \frac{(m_n + m_e)^2) - m_p^2}{2m_p} \simeq 1.806 \quad MeV \tag{2.8}$$

This energy threshold reduces significantly the fraction of electron antineutrinos from the reactor that can be detected since about 75% of them have an energy lower than this value. The figure 2.5 shows the energy spectrum of electron antineutrinos detected; this spectrum is obtained as the product between the reactor neutrino flux and the IBD cross section.

The reason why the IBD is the detector reaction choosen in essentially all reactor neutrino oscillations experiments is its relatively large cross section in addition of the extremely convenient correlated signature of the positron emission followed by the delayed and spatially correlated neutron capture.

Besides, the IBD cross section has been measured in the reactor-based short-baseline experiments [81]; namely in the Bugey4 and Daya Bay experiment thanks to the large statistics accumulated :

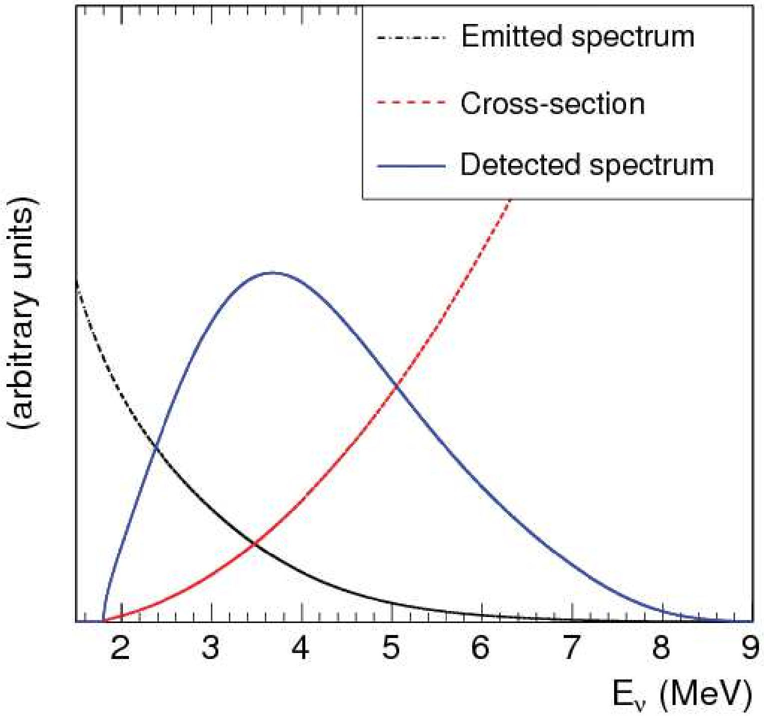

Figure 2.5: *Reactor $\overline{\nu}_e$ energy spectrum (in blue) obtained as a convolution between the IBD cross section (in red) and the reactor $\overline{\nu}_e$ flux (in black).*

$$\sigma_{exp}(Bugey4) = (5.75 \pm 0.08) \times 10^{-43} \quad cm^2/fission \tag{2.9}$$

$$\sigma_{exp}(DayaBay) = (5.92 \pm 0.14) \times 10^{-43} \quad cm^2/fission \tag{2.10}$$

Recent developments have reported a reactor antineutrinos flux and spectrum higher than the measurements [82], $\sigma_{measured}/\sigma_{expected} \simeq 0.94 \pm 0.03$. This discrepancy is generally attributed to the difficulty of fissile antineutrino modeling and an underestimation of contributions of unknown fission fragments to a generation of the antineutrino energy spectrum. In fact, this discrepancy is directly related to the reactor anomaly mentioned in section 1.8.4. The debate on this issue is not closed yet.

2.7 Energy calibration of the detectors

The calibrations of the detectors are essential since they allow to set the correlation between the number of photo-electrons as measured by the detector and the true energy deposited in it. For this purpose, radioactive sources, which have the advantage to release fixed and well-known energies, are used.

The calibrations of the DC detectors are performed during several campaigns at different periods with variated radioactive sources. Four radioactive sources have been used so far: ^{137}Cs, ^{68}Ge, ^{60}Co and ^{252}Cf.

The sample of events from the decays of these radioactive sources is obtained by subtracting, from the data collected during the calibration campaign, the background events. Here the background consists in all other events including the $\overline{\nu}_e$. The energy spectrum obtained is scaled to the duration of the calibration run and then subtracted to the energy spectrum obtained from the calibration run. According to the radioactive source involved, a different strategy is used.

- **Gamma sources (^{60}Co, ^{68}Ge and ^{137}Cs)** : the energy spectrum is fitted with a Gaussian function to measure the maximum value position. The peaks positions are expected at 2.505 MeV MeV for ^{60}Co, 1.022 MeV for ^{68}Ge and 0.661 MeV for ^{137}Cs.

- **^{252}Cf** spontaneously fissions by emitting gammas and neutrons. In this case each sample is fitted with two Gaussians, one for the Gd capture peak and the other for the H capture peak.

Two distinct systems are used for the deployment, in the detectors, of the four radioactive sources mentioned above. These systems are reffered to as the *The Z-Axis* and the *Guide Tube* systems.

2.7.1 *Z-Axis* calibration

The *Z-Axis* deployment system allows light sources and radioactive sources to be deployed directly into the Target along the Z axis from the top of the chimney all the way to the bottom of the NT.

On the *Z-Axis*, sources are deployed via a motorized pulley-and-line system down through the chimney of the detector to different vertical positions known each to a precision of 1 mm. For each of these positions data are collected during few hours depending the activity of the source and the amount of data needed. A glove box (cf. figure 7.1) mounted at the top of the detector chimney is used as a source deployment interface. The interior of the glovebox is pressurized with nitrogen above ambient pressure in order to maintain clean and radiopure detector conditions while in use.

2.7.2 *Guide Tube* calibration

Besides the *Z-Axis* system, radioactive sources are also deployed into the Gamma Catcher by means of a rigid, hermetic, looped, stainless steel *Guide Tube* (GT) as illustrated in figure 2.6. Sources are driven through the length of the tube on the end of a wire, driven by an electric motor.

The GT is designed to allow source deployment in the GC. It is made of stainless steel and runs along the outer wall of the NT and the inner wall of the GC, as depicted in the GC region in figure 2.6. Certain positions are chosen to place sources, and the calibration data at those locations are useful for studies such as detection systematics evaluation in the GC.

2.8 Event reconstruction

2.8.1 Pulse reconstruction

The first step in event reconstruction in DC is the pulse reconstruction. For that purpose, the total charge of the event signal , i.e. the sum of integrated amplitudes of the waveforms over all PMTs, and the corresponding time are extracted from the digitized waveform recorded by the flash-ADC [83]. To compute the pedestal value B_{mean}, which is the mean ADC counts, and its deviation, B_{rms}, periodic triggers are taken with a rate of 1 Hz for the full

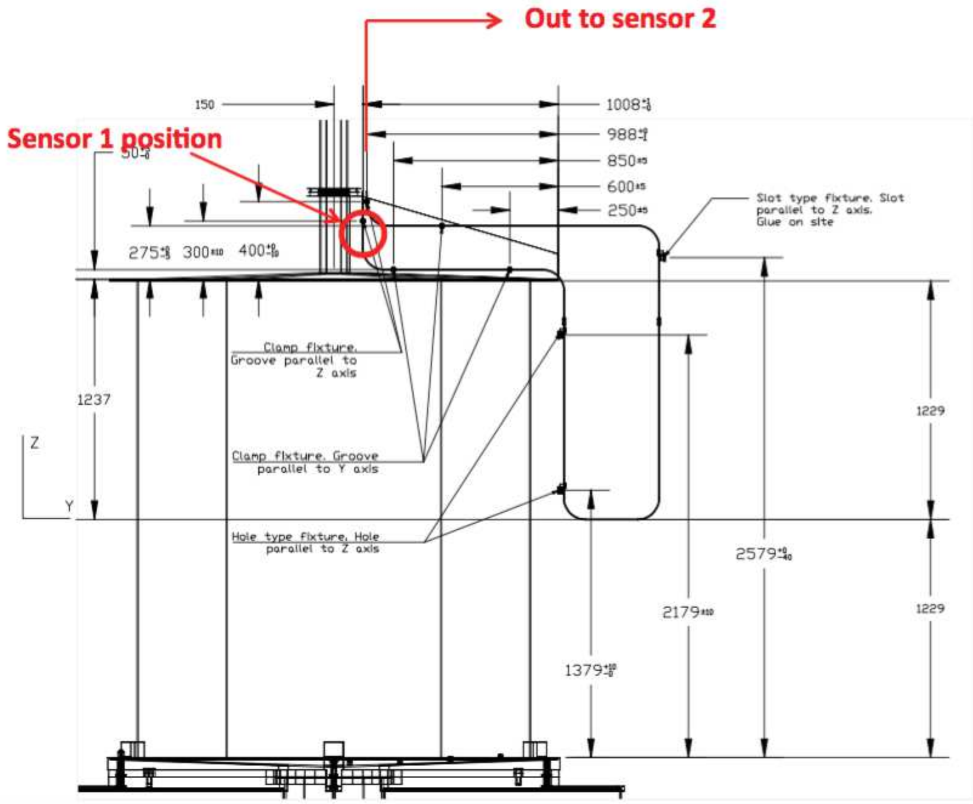

Figure 2.6: *GT deployment system. The path of the radioactive sources through the Guide Tube system allows different calibration positions in the Gamma Catcher. Within the tube, the position of sources is known to 1 cm.*

256 ns of the readout time window. Hence, the integrated charge is given as the difference between total counts during the integration time window and the pedestal value B_{mean}.

A default integration time of 112 ns, i.e. 56 unit time of 2 ns bins, has been chosen to optimize the charge resolution of single photo-electron (p.e) signal, energy resolution and charge integration efficiency [72]. In order to discriminate against noise fluctuations in the absence of an effective p.e. signal, the condition of $Q_{tot} > B_{rms} \times (N_s)^{1/2}$ is required; N_s being the number of samples in the integration window, thus $N_s = 56$ for a 112 ns window.

2.8.2 Vertex reconstruction

A dedicated maximum likelihood based algorithm, named RecoBAMA, using charge and time is used in DC to reconstruct the vertex position of each event. In this algorithm, the event is assumed to be a point-like light source while the light itself is assumed isotropic. The event likelihood is defined as follows

$$\mathcal{L}(X) = \prod_{q_i=0} f_q(0; q'_i) \prod_{q_i>0} f_q(q_i; q'_i) f_t(t_i; t'_i; q'_i) \tag{2.11}$$

where q_i and t_i are the observed charge and time for the i-th readout channel, respectively. q'_i and t'_i are the expected charge and time for each channel from a point-like light source with the position, time and light intensity per unit solid angle Φ given by $X = (x, y, z, t, \Phi)$. f_q and f_t are the probability to measure the charge and time given the predictions. The best possible set of X is found by maximizing $\mathcal{L}(X)$, which is equivalent to minimizing the negative log-likelihood function [84]:

$$F_V = -\ln \mathcal{L}(X) \tag{2.12}$$

A direct way to test the accuracy of the algorithm reconstruction is to use the radioactive calibration sources at different well known positions in the detector and then compare to the positions provided by the algorithm. Indeed, it was demonstrated that the vertex reconstruction reproduces the deployment positions of radioactive sources in calibration campaigns [85].

Beside RecoBAMA, another vertex reconstruction algorithm, called RecoJAPAN, has been developed by the Niigata group[5]. Figures 2.7 and 2.8 show comparisons of RecoBAMA and RecoJAPAN for the vertical and radial reconstructions. RecoJAPAN algorithm uses different pull term strategies and does not force vertices inside the detector, hence some differences arise with

---

[5] One of the DC work groups, based in Japan.

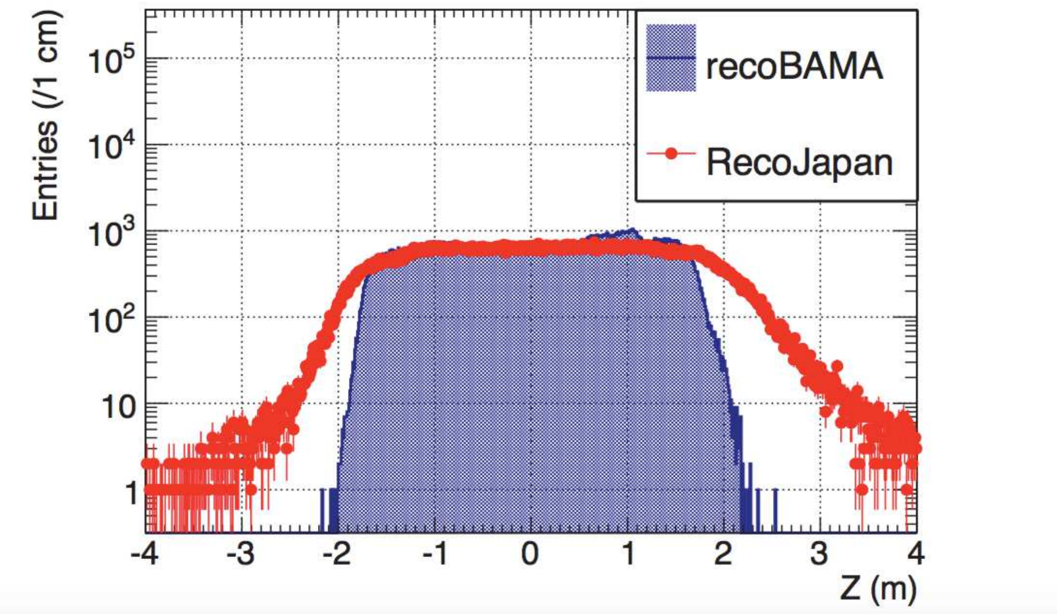

Figure 2.7: *Z coordinate distribution as reconstructed by RecoBAMA (blue) and RecoJAPAN (red).*

respect to RecoBAMA as it can be seen in these comparison figures [86]. Indeed, these particular differences are exploited for background subtraction in section 2.10.3.

2.8.3 Energy reconstruction

The total number of photo-electrons collected by the PMTs allow to reconstruct the visible energy E$_{vis}$, for the data and the MC, as following

$$E_{vis}^{Data} = N_{pe} \times f_u^{data} \rho, z \times f_{MeV}^{data} \times f_s(E_{vis}^0, t) \tag{2.13}$$

$$E_{vis}^{MC} = N_{pe} \times f_u^{MC} \rho, z \times f_{MC}^{data} \times f_{nl}(E_{vis}^0) \tag{2.14}$$

where the radial distance ρ from the detector central axis and the vertical coordinate z represent the vertex position; t is the event elapsed time. Different corrections, described in a series of sections below, for the uniformity (f_u), absolute energy scale (f_{MeV}), time stability (f_s) and non-linearity (f_{nl}) are applied to get the final visible energy. E_{vis}^0 is the energy after applying the uniformity correction, which is subsequently subject to the energy-dependent corrections for the stability and non-linearity [72].

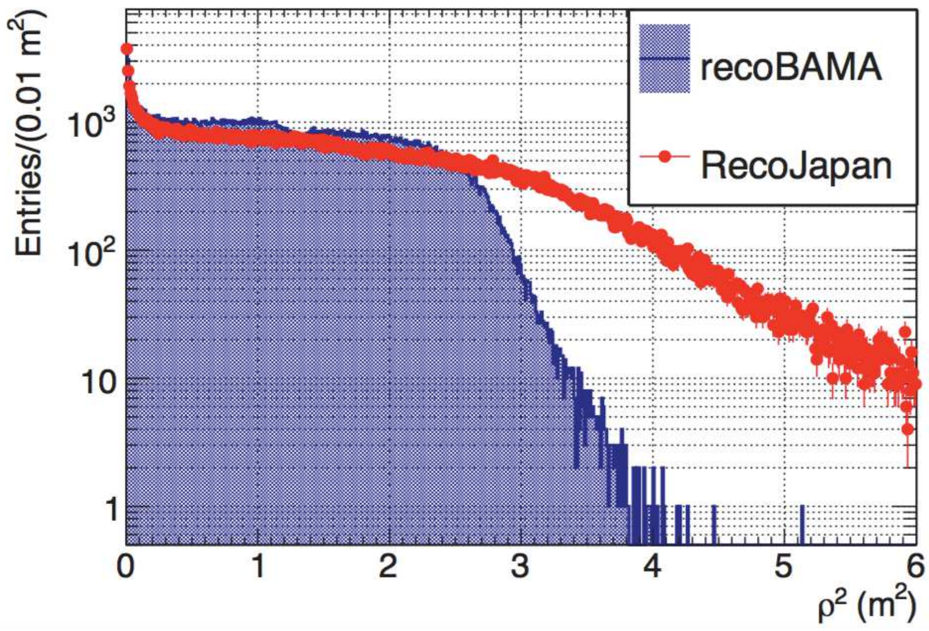

Figure 2.8: *Radial coordinate distribution as reconstructed by RecoBAMA (blue) and RecoJAPAN (red).* $\rho^2 = x^2 + y^2$.

The uniformity correction

The detector response, namely the number of collected photo-electrons N_{pe}, is dependent of the vertex position. It is in order to take into account this effect in the visible energy reconstruction that the uniformity correction is applied to convert N_{pe} into its equivalent if the vertex was at the center of the detector.

The figure 2.9 shows how the function $f_u(\rho, z)$ for the data is obtained using neutron captures on H, which peak at 2.2 MeV. The correction factor ranges up to around 5% inside the NT. The systematic uncertainty due to the non-uniformity of the energy scale is evaluated to be 0.36 % [72].

Non-linearity correction

The total number of photo-electrons is given by

$$N_{pe} = \sum_i \frac{q_i}{G_i(q_i, t)} \tag{2.15}$$

where q_i refers to the charge collected in each readout channel. The gain G_i is a charge-to-p.e. conversion factor extracted by calibration and which has a time and charge dependence. This is referred as the gain non-linearity.

To measure the gain non-linearity, calibration data are taken at different pe-

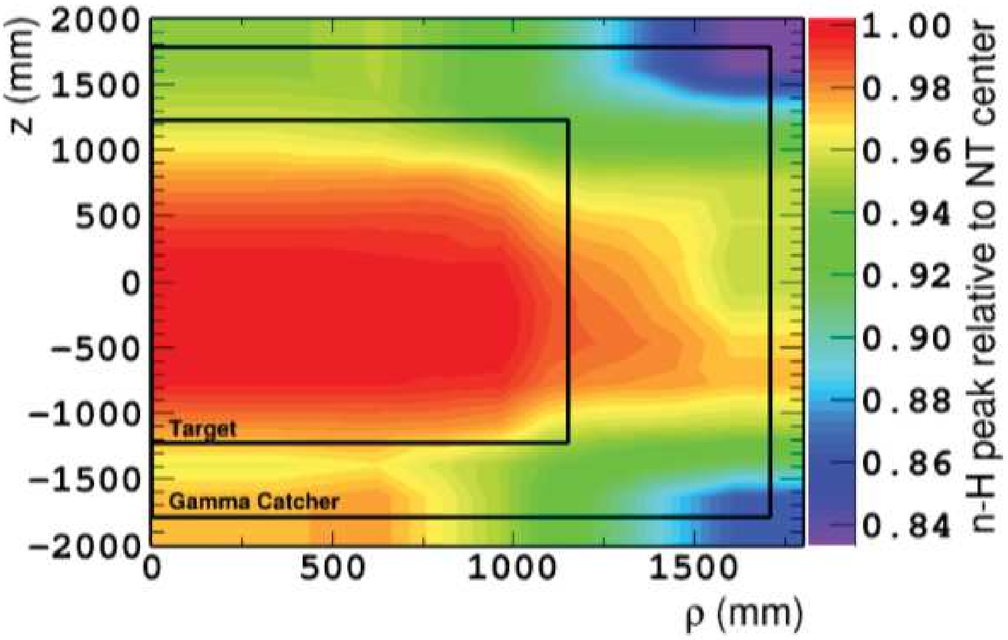

Figure 2.9: *Uniformity correction map for the data obtained by fitting the neutron capture peak on hydrogen.*

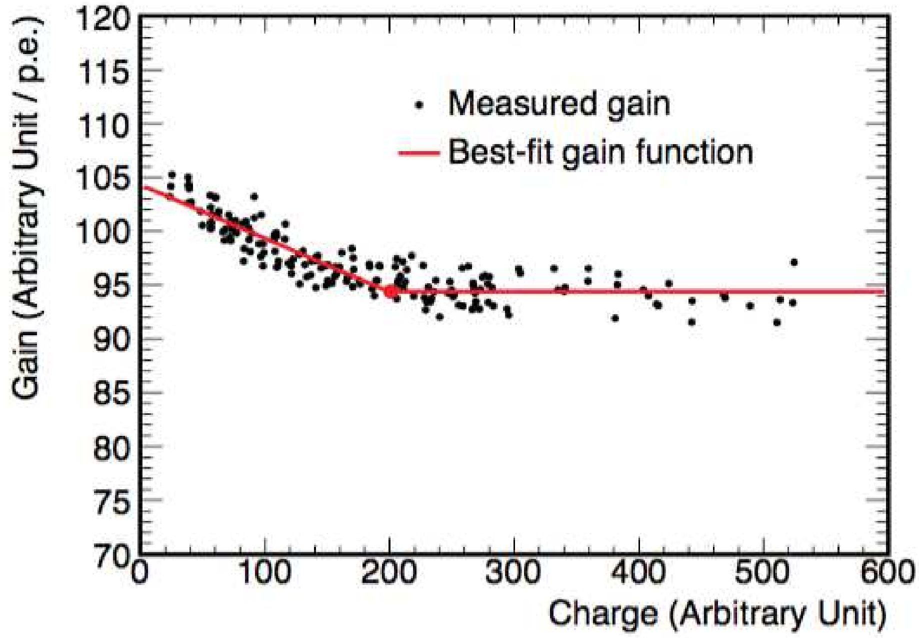

Figure 2.10: *Gain as a function of integrated charge for a typical readout channel. The gain function is obtained as a fit, in red, of the measurements data points.*

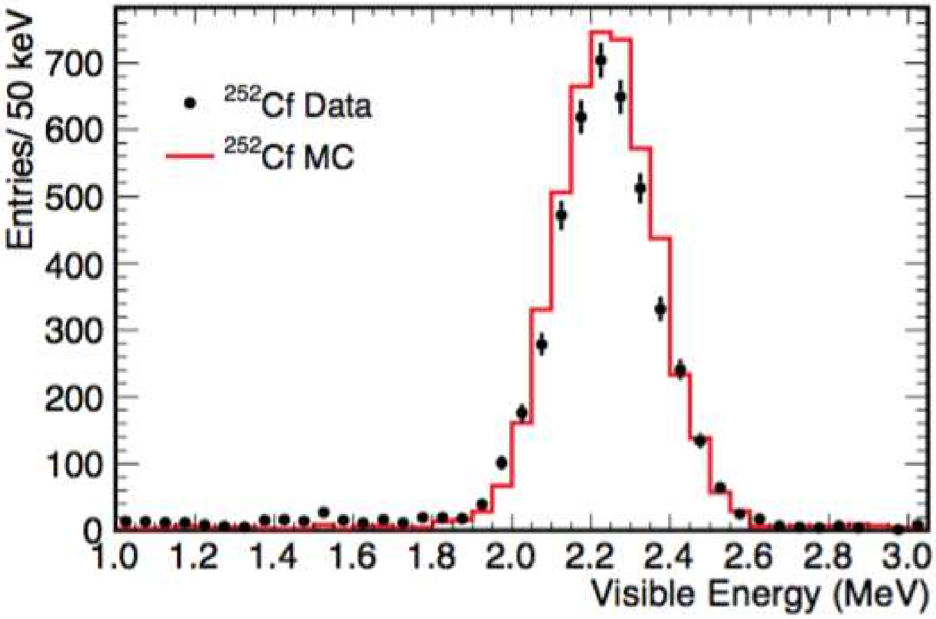

Figure 2.11: *Neutron capture peak on hydrogen: points show the data taken with ^{252}Cf neutron source deployed at the center of the detector and the histogram shows the corresponding MC simulation.*

riods and with different light intensities and positions. The measured gain as a function of integrated charge is shown in figure 2.10 where the gain correction function is characterized by a constant gain at high charge and a linear slope at low charge.

Energy scale calibration

The absolute energy scale that provides the p.e. to MeV conversion is determined by the position of the well known 2.2 MeV peak of neutrons capture on H as shown in figure 2.11. For this purpose the data are taken with a ^{252}Cf neutron source deployed at the center of the detector. The absolute energy scale was found to be 186.2 p.e./MeV for the data and 186.6 p.e./MeV for the MC [72].

Energy non-linearity correction

The visible energy as provided by the MC and the data are not linearly correlated. This non-linearity arises from two others that are the charge nonlinearity (QNL) and the light non-linearity (LNL) observed in data. Indeed, QNL is associated with the modeling of the readout system and charge integration algorithm, whereas the LNL correction arises from the scintillator modeling.

The energy non-linearity correction function is given as

$$f_{nl}(E^0_{vis}) = (0.0023 \times E^0_{vis}[MeV] + 0.9949) \times (-0.027/E^0_{vis}[MeV] + 1.008). \tag{2.16}$$

where the two factors account respectively for the QNL and the LNL corrections.

In sunmmary, the discrepancy of the energy response between the data and MC can be understood as a consequence of systematic bias in the modeling of the scintillator and of the charge reconstruction algorithm.

Stability correction

Since the mean gain and the detector response variate over time, the reconstruction of the data visible energy is affected and, then, needs to be corrected of this variation. This correction is performed, to monitor stability, by using together the muon-induced spallation neutrons captures and the α decays of ^{212}Po [6] [87]. The original 8.8 MeV of ^{212}Po α particles ends in a visible energy energy of about 1 MeV as a consequence of the quenching effects; this allows to monitor the stability in the low energy region distinctly below neutron capture peaks (2.2 MeV for H and 8 MeV for Gd).

The stability of the peak energy of ^{212}Po α decays and neutron captures on H and Gd after the application of the correction is shown in figure 2.12. Time variations of the visible energy are measured to be 0.70% at 1 MeV, 0.17% at 2.2 MeV and 0.25% at 8 MeV from the standard deviations of the peak energies.

2.8.4 Muon track reconstruction

The algorithm that reconstructs the muon track uses mainly the time information from the ID and IV, and the spatial information from the OV if the muon has crossed this detector. The algorithm assumes that muons are through-going, but if the energy deposited suggest that a muon may have stopped in the ID, the algorithm also performs a fit under this hypothesis.

In a first time the algorithm fits each muon event by ignoring the OV information and then, later on, fits again the event with the OV as a constraint. Among the fits performed, one result is chosen as the best using the criteria

---

[6] ^{212}Po are collected using the ^{212}Bi- ^{212}Po decay chain coincidence signals

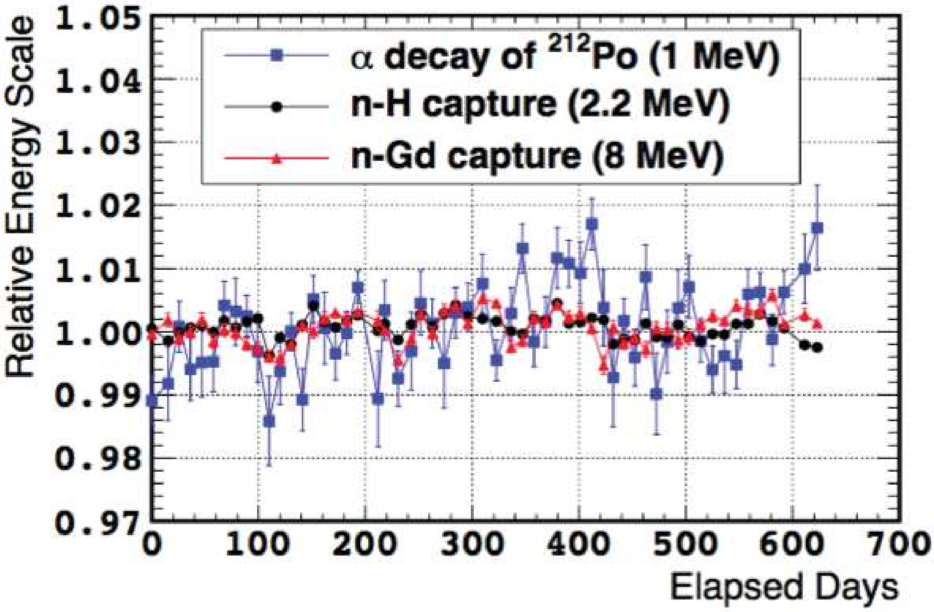

Figure 2.12: *Ratio of the peak energy of* ^{212}*Po decay (blue) and neutron captures on H (red) and Gd (black), after application of the stability correction, to their nominal value as a function of time. Error bars show the statistical uncertainty of the peak energy.*

of the relative goodness-of-fit [88].This algorithm has demonstrated a spatial resolution of about 40 mm for muons crossing the central volume [88].

2.9 IBD candidates selection

The IBD candidates selection involves several stages of cuts. First, an event must fullfil a set of conditions to be considered as a valid trigger. Next, the selection of prompt and delayed events under some unicity and coincidence conditions is applied to the valid triggers to obtain IBD candidates.

According to the nucleus on which is captured the IBD neutron, three distinct selections are possible in the DC analysis: the H, the Gd and the Gd++ analysis:

- **H selection** collects IBD candidates with a delayed energy in [1.3 , 3] MeV i.e around the 2.2 MeV of neutron capture on H. The prompt and the delayed signal are here required to occur within 800 μs i.e about 4 times the mean neutron capture time on H ($\simeq 200\mu s$).
- **Gd selection** collects IBD candidates with a delayed energy in [3 , 10] MeV i.e around the 8 MeV of neutron capture on Gd. The prompt and the delayed signal are here required to occur within 150 μs i.e about 5 times the mean neutron capture time on H ($\simeq 30\mu s$).
- **Gd++ selection** with a larger delayed energy window, [1.3 , 10] MeV, collects IBD candidates with a delayed signal compatible with a capture on H or Gd. The selection time window of the H selction, larger than the Gd selection one, is therefore used here.

Hence, the selection volume of delayed signals in Gd analysis is restricted to the Target while in the Gd++ selection this volume extends up to the Gamma Catcher providing thus more statistics. We describe below each stage of the IBD candidates selection summarised in tables 2.4 and 2.5 for both Gd and Gd++ analysis.

2.9.1 Valid trigger

Most of the uncorrelated background can be rejected at the single trigger level by the definition of a valid trigger. To be considered valid, a trigger must not be a muon, a light noise, a random trigger or a muon-correlated event. Moreover, the energy deposited in the ID by a valid trigger must be within [0.3 , 100] MeV.

The condition to tag an event as a muon is a large energy deposition in either the ID or the IV. In the ID, the muon threshold is set to 100 MeV, and in the IV, the threshold is set at 30 000 DUQ (digital units of charge) in ND and FD-I while it is set at 50 000 DUQ in FD-II. After a muon event, an excess of triggers is seen due to backgrounds generated by the muon, mostly consisting of events from short-lived muon-induced radioisotopes. Hence, in order to reject these subsequent events a veto is applied to all events in the following 1 ms for Gd selection and 1.25 ms for the Gd++ selection.

Light noise (LN) events are produced by individual PMTs spontaneously emitting light from their bases. They can be rejected due to the fact that light from these events is mainly collected by a single PMT, in contrast to the more homogeneous distribution of hit PMTs seen for physics events. Therefore, to remove such events, we select the PMT with the maximum charge in the event (henceforth the Qmax PMT) and compare this charge (denoted Q_{max}) to the charges collected by other PMTs. The first cut is applied on the ratio of the charge in the "max PMT" to the total charge of the event, Q_{max}/Q_{tot}. We require this ratio to be small. Next, we look at the difference between the charge in the max PMT and that of its neighbouring PMTs, a quantity known as Q_{diff}, which is defined by:

$$Q_{diff} = \frac{1}{N}\sum_{i}^{N}\frac{(Q_{max}-Q_i)^2}{Q_i} \tag{2.17}$$

where N is the number of PMTs within a radius of 1 m from the max PMT, and Q_i is the charge in each of these PMTs. Again, we require this ratio to be small, to eliminate light noise events. A third type of cut relies on the standard deviation of the charge (RMS_Q) and pulse start time (RMS_{Tstart}) distributions in the PMTs in the event. Candidates that fullfil the conditions in table 2.3 are identified as LN.

FD-I	
	$Q_{max}/Q_{tot} > 0.12$ $Q_{diff} > 30,000$ DUQ $RMS_{Tstart} > 36$ or $RMS_Q > 464 - 8 \times RMS_{Tstart}$
FD-II and ND	
	$Q_{max}/Q_{tot} > 0.20$ $Q_{diff} > 100000$ DUQ $RMS_{Tstart} > 36$ or $RMS_Q > 1680 - 28 \times RMS_{Tstart}$

Table 2.3: *Definition of light noise cuts in all detectors configurations. Events which satisfy these conditions are tagged as LN and therefore invalid triggers.*

The application of the above global LN cuts depicted in figure 2.13 has a remarkable visible cleansing effect. The resulting spectrum exhibits clearly

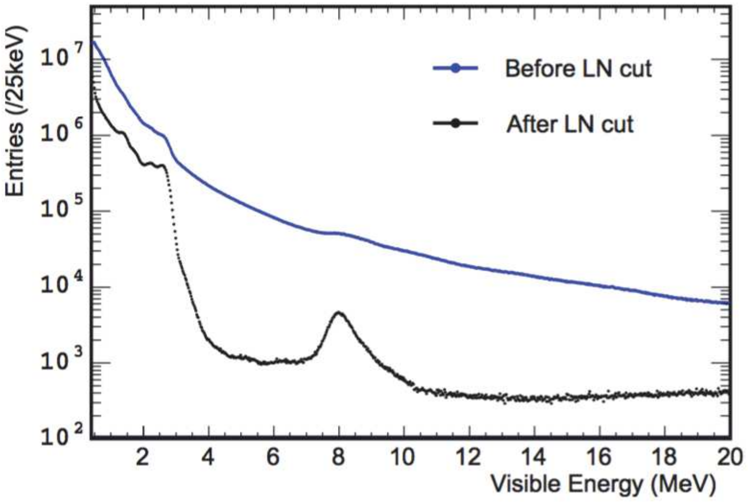

Figure 2.13: *Typical far detector visible energy spectrum of singles, before and after the global LN cut has been applied [73].*

the Gd capture peak at 8 MeV, and the highest gamma peak from natural radioactivity, at ~2.6 MeV, induced by the beta decay of ^{208}Tl into ^{208}Pb.

In addition to light noise events, we remove events initiated by the random external trigger i.e the fixed-rate 2 Hz trigger used for monitoring deadtime.

Valid trigger	Not a muon. Not a light noise. Not a random trigger. $\Delta T_{muon} > 1$ ms. Visible energy $\in [0.3, 100]$ MeV.
Unicity	No other valid trigger in the [-600, 0.5] μs around prompt event. A single valid trigger, the delayed candidate, in the [0.5,600] μs after the prompt candidate.
Coincidence	$\Delta R < 1$ m. $\Delta T \in [0.5, 150]$ μs. Delayed visible energy $\in [4, 10]$ MeV.

Table 2.4: *IBD candidates selection criteria for the Gadolinium analysis.*

2.9.2 Unicity

The selection of prompt and delayed events is applied to the valid triggers to obtain IBD candidates. There can be no valid trigger in the prompt isolation window [$-\Delta T_{before}$, 0.5] μs before a prompt candidate, and only one delayed candidate in the delayed isolation window [0.5, ΔT_{after}] μs after the prompt candidate. The unicity criterion is meant to ensure that a prompt trigger does not directly follow another potential candidate, and thus cannot be a delayed trigger misidentified as a prompt. ΔT_{after} on the other hand, helps to reduce high multiplicity events, that cannot be IBD since IBD events only have two triggers.

2.9.3 Coincidence

The last step in the selection of IBD candidates is done by requiring the coincidence in time and space of two valid triggers corresponding to a possible positron (prompt trigger) and subsequent neutron capture on Gd or H (delayed trigger).

The space coincidence between the prompt and delayed candidates is set to less than 1 m i.e $\Delta R < 1$ m. Indeed, since the positron and the neutron of the IBD originate from the same interaction point they are expected to deposit their energy very closely in space.

The mean time for neutron thermalisation and capture on Gadolinium is about 30 μs, so the prompt and delayed signals coincidence window of $\Delta T \in [0.5, 150]\mu s$ contains most IBD events, but is short enough to keep the contamination with accidentals low. The high energy window of the delayed event, made possible by the high Gadolinium de-excitation energy ($\simeq$ 8 MeV), further reduces backgrounds. This time coincidence window is expanded to $[0.5, 800]\mu s$ in Gd++ selection due to a higher mean time ($\simeq 200\mu s$) of neutron capture on Hydrogen.

Valid trigger	Not a muon. Not a light noise. Not a random trigger. $\Delta T_{muon} > 1.25$ ms. Visible energy $\in [0.3, 100]$ MeV.
Unicity	No valid trigger in the [-800, 0.5] μs around prompt event. A single valid trigger, the delayed candidate, in the [0.5,900] μs after the prompt candidate.
Coincidence	$\Delta R < 1$ m. $\Delta T \in [0.5, 800]$ μs. Delayed visible energy $\in [1.3, 10]$ MeV.

Table 2.5: *IBD candidates selection criteria for the Gd++ analysis.*

Finally, delayed event candidates are selected in an energy window between 4 and 10 MeV for Gd selection and between 1.3 and 10 MeV for the Gd++ selection. These windows were chosen to encompass most of the n-Gd and n-H capture signal without introducing a significant rate of background events.

2.10 Background

Different physical and non-physical processes can mimic the inverse beta decay signature, i.e the DC signal; these processes constitute the background of the experiment. The background encountered in DC is of two types: correlated and uncorrelated.

The first category, i.e correlated background, refers to the coincidence between a prompt-like and a delayed-like signal that originate from the same physical process. In DC, the correlated backgrounds are all muon-induced as described lower. The uncorrelated background are due to either a non-physical process or to a random coincidence of two unrelated physics processes that happen to fall in the time and space coincidence selection window.

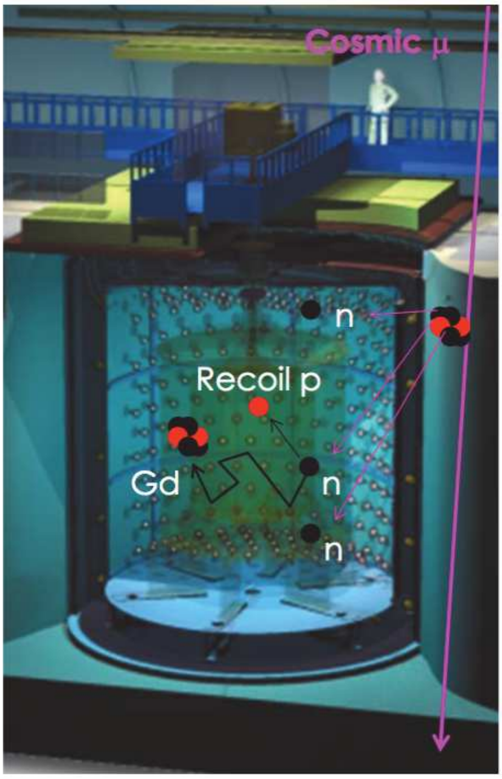

Figure 2.14: *Fast neutrons events topology. Neutrons enter the inner vessels, loose their energy by collisions on protons of the medium. The recoil energy in addition of the later gammas due to the capture of the incident (or another) neutron imitate the IBD signal.*

2.10.1 Correlated background

The passage of cosmic muon through or beside the detectors is responsible of three different background in DC.

- **Fast neutrons**

  Fast neutron (FN) background is due to high energy neutrons created by cosmic muons interacting outside the detector, typically through spallation reactions with the surrounding rock. As illustrated in figure 2.14, when the fast neutrons enter the inner vessels, they loose their energy by collisions on protons of the medium. The recoil of these protons creates then a signal in the liquid scintillator. Once the fast-neutrons are thermalised, they can be captured on a Gd or H nucleus. Therefore, proton recoils and the subsequent neutron captures, physically correlated, mimic the $\overline{\nu_e}$ signal.

  Since FN are generated with high multiplicity, some of them are expected to deposit energy in both the ID and the IV; the fast neutrons

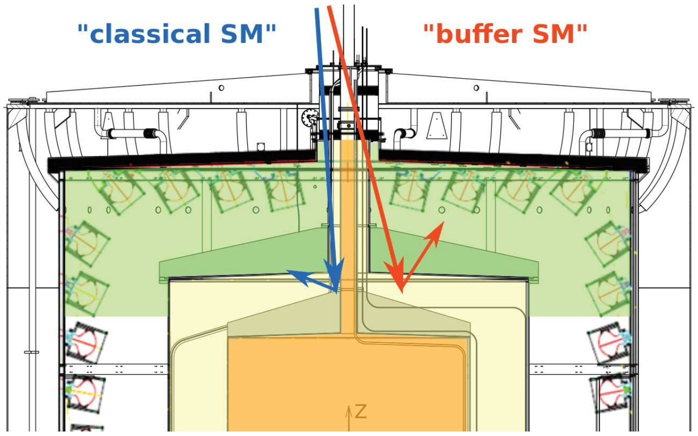

Figure 2.15: *Classical and Buffer stopping muons events topology. Muons stopping and then decaying in the upper part of the detector mimic the IBD signature. In the Near Detector, the leak of the liquid scintillator into the Buffer, built originally to be non-scintillating, is at the origin of the so-called "Buffer stopping muons".*

loosing some energy within the IV can be then tagged using this IV information. The DC DAQ system is designed in such a way that both ID and IV detectors are read-out whatever detector causes the trigger. Fast neutrons therefore can be tagged if an energy deposition in the ID occurs in coincidence with an IV event.

The study and the estimation of this particular background (cf. chapter 3) in DC is one of the achievements of this thesis where the techniques and methods to measure the contamination fraction of fast neutrons among the IBD candidates are presented in great details.

- **Stopping muons**

  - ***Classical Stopping Muons***

    Ideally a muon crossing the detector is supposed to trigger either the upper or the lower OV. However, from time to time, technical problems prevent the OV to be permanently operational. Hence, a muon stopping in the upper part of the detector may deposit some energy below the muon rejection threshold and then fall in the prompt window. Later on, the electron (or positron) created by the muon decay provides the delayed-like signal.

    Stopping muons are also possible even though the OV is active. Indeed, as depicted in figure 2.15, the chimney constitutes an uncovered zone through which a muon can enter and stop in the ID without triggering the OV.

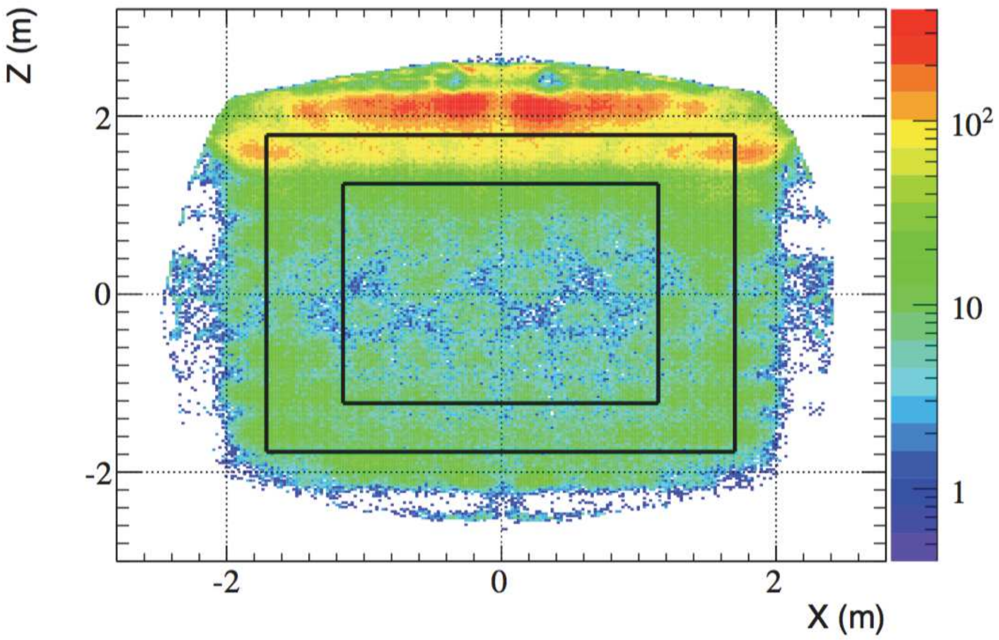

Figure 2.16: *Events vertices distribution in the X-Z plane. Some events are reconstructed largely outside of the active volumes (the Target and the Gamma Catcher are shown in black lines). They show a pattern corresponding to the position of the PMT in the Buffer, which means they happened close to the PMT, and do not result in a mis-reconstruction.*

- ***Buffer Stopping Muons***

  In addition of these "classical" stopping muons, it has been evidenced the existence of the so-called "Buffer stopping muons". Indeed, during the commissioning of the Near Detector, tests were performed to evaluate the amount of light noise (cf. section 2.10.2). During these tests, it was found that some events at the top of the detector were reconstructed outside of the Gamma Catcher, in the Buffer. These events show patterns that correspond to the position of the PMTs, as shown in figure 2.16, thus ruling out the possibility of them being simply mis-reconstructed. Besides, the top of the buffer happened to be more opaque to the calibration LED light than expected.

  This behaviour is explained by a leak of Gamma Catcher scintillator into the buffer. Since the contamination of Gd in the buffer is small, these Buffer events only appear close to PMTs where the light collected is high enough to pass the trigger thresholds. [86]

- **Double neutrons capture**

The high multiplicity of neutrons created by the spallation reaction of muons with rocks in the vicinity of the detector can result in a double capture, separated in time, of two neutrons in the ID. Hence, if the two captures fall in the good time and space windows, they may survive easily the selections criteria and mimic perfectly the IBD prompt and the delayed signals.

In this thesis (cf. chapter 4) a dedicated technique has been developed to study and estimate this double capture background.

- **Cosmogenic nuclides**

A cosmogenic nuclide is a radioisotope resulting of a spallation process on an atom nucleus induced by a high-energy cosmic muon, causing nucleons to be expelled from the atom. This process, depicted here in figure 2.17, occurs also in DC detector and leads to the creation of a certain number of these cosmogenic nuclides which are, mostly, not critical for DC. Indeed, they either have a half-life well below 1 ms and are hence rejected by the after-muon deadtime time or their decay yields only a single signal instead of the two necessary to mimic the prompt and the delayed signals of the IBD.

However, some cosmogenic nuclides are $\beta - n$ isotopes i.e they decay by emitting an electron and a neutron [89] imitating perfectly the IBD signature. In DC, two $\beta - n$ nuclides are produced, ^{8}He and ^{9}Li, as cosmic muons interact with the ^{12}C nuclei present in the detector medium[7].

$$\begin{aligned} &\mu +^{12} C \rightarrow^{8} He,^{9} Li, etc. \\ &^{9}Li \rightarrow e^{-} + \overline{\nu}_{e} + n + 2^{4}_{2}He \\ &^{8}He \rightarrow e^{-} + \overline{\nu}_{e} + n +^{7} Li \end{aligned} \tag{2.18}$$

The decays of the β-n emitters give a prompt signal in the detector thanks to the electron of the beta decay, while the neutron is captured on Gadolinium or Hydrogen providing a delayed signal. Due to their relatively long lifetimes ($\tau_{^{9}Li} = 257$ ms, $\tau_{^{8}He} = 172$ ms) well above the after-muon dead-time, an event by event discrimination is not possible since a veto after the muon can not be applied.

Cosmogenic nuclides are correlated in space and time with the muon that led to their creation. Moreover, the process of cosmogenic nuclides creation is accompanied by multiple neutrons due to the passage of the muon through its interaction with the scintillator complex.

---

[7] DC as an organic scintillator is essentially composed of Hydrogen and Carbon. Hence ^{8}He and ^{9}Li creations are possible only though spallation on carbon nuclei.

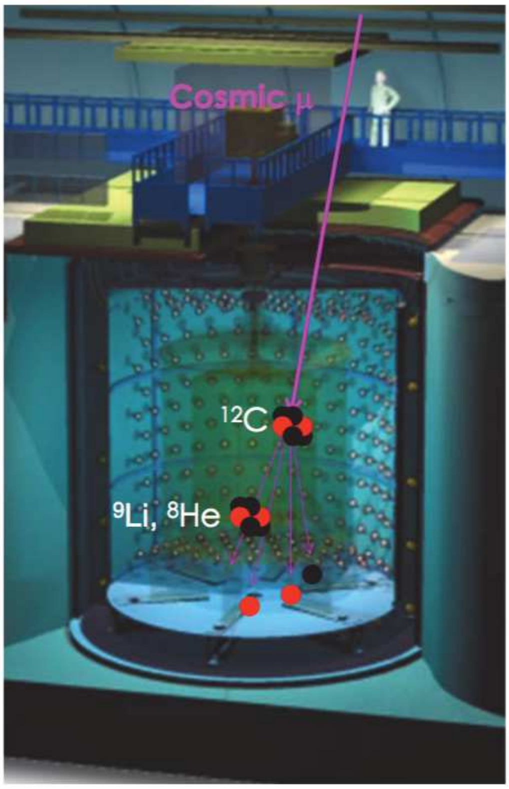

Figure 2.17: *Cosmogenic background events topology. Beta emitters nuclides are created through nuclear spallation reactions as the muons cross the detector. Emitted electron and neutron as the cosmogenic nuclides decays mimic the two-fold coincidence signature of the IBD signal.*

Therefore, in order to tag the cosmogenic background we use, as selection variable, a likelihood based on the number of neutron following a muon and on the distance between the neutron candidates vertex positions and the muon track. The neutron candidates were selected in a sample of event occurring within the 1 ms time window after a muon. For each muon, the number of neutron candidates and the distribution of their vertex position and the muon track are computed. From that, a likelihood value, that serves later as selection criteria, is computed for each prompt candidate.

However, the efficiency of this veto lies between 25% and 50%[73, 90]. The cosmogenic background is referred in short as ^{9}Li/^{8}He background in DC.

2.10.2 Uncorrelated background

Besides the muon-induced background described above, DC encounters two major uncorrelated backgrounds.

- **Accidental background**

  Accidental background is the random coincidence of a prompt trigger from natural radioactivity and a subsequent neutron-like candidate. Figure 2.18 depicts the toplogy of such events. The radioactivity is mostly due to the surrounding rocks or the detector material, including the PMTs. The natural radioactive nuclei with the highest photon energy release being the Thallium nuclei ($\simeq 2.6$ MeV) [91], the accidental background contaminates essentially the low energy component of the prompt energy spectrum of the IBD candidates in DC.

  The accidental background fraction in Gd++ analysis is greater than in Gd analysis because, first, of the higher mean time ($\simeq 200\mu$s) of neutron capture on Hydrogen and, secondly, because the hydrogen capture component of the delayed signal (2.2 MeV) falls in the natural radioactivity energy range. One direct way to reduce the number of accidentals is to impose an additional cut on the distance between the prompt and delayed event. Indeed, the kinematics of a true IBD allows, in average, a spatial separation of less than 1 m between the vertices of the positron and the neutron. Hence, imposing a cut on distance as described in section 2.9 is enough to reduce a great portion of the accidental backgrounds. In addition to this cut on distance, DC has developed a neural network, designed as ANN, that selects efficiently the accidental background.

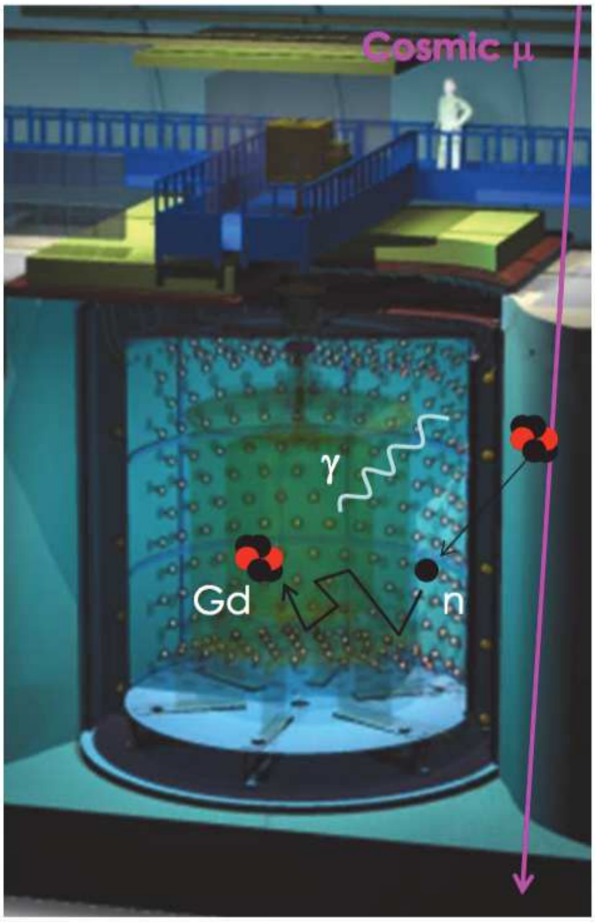

Figure 2.18: *Accidental background events topology where a prompt trigger from natural radioactivity and a subsequent neutron-like candidate happen to fall in the IBD selection window.*

- **Light Noise**

  In contrast with all the backgrounds described so far, The light noise (LN) background, so-called in DC, does not originate from any physics interaction but from the PMTs. Indeed, It is due to spontaneous flashes from some PMT bases discovered during the commissioning of the Far Detector.

  The study of this phenomenon carried out in-situ, and in an external laboratory, has identified the LN mechanism as arising from the light emission localized on the photomultiplier base and produced by the combined effect of heat and high voltage across the transparent epoxy resin covering the electric components. The correlation of the rate and the amplitude of the signal with the temperature has been observed [92].

  As a consequence of their non-physics origin, most light noise events present very unusual pulse shapes with a light distribution concentrated at a single PMT. Dedicated cuts (cf. section 2.9) have been developed and allow to reject efficiently the LN.

  When the light burst happens to be longer than the time window of the DAQ, light noise events exceptionally create a kind of "correlated" background. In this case the signal is still strong enough at the end of the time window and triggers the DAQ again immediately. These correlated light noise events can be identified thanks to their very short time difference between the prompt and the delayed events. Hence, they can be removed by imposing a lower limit on the coincidence time window [93].

2.10.3 DC correlated background vetoes

After initial selection of IBD candidates described in section 2.9, different additional vetoes are applied in order to remove the specific backgrounds detailed above. These vetoes have defined, tuned and optimized with the constraint of a very low inefficiency (< 0.1) % in order to preserve, as much as possible, the true IBDs signals . Besides, the analysis of the Off-Off data has revealed a remarkable global rejection efficiency (>98%).

The DC background vetoes include namely the IV veto, which uses low-energy signals in the IV to select Fast Neutrons background presented in this work; the Functional Value (FV) Veto which uses the output log-likelihood of the RecoBAMA reconstruction algorithm to select non-pointlike energy depositions, and which is particularly good at eliminating background due to Stopping Muons (SM); the OV veto, which additionally vetoes both FN and SM; and the cosmogenic isotopes Veto, which uses information about muons preceding the candidate in order to veto ^{9}Li/^{8}He background.

2.11 Proton number

A precise accounting of the number of hydrogen nuclei (or "*proton number*") available for IBD reactions in the detector is essential for a sensitive θ_{13} measurement. Indeed, the proton number is a critical parameter for the experiment. It determines the number of reaction targets for the inverse beta decay and its uncertainty is directly related to the uncertainty of the neutrino flux. A one percent lower proton number would lead to a one percent decrease of the detected number of neutrinos. This is the reason why only pure chemicals with well-known compositions are used in the detector liquids. For instance, linear alkyl benzene (LAB), which is a recent choice for large-scale neutrino detectors, was not considered suitable for this purpose. Instead, Double Chooz opted for pure n-dodecane ($C_{12}H_{26}$) as the solvent.

The weight of each scintillator component was measured precisely during mixing, and the impurities in each of the liquids were taken into account. The variations of the gravitational acceleration with the location were measured and compensated as well. By weighting the tank at the beginning and the end of the filling procedure, the mass of Target liquid that is actually in the detectors was determined with a precision of 0.04 % [93].

From this information, the absolute number of protons can be calculated as

$$N_p = f_p \frac{M_{Target}}{M_H} \tag{2.19}$$

where f_p is the hydrogen fraction (by mass) of the mixture, M_{Target} and M_H are respectively the mass of the Target liquid in the detector and of a single Hydrogen atom.

The proton number of the Gamma-Catcher is known with less accuracy with respect to the one of the Target since the liquid scintillator was not weighted prior to filling. Indeed, for a longtime, the idea to perform an analysis on hydrogen was not contemplated, and thus a precise knowledge of the Gamma Catcher was not mandatory [86].

2.12 Reactor Off-Off data

In the favor of the reactor plant configuration, Double Chooz is the only $\overline{\nu}_e$ reactor experiment able to take data when no reactor cores are running.

DC has encountered so far two periods, called reactor "*Off-Off*" or "*2-Reactor Off*", when no reactor is running. These Off-Off data are of a great importance, especially in the background study, estimation and model validation.

However, even when the two reactors cores are off, the expected $\overline{\nu}_e$ flux is not zero. Indeed, decays from fission products still occurr in the reactor core. These decays produce a residual power which is responsible of about 6% of the reactor core total power after the shutdown. It decreases exponentially due to the fission products decays. As already mentioned earlier, an IBD interaction has a threshold energy of 1.806 MeV; the number of fission products with a long enough lifetime and producing such high energy $\overline{\nu}_e$ is reduced. There are nevertheless six fission fragments with sizable fission yield, and Q > 1.8 MeV: ^{97}Zr, ^{132}I, ^{93}Y, ^{106}Ru, ^{144}Ce, and ^{90}Sr. The first three of them reach equilibrium within $\sim$ 10 days, the next two have half-lives of 367 and 284 days, and ^{90}Sr has $T_{1/2} = 28.8$ years and decays into ^{90}Y with Q = 2.28 MeV [94].

2.13 Measurement of θ_{13} with DC

Two methods are used in DC to measure the θ_{13} mixing angle : The *"Rate+Shape (RS)"* and the *"Reactor Rate Modulation (RRM)"*. The first is based on a combination of a fit of the rate and of the spectral shape while the second extracts the θ_{13} value from the observed and predicted rates at different reactor powers.

2.13.1 Rate + Shape method

In the Rate+Shape method the θ_{13} value is extracted from the fit of the prediction to the observed energy spectrum of IBD candidates after the removal of all identified backgrounds[8]. Here the fit involves both the rate of IBD candidates and the spectral shape information to constrain the systematic uncertainties on θ_{13}.

Since DC has not always been a multiple detector experiment, different approches have been used over time. In the single detector phase, from April 2011 to December 2015, data have been compared to MC prediction; this is the *Data-to-MC* method. In the current multiple detector phase, the Near Detector data stand for the prediction for the Far Detector data. This is known as the *Data-to-Data method*. The main advantage of this technique is to reduce the dependency to the MC, and therefore to reduce the potential

---

[8] The efficiency of the background vetoes not being of 100%, it is clear that a little but non-zero fraction of background is still present in the final sample.

bias due to the MC modelling. However, as a cross-check, the Data-to-MC approach is still used presently.

To perform the Rate+Shape fit, the spectrum of the selected events is first divided into k bins. The resulting histogram is fitted with the predicted distribution depending on θ_{13}. The best fit is obtained by minimizing the test quantity χ^2 given by [72] :

$$\begin{aligned}\chi^2 =& \sum_{i=1}^{k}\sum_{j=1}^{k}(N_i^{obs} - N_i^{exp})M_{ij}^{-1}(N_j^{obs} - N_j^{exp}) + \sum_{i=1}^{5}\frac{\varepsilon_k^2}{\sigma_k^2} \\ &+ (\varepsilon_a, \varepsilon_b, \varepsilon_c)\begin{bmatrix}\sigma^2 & \rho_{ab}\sigma_a\sigma_b & \rho_{ac}\sigma_a\sigma_c \\ \rho_{ab}\sigma_a\sigma_b & \sigma_b^2 & \rho_{bc}\sigma_b\sigma_c \\ \rho_{ac}\sigma_a\sigma_c & \rho_{bc}\sigma_b\sigma_c\sigma_c^2 & \sigma_c^2\end{bmatrix}\begin{bmatrix}\varepsilon_a \\ \varepsilon_b \\ \varepsilon_c\end{bmatrix} \\ &+ 2[N_{off}^{obs}\ln(\frac{N_{off}^{obs}}{N_{off}^{exp}}) + N_{off}^{exp} - N_{off}^{obs}]\end{aligned} \tag{2.20}$$

where

- In the first term : N^{obs} and N^{exp} refer, respectively, to the observed and expected number of IBD candidates in the i-th energy bin. Neutrino oscillation is accounted for in N_{exp} by equation 1.37. Data are divided into k energy bins suitably spaced between 0.5 and 20 MeV to examine the oscillatory signature given as a function of E_ν/L and statistically separate the reactor $\overline{\nu}_e$ signals from the background by the different spectral shapes. M_{ij} is a covariance matrix to account for statistical and systematic uncertainties in each bin and the bin-to-bin correlations. M_{ij} consists of the following matrices:

  $$M_{ij} = M_{ij}^{stat} + M_{ij}^{flux} + M_{ij}^{eff} + M_{ij}^{Li/He(shape)} + M_{ij}^{acc(stat)} \tag{2.21}$$

  where M_{ij}^{stat} and $M_{ij}^{acc(stat)}$ are diagonal matrices for the statistical uncertainty of the IBD candidates and statistical component of the uncertainty of the accidental background rate; M_{ij}^{flux} accounts for the uncertainty on the reactor $\overline{\nu}_e$ flux prediction; M_{ij}^{eff} is given as $M_{ij}^{eff} = \sigma_{eff}^2 N_i^{exp} N_j^{exp}$ where σ_{eff} represents the uncertainty on the MC normalization. $M_{ij}^{Li/He(shape)}$ encodes the shape error in the measured ^{9}Li/^{8}He spectrum.

- In the second term : N^{exp} is corrected for systematic effects in the fit with eight parameters (ε_x). Constraints on the ε_x are given by a matrix in which correlations are taken into account with the parameters ρ_{ab}, ρ_{bc} and ρ_{ac}.

- The last term in the χ^2 definition represents the contribution to the χ^2 from the reactor-off running. As the statistics in the reactor-off running is low, only the number of IBD candidates (N^{obs}) is compared with the prediction (N^{exp}) by a log-likelihood based on Poisson statistics.

The final θ_{13} value is the one corresponding to the minimum χ^2 after scanning the χ^2 over a wide range of $\sin^2 2\theta_{13}$.

2.13.2 Reactor Rate Modulation method

The RRM analysis is based on a fit to the observed IBD candidate rate as a function of the prediction, which depends on the number of operating reactor cores and their thermal power. Three scenarios are then possible :

- Two reactors are on (2-On)
- One reactor is off (1-Off)
- Both reactors are off (2-Off)

The θ_{13} meausurement in this method is extracted by comparing the observed rate of IBD candidates R^{obs} at different reactor powers to the corresponding expected rate R^{exp}. The linear correlation between R^{obs} and R^{exp} provides both θ_{13} and the total background rate B :

$$R^{obs} = B + R^{exp} = B + (1 - \alpha_{osc} \sin^2 2\theta_{13}) R^{\overline{\nu}_e} \tag{2.22}$$

where $R^{\overline{\nu}_e}$, the expected rate of $\overline{\nu}_e$ in the non-oscillation hypothesis. The mean disappearance coefficient has been computed by means of simulation for each of the data points [77, 95],

$$\alpha_{osc} =< \sin^2(\Delta m^2 L/4E) > \tag{2.23}$$

The χ^2 of the RRM fit is defined as follows

$$\chi^2 = \chi^2_{on} + \chi^2_{off} + \chi^2_{bg} + \Delta\chi^2 \tag{2.24}$$

where

$$\chi^2_{on} = \sum_{i=1}^{k} \frac{(R_i^{obs} - R_i^{exp} - B)^2}{(\sigma_i^{stat})} \tag{2.25}$$

$$\chi^2_{off} = 2[N^{obs}_{off} \ln(\frac{N^{obs}_{off}}{N^{obs}_{off}}) + N^{exp}_{off} - N^{obs}_{off}] \tag{2.26}$$

$$\chi^2_{bg} = \frac{(B - B^{exp})^2}{\sigma^2_{bg}} \tag{2.27}$$

N_{off}^{obs} and N_{off}^{exp} are the observed and expected number of IBD candidates. σ_i^{stat} is the statistical uncertainty on the rate measurement. $\Delta\chi^2$ apply the constraints to the fit parameters from the estimated systematic uncertainties.

2.14 The latest final fit results

The latest θ_{13} value by DC has been delivered in September 2016 at the Cern Experimental Physics Seminar (EP Seminar). The χ^2 function defined in equation 2.20 includes the three detectors (FD-I, FD-II and ND) and their correlations, i.e. the three spectra are fitted at the same time. Figure 2.19 shows the prompt energy spectrum for each detector for the Gd++ analysis presented at Cern EP seminar. The fitted spectra of individual backgrounds are superimposed to the data and the blue line corresponds to the un-oscillated best fit.

Figure 2.20 shows the ratio of the data with subtracted backgrounds to the un-oscillated prediction. The yellow boxes show the systematic uncertainties with the assumption of only one detector and the green boxes show the fraction of the systematic uncertainties that can be reduced in the multi-detector treatment. The Near Detector is slightly impacted by θ_{13}, thus, a small deficit should be visible when comparing to the un-oscillated prediction. The deficit is not observed, hinting towards a possible bias in the flux normalization of the MC in the Near Detector.

The measured value for $\sin^2 2\theta_{13}$ is $\sin^2 2\theta_{13} = 0.119 \pm 0.016$ with a $\chi^2/d.o.f. = 236.2/114$, corresponding to an exclusion of the no-oscillation hypothesis at 2.2σ C.L. In parallel, a data-to-data fit is performed as a cross-check.

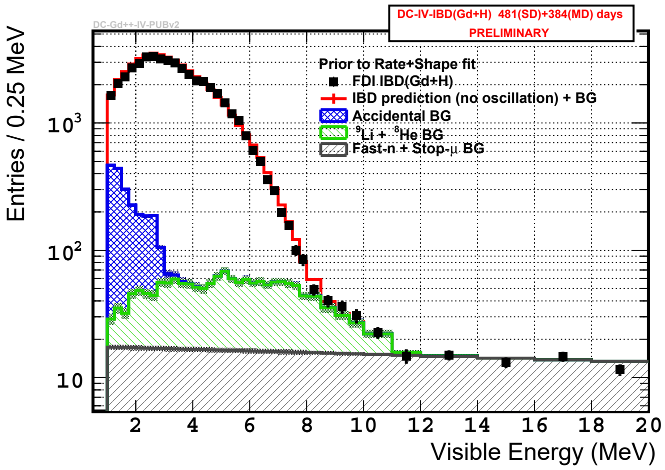

(a) ND

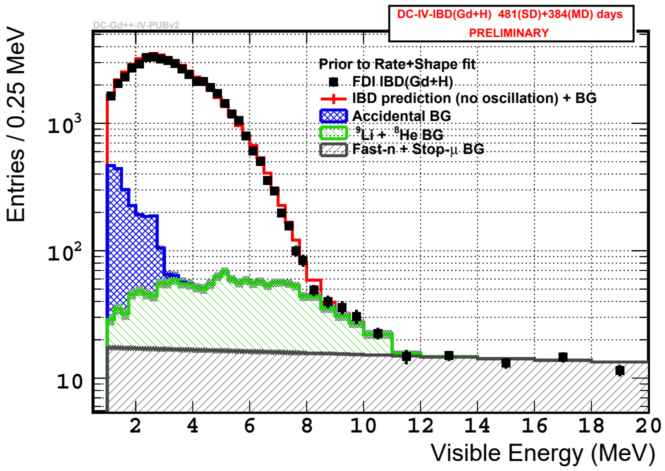

(b) FD-I

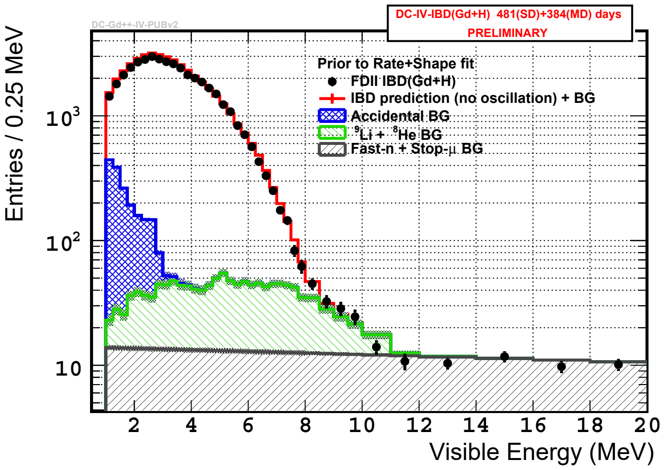

(c) FD-II

Figure 2.19: *Prompt energy spectra of the DC-IV Gd++ analysis presented at Cern. The black dots are the data points, the blue line is the un-oscillated prediction, and the coloured histograms are the individual backgrounds.*

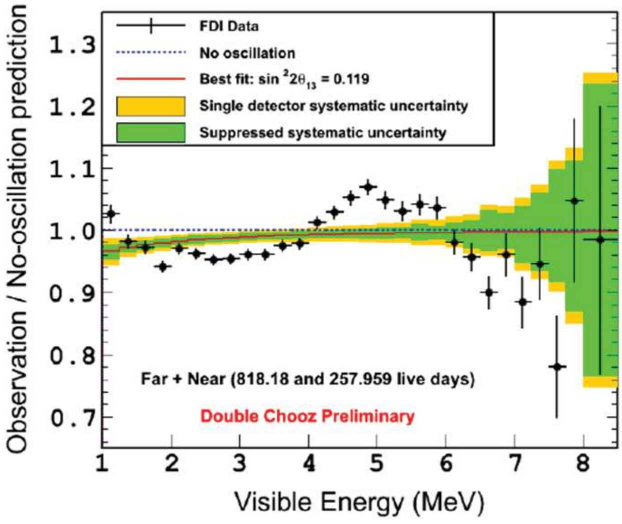

(a) ND

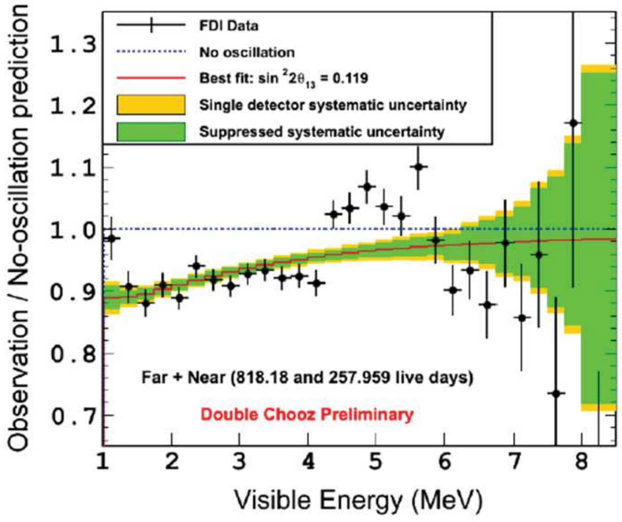

(b) FD-I

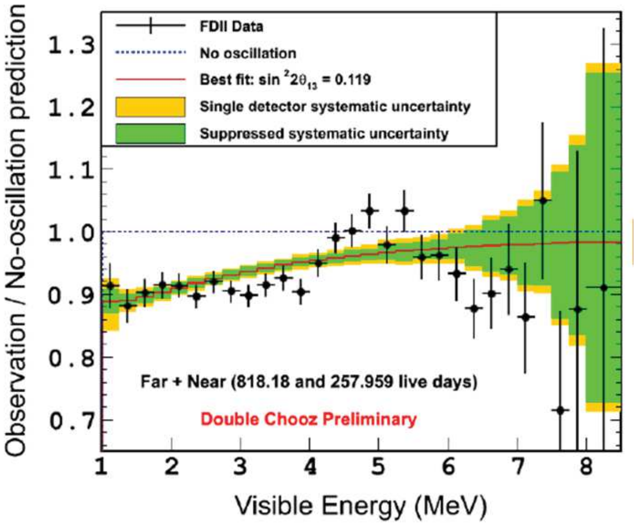

(c) FD-II

Figure 2.20: *Ratio of the data to un-oscillated prediction after subtraction of the background model:*
(a) Ratio of the data to prediction ND
(b) Ratio of the data to prediction FD-I
(c) Ratio of the data to prediction FD-II.

Chapter 3

Inner Veto veto

> *"Nobody ever figures out what life is all about, and it doesn't matter. Explore the world. Nearly everything is really interesting if you go into it deeply enough."*
>
> Richard Feynman

3.1 Introduction

Three different background in DC, namely FN, $\gamma - \gamma$ events and SM, can be tagged using their IV information.

- Fast neutron background is due to high energy neutrons created by cosmic muons interacting outside the detector, typically in the surrounding rock. As schematised in box 1 of figure 7.3, when the fast neutrons enter the inner vessels, they loose their energy by collisions on protons of the medium. The recoil of these protons creates then a signal in the liquid scintillator. Once the fast-neutrons are thermalised, they can be captured on a Gd or H nucleus. Therefore, proton recoils and neutron captures, physically correlated, mimic the $\overline{\nu_e}$ signal. Since FN are generated with high multiplicity, some of them are expected to deposit energy in both the ID and the IV; the fast neutrons loosing some energy within the IV can be then tagged using this IV information. The DC DAQ system is designed in such a way that both ID and IV detectors are read-out whatever detector causes the trigger. Fast-neutrons are therefore tagged if an energy deposition in the ID occurs in coincidence with an IV event.

- $\gamma - \gamma$ events are photons, from natural radioactivity and from neutrons captures in the surrounding materials, that undergo Compton scattering in the IV and in the ID where, in accidental coincidence with a thermal neutron capture, will mimic the signal. This background topology is schematised in box 2 of figure 7.3. $\gamma - \gamma$ events can therefore be tagged by means of their energy deposition in IV.
- Stopping muon background comes from the fact that there is a hole in the IV: the chimney. Box 3 of figure 7.3 shows that muons could enter into the ID through the chimney without triggering the IV. Nevertheless, some of these stopping muons cross the corners of the chimney, depositing some energy within the IV. This low energy deposition, below the muon rejection threshold, can be used to tag the stopping muons even though the IV efficiency for these events is expected to be low.

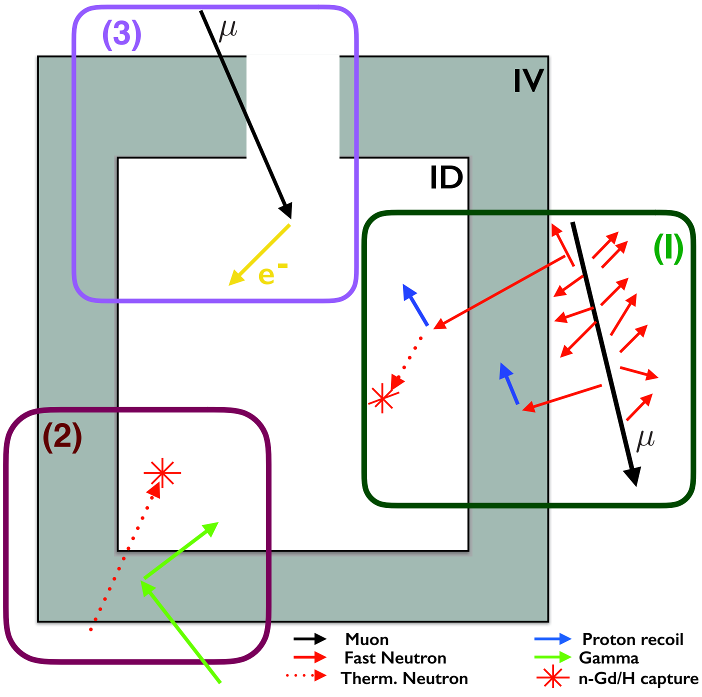

Figure 3.1: *FN, SM and $\gamma - \gamma$ events topology. Box 1 schematises FN event to be vetoed by IVV. Box 2 schematises $\gamma - \gamma$ events generated by low energy from natural radioactivity : the γ undergoes Compton scattering in the IV and in the ID where, in accidental coincidence with a thermal neutron, it mimics the $\overline{\nu_e}$ signature. Box 3 schematises the particular case of a SM event crossing the corners of the chimney and depositing some energy within the IV.*

It is expected that a part of this background, coming from outside of the detector, occurs simultaneously with an energy deposition in the Inner Veto.

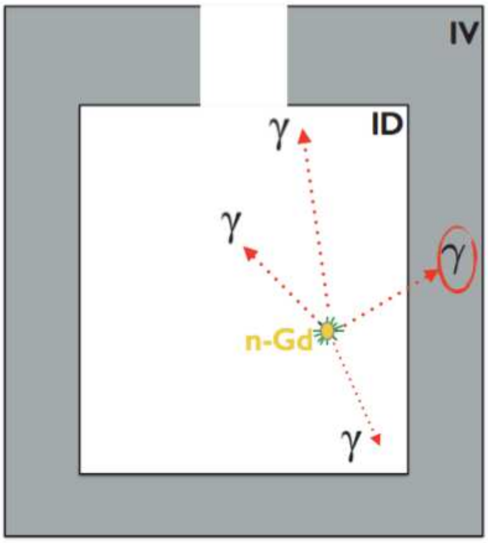

Figure 3.2: *Schematic description of how Delayed-IVV can tag signal in Gd selection. Gd de-excitation* γs *hitting the IV cause Delayed-IVV to tag signal leading then to relatively high inefficiency.*

If this energy deposition is lower than the muon threshold in the IV, the event will not be tagged automatically by the DAQ system as a muon. The Inner Veto veto (IVV) is the technique based on the IV and developed in DC to tag the three backgrounds described above.

In view of the background to tag, two types of IVV are necessary. The first one is applied to reject the prompt signals which are in coincidence with an energy deposition in the IV while the second one rejects the delayed signals which are in coincidence with an energy deposition in IV. We name the two IVV respectively Prompt-IVV and Delayed-IVV.

Preliminary investigations, illustrated here in figure 3.2, showed that Delayed-IVV rejects antineutrino events due to γ from the Gadolinium neutron captures escaping from the ID into the IV, causing an increase of the inefficiency. The Delayed-IVV is efficient to tag mainly $\gamma - \gamma$ background events depositing energy within the IV in coincidence with a non-IBD originated delayed energy deposition in ID. This is only possible in Hydrogen selection where the energy required to mimic the delayed signal relatively low (< 3 MeV) falls right in the energy window of gammas originating from natural radioactivity background[1]. However, none of radiative physical processes occurring outside the detector would release γs of enough energy to deposit

---

[1] For instance the 2.6 MeV γ released during the transition from ^{208}Tl to ^{208}Pb via beta decay. Furthermore, this energy is the highest reached by a natural radioactivity gamma.

the $\simeq$ 8 MeV required in Gd delayed selection after having deposited priorly some energy in the IV. The γs with energy within 4-10 MeV, as required in delayed signal for this selection in table 2.4, are mainly gammas due to the neutron capture on Gd[2]. Hence, Delayed-IVV happens to tag $\overline{\nu}_e$ signal in Gd selection. Therefore, decision has been taken to apply it only in H selection i.e for events with a delayed energy less than 3 MeV.

The IVV consists in a set of cuts that need to be tuned in order to reject a pure sample of correlated background with the constraint of a negligible inefficiency.

The cuts entering in IVV definition concerns four variables, all related to IV:

1. IV PMT multiplicity
2. Total charge deposited in IV
3. ID-IV space coincidence
4. ID-IV time coincidence

Up to DCIII[3] the ND did not start taking data, IVV was then tuned only for FD as presented in table 3.1.

3.2 Data set

The tuning of IVV and the measurement of the associated inefficiency have been performed for two different analysis of DC: the Gadolinium selection and the so-called "Gadolinium++ selection". This later analysis is a special DC analysis which selects events via the capture of the IBD neutron on both Gadolinium and Hydrogen unlike in the Gd analysis where events are selected via the only captures on Gadolinium.

The data sample, referred as DC-IV[4], used for the present analysis is summarized for each detector in table 3.2.

3.3 Inner Veto Veto tuning for DC-IV

Data taking in the ND started in December 2014, meanwhile the complete electronics of the FD have been changed after DC III. A new tuning of IVV

---

[2] In very rare cases a neutron can be captured on iron in the detector shielding material with a released energy of the same range as in Gd.

[3] The third DC data release and analysis campaign

[4] The fourth DC data release and analysis campaign corresponding to roughly 24 Months of data taken in ND and FD-II.

Hydrogen selection

Prompt-IVV

IV PMT multiplicity : nPMT ≥ 2
Total charge in IV : IV Charge < 400 DUQ
ID-IV space coincidence : $\Delta R_{IV}^{ID} < 4$ m
ID-IV time coincidence : $-110 < \Delta t_{IV}^{ID} < -20$ ns

Delayed-IVV

IV PMT multiplicity : nPMT ≥ 2
Total charge in IV : IV Charge < 400 DUQ
ID-IV space coincidence : $\Delta R_{IV}^{ID} < 4$ m
ID-IV time coincidence : $-110 < \Delta t_{IV}^{ID} < -20$ ns

Gadolinium selection

Prompt-IVV

IV PMT multiplicity : nPMT ≥ 2
Total charge in IV : IV Charge < 400 DUQ
ID-IV space coincidence : $\Delta R_{IV}^{ID} < 3.7$ m
ID-IV time coincidence : $-110 < \Delta t_{IV}^{ID} < -10$ ns

Table 3.1: IVV cuts as tuned in DC-III.

	ND	**FD-I**	**FD-II**
# Runs	8338	12286	9239
Livetime (days)	414.81	538.874	391.04

Table 3.2: *Data set used for the present volume analysis.*

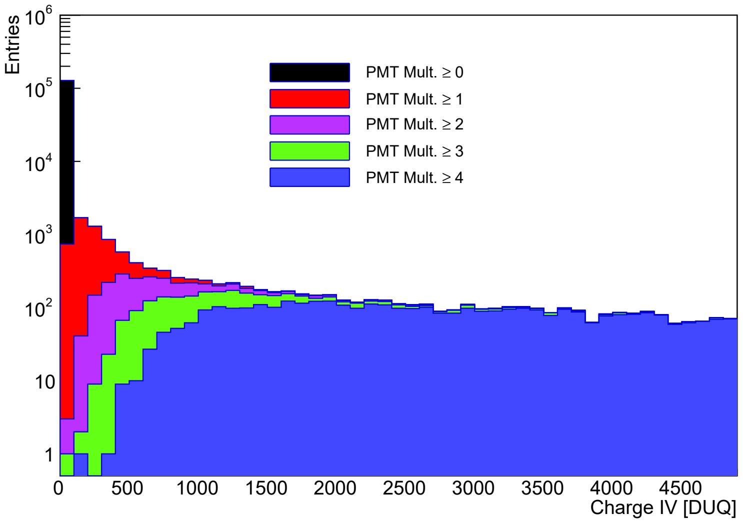

Figure 3.3: *The IV charge spectrum obtained for different IV PMT multiplicity conditions.*

for FD and a first tuning for ND had been done for DC-IV in this PhD work. The setting of IVV cuts in DC-IV and the measurement of the associated inefficiency are contributions of my PhD work. We present here the IVV tuning process in details.

The analysis is performed on the data set of section of 3.2 where the conditions described in tables 2.4 and 2.5 have been applied.

3.3.1 PMT multiplicity condition

The first IVV cut proposed is based on PMT multiplicity nPMT. An event is, thus, IV-tagged if 2 or more IV-PMTs are hit in coincidence with energy deposition in the ID. Figure 3.3 shows the IV charge spectrum obtained for different values of PMT multiplicity. It is important to notice that requiring the PMT multiplicity to be at least 2 rejects most of the low energy events likely due to PMT radioactivity and dark noise.

The IV PMT multiplicity condition sets an energy threshold to ensure that whatever triggers the IV is more likely to be caused by the energy deposition from a fast neutron, a γ ray or a stopping muon entering into the detector rather than a single PMT radioactivity or light noise.

3.3.2 Space correlation tuning

The tuning of spatial correlation cut in IVV is guided by geometric considerations. Indeed, due to the detector size and geometry the distance between

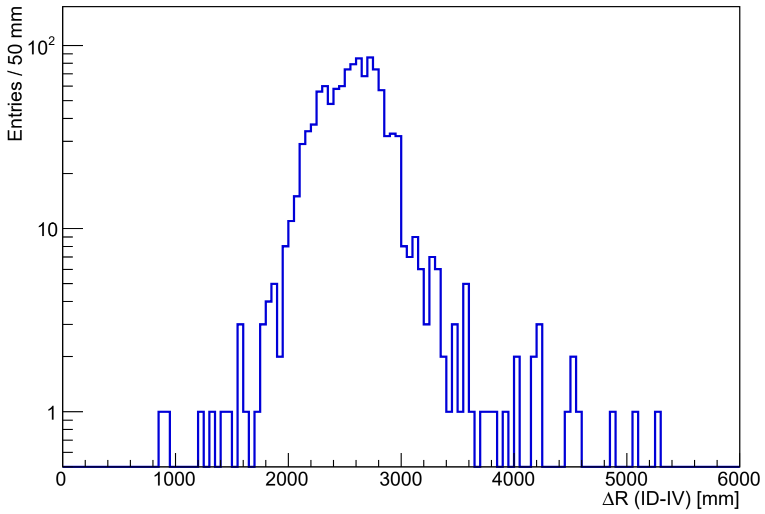

Figure 3.4: *Spatial correlation between ID and IV delayed events selected in coincidence with OV and requiring the IV PMT multiplicity > 1.*

the reconstructed interaction vertex in ID and the one in IV should present logically a maximum above which the correlation is simply geometrically impossible; the ID and IV events being too distant to be physically correlated. In order to obtain a sample of muons induced background which is the background to be vetoed by IVV, we selected events in coincidence with OV. In addition to the OV coincidence condition, we applied the IV PMT multiplicity cut defined above.

Events in figure 3.4 with ID-IV spatial coincidence above $\simeq 3.7$ m happen to be too distant to be physically correlated in view of the detector geometry. The ID-IV spatial coincidence cut has been set at this point : 3.7 m.

The two basic IVV cuts that are PMT multiplicity and IVV spatial correlation will be referred in the next sections as *Minimal IVV.*

3.3.3 ID-IV time coincidence tuning

Figures 3.5, 3.6 and 3.7 show, for ND and FD, the distributions of Δt_{IV}^{ID} of all events and of events selected by the minimal IVV mentioned above. Since correlated, the FN and the SM backgrounds are expected to have a Δt_{IV}^{ID} distribution, in blue, around a peak whereas uncorrelated events should exhibit a flat shape. Therefore, the peak region of the spectrum delimited by vertical red dashed lines and corresponding to the correlated background is the one to be vetoed by the IVV. Events of the second peak around ~ 100 ns, not selected by the minimal IVV, are neither FN nor SM. Indeed, events constituting this 100 ns peak happen to have no IV energy deposition.

Detector	Prompt-IVV	Delayed-IVV
ND and FD-II	[-40 ns , 70 ns]	[-30 ns , 60 ns]
FD-I	[-100 ns , -10 ns]	[-100 ns , -30 ns]

Table 3.3: *IVV tuned selections on time coincidence between ID and IV in all configurations. We recall here that Delayed-IVV is applied only in Gd++ selection and only for events with a delayed energy below 3 MeV.*

Decision has been taken, for the simplicity of the analysis, to have the same ID-IV time coincidence cuts both for Gd and Gd++ selections. Therefore, the cuts have been tuned for Gd++ selection as shown in figure 3.5.

The same cuts as provided by the Gd++ selection have been applied on Gd selection to test the agreement. The figure 3.6 demonstrates that the cuts range, inherited from the Gd++ selection and indicated by the red dashed lines select, as well, the peak region in Gd selection as expected.

The table 3.3 summarises the chosen cuts for all detectors in all configurations. As said above the Δt_{IV}^{ID} cuts are the same in both Gd and Gd++ selections. The ND and the FD-II having the same electronics, this explains the difference in the values entering in their cut definition with respect to FD-I.

3.3.4 The IV charge cut tuning

The last parameter to be tuned in IVV is the IV charge cut. The figures 3.8 to 3.10 represent at different IV charge cuts the ID visible energy spectra of events selected by the previous tuned cuts (i.e the nPMT, ΔR_{IV}^{ID} and Δt_{IV}^{ID}). One can notice the shape of the spectra remains unchanged whatever the IV charge cut is; this combined to the number of entries relatively close from a cut to another indicate that the IV charge has almost no impact on the selection efficiency.

Since efficiency is not affected by the IV charge cut, the cut has been tuned by means of IVV inefficiency. The IVV inefficiency is the fraction of IBDs rejected by the cut. One method to measure this inefficiency consists in computing the probability of rejecting an IBD in random coincidence with an IV event; this inefficiency is referred as *random inefficiency*. For this purpose one has to select a sample of events with only accidental correlations between ID and IV. To fulfill this last requirement we made use of the sample of random events which are registered by the detector electronics at a fixed rate, the "external trigger sample" (cfr. section 2.9.1).

We used IV events of the external trigger sample and used them forcing a coincidence with IBD events in order to compute the inefficiency. To have enough statistics, a larger sample is obtained by associating to each ID signal

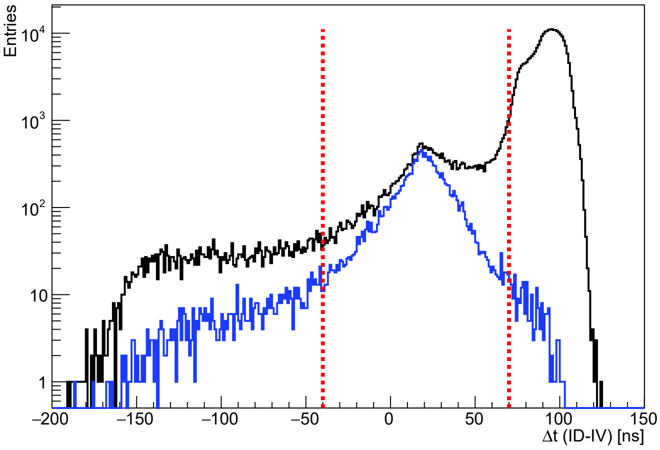

(a) ND

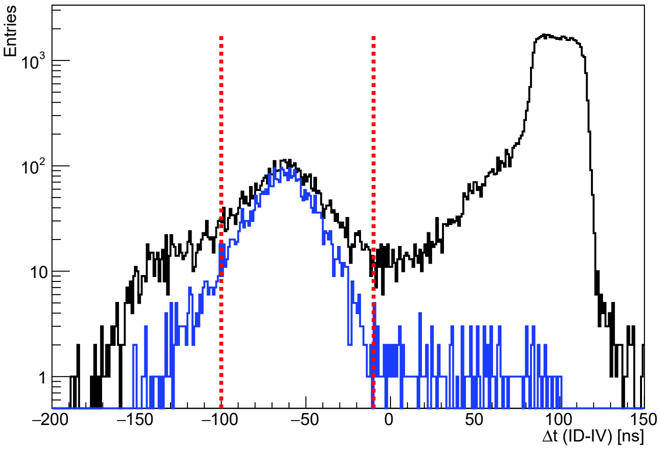

(b) FD-I

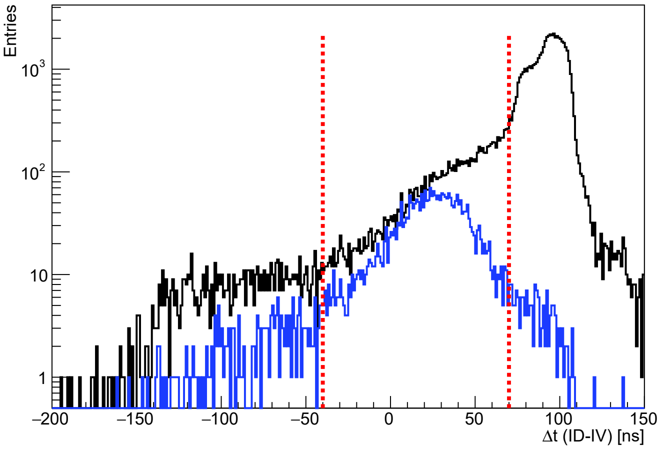

(c) FD-II

Figure 3.5: *Time coincidence* Δt_{IV}^{ID} *between ID and IV of prompt events for the Gd++ selection. In black the distribution for all IBD candidates and in blue the distribution of events selected by minimal IVV. The two red dashed lines indicate the range selected as IVV cuts : [-40,70] ns for FD-II and ND, [-100, -10] ns for FD-I.*

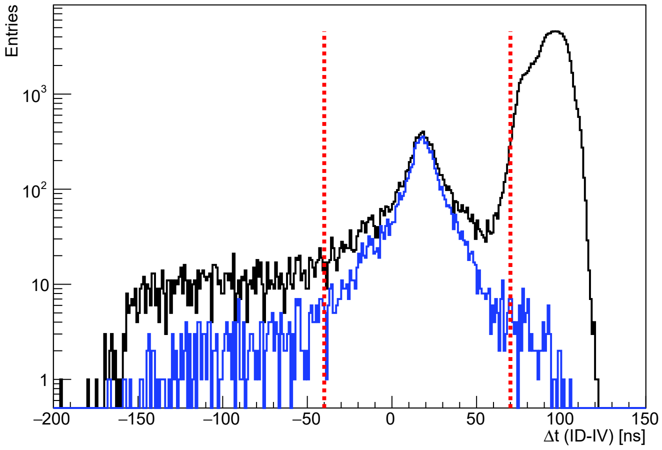

(a) ND

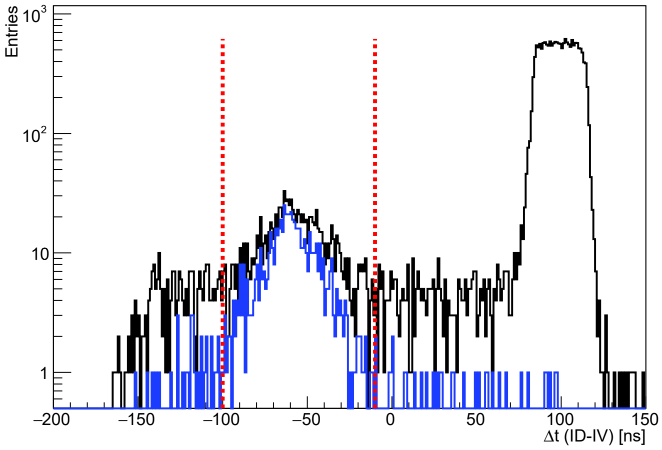

(b) FD-I

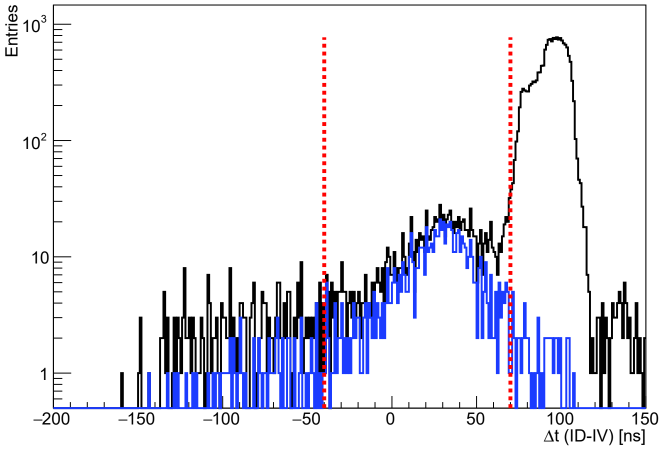

(c) FD-II

Figure 3.6: *Time coincidence Δt_{IV}^{ID} between ID and IV prompt events for the Gd selection. In black the distribution for all IBD candidates and in blue the distribution of events selected by minimal IVV. The cuts range, inherited from the Gd++ selection and indicated by the red dashed lines select, as well, the peak region in Gd selection as expected.*

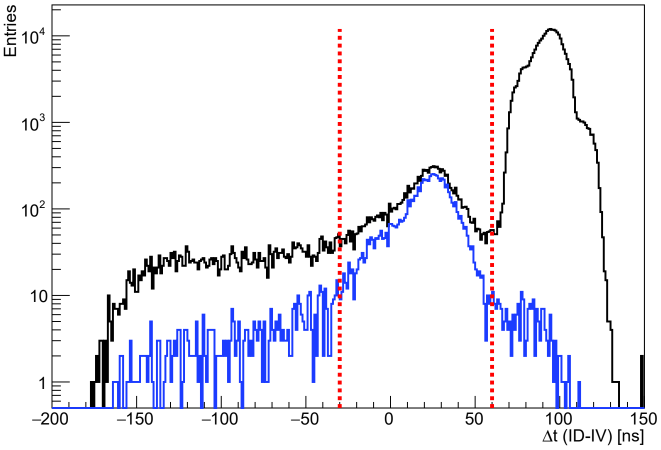

(a) ND

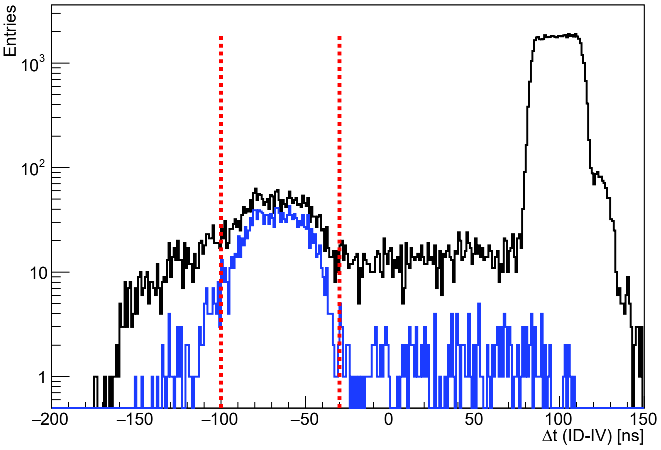

(b) FD-I

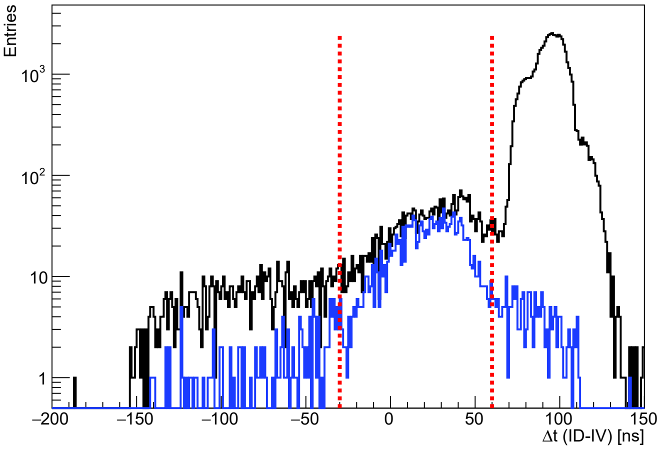

(c) FD-II

Figure 3.7: *Time coincidence Δt_{IV}^{ID} between ID and IV of delayed events for Gd++ selection. In black the distribution for all IBD candidates and in blue the distribution of events selected by minimal IVV. The two red dashed lines indicate the range selected as IVV cuts : [-30,60] ns for FD-II and ND, [-100, -30] ns for FD-I.*

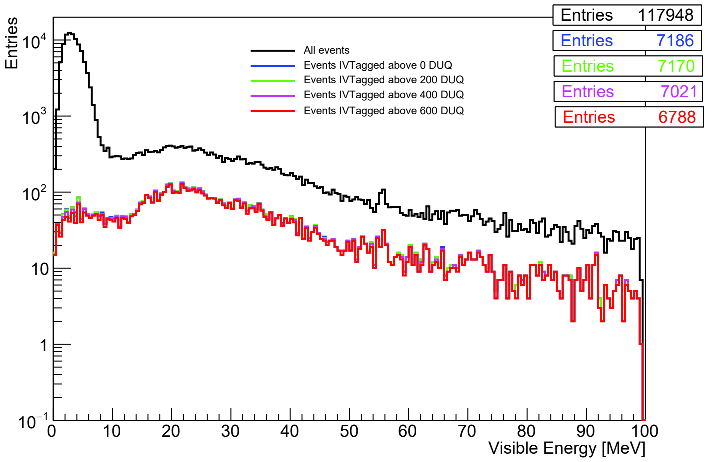

(a) ND

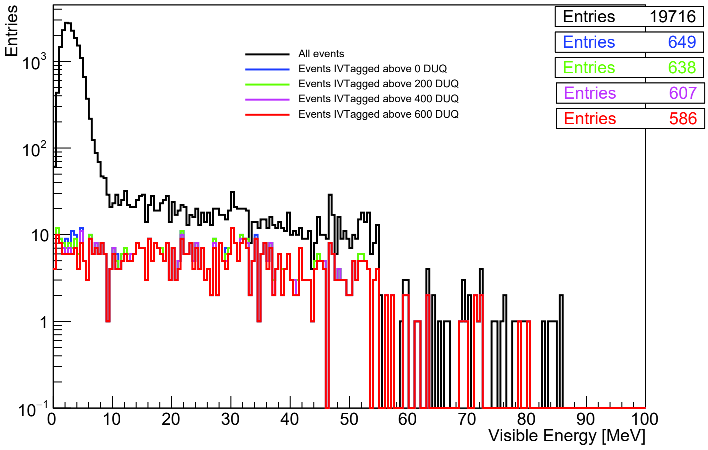

(b) FD-I

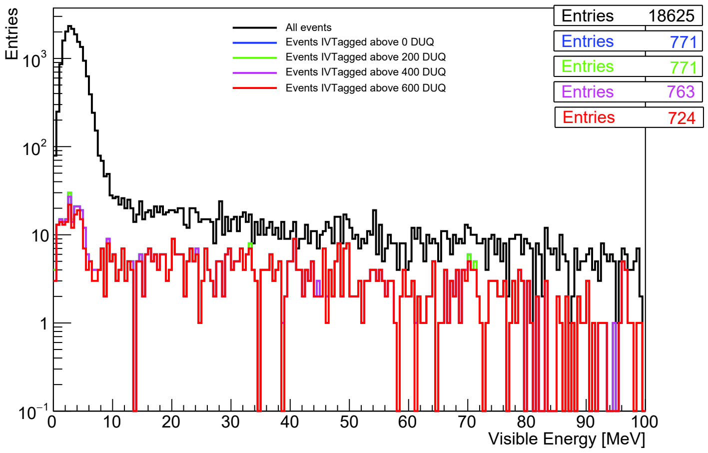

(c) FD-II

Figure 3.8: *ID visible energy for different DUQ cuts on charge deposited in IV by prompt events for the Gd selection.*

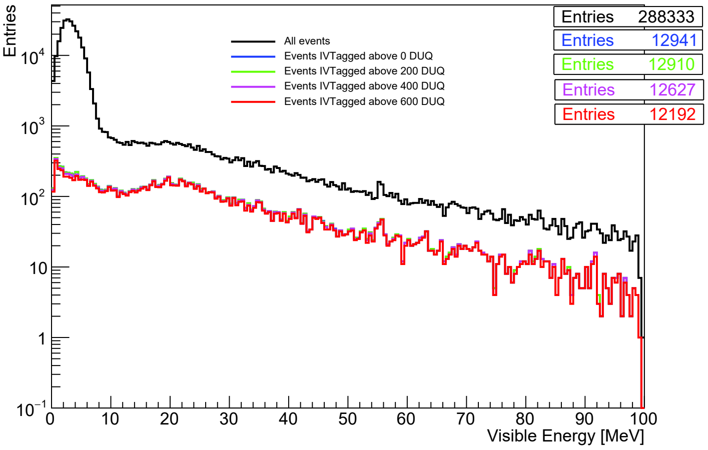

(a) ND

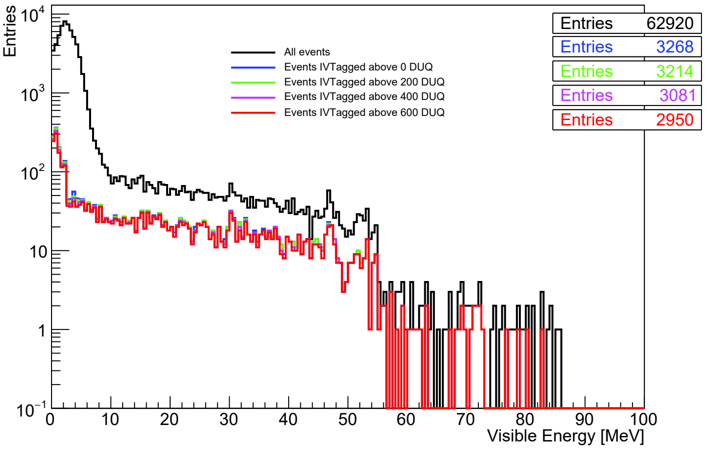

(b) FD-I

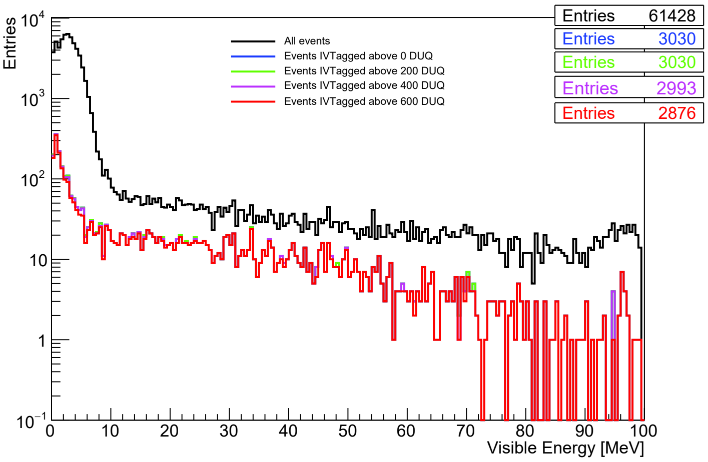

(c) FD-II

Figure 3.9: *ID visible energy spectra events for different cuts on IV charge deposited in IV by prompt events for the Gd++ selection.*

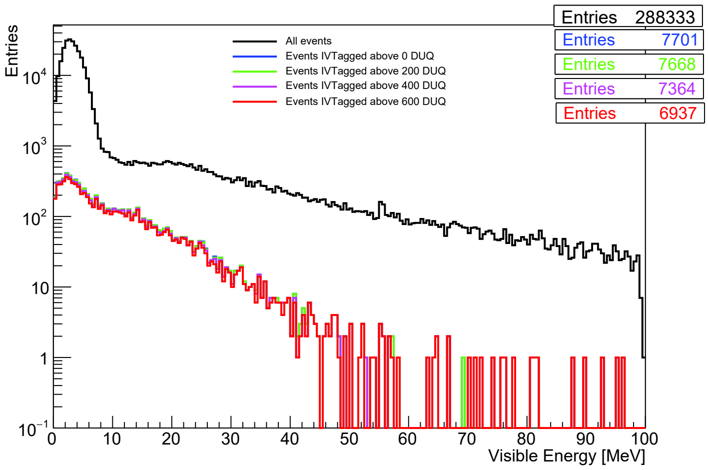

(a) ND

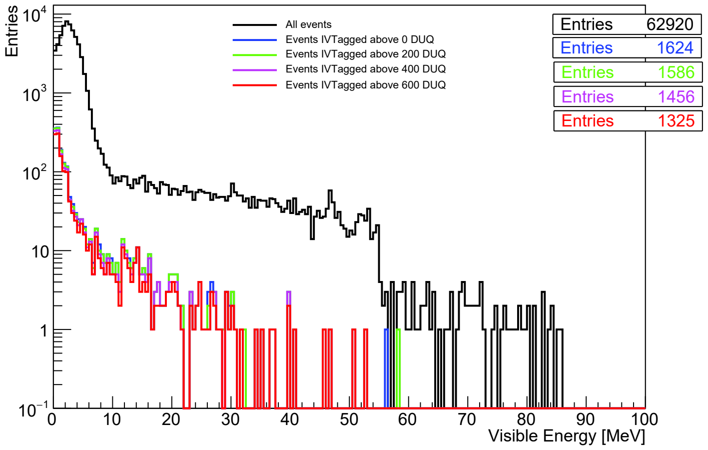

(b) FD-I

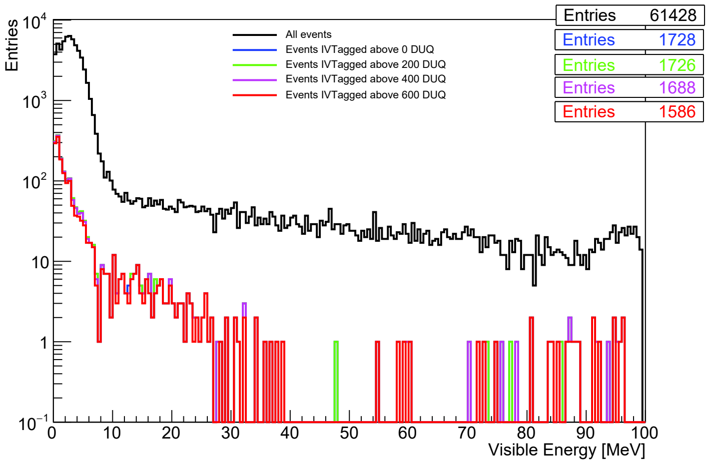

(c) FD-II

Figure 3.10: *ID visible energy spectra of prompt events for different cuts on IV charge deposited in IV by delayed events for Delayed-IVV tuning purpose for the Gd++ selection.*

10 IV events of the external trigger with charge larger than 0. The later 10 events were selected randomly. Hence :

- The probability of rejecting IBD events with IVV (the random inefficiency, ε_{IVV}^{Rand}) is the probability of rejecting IBD events in random coincidence with IV events (left box of equation 3.1) times the probability of having such a coincidence (right box of equation 3.1)

  $$\varepsilon_{IVV}^{Rand} = \boxed{\frac{nIVV}{10 \times nIBD}} \times \boxed{\frac{nEXT_{IV>0}}{nEXT}} \times T_f \tag{3.1}$$

  Where $nIVV$ is the number of events rejected by the IVV in the larger sample and $nIBD$ the number of IBD events selected in the final version of the Gd/Gd++ analysis; $nEXT_{IV>0}$ is the number of events of the External trigger with IV information while $nEXT$ is the total number of events of the External Trigger. The ratio between $nEXT_{IV>0}$ and $nEXT$ gave 0.019, 0.009 and 0.01 for respectively FD-I, FD-II and ND. A DC event consists in an energy deposition occuring within a 256 ns time window; however, in the present IVV tuning the ID-IV time coincidence window is not 256 ns large (cfr table 3.3). The last multiplicative factor T_f has been added to take into account this fact. T_f is the ratio between 256 ns and the width of the ID-IV time selection window corresponding to the IVV type and the detector studied. Table 3.4 gathers the obtained values of T_f.

Detector	T_f for Prompt-IVV	T_f for Delayed-IVV
ND and FD-II	0.43	0.35
FD-I	0.39	0.50

  Table 3.4: *T_f factor values computed for different detectors and IVV types.*

- ε_{IVV}^{Rand} was computed for different DUQ cuts.

For different IV DUQ cut, ε_{IVV}^{Rand} has been measured according to the method described above. The figure 3.11 shows the exponential decrease of ε_{IVV}^{Rand} as a function of IV charge cuts. Indeed, it can be noticed that ε_{IVV}^{Rand} is negligible (<0.1 %) and decreases very quickly as the charge cuts increase. This demonstrates the very weak random inefficiency of IVV as tuned up to now.

The negligible values of random inefficiency obtained facilitates the constraints on the choice of the IV charge cut in these conditions. We required one cut for all the configurations with the condition of $\varepsilon_{IVV}^{Rand} < 5 \times 10^{-3}\%$. This condition is satisfied above 300 DUQ in ND and FD-II in figure 3.11. The IV charge condition for FD-I has been kept as inherited from DC-III i.e IV Charge > 400 DUQ.

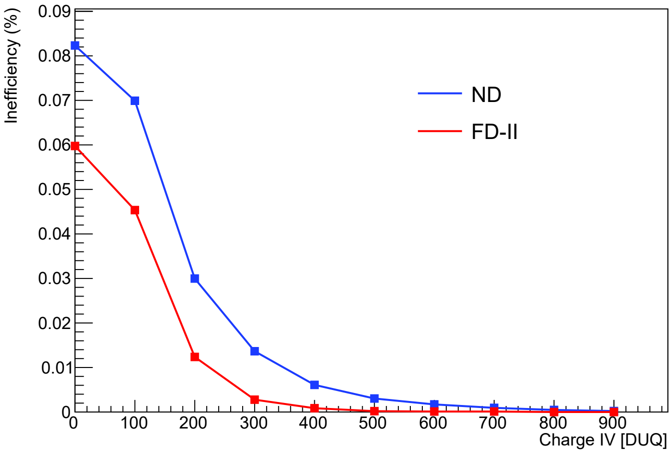

(a) Prompt-IVV : Gd

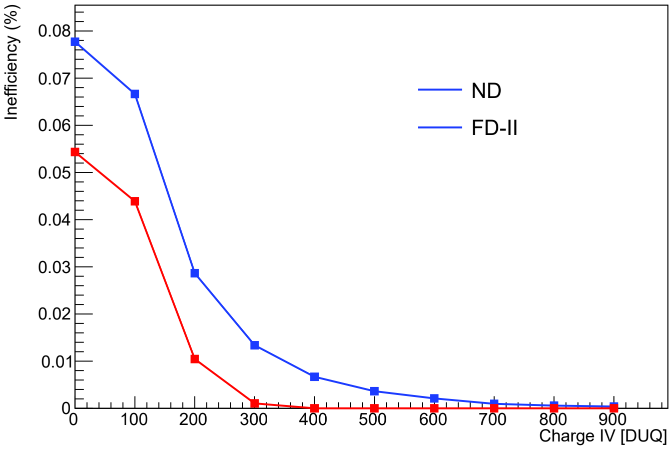

(b) Prompt-IVV : Gd++

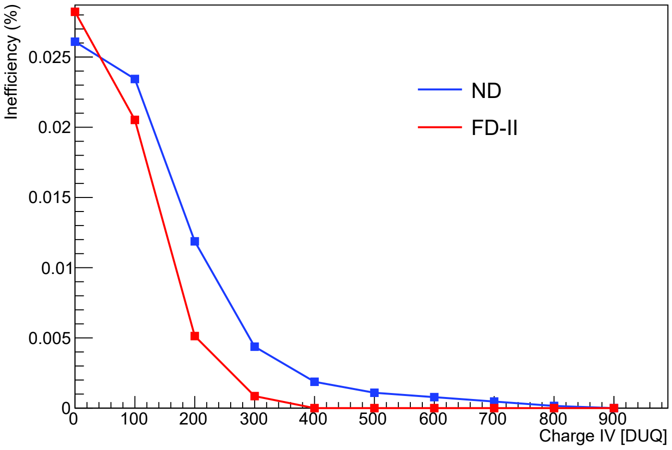

(c) Delayed-IVV : Gd++

Figure 3.11: *Prompt-IVV random inefficiency* $\overline{\varepsilon}_{IVV}^{Rand}$ *as a function of cuts on charge deposited in IV by prompt events for the Gd selection.*

3.4 Correlated IVV inefficiency measurement

3.4.1 Method

The robustness of a background veto relies not only on its tagging efficiency but also on its inefficiency i.e the ability to preserve the signal of interest when applied on the data. In view of its basic assumptions, the IVV is susceptible to tag true IBDs that happen to be in coincidence with an energy deposition in the IV. This IV energy deposition can be either accidental or correlated to the IBD:

- An accidental coincidence between an $\overline{\nu_e}$ interacting in the ID and an energy deposition in the IV due to a γ from natural radioactivity or thermal neutron capture on H in IV could be tagged by IVV.
- Correlated IV energy deposition that occurs when a γ from the positron annihilation or from the neutron capture escapes from the ID into the IV. This second kind of IV energy deposition is more likely to occur in the Hydrogen selection since the IBD reactions can occur closer to the IV, in the GC.

Thus, the main challenge in tuning IVV cuts is to avoid such rejection of IBDs. A dedicated inefficiency study is presented in section 3.4.

The investigation on the IVV correlated inefficiency $\overline{\varepsilon}_{IVV}^{Cor}$started by looking at the visible ID energy spectra of events selected by IVV after all other background vetoes have been applied. The red curve in figure 3.12 corresponds to the IVV vetoed events in each configuration.

The shape of the prompt energy spectrum of events selected by IVV gives a first indication of the inefficiency. The particular case of Gd selection (cfr. red curves of figure 3.12) where the spectra of events selected by Prompt-IVV present a bump around 3 MeV, especially for ND and FD-II, has been deeply investigated. Indeed, knowing that such a bump is expected in the prompt energy spectrum of the $\overline{\nu_e}$ signal, it became then crucial to investigate on these events. Analysis of the vertices location and of the time correlation distributions between prompt and delayed signals of these particular events showed finally that they were not IBDs. We present in section 3.4.3 an additional proof of this assertion based on Monte Carlo simulation.

Measuring the IVV correlated inefficiency permits to evaluate the fraction of true IBDs that is rejected by IVV. For that purpose we made use of Monte Carlo files containing, by construction, a pure sample of simulated IBDs. The method is to apply IVV on the MC pure IBDs sample and compute the percent of IBDs rejected. It was decided, as preliminary to this analysis, to

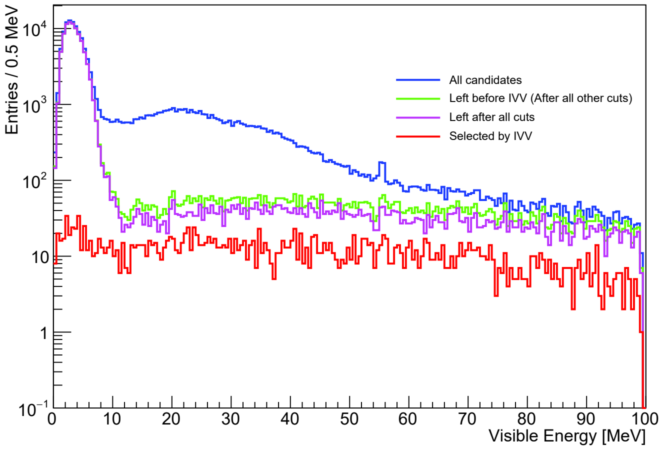

(a) ND

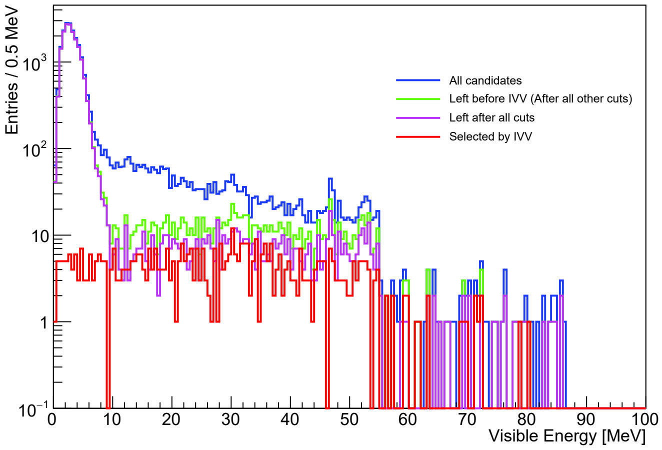

(b) FD-I

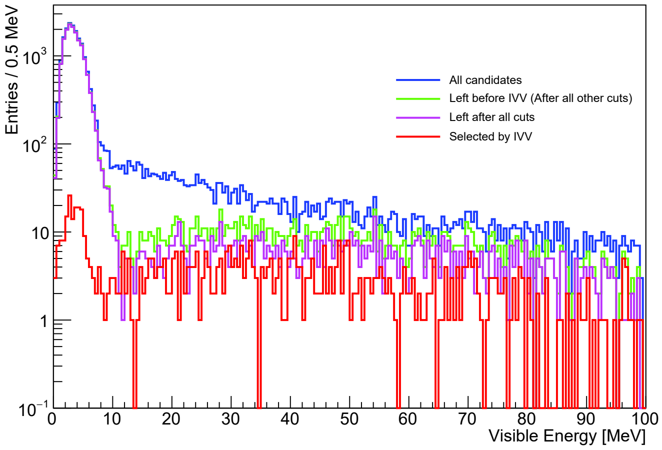

(c) FD-II

Figure 3.12: *Visible prompt energy spectra before and after background subtraction for Gd selection. In red the spectra of events selected by Prompt-IVV.*

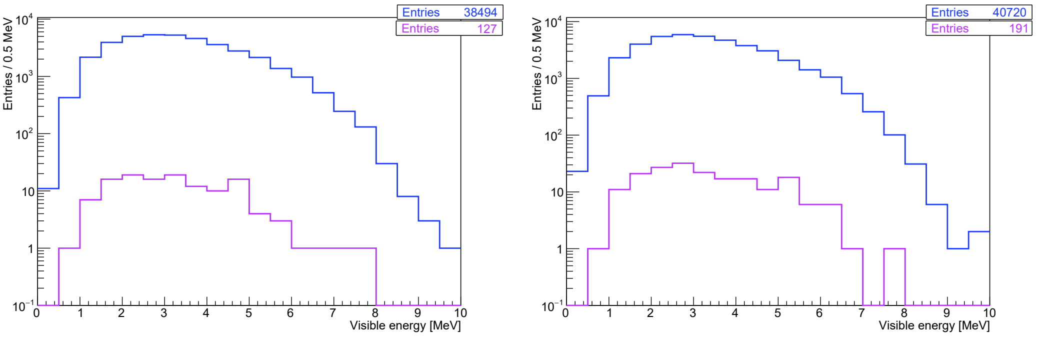

(a) ND (b) FD-II

Figure 3.13: ***Monte Carlo**: Visible energy spectrum of events, in purple, selected by Delayed-IVV compared to all candidates energy spectrum in blue.*

Detector	$\bar{\varepsilon}_{D-IVV}$ **(Monte Carlo)**	$\bar{\varepsilon}_{D-IVV}$ **(Data)**
ND	0.33±0.03 %	0.50±0.02 %
FD-II	0.47±0.03 %	0.85±0.07 %

Table 3.5: *Comparative table of Delayed-IVV inefficiency between MC and data. Values are obtained by doing the ratio between the number of events selected by the Delayed-IVV and the number of all candidates for each subfigure of figure 3.14. Errors computed here are purely statistical.*

probe the validity of our Monte Carlo on which relies the whole study of correlated IVV inefficiency.

3.4.2 Monte Carlo validation

The Monte Carlo happens to be a key element in this inefficiency measurement method, it is then important to know at which extent one can trust the provided Monte Carlo. A useful tool has been used to answer this question : the Delayed-IVV. Indeed, as stated in the introduction of the present chapter, the Delayed-IVV is highly inefficient in Gd selection. Hence, comparable Delayed-IVV inefficiency values $\bar{\varepsilon}_{D-IVV}$ between data and Monte Carlo are expected. The figures 3.13 and 3.14 show this comparison between Monte Carlo and data for ND and FD-II.

The inefficiency values of table 3.5 are computed as the ratio of the number of events selected by the Delayed-IVV to the number of all candidates, numbers provided by the figures 3.13 and 3.14. The assigned errors are purely statistical.

Values of inefficiency obtained on Monte Carlo are visibly lower than the data ones as it can be seen on table 3.5. This is expected since, unlike in MC,

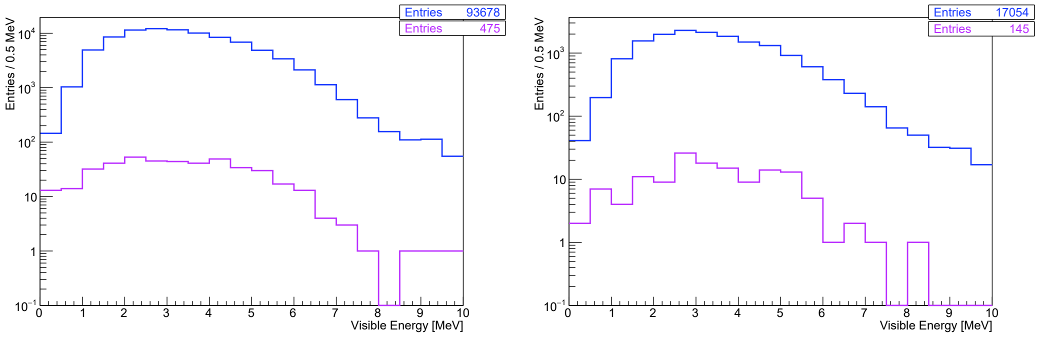

(a) ND

(b) FD-II

Figure 3.14: ***True Data***: *Visible energy spectrum of events, in purple, selected by Delayed-IVV compared to all candidates energy spectrum in blue. The blue curve is the spectrum provided by the final sample of IBDs after the subtraction of all the backgrounds.*

the final sample of data after the subtraction of all the backgrounds still contains few background contamination remaining. Hence, Delayed-IVV applied on data selects more events, IBDs and some background events, leading to an overestimation of the inefficiency. Nevertheless, the ranges of the obtained values in these conditions validate sufficiently the Monte Carlo used in the coming section.

3.4.3 IVV inefficiency on Monte Carlo data

Prompt-IVV applied on Monte Carlo data for Gd selection cuts only 3 events over respectively 38494 and 40720 events in ND and FD-II as it is shown in figure 3.15, which is very negligible : 0.0078± 0.0044 $\%$ of events for ND and 0.0073± 0.0042 $\%$ of events for FD-II. One notices first the absence of the bumps observed in the data (Cfr. figure 3.12 (a) and (c)), this confirms the non-IBD origin of the bumps. The correlated inefficiency $\overline{\varepsilon}^{MC}_{Cor}$ is computed here as the ratio of the number of events selected to the total number of IBDs present in the MC.

However, although the non-IBD origin of the bump events of figure 3.12 is established, more investigations are to be done for their characterisation.

The same analysis scheme has been used in Gd++ selection for the prompt and delayed IVV. The table 3.6 gathers the values of inefficiency obtained for the MC data in all these configurations.

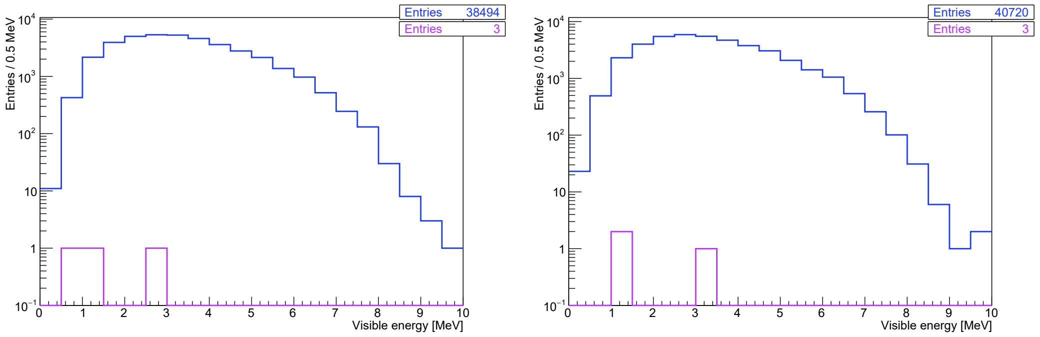

(a) ND (b) FD-II

Figure 3.15: *Energy spectrum of events selected by Prompt-IVV on Gd-MC. All candidates spectrum is shown in blue for comparison.*

	Prompt-IVV $\overline{\varepsilon}^{MC}_{Cor}$		Delayed-IVV $\overline{\varepsilon}^{MC}_{Cor}$
	Gd	**Gd++**	**Gd++**
ND	$0.0078 \pm 0.0044\%$	$0.027 \pm 0.006\%$	$0.072 \pm 0.011\%$
FD-II	0.0073 ± 0.0042 %	0.014 ± 0.007 %	0.055 ± 0.014 %

Table 3.6: *Correlated IVV inefficiency $\overline{\varepsilon}^{MC}_{Cor}$ for the MC data in all the configurations.*

3.5 Summary

The performed analysis had for final goal to tune the IVV rejection conditions on the IBD candidates to identify event-by-event those originating from outside the detector, especially the FN. The challenge was to set up the IVV by minimising as much as possible the inefficiency to avoid rejection of IBDs. This challenge was achieved by reaching inefficiency values very negligible.

The IVV has been tuned for all detectors in all configurations. Tables 3.7 and 3.8 present, in summary, the cuts for each detector in all configurations (i.e, Prompt and Delayed IVV, Gd and Gd++ selections). As stated in section 3.1 Delayed-IVV is to be applied only in Gd++ selection for events with delayed energy less than 3 MeV.

Variables	ND and FD-II	FD-I
PMT multiplicity	nPMT ≥ 1	nPMT ≥ 1
DR (ID-IV)	$\leq 3.7m$	$\leq 3.7m$
Dt (ID-IV)	[-40 ns , 70 ns]	[-100 ns , -10 ns]
IV Charge	300 DUQ	400 DUQ

Table 3.7: *Prompt-IVV cuts final definition and the associated number of events selected*

Variables	ND and FD-II	FD-I
PMT multiplicity	nPMT ≥ 1	nPMT ≥ 1
DR (ID-IV)	$\leq 3.7m$	$\leq 3.7m$
Dt (ID-IV)	[-30 ns , 60 ns]	[-100 ns , -30 ns]
IV Charge	300 DUQ	400 DUQ

Table 3.8: *Delayed-IVV cuts final definition and the associated number of events selected. Delayed-IVV is to be applied only in Gd++ selections for events with delayed energy less than 3 MeV.*

The IVV so tuned has been admitted officially as baseline by the Double Chooz collaboration in DC-IV, the 15 months data release and analysis campaign. The sample of events selected by the IVV was used to define a shape model of the correlated background and to measure the corresponding rate as presented in the following section.

3.6 Correlated background spectrum shape and rate

3.6.1 Correlated background shape

The sample of events selected by the Prompt-IVV can be used to infer the energy spectrum of the remaining correlated background and define a shape model in agreement with it. The defined shape model will then be used to measure the remaining correlated background rate. The precise knowledge of the shape models of the remaining background in the final IBD sample is determining since, as reported in section 2.13, these shapes are inputs of the final fit from which emerges the value of θ_{13} mixing angle. To ensure a precise final value of θ_{13} the correlated background shape must be well known. This section is devoted to this task.

The IVV selects mainly FN and, to a lesser extent, SM and $\gamma - \gamma$ events. Hence, in order to have a likely pure sample of correlated background the IV charge cuts of table 3.7 need to be be raised up to remove the $\gamma - \gamma$ events from the IVV sample. Figures 3.16 and 3.17 show the higher IV charge cuts choice for each configuration. Several other cuts have been tested and happened to be either less efficient or decreasing the statistics with roughly the same efficiency. The selected cuts values are summarised in table 3.9.

The impact, on IVV energy spectrum, of the cuts listed in table 3.9 are visible on the figures 3.18 and 3.19 where it is shown at which extent raising up the IV charge cut removes the accidental background peak in the IVV spectrum. We refer as IVT (Inner Veto tag) the subsample of IVV events vetoed by the IV charge cuts listed in the above table. The IVT sample is the pure correlated background sample on which relies the shape definition and the

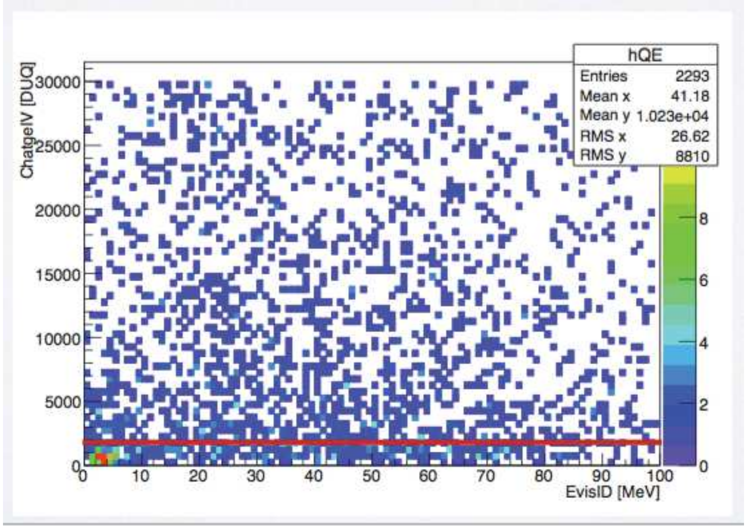

(a) ND

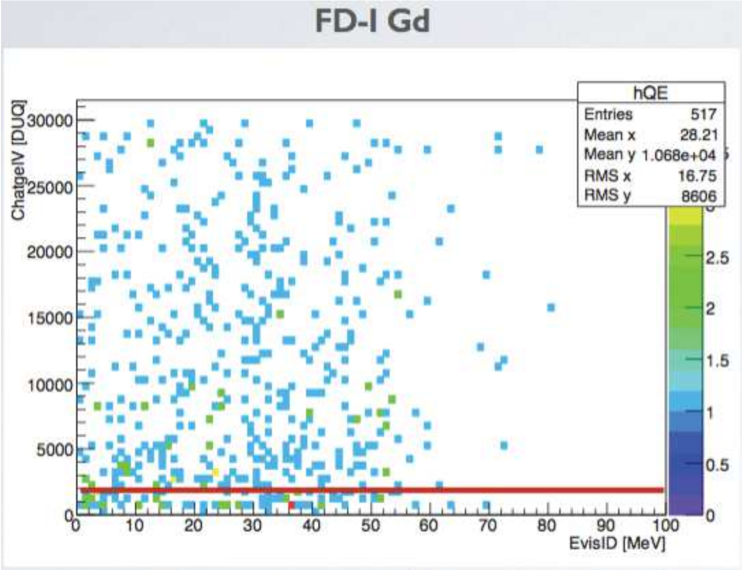

(b) FD-I

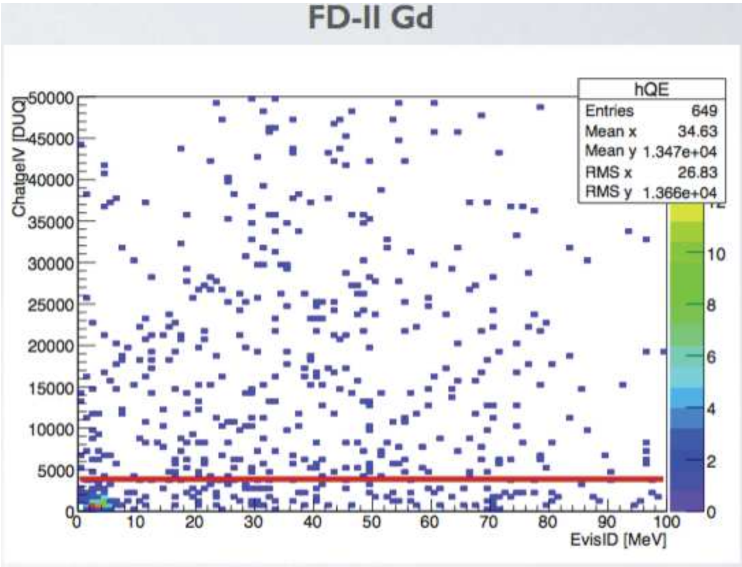

(c) FD-II

Figure 3.16: *IV charge versus visible energy distribution of events selected by IVV for the Gd selection. The red thick line indicates the IV charge cut chosen in order to remove $\gamma - \gamma$ events from the IVV sample.*

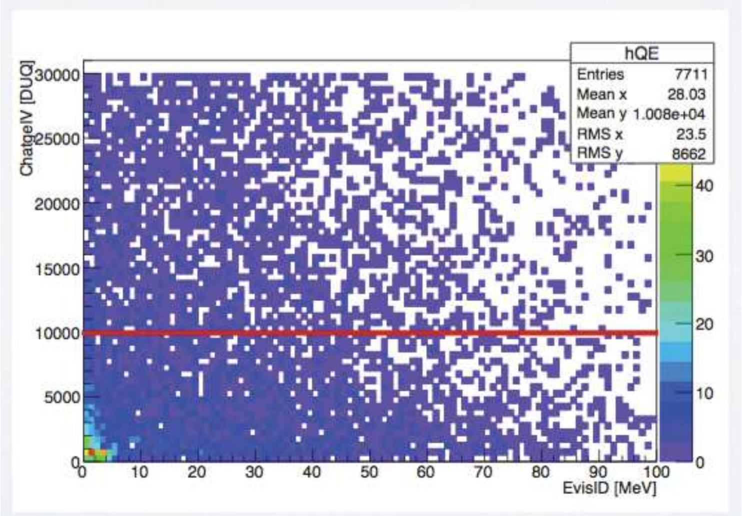

(a) ND

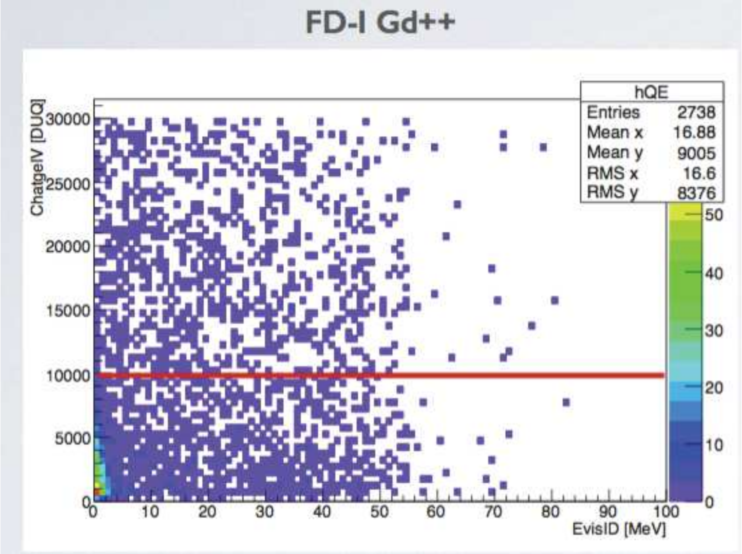

(b) FD-I

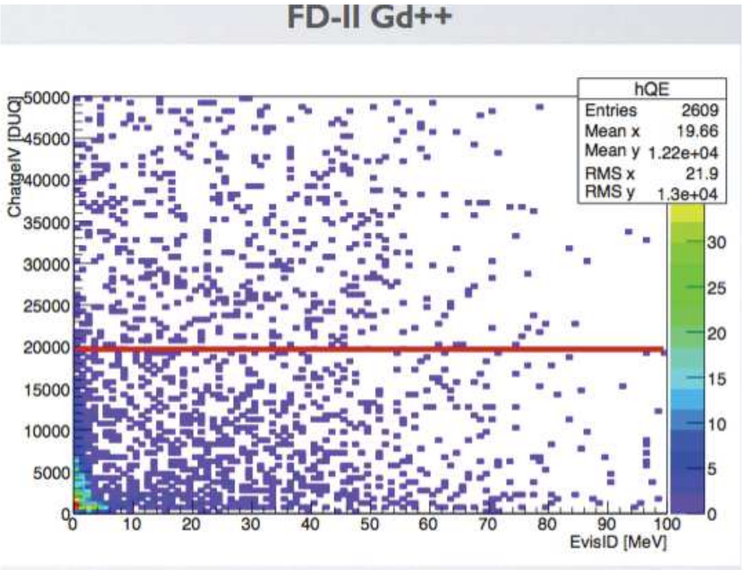

(c) FD-II

Figure 3.17: *IV charge versus visible energy distribution of events selected by IVV for the Gd++ selection. The red thick line indicates the IV charge cut chosen in order to remove the $\gamma - \gamma$ events from the IVV sample.*

Detector	Gd selection	Gd ++ selection
ND	2000	10000
FD-I	2000	10000
FD-II	4000	20000

Table 3.9: *IV Charge (in DUQ) cuts chosen to remove the $\gamma - \gamma$ events from the IVV sample.*

rate measurement.

The low energy peaks, corresponding to the $\gamma - \gamma$ background contamination in the IVV sample in figure 3.18, are visibly suppressed in the IVT spectra, especially in ND and FD-II where they are particularly prominent. The same observation is valid on Gd++ selection as shown in figure 3.19; increasing the IV charge cut in IVV removes the $\gamma - \gamma$ events from the IVV sample.

The IVT sample was found to be consistent with the exclusive presence of FN. The remaining Stopping Muon contamination R_{SM}^{FV} after application of the Functional value cut (cf. section 2.10.3) has been measured over 467.903 live days of data taking in [86] and found consistent with zero: $R_{SM}^{FV} = (1.9^{+0.8}_{-0.7} \pm 0.7) \times 10^{-2}$ day^{-1}. Thus, we refer henceforth in the text as FN the background selected by the IVT, instead of the general term "correlated background" used so far.

Beside the IVT sample, another likely pure correlated background sample is possible by means of the Outer Veto. Indeed, events in coincidence with an activation of the OV form pratically a correlated background sample. The location of the OV above the detector and its design allow to have a high efficiency for vetoing muons, as well as to give precise coordinate information on the detected muons for the purposes of muon tracking. Hence, the OV can veto fast neutrons and stopping muons, as these backgrounds occur coincident with the muon signal in the OV.

We refer the OV based selection as OVT (Outer Veto tagging). Hence, since both OVT and IVT select correlated background, the comparison of their respective spectra may be a source of information while the FN rate provided by the OVT sample serve, in the next section, as cross check to the one from the IVT sample. Figures 3.20 and 3.21 show, respectively for the Gd and Gd++ selections, the visible energy spectra of events selected by IVT, in red, and by OVT, in blue.

The two samples spectra, IVT and OVT, are in relatively good agreement in their shapes as it can be seen in figure 3.20 and 3.21. The differences can be imputed, as shown in figure 3.22, to the presence of a greater amount of SM in the OVT sample with respect to IVT sample. Indeed, the OVT and the IVT do not tag exactly the same events since if OVT collects only events in

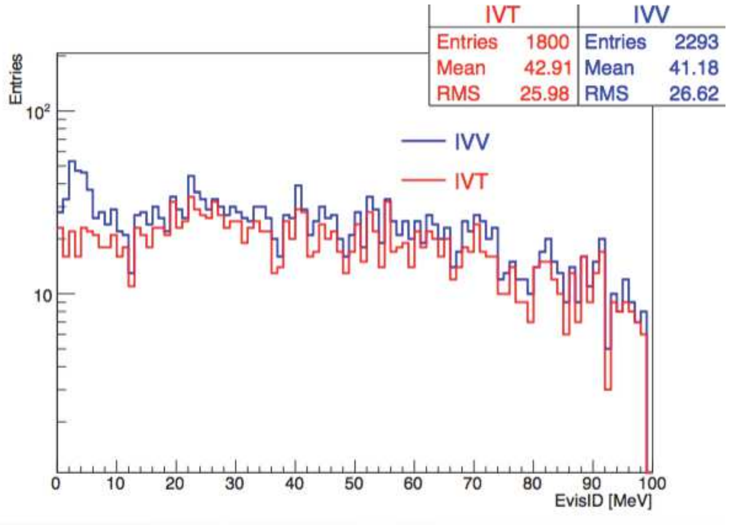

(a) ND

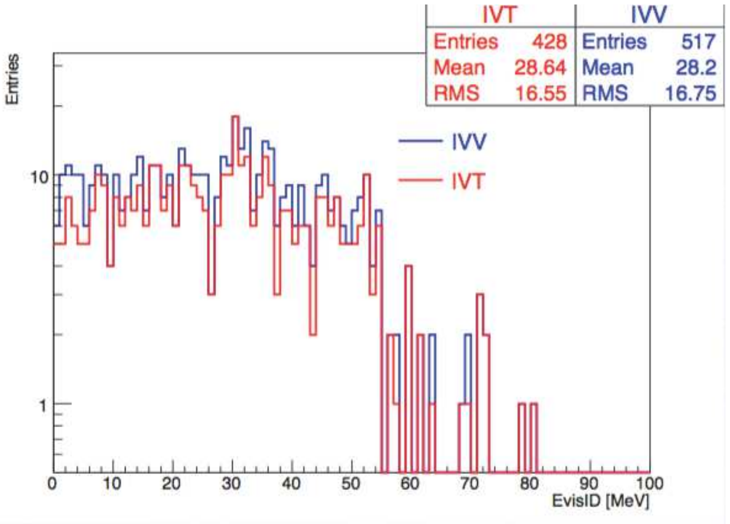

(b) FD-I

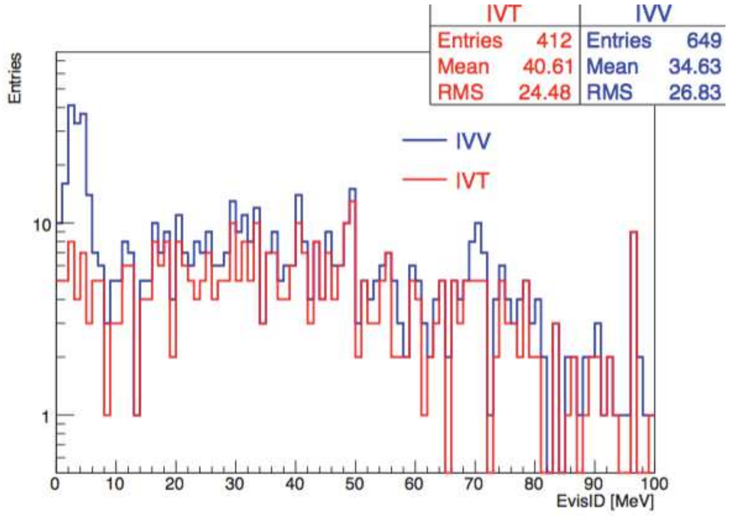

(c) FD-II

Figure 3.18: *Visible ID energy spectrum of prompt events selected by IVV (in blue) and IVT (in red) on Gd selection.*

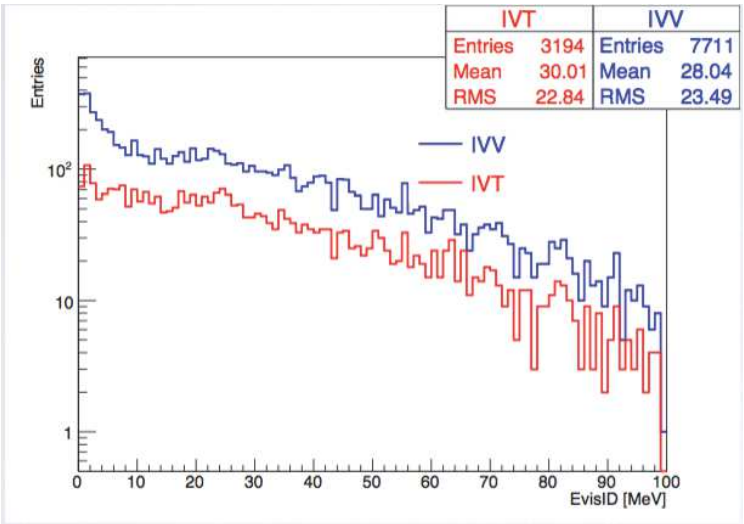

(a) ND

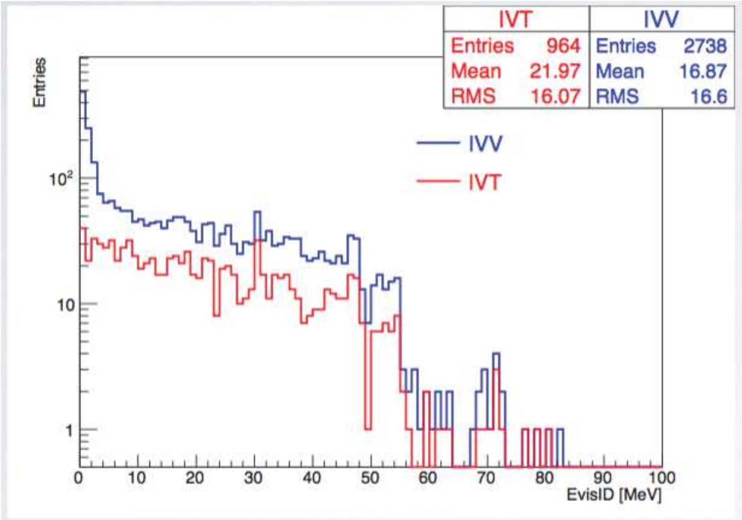

(b) FD-I

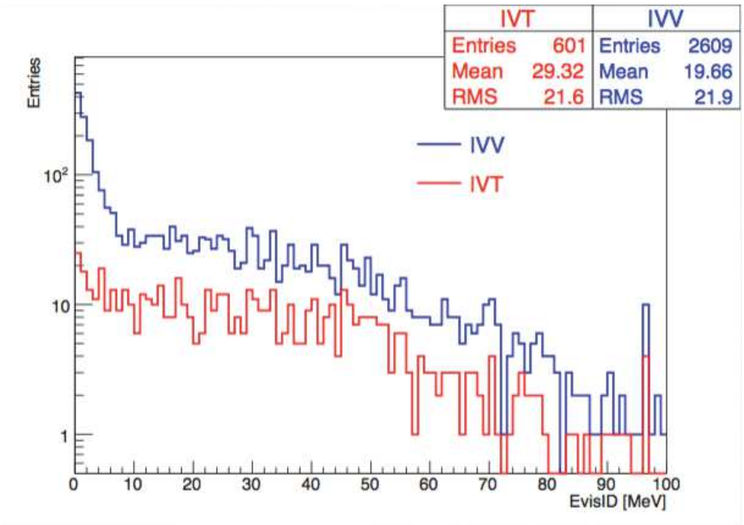

(c) FD-II

Figure 3.19: *Visible ID energy spectrum of prompt events selected by IVV (in blue) and IVT (in red) on Gd++ selection.*

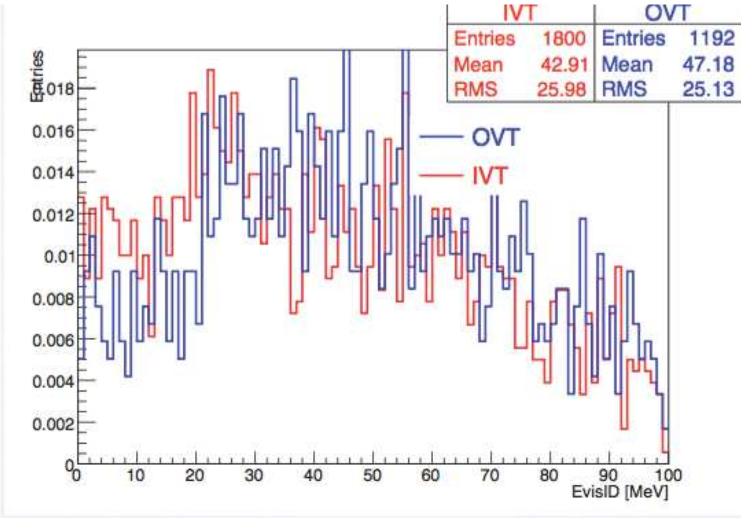

(a) ND

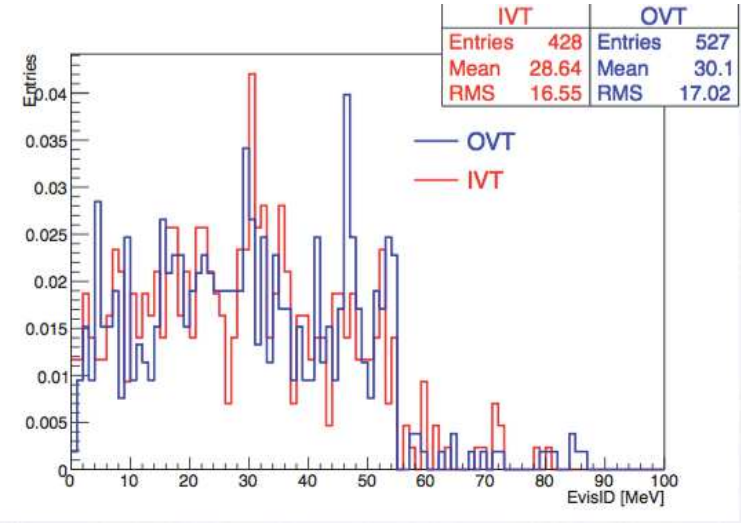

(b) FD-I

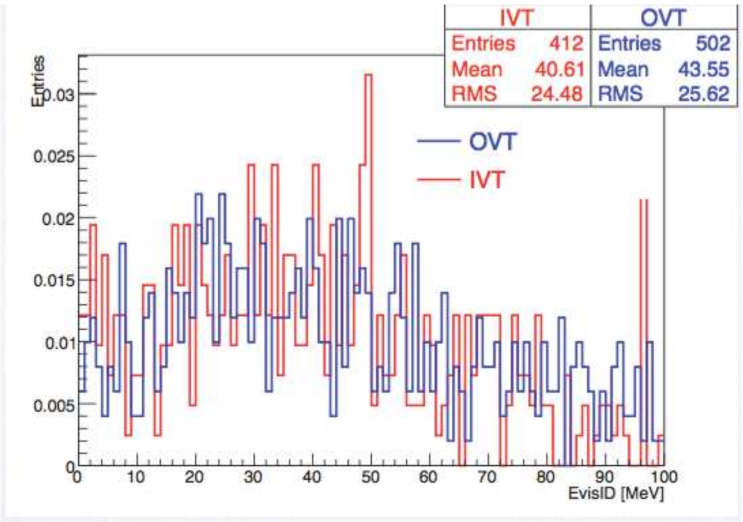

(c) FD-II

Figure 3.20: *Visible energy spectra of prompt events selected by IVT (in red) and OVT (in blue) for the Gd selection.*

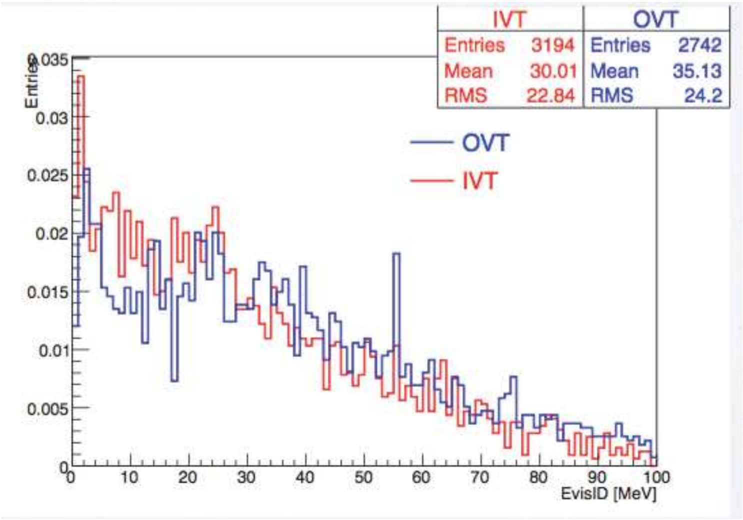

(a) ND

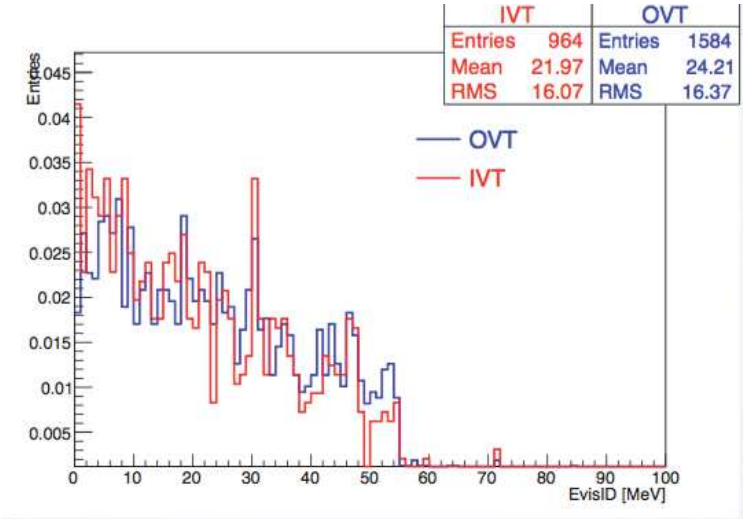

(b) FD-I

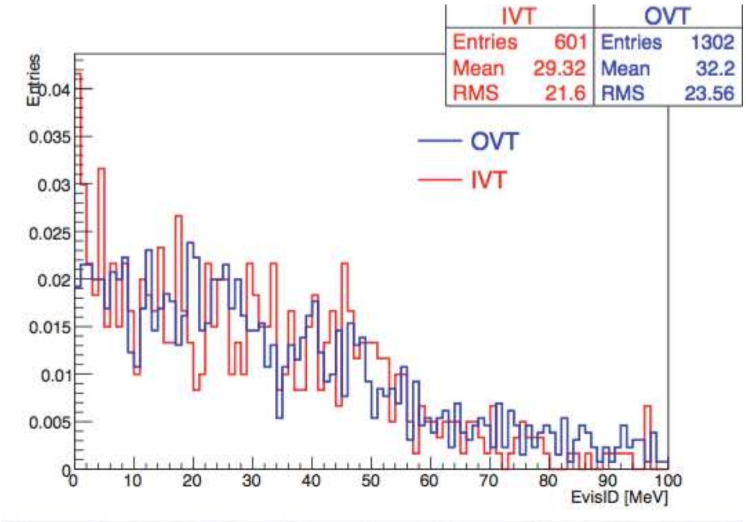

(c) FD-II

Figure 3.21: *Visible energy spectra of prompt events selected by IVT (in red) and OVT (in blue) for the Gd++ selection.*

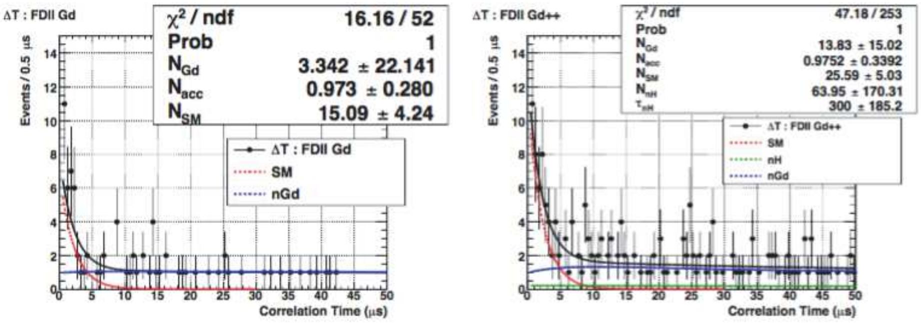

Figure 3.22: *SM contamination in OVT sample for the Gd (left) and Gd++ (right) IBD selection cuts, on the FDII data set. The candidates time correlation is fit with an empirical function, based on exponentials, where the μ decay component, in red, could be extracted. The captures on Gd and H are represented by the blue and green lines, respectively.*

coincidence with OV, the IVT collects as well neutrons induced by muons that have not crossed the OV panels. These particular neutrons, thus created further, reach the detector with a lower energy. This is particularly visible in the ND where the IVT spectrum is well above the OVT one in the low energy region.

The Gd++ selection in figure 3.21 reveals more events in the low energy region for IVT spectra than for OVT as expected; the Gd++ selection collects indeed more low energy events due to the partial energy deposition in ID by events that occur close to the borders of the GC. Moreover, a greater accidental background contamination due to the neutrons capture on hydrogen is expected in Gd++ selection.

3.6.2 Correlated background rate measurement

Two independent methods are used to measure the rate of FN background in DC experiment : The "No-Fit" and the "Fit" methods.

The "No-Fit" method

The rationale leading to the correlated background rate measurement without requiring any shape model is the following : under the hypothesis that above 20 MeV in the IBD candidates sample we have only FN, we compute first the FN identification rate by IVT as :

$$\xi_{IVT}^{FN} = \frac{n_{IVT}^{[20;100]}}{n_{IVV}^{[20;100]}} \tag{3.2}$$

Samples	Events in [0;20] MeV	Events in [20-100] MeV
IVV	$181(174 \pm 20)$	336
IVT	146	282
IBD cand.	$--$	562

Table 3.10: *Number of events in the ND IVV and IVT samples, for the Gd selection, at different energy ranges. FN numbers as computed by the "No-Fit" method are written in red.*

where $n_{IVV}^{[20;100]}$ and $n_{IVT}^{[20;100]}$ stand respectively for the numbers of events selected by IVV and IVT in the [20;100] MeV region. Then, given the IVT efficiency value, the number of FN expected below 20 MeV in the IVV sample is :

$$n_{FN-IVV}^{[0;20]} = \frac{n_{IVT}^{[0;20]}}{\xi_{IVT}^{FN}} \tag{3.3}$$

The fraction R of FN below 20 MeV with respect to the FN above 20 MeV is given by, for the IVV sample :

$$R = \frac{n_{FN-IVV}^{[0;20]}}{n_{FN-IVV}^{[20;100]}} \tag{3.4}$$

Considering $n_{FN-Cand}^{[20;100]}$ the number of IBD candidates above 20 MeV, the estimate of FN below 20 MeV in the IBD sample is finally :

$$nFN = n_{FN-Cand}^{[20;100]} \times R. \tag{3.5}$$

The simple ratio of nFN over the data lifetime gives the rate measurement.

For instance, following the steps of FN estimation described above, the Gd analysis at the ND provides $\xi_{IVT}^{FN} = 0.84 \pm 0.07$, the number of FN expected below 20 MeV $n_{FN-IVV}^{[0;20]} = 174 \pm 20$, the fraction R of FN below 20 MeV with respect to the FN above 20 MeV is 0.52 ± 0.07 for the IVV sample. These numbers are gathered in table 3.10. Considering that 562 FN are present in IBD candidates above 20 MeV, 291 ± 39 FN are expected in the [0;20] MeV region i.e 0.63 ± 0.08 FN per day, given the 460.5 days of livetime. Table 3.11 gathers for all the configurations the FN rate values as obtained by the "No-Fit" method.

The "No-Fit" rate measurement method applied on the OVT sample introduced in the preceding section may serve as an alternative estimate of FN rate. The results obtained are gathered in table 3.12.

The comparison of tables 3.11 and 3.12 shows an agreement between IVT and OVT for FD-I and FD-II in Gd selection as expected. Indeed the two

Configurations	Total FN [0;20] MeV	Livetime (days)	Rate per day
ND Gd	1473 ± 99	272.85	5.4 ± 0.4
FD-I Gd	291 ± 39	460.9	0.63 ± 0.08
FD-II Gd	247 ± 34	366.1	0.68 ± 0.09
ND Gd++	7863 ± 339	272.85	28.8 ± 1.2
FD-I Gd++	1721 ± 142	460.9	3.7 ± 0.3
FD-II Gd++	1218 ± 118	366.1	3.3 ± 0.3

Table 3.11: *Fast neutrons rate values as obtained by the "No-Fit" method with the IVT sample.*

Configurations	FN estimate [0;20] MeV	Rate per day (OVT)
ND Gd	906 ± 74	$\mathbf{3.3 \pm 0.3}$
FD-I Gd	256 ± 26	$\mathbf{0.56 \pm 0.06}$
FD-II Gd	203 ± 24	$\mathbf{0.55 \pm 0.07}$
ND Gd++	5281 ± 223	$\mathbf{19.4 \pm 0.8}$
FD-I Gd++	1364 ± 77	$\mathbf{3.0 \pm 0.2}$
FD-II Gd++	1034 ± 64	$\mathbf{2.8 \pm 0.2}$

Table 3.12: *Fast neutrons rate values obtained by the "No-Fit" method with the OVT sample.*

samples, OVT and IVT, have roughly the same visible energy spectrum for FD-I and FD-II (cfr. figure 3.20). However, the OVT estimate of FN is typically smaller than the IVT one in all the configurations. The spectrum shape difference in figures 3.20 and 3.21 with less events at low energy for OVT explains this global feature as already mentioned in the conclusion of section of the preceding section.

The "Fit" method

Different shapes of the remaining FN background in the final IBD sample have been tested. The simplest mathematical functions in agreement with the pure correlated background spectra shapes as provided by the IVT sample have been found.

We present in this section the whole process that led to the determination of the remaining FN shape models for Gd and Gd++ selection, labelled respectively in the text $Fit_{Gd}^{FN-IBD}(x)$ and $Fit_{Gd++}^{FN-IBD}(x)$.

The details are shown for Gd selection while only the final results are presented for Gd++ selection. Distinction has to be made between the functions fitting the IVT spectrum shape, referred as $Fit(x)^{IVT}$ in the text, and the remaining FN background shape models $Fit_{Gd}^{FN-IBD}(x)$ or $Fit_{Gd++}^{FN-IBD}(x)$ used to estimate the FN in the final IBD sample. Indeed, the $Fit_{Gd/Gd++}^{FN-IBD}(x)$ parameters are derived from $Fit(x)^{IVT}$ as explained further.

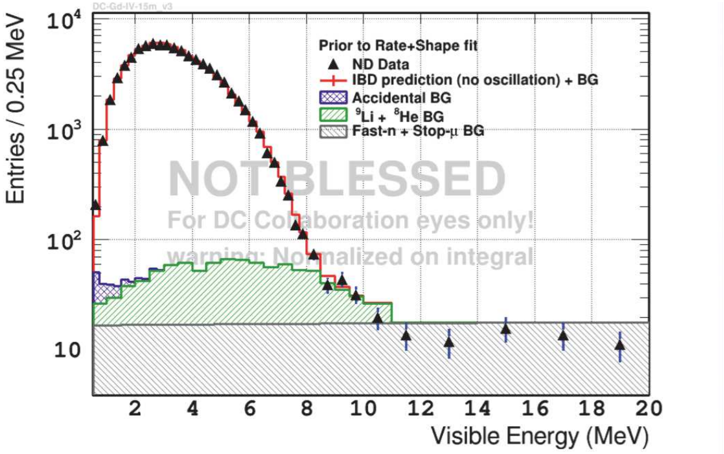

(a) ND

Figure 3.23: *Final visible ID energy spectrum of IBDs. The remaining FN background estimate, provided by the fit of the IVT spectrum shape between 0 and 100 MeV with a second order polynomial, happens to be higher than data in the region above 10 MeV.*

In order to obtain FN rates, two features had to be taken into account, namely the presence of muons capture events in the IVT spectrum and the energy dependence of the IVT inefficiency. First attempts of shape definitions without considering these features led to an inconsistency as shown in figure 3.23; the data points happened to be below the FN shape above 10 MeV. Extending the plot up to 100 MeV showed that the FN estimate is higher than data precisely in the [10,20] MeV region i.e. the precise region used in the final fit to set the FN normalisation. The need of a more accurate FN estimation was then evident.

We describe below the presence of muons capture events in the IVT spectrum and the energy dependence of the IVT inefficiency; their impact on the FN estimate is demonstrated.

The presence of muon capture events in Gd selection

The IVT energy spectrum in the Gd analysis, shown here in figures 3.24, 3.25 and 3.26 for each detector, reveals the presence of an uncommon bump between 10 and 30 MeV for the Gd selection, in particular for ND. The events of this bump were found to originate very likely from muon capture on ^{12}C . Indeed, they have the signature of muons capture events as they are located in the upper part of the detector with a time correlation between prompt and delayed signals inconsistent with SM and a spectrum shape corresponding to the buffer SM (cf. section 2.10.1).

In the muon capture case the energy lost by the μ^- before its capture and the

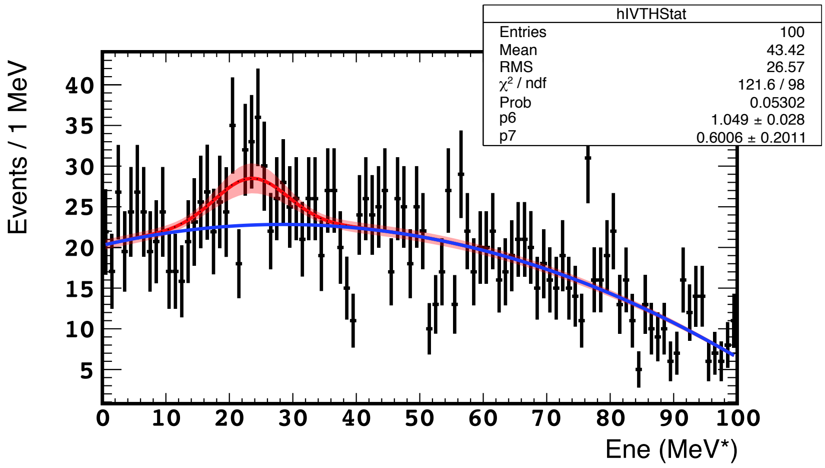

Figure 3.24: *Correlated background spectrum shape of events selected by IVT in ND for Gd selection. In blue is drawn the second order polynomial shape of the FN background while red curve is the function defined in equation 3.6 fiting both the FN and the muon capture events present in the IVT spectrum. The two fit curves, red and blue, curves are normalised for [20, 100] MeV range.*

produced neutron mimic respectively the $\overline{\nu}_e$ prompt and delayed signals.

The muon capture events are rejected by IVT and OVT but not from the delayed signal since the delayed signal is a neutron like in IBD case. They are therefore not present, at least in a visible fraction, in the final IBD sample.

Therefore, to a simple second order polynomial a Gaussian function must be added as follows :

$$Fit(x)^{IVT} = a_0 + a_1 x + a_2 x^2 + N_0 e^{\frac{-(x-x_0)^2}{2\sigma^2}} \tag{3.6}$$

to fit also the muon capture background bump present in the IVT spectrum. The figures 3.24, 3.25 and 3.26 show how the addition of the Gaussian function allows to fit both the FN and the muon capture events present in the IVT spectrum.

Since muon capture events are not present in the final IBD sample, only the second order polynomial of equation 3.6 is used to fit the remaining FN background spectrum. Hence we have

$$Fit^{FN-IBD}_{Gd}(x) = a_0 + a_1 x + a_2 x^2 \tag{3.7}$$

with $a_0 = 1.93101 \times 10^{-2}$, $a_1 = 1.72250 \times 10^{-1}$ and $a_2 = -3.03473 \times 10^{-3}$ provided by the fit of the IVT spectrum shown in figure 3.24.

The shape as fixed from the ND was used as well to fit the IVT spectrum in FD-I and FD-II as it can be seen in figures 3.25 and 3.26. The consistency between the 3 detectors is remarkable. It is expected indeed that within a

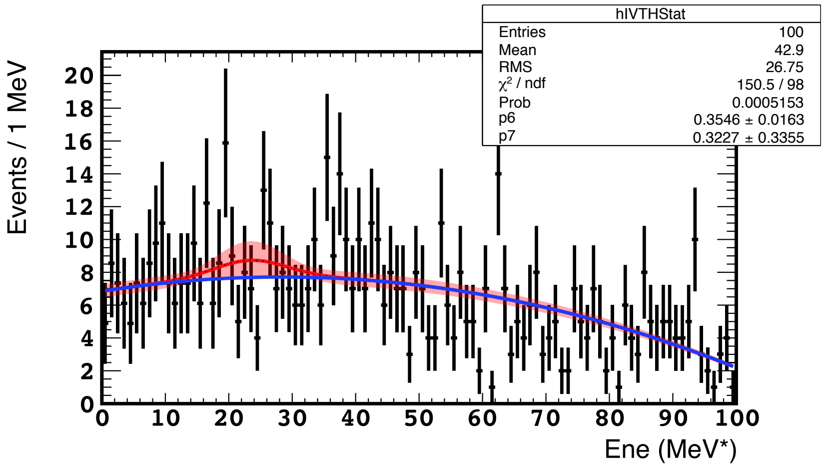

Figure 3.25: *Correlated background spectrum shape of events selected by IVT in FD-I for Gd selection. In blue is drawn the second order polynomial shape of the FN background while red curve is the function defined in equation 3.6 fiting both the FN and the muon capture events present in the IVT spectrum. The two fit curves fixed from the ND are normalised for [20, 100] MeV range.*

selection the same background will present the same shape. The relative abundance of the muon capture events in the ND is explained by the Gd leak in the GC introduced in section 2.3.1 and detailed in the next chapter of this volume.

The addition of physical corrections to the IVT spectrum shape $Fit(x)^{IVT}$ allows to fix accurately the coefficients of the shape models from which is deduced the estimate of the remaining FN in the final IBD sample.

Another correction to be added to the spectra shape $Fit_{Gd}^{FN-IBD}(x)$ in order to obtain the final FN estimates in agreement with the data is due to the energy dependence of the IVT efficiency described below.

Energy dependence of IVT efficiency

The IVT efficiency, defined as the ratio of events selected by IVT out of IBD candidates, was investigated. The correlation between energy and the IVT efficiency is depicted in figure 3.27. Although consistent with a null slope the linear regression line remains nevertheless, due to the large errors, compatible with a non-zero slope. The idea here, in view of these large errors, is to presume the linear dependency and then check the compatibility with the fit of the remaining FN background in the final IBD spectra.

Hence, in order to take into account this correlation the fit function $Fit_{Gd}^{FN-IBD}(x)$ is refined as :

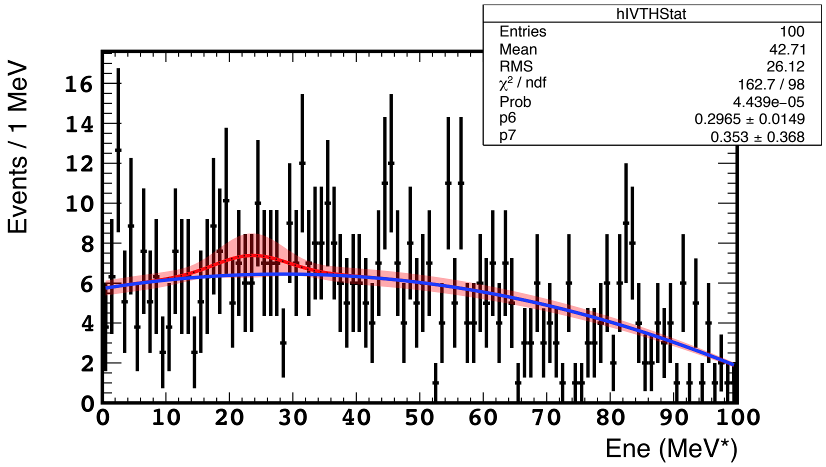

Figure 3.26: *Correlated background spectrum shape of events selected by IVT in FD-II for Gd selection. In blue is drawn the second order polynomial shape of the FN background while red curve is the function defined in equation 3.6 fiting both the FN and the muon capture events present in the IVT spectrum. The two fit curves, red and blue, curves are normalised for [20, 100] MeV range.*

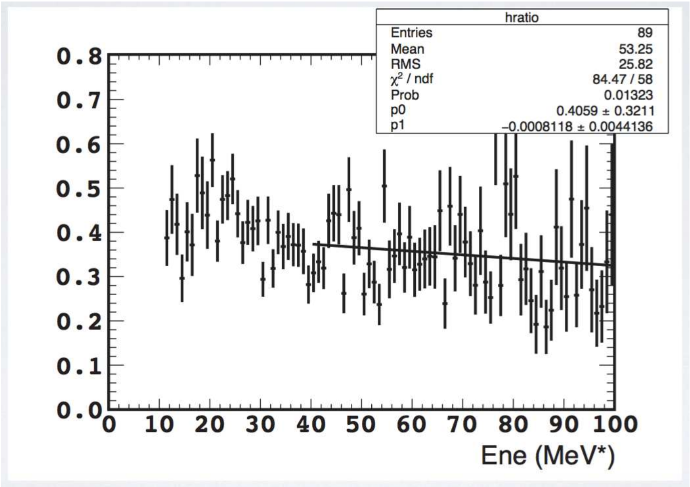

Figure 3.27: *IVT efficiency as a function of energy. The energy dependence of IVT efficiency is consistent with a linear correlation with $y = po + p_1 x$ as regression line, drawn in black.*

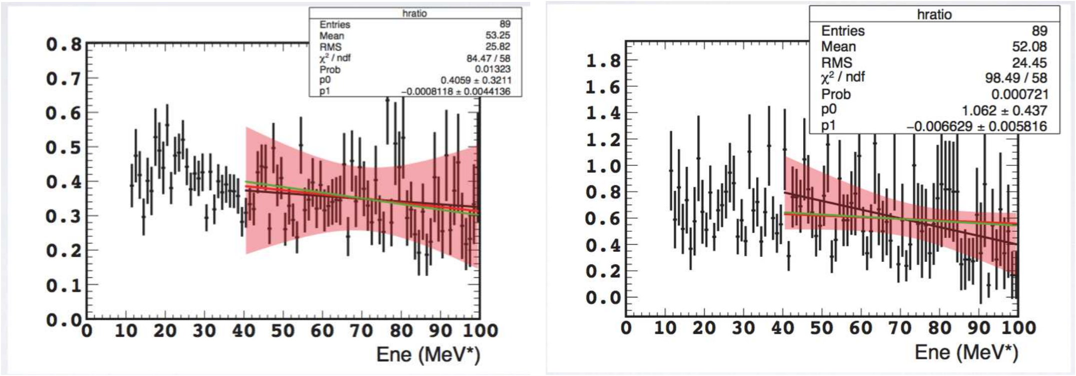

(a) ND (b) FD

Figure 3.28: *Linear regression line characterising the energy dependence of IVT efficiency as obtained by the fit of the remaining FN background in the final IBD spectrum for ND and FD. In red and green respectively the slope from the fit in Gd and Gd++ selection. The two are compatible with the slope, in black, from figure 3.27 where the energy dependence of the IVT efficiency is investigated.*

$$Fit_{Gd}^{FN-IBD}(x) = \frac{a_0 + a_1 x + a_2 x^2}{p_0 + p_1 x} \tag{3.8}$$

Where a linear regression line characterising the energy dependence of IVT efficiency is added as divisor.

The same slope of energy dependence from figure 3.27 has been later used in all configurations (detectors and selections) since, as evidenced in figure 3.28, the different particular slopes have been found consistent within errors.

The figure 3.29 shows the impact of the integration of the IVT efficiency energy dependence in the FN background shape for the Gd selection. Indeed, the corrected shape, in red, is lower than the uncorrected one in blue especially below 20 MeV solving thus the FN estimate issue shown in figure 3.23.

Originally the Gd++ IVT spectrum was found mathematically consistent with a combined function of a first order polynomial and an exponential. Since the muon capture events are not seen in Gd++ selection, only the correction due to the energy dependence of the IVT efficiency has been brought to its IVT spectrum shape as :

$$Fit_{Gd++}^{FN-IBD}(x) = \frac{N_0 e^{-\alpha x} + N_1 x + N_2}{p_0 + p_1 x} \tag{3.9}$$

The fit of the remaining FN background spectrum in the final IBD spectrum fix the 5 coefficients of $Fit(x)_{Gd}^{FN-IBD}$ and the 6 coefficients of $Fit(x)_{Gd++}^{FN-IBD}$.

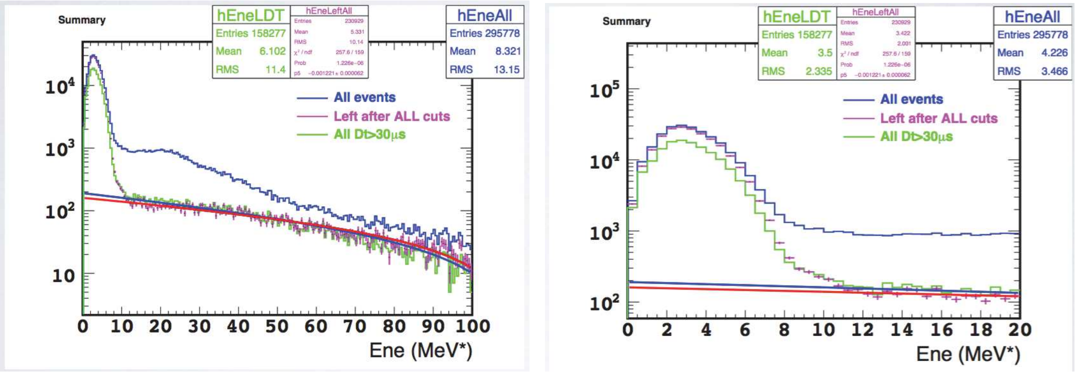

(a) (b)

Figure 3.29: *Correlated spectrum background shapes in the final IBDs sample before (blue curve) and after the IVT efficiency energy dependence correction (red curve). A visible impact is demonstrated in (a) where the two shapes differ sensibly. In (b) a zoom in the region below 20 MeV allows to see how better FN estimate falls in agreement with the data. The two fit curves are normalised for [20, 100] MeV range. The analysis has been performed for illustration on ND data set for the Gd selection.*

Finally, the ratio of functions 3.8 and 3.9 integrals to the corresponding livetime provides the daily rate of FN remaining in the final IBD sample. The table 3.13 lists the final rates obtained as by the "Fit" method. The rate values obtained by the "No Fit" method, shown for simple comparison, are typically higher. This could be explained if one remembers that the "No-Fit" method is based on the naive assumption that above 20 MeV in the IBD candidates sample we have only FN . Hence, in this method muon capture events, for instance, are counted as FN leading then to an overestimation. Moreover, the "No-Fit" method ignores the energy dependence of the IVT efficiency. Nevertheless, the "No-Fit" method provides a first and quick estimation of FN while the Fit method values are the official ones in DC final tables.

3.7 Conclusion

We conclude the present chapter with a brief summary of what we have done and learnt from the analysis performed.

The IV veto which uses low energy signals in the IV to select FN background has been tuned for DC-IV and admitted as official by the DC collaboration. The associated inefficiency measured for all the configurations has been found very negligible ($< 0.1\%$), beyond the expectations.

The IVV sample of events allowed coherent FN spectra shape definitions.

Configurations	**Rate per day (No Fit)**	**Rate per day (Fit)**
Gadolinium		
ND	5.4 ± 0.4	4.00 ± 0.15
FD-I	0.63 ± 0.03	0.43 ± 0.03
FD-II	0.68 ± 0.09	0.51 ± 0.04
Gadolinium++		
ND	28.8 ± 1.2	20.77 ± 0.43
FD-I	3.7 ± 0.3	2.60 ± 0.11
FD-II	3.3 ± 0.3	2.48 ± 0.10

Table 3.13: *FN estimates per day in the final IBD sample for all the configurations. The rates are given for the [0.5,20] MeV region in Gd selection and [1,20] MeV region in Gd++ selection. The values as provided by the "Fit" and the "No-Fit" methods are put in comparison.*

All the detectors configurations (ND, FD-I and FD-II) use one shape, a second order polynomial, in Gd selection. The FN spectrum has been found consistent with an exponential shape growing at low energies for the Gd++ selection for the three detectors configurations. Finally, the FN remaining rates in the final IBD sample have been measured. These two informations (spectral shapes and background rate) serve as inputs in the final fit whence is determined the θ_{13} value.

Chapter 4

Double neutron capture background

> *"Le savant doit ordonner; on fait la science avec des faits comme une maison avec des pierres; mais une accumulation de faits n'est pas plus une science qu'un tas de pierres n'est une maison."*
>
> H. Poincaré

The double neutrons capture (DnC) background is the last background investigated in DC. Indeed, due to the lack of clear signature, this background has been for longtime ignored and not accounted in the final fit inputs unlike all the other backgrounds. The present chapter presents the most recent study of double neutron capture background.

4.1 Interactions of fast neutrons in DC

As already mentioned in previous chapters, muons constitute the most important origin of background in DC experiment. Indeed, the muon induced backgrounds are consequent of interactions of muons either inside or outside the detectors. The first case leads to stopping muons and cosmogenic backgrounds while, in the second case, the interactions of muons with the surrounding rocks result in a high multiplicity fast neutrons production; as a result of induced nuclear spallation reactions [96]. Due to their high penetrating capacity, fast neutrons constitute a specific background in DC as they enter the detector medium.

Mostly, a fast neutron entering into matter loses its energy by scattering

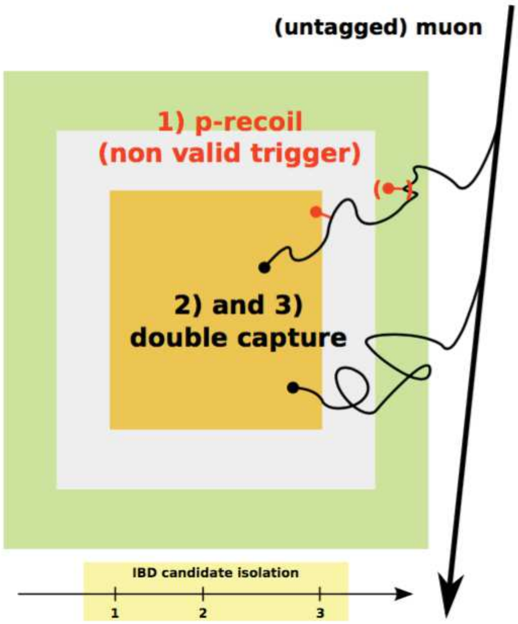

Figure 4.1: *Double neutrons capture event topology. The existence of a preceding recoil proton not identified as valid trigger leads to the contamination of DnC events in the final IBD sample*

back and forth on the nuclei, both elastically and inelastically, until it comes into thermal equilibrium with the surrounding atoms. At this point, it will diffuse through matter until it is finally captured by a nucleus [84]. This is the classical process undergone by fast neutrons in DC detectors where they mainly lose energy through elastic scattering with the hydrogen nuclei abundantly present in the scintillator chemical complex. The energy transferred by the fast neutron is then converted into recoil energy of the nucleus.

4.2 Multiple capture of neutrons

The foregoing shows that more than one neutron can be captured in the time window required for a prompt and a delayed signals coincidence. Therefore, different scenarios are possible but the only one in which the multiple captures can mimic the IBD candidates signature is a double neutron capture (DnC) where the two captures are well separated in time but still in the same IBD coincidence window (cf section 2.9). The figure 4.1 schematizes the topology of a DnC event as occurring in DC detectors.

Once can imagine three captures where two captures occur quasi simultaneously and at quasi the same position in order to be, at the limit of the time and reconstruction resolutions, be registered as one and unique event by the

DAQ. However, the probability to observe such events is nearly zero due to the multiple coincidences required for their occurence. This type of events, "1+ twin captures", have not been investigated neither observed.

In view of the topology illustrated in figure 4.1, four different cases of DnC are then possible.

- The two neutrons are captured on H (nH-nH)
- The two neutrons are captured on Gd (nGd-nGd)
- The first neutron is captured on H and the second on Gd (nH-nGd)
- The first neutron is captured on Gd and the second on H (nGd-nH)

Since neutrons of double capture come essentially from outside the detectors and therefore they are more likely susceptible to interact in the Gamma Catcher, which is Gd free, the nH-nH scenario is expected to be, by far, preponderant with respect to others.

4.3 Observation of DnC events in the Near Detector

In accordance with the fact that both the prompt and the delayed signals are neutrons capture, a sample of DnC events is expected to exhibit, unlike any other background observed so far, a peculiar prompt energy spectrum shape with a distinguishable two-peaks structure; the first peak around 2.2 MeV for n-H captures and the second, less high, at 8 MeV corresponding to captures on Gd.

Different physical signatures that would allow an extraction, out of the whole data, of a relatively pure sample of DnC events have been investigated. Indeed, before their captures the two neutrons may have interacted clearly in the IV. In this case they can be tagged and then removed by the Inner Veto veto along with fast neutrons, stopping muons and gamma-gamma events as described in the preceding chapter. Also, a DnC may often be rejected with the unicity cut by the identification of a proton recoil in the ID preceding the neutrino candidate (or also proton recoil in IV reaching the charge threshold to enter into the muon definition). Indeed, as summarized in section 2.9, events are not selected as IBD candidate when there exists a valid trigger in the 800 μs preceding the prompt event. This is known as the unicity condition.

However, it could happen that the proton recoil preceding the prompt event in ID does not pass the condition of a valid trigger for, at least, two reasons :

IBD candidate	An IBD candidate after all other backgrounds vetoes have been applied.
DnC condition	- At least one invalid trigger in the **800** μs preceding the prompt event (**Gd++ Analysis**).

Table 4.1: Double neutron capture candidates selection criteria for the Gd++ analysis in DC-IV.

- Very low energy deposit in the ID (E$_{vis}$ < 0.3 MeV)
- Multiple proton recoils close to a PMT.

In the first case the energy deposited is below the 0.3 MeV threshold required to be kept as valid trigger. Events of the second case exhibit a non homogenous distribution of hit PMTs and are therefore rejected by light noise cut . Hence, in such cases, the unicity cut is not working as it applies to valid triggers only.

Hence, we looked, as summarized in table 4.1, for the presence of non-valid triggers inside the isolation window and up to a delay of 800 μs preceding the prompt event of all IBD candidates in the Gd++ selection of DC-IV. Figure 4.2 shows the prompt spectrum of IBD candidates that have a non valid trigger event as preceding. This spectrum, in red, reveals in a distinct manner the characteristic two peaks, at 2.2 MeV and at 8 MeV, as expected for DnC events. The expectation of a lower Gd peak with respect to the H one is also evidenced. This validates the mechanism of "ante-tagging of a non-valid proton recoil" and demonstrates the existence of double neutron capture contamination in DC-IV Gd++ candidates.

4.3.1 The DnC rate measurement

The observation of DnC events has allowed the measurement of the associated rates. For that purpose the *TFractionFitter* method has been used to evaluate it [97]. As it can be seen in figure 4.2 the number of DnC corresponds to number of events present in each of the two capture peaks once the IBDs spectrum is subtracted. The rates are thus obtained as the ratio of the number of DnC with the corresponding livetime.

TFractionFitter has been used to measure the DnC rates in the ND. Indeed, *TFractionFitter* is a Root[1] tool which allows a fit of an histogram as the sum

---

[1] The object-oriented program and library developed by the CERN and designed for

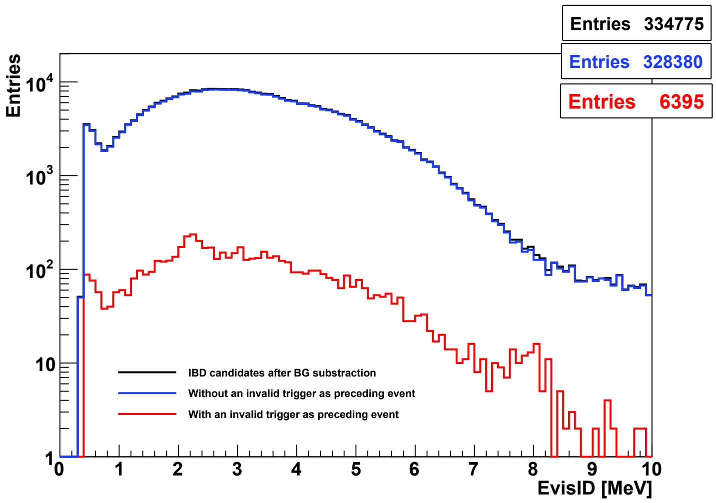

(a)

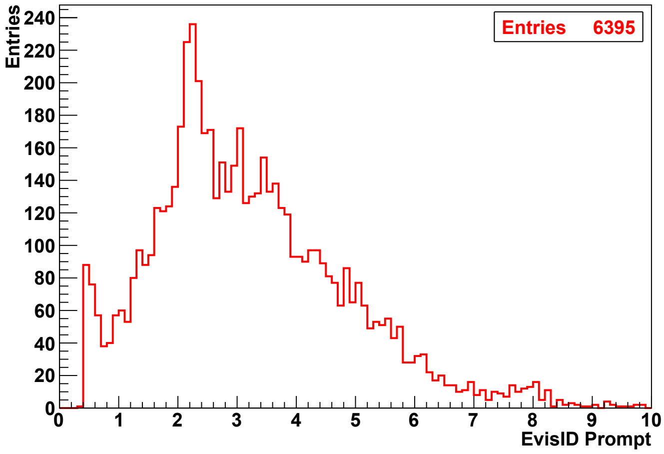

(b)

Figure 4.2: *(a) Prompt visible energy spectrum of IBD candidates after background subtraction (in black). In blue is plotted the subsample of these IBD candidates having no invalid trigger as preceding event. The spectrum of interest (in red), of IBD candidates having an invalid trigger as preceding, plotted alone in (b) for a better scale exhibits the two neutrons capture peaks that characterize a double neutrons capture.*

of several histograms. The virtue of this fit is that it takes into account statistical uncertainties of all the histograms involved. The way in which this is done is through a standard likelihood fit using Poisson statistics; however, the template (MC) predictions are also varied within statistics, leading to additional contributions to the overall likelihood. This leads to many more fit parameters (one per bin per template), but the minimisation with respect to these additional parameters is done analytically rather than introducing them as formal fit parameters.

Two assumptions need to be made for the fit procedure to be carried out; first the total number of events in each template is not too small so that its Poisson uncertainty can be neglected. The number of events in each bin is much smaller than the total number of events in each template so that multinomial uncertainties can be replaced with Poisson uncertainties [98].

As it can be seen in figure 7.4 the energy spectrum of IBD candidates with a non-valid trigger as preceding event, is fitted as the sum of:

- The IBD candidates energy spectrum
- The energy spectrum of delayed captures on both H and Gd.

As output, the fit provides

- The number of IBD candidates
- The number of n-H captures
- The number of n-Gd captures

The fits have been performed in all configurations. The output numbers, also visibles on the plots frame, are summarized in table 4.2 where it worths to notice the ratio of n-Gd/n-H rates. Indeed, this ratio found to be 4.6 ± 0.7 , is supposed to be of the same order than the ratio of ND FN rates between the Gd and the Gd++ analysis. The numbers in table 3.13 provide a ratio of FN rate Gd++/Gd of 5.2 ± 0.2 The consistency of the two numbers is an additional validation of the method developped here to tag DnC events.

The fractions of each DnC scenario mentioned in section 4.2 have been measured as well and listed in table 4.3. The expectation of a nH-nH scenario more frequent than the others mentioned in section 4.2 is confirmed.

This estimate is a lower limit, since it counts number of double capture events preceded by one or more invalid triggers, and it is possible that some proton recoil events are not tagged as invalid triggers, but do not trigger at all (remain undetected).

---

particle physics data analysis.

	#Events	**Rates / day**
n-H	465.5 ± 45.1	1.19 ± 0.11
n-Gd	101.7 ± 13.9	0.26 ± 0.03
Total	567.2 ± 47.2	1.45 ± 0.11

Table 4.2: *Number of Double neutrons capture events as calculated by the FitterFraction method.*

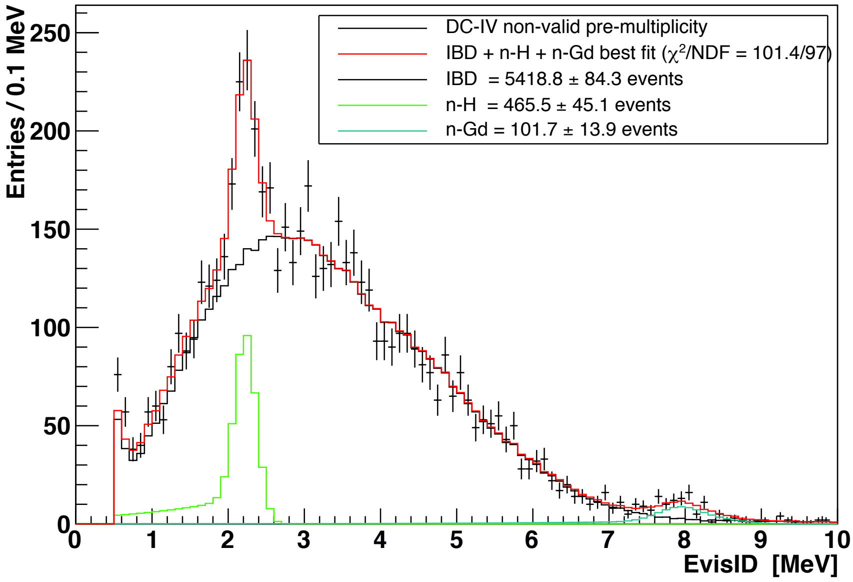

Figure 4.3: *Fit of the energy spectrum of DnC events (in red) as the sum of the IBD candidates energy spectrum (in black) and of the energy spectrum of delayed captures on H and Gd. The fit, performed using the TFractionFitter method, provides as output the neutrons capture histograms (green for H and blue for Gd) and the associated integrals. [ND & Gd++ Analysis]*

Scenario	# Events	**% of events**
nH-nH	75719	61.9 ± 0.3
nH-nGd	46525	38.1 ± 0.3
Total	122244	

Table 4.3: *Number of DnC events for each capture scenario as provided by the prompt energy spectrum of figure 4.2 and its corresponding delayed energy spectrum. Official neutron captures energy ranges are used here : [1.3; 3] MeV for H and [4;10] MeV for Gd.*

Periods	# Months	Livetime (days)	n-H rate	n-Gd rate
1	5	76.1592	0.88 ± 0.22	0.16 ± 0.06
2	5	95.7780	1.29 ± 0.24	0.27 ± 0.07
3	5	96.1339	1.47 ± 0.25	0.26 ± 0.06
4	5	84.1283	1.08 ± 0.24	0.29 ± 0.07
5	4	38.8386	0.90 ± 0.38	0.43 ± 0.14

Table 4.4: *Periodic and Daily rates of DnC events (H and Gd) for ND. The 24 months data are divided in four periods of 4 months plus one period of 4 months.*

4.3.2 Evolution of the DnC rates

The stability over time of the DnC rates as measured in the previous sections has been investigated. Indeed, the observation of a stability would establish the DnC as a permanent background, rejecting the hypothesis of a sporadic origin or/and a statistical fluctuation. For this purpose, the 24 months data used so far have been divided chronologically in five sets: 4 periods of 5 months and one period of 4 months.

The periodic rate values have been measured by means of the *TFractionFitter* method and gathered here in table 4.4. The figure 7.5 shows graphically that this evolution, for both n-H captures and n-Gd captures, is compatible with stable rates over time. This observation states that this background has always been present in DC data and, therefore, discards the sporadic hypothesis of DnC events.

4.4 Observation of DnC events in the Far Detector

The number of DnC in FD is expected to be much lower than in ND ($N^{DNC}_{ND} > \times N^{DNC}_{FD}$); this is consistent with the fact that there are less muons in FD, thus less spallation neutrons, due to a greater overburden.

The same method of "ante-tagging of a non-valid proton recoil" has been used for the FD data in the seek of DnC events sample. The figure 4.5 shows the energy spectrum of prompt events as provided by the method and where the double capture peaks signature of DnC events is not evidenced at all. Although the rate of DnC events in the FD is expected to be lower with respect to the ND because of a lower muons rate consequent to a greater overburden, the rates obtained in the FD are inconsistently compatible with null values as it can be seen in figure 4.6.

Different approaches to extract a relatively pure sample of DnC events in FD have been tested without success. We know now that the failure of the "ante-tagging of a non-valid proton recoil" method in the particular case of

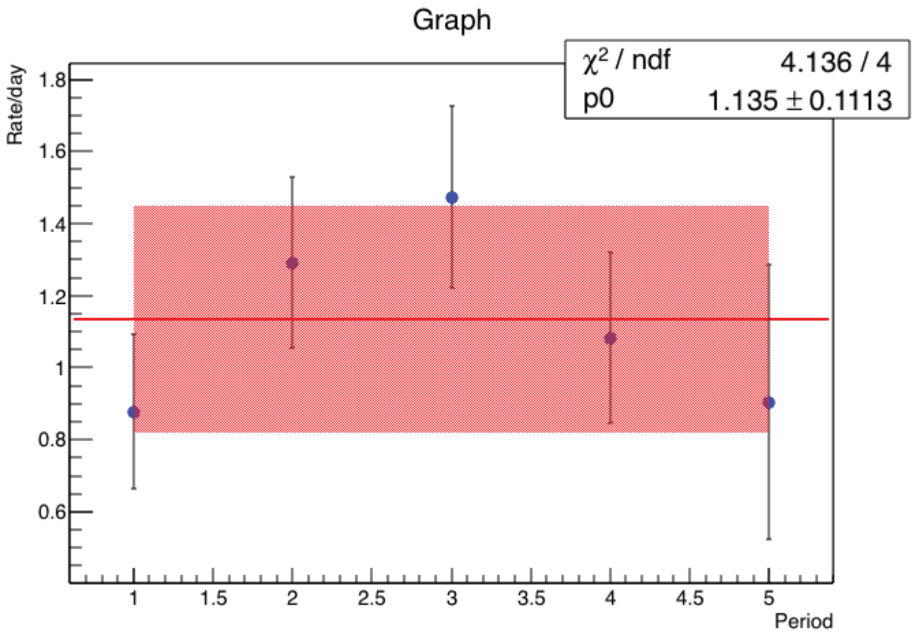

(a)

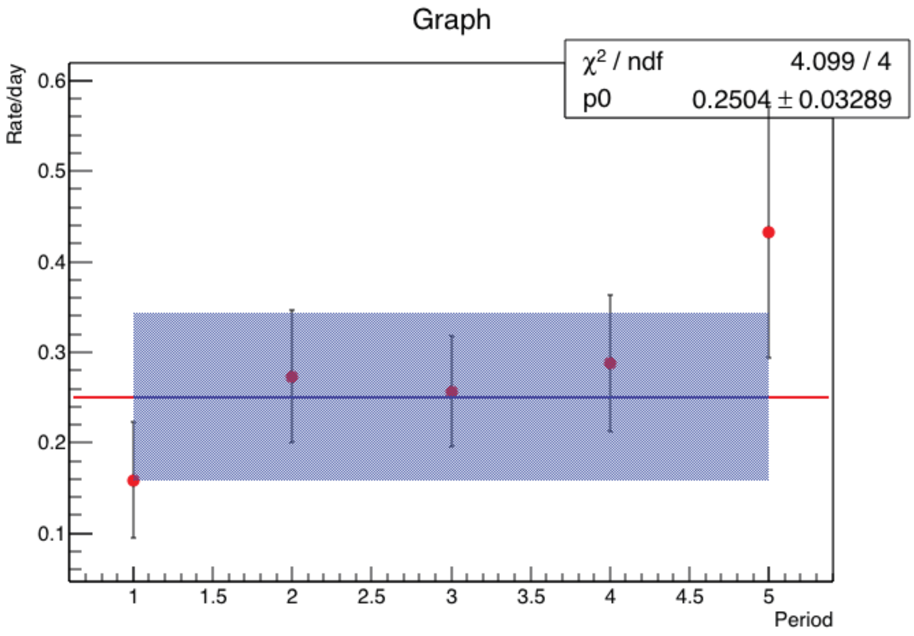

(b)

Figure 4.4: *Evolution of DnC events rate over five time periods. Both the n-H events (a) and n-Gd (b) events are compatible with stable rates.*

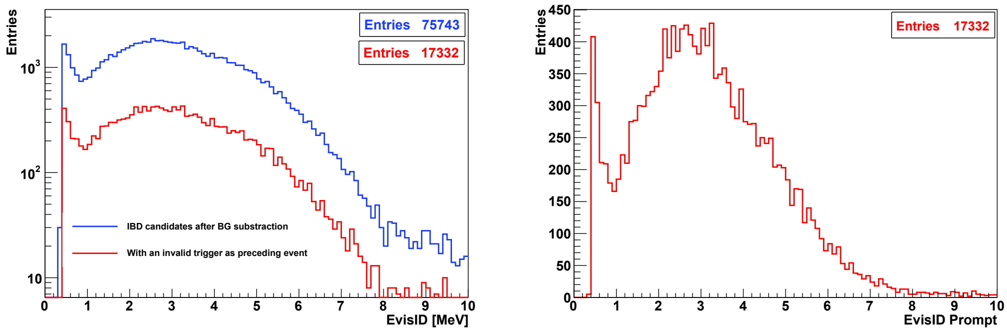

(a) (b)

Figure 4.5: *(a) Prompt visible energy spectrum of IBD candidates after background subtraction (in black). In blue is plotted the subsample of these IBD candidates having no invalid trigger as preceding event. The spectrum of interest (in red), of IBD candidates having an invalid trigger as preceding, plotted alone in (b) for a better scale does not exhibit the two neutrons capture peaks that characterize a double neutrons capture.*

FD data is due to LN abundance as described in the section below.

4.4.1 Evolution of the light noise in FD

The LN emission rate of each single photomultiplier has been unstable over the data taking. Some PMTs showed an increasing emission which, for a subset of them, returned to normal.

However despite the actions taken during the commissioning phase to reduce the light emission, the overall LN rate increased sensibly whereas the rate of the physics events remained stable in the same period of time as it can be seen in figure 4.7. Indeed, variations of the temperature ($\simeq 0.5$ °C) have been measured and it has been shown in [92] that the rate of LN events increases with a positive gradient of the temperature while negative temperature gradients (especially in winter seasons) do not reverse the effect. As a result a total rate of LN events measured after three years of operations, was already more than the double of the initial value.

Hence, the high rate of the LN events can explain the difficulty to extract, based on the "ante-tagging of a non-valid proton recoil" method, a DnC events sample in the FD data. Indeed, as it can be noticed in figure 4.8, LN events in the FD constitute the majority of events that precede the prompt candidates to the detriment of non-valid proton recoil. It appears that $\simeq$ 95% of invalid triggers preceding IBDs in the FD data are removed by the LN vetoes.

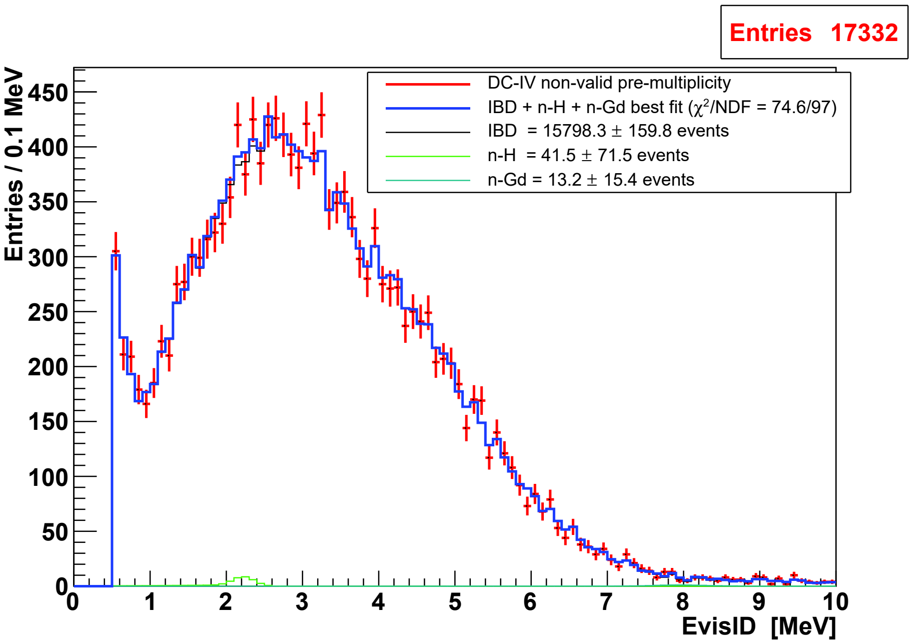

Figure 4.6: *Fit of the energy spectrum of DnC events (in red) as the sum of the IBD candidates energy spectrum (in black) and of the energy spectrum of delayed captures on H and Gd. The fit, performed using the TFractionFitter method, provides as output the neutrons capture histograms (green for H and blue for Gd) and the associated integrals. [FD & Gd++ Analysis]*

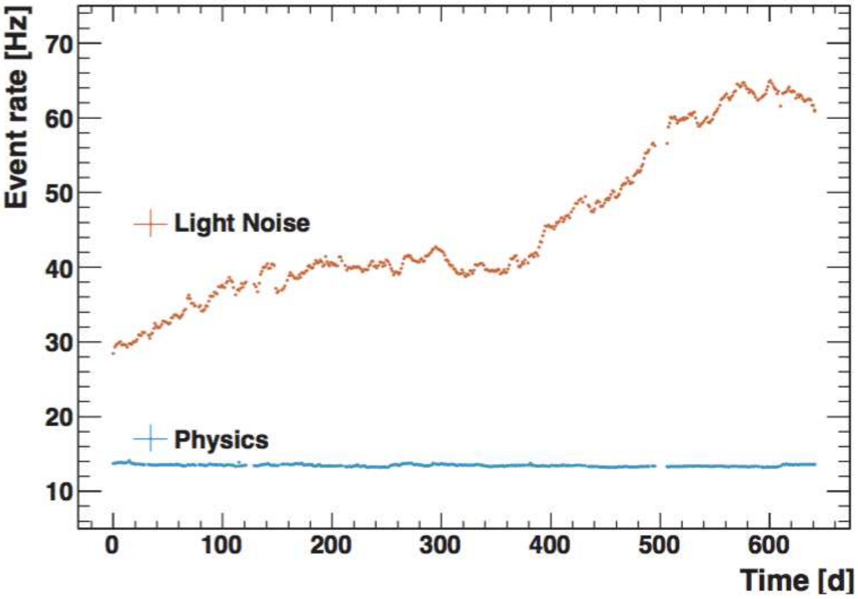

Figure 4.7: *Evolution of the LN rates over time for physics (blue) and LN event (orange) in the FD.*

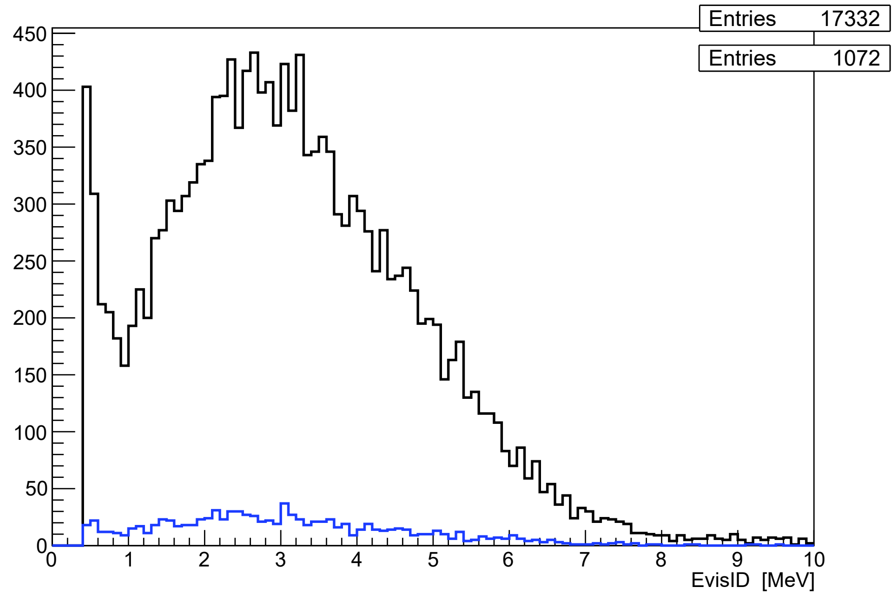

Figure 4.8: *Prompt energy spectrum of FD IBDs preceded by invalid trigger (black curve). The subsample of IBDs preceded by an invalid trigger distinct from LN is plotted in blue.*

4.4.2 DnC rate estimation at the FD

Despite the high rate of LN events that prevents a direct measurement of the DnC rates in the FD, an estimation can be provided indirectly by means of the fast neutrons (FN) rate as measured in the previous chapter and gathered in table 3.13. Indeed, FN and DnC are muon-induced and both consequent of spallation reactions occurring outside the detectors then they are expected to have the same rates ratio between in the ND and FD. An estimation of n-H and n-Gd DnC respectively of 0.23 ± 0.02 and 0.050 ± 0.006 per day in FD data emerges from this extrapolated calculation.

4.5 DnC in the Off-Off data

The presence of DnC events has been investigated in the Off-Off data taken between August and October 2017 and summarized in table 4.5 . For this purpose all the other backgrounds encountered in DC have been removed through dedicated cuts. Therefore, the prompt energy spectrum of the remaining events in the Off-Off data plotted is expected to exhibit, a priori, the presence of DnC. These spectra are shown, for the ND and FD respectively, in figures 4.9 and 4.10 where the DnC events should be the main contribution around 2.2 MeV and 8 MeV of the grey spectrum obtained af-

Periods	**# Runs**	**Livetime (days)**
01/Aug	16 15	0.499 0.593
02/Aug	12 12	0.361 0.475
Oct	388 401	12.014 15.838
Total	416 428	12.874 16.907

Table 4.5: *Reactors Off data set. ND and FD numbers are respectively in black and red.*

ter successive application of all the other background vetoes as listed in the legends. The remaining accidental background constitutes principally the low energy component (< 2 MeV) of the spectrum. However, the few statistics of these background subtracted Off-Off data (1105 events for ND and 318 events FD) limit any accurate analysis.

Hence, to obtain the measurement of DnC events rate the whole Off-Off data spectrum has been fitted with each of background shape encountered in DC. For this purpose the fit has been performed with all the backgrounds. Moreover, an error of 20 % on the remaining neutrinos shape has been applied to take into account the fact that the reactor fuel isotopes are still radioactive well after the shutdown. Figure 4.11 shows the fit as performed in these conditions. It worths to notice that the rate of 1.8 ± 0.9 n-H DnC per day that emerges from this fit is consistent within errors with the one measured in a different approach in section 4.3.1.

In a second step, a reduced sample of Off-Off data has been used. In this sample, the fit is performed only on Off-Off data taken beyond 15 days from the shutdown; this ensures to reduce the remaining neutrino contamination. To this end, the backgrounds are all constrained due to the few statistics. This fit as it can be seen in figure 4.13 provides a rate of 5.2 ± 1.8 n-H DnC per day.

The rate values obtained with the later fits are to relativise since the residual neutrinos are part of this rate value. Moreover, as mentioned in section 2.12 the antineutrino flux from spent nuclear fuel (SNF[2]) has a non-negligible contribution in the Off-Off data, particularly in the nH capture region as it can be noticed in figure 4.12. Indeed, results from [99] and [100] show that the SNF contribution to the total antineutrino flux is about 0.26% - 0.34%, and the shutdown impact is about 20%. The SNF spectrum was found to alter the softer part of the antineutrino spectra with the maximum contribution from the SNF being about 3.0%.

---

[2] spent fuel from nuclear reactors stored in specially designed pools at the reactor site.

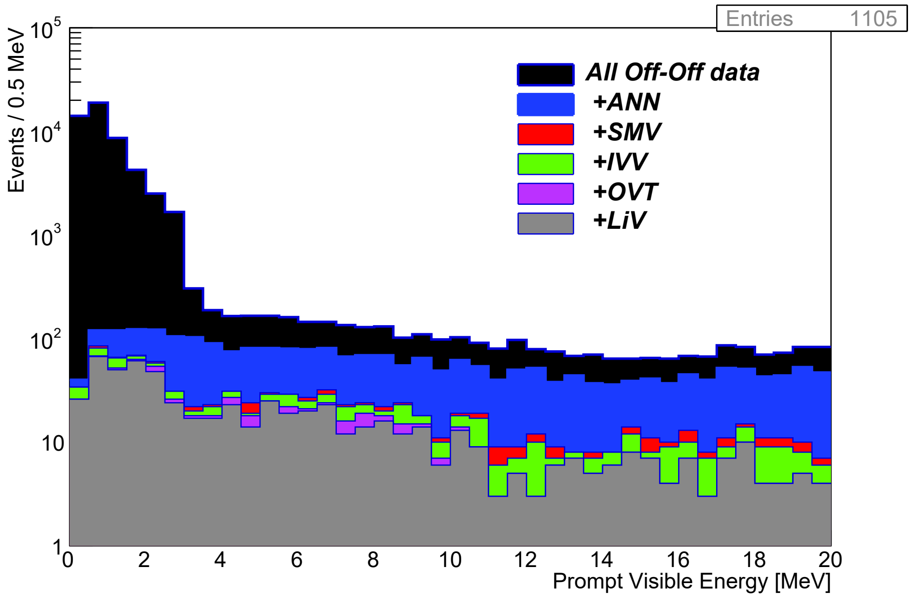

Figure 4.9: *Prompt energy spectrum before and after successive applications of all the other background vetoes, except DnC, in the ND Off-Off data. The grey spectrum is obtained after the background vetoes listed in the legend have been applied. In the legend, ANN, SMV, IVV, OVT and LiV refer to the different background vetoes developed in DC as introduced in section 2.10.*

4.6 Impact of DnC on θ_{13}

So far and before the work undertaken in the present volume, the DnC background has not been integrated in any DC analysis or publication. This is simply because this particular background was not clearly evidenced yet. Therefore, further to the measurements obtained in this chapter, the impact on the θ_{13} value of the DnC rates has been investigated.

In fact, as already mentioned in section 2.13.1 the estimated remaining rates of each background serve as input for the final fit that provides the θ_{13} value; these rates add constraints to the final fit and thus have a direct impact on θ_{13} value. This impact has been studied by comparing the outputs of fits on two sets of fake data, with and without DnC background included.

4.6.1 Nominal fit with Fake-Data

Figures 4.14 shows for ND and FD, the performance of a Data-to-Monte Carlo *Rate + Shape* fit (cf. section 2.13.1) on a set of fake data containing DnC background.

Table 7.1 presents in a comparative manner the outputs of the two different

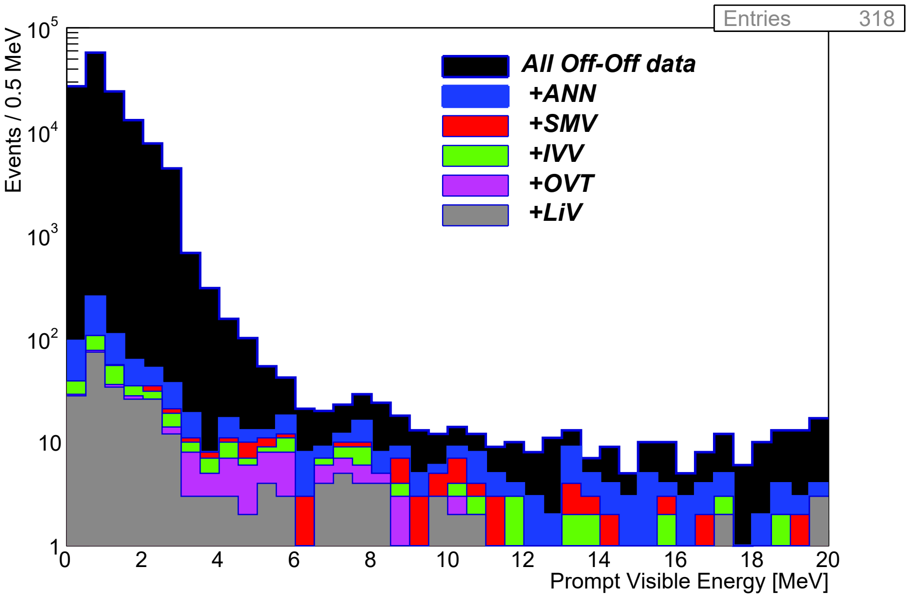

Figure 4.10: *Prompt energy spectrum before and after successive applications of all the other background vetoes, except DnC, in the FD Off-Off data. The grey spectrum is obtained after the background vetoes listed in the legend have been applied. In the legend, ANN, SMV, IVV, OVT and LiV refer to the different background vetoes developed in DC as introduced in section 2.10.*

fits mentioned above. It appears the sensitivity of the fit to the DnC background is very limited and depends on the absolute rate. Indeed, not including DnC in the nominal fit causes only a minor shift (-0.08σ) on the central value of $\sin^2 2\theta_{13}$ and a slight increase in the cosmogenic background rates (2.7% FD and 7.3% ND) while the minimum χ^2 also decreases. However, the variation of the central value of $\sin^2 2\theta_{13}$ is about ten times smaller than the associated error is compatible with a null variation. This analysis is to be redone wit a greater amount of data to probe again the DnC background impact on θ_{13} and the associated values. Anyway, the DC collaboration has admitted the idea to include, from now on, the DnC background in the final fit.

4.7 Conclusion

The contamination of the final IBD sample, in DC-IV, by the DnC background events have been evidenced by the clear presence of neutrons capture peaks in the prompt energy spectrum of IBD candidates events which have, as preceding event, one or more invalid triggers. Such events are not rejected by the multiplicity cut neither by the Inner Veto veto, based both on

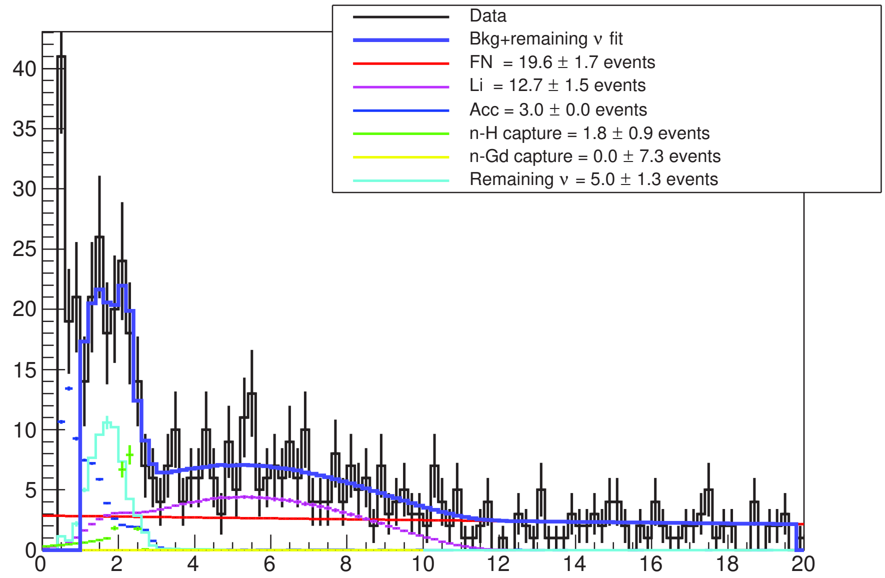

Figure 4.11: *Prompt energy spectrum of remaining events after application of background cuts in the whole ND Off-Off data. The corresponding livetime is equal to 12.04 days. The fit provides the rates of fast neutrons (FN), cosmogenic background (Li), accidental background (Acc) and the double neutron capture (n-H and n-Gd). The remaining neutrinos rate is also obtained.*

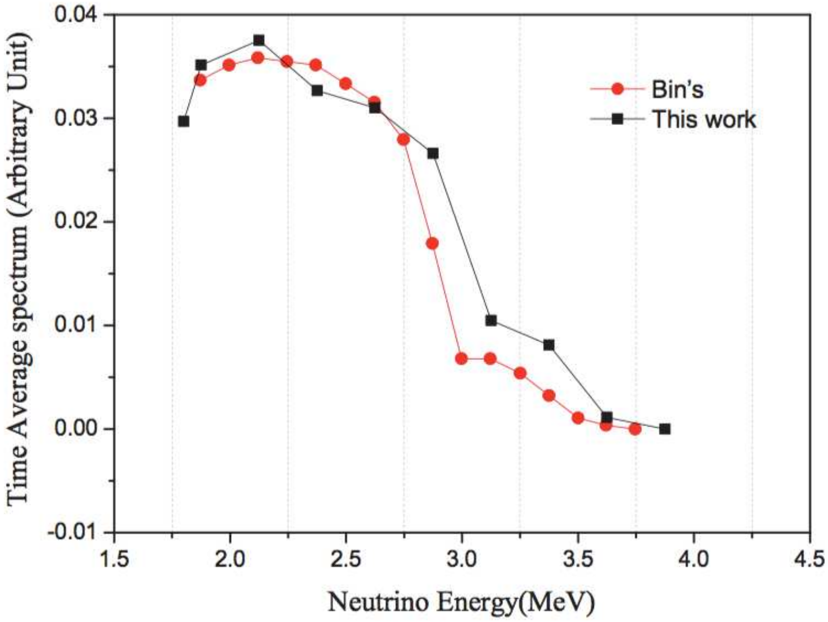

Figure 4.12: *Comparison of time average SNF spectrum between [99] (black squares) and [100] (red dots). The legend "this work" refers to [99] work. From [99]*

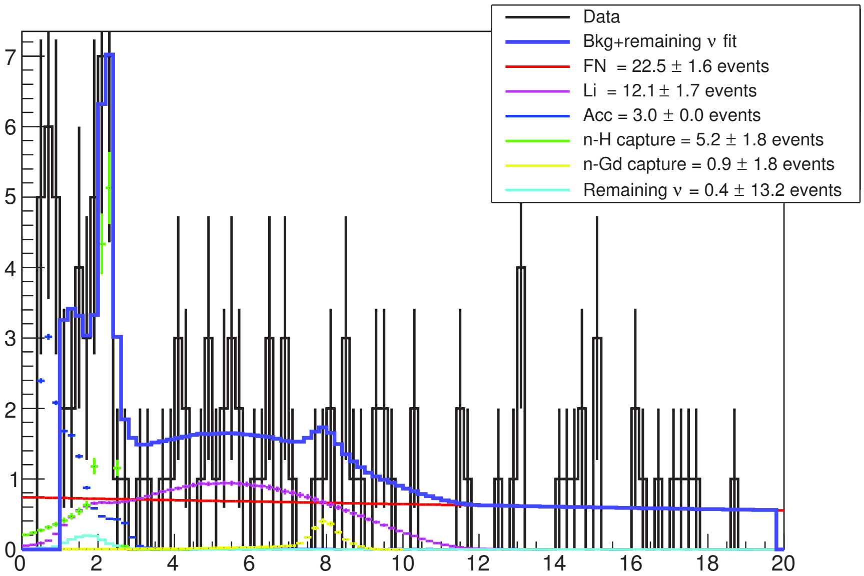

Figure 4.13: *Prompt energy spectrum of remaining events after application of background cuts in the ND reduced Off-Off data. The reduced sample consists of Off-Off data taken beyond 15 days after the reactors shutdown, this corresponds to a livetime of 2.78 days. The fit provides the rates of fast neutrons (FN), cosmogenic background (Li), accidental background (Acc) and the double neutron capture (n-H and n-Gd). The remaining neutrinos rate is also obtained.*

	Input	**Fake data without DnC**	**Fake data with DnC**
$\sin^2 2\theta_{13}$	–	0.1000 ± 0.0141	0.0989 ± 0.0141
χ^2	–	–	1.40
Acc ND	3.110 ± 0.004	3.110 ± 0.004	3.110 ± 0.004
Acc FD	4.32 ± 0.02	4.32 ± 0.02	4.32 ± 0.02
Corr ND	20.77 ± 0.43	20.77 ± 0.31	20.75 ± 0.43
Corr FD	2.540 ± 0.070	2.540 ± 0.054	2.540 ± 0.054
Li ND	12.3 ± 2.0	12.3 ± 1.15	13.2 ± 1.6
Li FD	3.01 ± 0.60	3.01 ± 0.30	3.09 ± 0.32

Table 4.6: *Output of a nominal fit on fake data containing DnC background.*

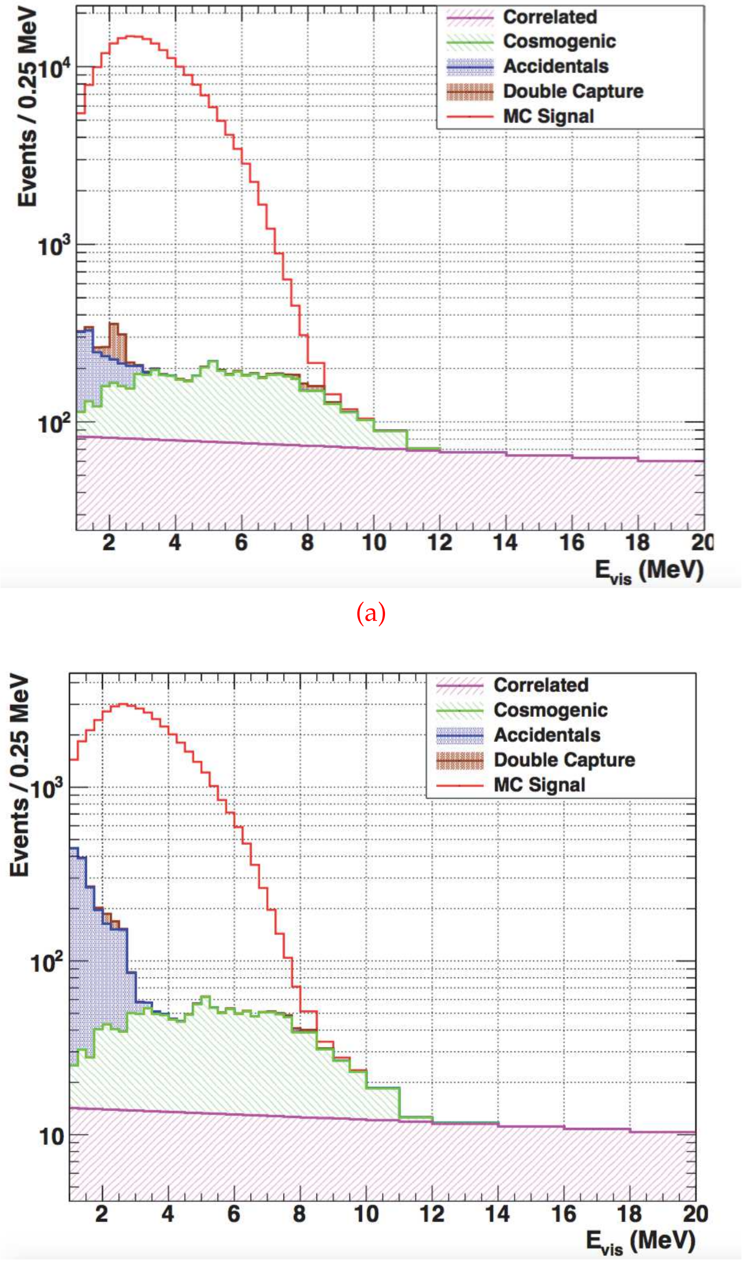

(a)

(b)

Figure 4.14: *Nominal fit on fake data containing DnC background for ND(a) and FD(b).*

valid triggers.

Dedicated methods have allowed the measurement of the daily rates of DnC; this contamination of the DnC background is obtained to be respectively of 1.19 ± 0.11 events/day and 0.23 ± 0.02 events/day for the ND and the FD. The question of stability, or not, of DnC events over time has been answered by the affirmative.

Nevertheless, these rates estimates are to be interpreted as lower limits, since they are accounting only for the fraction of DnC that are effectively preceded by invalid triggers; it is, indeed, possible that some proton recoil events are not tagged as invalid triggers, but do not trigger at all (remain undetected).

The impact of DnC background on the θ_{13} value has been evidenced as negligible; including the DnC rates in the final fit lets the central value of θ_{13} quasi unchanged.

Chapter 5

A brief study of the Gd leak at the Near Detector

> *"La vérité s'inscrit toujours en négatif des apparences"*
>
> Hegel

5.1 Introduction

As described in details in section 2.3, the DC detector has its innermost volume, the Target, doped with Gd, immediately surrounded by the Gamma Catcher volume which, unlike the Target, is free of Gd. The two liquid scintillators are viewed in all directions by photomultiplier tubes (PMTs) immersed in non scintillating mineral oil. This particular configuration has a great importance since designed to optimize both the detection efficiency and the background reduction. Indeed, several advantages are due to this configuration: the addition of a isotope with a high neutron capture section such as Gd in the Target shortens to 30μs the capture time; the relatively large thickness of the GC ($\simeq 1.16$ m) not only prevents the leakage of the prompt signal gammas from the Target but also allows to fully collect the gammas from events occurring at the boundary of the target liquid scintillator. Another important point is that the analysis selecting neutrons capture on Gd, in this detector configuration, allows a greater background reduction; first because the 8 MeV required as delayed signal energy is well above many backgrounds energy range; secondly because the vertex position of the delayed signal must be located in the Target, the only volume that contains Gd. These two only criteria of selection, possible in this configuration of detectors, constitue an efficient background suppressor.

Gamers	Event with delayed signal in the GC
H-Gamers	Gamers with $1.3 < E_{delayed} < 3$ MeV
Gd-Gamers	Gamers with $4 < E_{delayed} < 10$ MeV

Table 5.1: Definition of "Gamers" events.

Unfortunately, the analysis of 15 Months of data taken at the ND has revealed an unexpected issue which is the leak of Gd from the Target into the Gamma Catcher, breaking the equilibrium of the configuration described above. So far, the origin of this leak has not been clearly identified yet; this may have happened most probably at the filling moment of the ND. The present chapter presents an evidence of the leak, the physics implications and, further, the attempts to measure and localize the leak in question.

5.2 Localization of the leak

One direct way to probe is through the measurement of the relative abundance of events whose delayed signal is in the GC. We have named these events, in short, "*Gamers*[1]" in table 5.1. Indeed, in the absence of the leak, Gamers are susceptible to have a neutron capture on H as delayed signal since, in this case, the Gamma catcher does contain only hydrogen as capturing nuclei. However, because of the leak the captures in GC are shared with Gd nuclei. Therefore, with respect to the FD, the relative abundance of H-Gamers is expected to be sensibly lower in the ND. This assumption constitutes the cornerstone of the present analysis.

5.2.1 Gamers in the MC data

In order to validate our basic assumption, namely quasi the same fraction of Gamers expected both in ND and FD in absence of the leak, the Monte Carlo data as a pure sample of IBDs offer an ideal test. For this purpose, a first analysis has been performed on MC data. MC Gamers events have been counted from figure 5.1 and gathered here in table 5.2 where it can be noticed that the fractions of Gamers in ND and FD are equal within errors

---

[1] A funny acronym for *in **GAM**ma catcher **E**vents **R**etarded **S**ignal*.

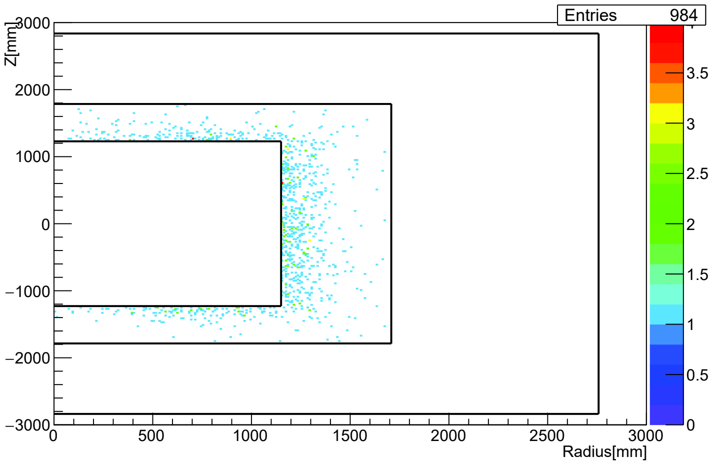

(a) ND

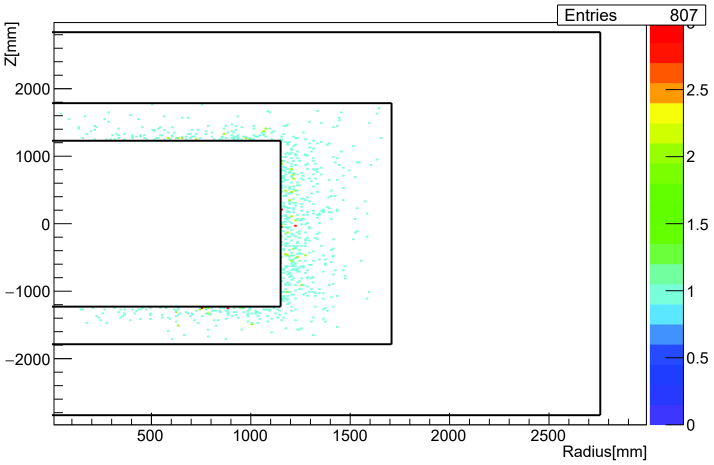

(b) FD-II

Figure 5.1: ***Monte Carlo***: *Vertices distribution of Gd-Gamers in the ND and FD.*

as assumed higher. Hence, the presence of Gd in the Gamma Catcher is expected to break this balance. Moreover, the MC fraction of Gamers as listed in table 5.2 are roughly the same in the top and the bottom for each detector. This is the reason why, after dividing the detector laterally in the middle, the symmetry top/bottom of Gamers distribution in the GC has been investigated. Indeed, it worths to know how isotropic or local is the leak.

Ideally there should be no capture on Gd in the Gamma Catcher and the fractions of Gd-Gamers would have been null in MC data. However, the DC reconstruction algorithm, also applied as possible in MC data, exhibits an error on DC vertex reconstruction which is known to be of about 15 cm as shown in figure 5.2. Hence, some events are wrongly located in the Gamma

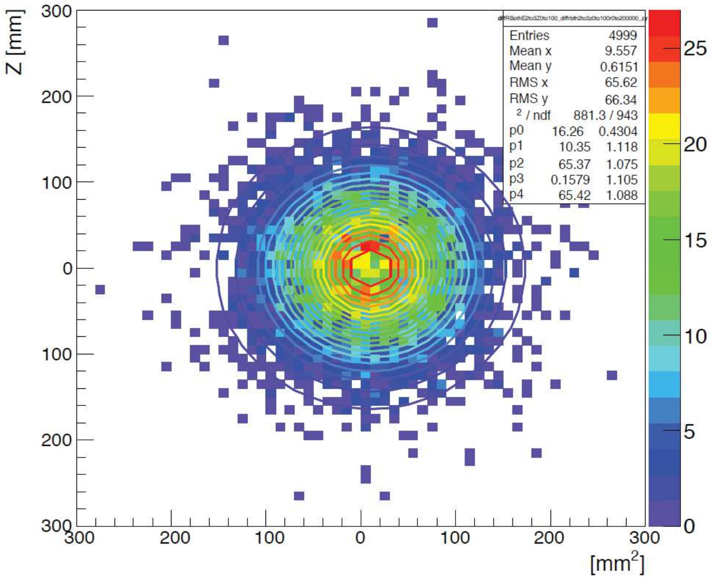

Figure 5.2: *Uncertainty of the DC vertex reconstruction algorithm. Gammas from a radioactive source positioned beforehand at the center of the detector (Z=0 and Radius= 0) are reconstructed with an extension of about 15 cm around the exact central position.*

Catcher by the reconstruction algorithm. This is evidenced in figure 5.1 where it can be seen that the majority of Gd-Gamers in the MC are located on the edge of the Target where they should be unless the reconstruction error.

We assume that in the true data the fractions of events with true vertex in the Target but wrongly reconstructed in the GC and vice-versa are roughly the same and cancel themselves.

5.2.2 Gamers in the true Data

After background subtraction

The vertices positions, in ND and FD, of Gd-Gamers delayed signals are shown in figure 5.3 where the presence of Gd-Gamers close to the Target in the FD is due to the error on vertex reconstruction whereas the relatively high abundance of the Gd-Gamers and their wider spatial distribution in the ND is explained by the leak i.e the presence of Gd in the GC. To offer a comparison with the values obtained on the MC data in the preceding section, the analysis is performed, at this step, on the remaining data i.e after application of all background vetoes listed in section 2.10.3. Also, a supplementary condition that requires the Gamer to have a prompt energy below 10 MeV just like in the MC is added. This ensures a more coherent com-

	H-Gamers	**Gd-Gamers**
All	93.88 ± 1.00	6.12 ± 0.19
	94.60 ± 1.07	5.39 ± 0.19
Top	93.80 ± 1.42	6.20 ± 0.27
	94.59 ± 1.51	5.40 ± 0.27
Bottom	93.95 ± 1.40	6.05 ± 0.26
	94.62 ± 1.53	5.38 ± 0.27

Table 5.2: *Fractions of Gamers in the MC data. ND and FD values are respectively given in black and red.*

parison with the MC but also reduces the remaining background contamination that compose essentially the high energy part of the prompt energy spectrum. The concentration of events observed at the top of the detector is consistent with the presence of Stopping Muons (SM) that are later removed by the SM vetoes.

The relative abundance of H-Gamers and Gd-Gamers have been computed and gathered in table 7.2. Several conclusions can be derived from table 7.2. Indeed, it worths to notice that:

- The fractions of Gamers between MC and true data are consistent for the FD. This simply means that the FD behaves as the predictions.
- Unlike the FD, the ND numbers in true data deviates sensibly from the MC. This demonstrates the competition between captures on Gd and H in the ND Gamma Catcher.
- The differences are larger between FD and ND in true data with respect to the MC. The two detectors number of Gamers are no more equal even within errors.
- The top part of the ND, with respect to the bottom, reveals a higher number of Gd-Gamers from the FD. This suggests a greater leak (or a greater Gd concentration) in the top part of the ND.

Prior to background subtraction

The same analysis of the preceding section has been performed on true data, this time, prior to the background. At this step, any reference to the MC can be done but a comparison between FD and ND is still relevant. The numbers of Gamers obtained from are listed in table 5.4. The values obtained still validate the conclusions formulated for the background-free true data with 2 major emphasises.

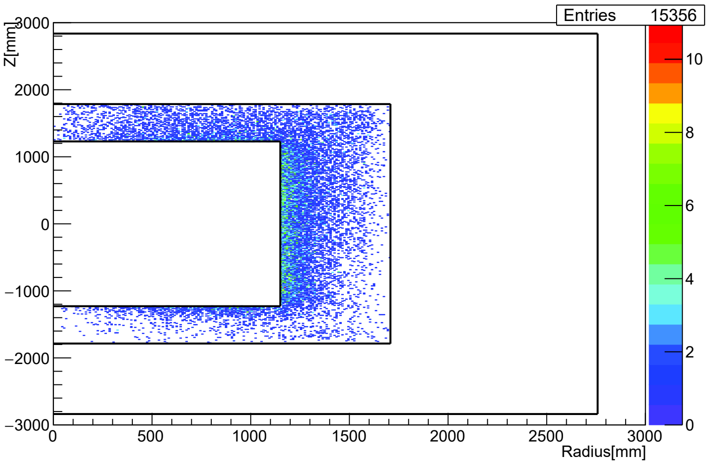

(a) ND

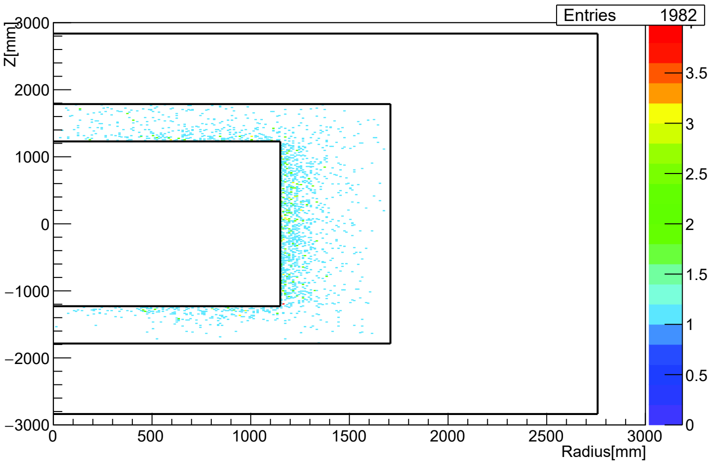

(b) FD-II

Figure 5.3: ***True data***:*Vertices distribution of Gd-Gamers in the ND and FD after background subtraction. While the presence of Gd-Gamers close to the Target in the FD is attributed to the error on vertex reconstruction, the abundance of the Gd-Gamers and their spatial distribution in the ND is explained by the leak i.e the presence of Gd in the GC.*

	H-Gamers	**Gd-Gamers**
All	92.06 ± 0.32 95.51 ± 0.68	8.14 ± 0.07 4.50 ± 0.11
Top	91.07 ± 0.43 95.40 ± 0.94	8.93 ± 0.10 4.59 ± 0.15
Bottom	93.12 ± 0.46 95.61 ± 0.97	6.91 ± 0.09 4.38 ± 0.15

Table 5.3: *Fractions of Gamers in true data after background subtraction. The values in black refer to the ND while the FD numbers, just below, are in red.*

	H-Gamers	**Gd-Gamers**
All	87.66 ± 0.31 94.17 ± 0.60	12.34 ± 0.08 5.83 ± 0.11

Table 5.4: *Fractions of Gamers in true data prior to background subtraction. The values in black refer to the ND while the FD numbers, just below, are in red.*

- The fraction of Gd-Gamers is ~ 1.5 times higher.
- The difference ND-FD as roughly doubled.

These features are expected because of, inter alia, stopping muons (SM) contribution whose delayed signal, the michel electron (cf. section 2.10.1), is susceptible to interact in the GC due to the topology of SM events depicted in figure 2.15. Moreover, the michel electron has a relatively wide energy range, from 0 up to 60 MeV, which includes the Gd capture window. Some fast neutrons, as well, are susceptible to have their delayed signals in the GC in view of their topology presented in figure 7.3.

5.3 Estimation of the leak

A dedicated analysis has been performed in order to estimate the amount of the leak i.e the concentration (in μg/cm^3) of Gd in the ND GC. This concentration is referred in the present volume as *Gd-GC*. The method used is based on a comparison of the spherical distribution (r^3) of events in the true data and the MC. Indeed, although the DC detector has a cylindrical symetry, the r^3 distribution of events gives a quick and direct evaluation of iso-volumes events distribution.

The asymetry of number of events between the ND and FD can be defined as

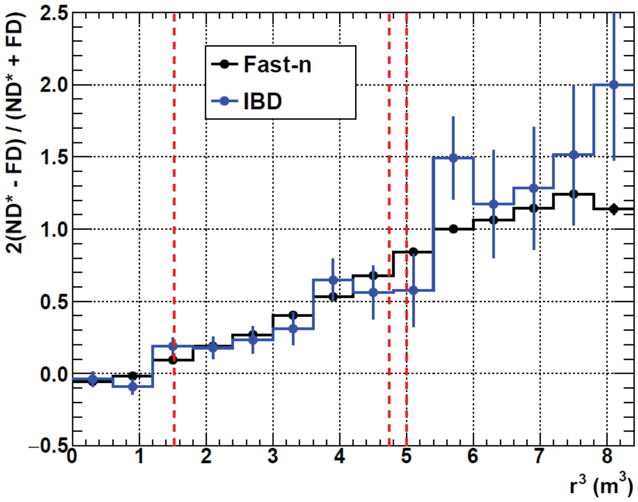

Figure 5.4: *ND-FD Events asymetry as a function of r^3 in the true data.*

$$A = \frac{2 \times (ND^* - FD)}{ND^* + FD} \tag{5.1}$$

where FD and ND* refer respectively to the number of events in the FD and in the ND scaled to the FD Target volume. This asymetry of number of events as a function of r^3 is expected to exhibit the same shape for two different sample of events, for instance for the Fast Neutrons (FN) and the IBD samples. This expectation is evidenced in figure 5.4 where it can be observed that the FN and the IBD asymetries, as a function of r^3 coincide and present the same spectral shape for the true data. Indeed, it can be demonstrated that IBDs and FN events are quasti isotropically distributed within the detectors.

Due to the presence of Gd in the ND GC, the default MC used so far presents a r^3 IBD asymetry that deviates sensibly, as it can be seen in figure 5.5, from the FN one, unlike what is observed in true data in figure 5.4. Therefore, new MC files with different Gd concentration in the ND GC (*Gd-GC*) have been generated in the search of the ideal concentration that renders the asymetry observed in the data. Hence, the leak would have been measured.

Several concentrations of Gd in the GC have been tested in the MC. The illustration case of an excessive concentration of 2.4 μg/cm^3 is shown in figure 5.6 where the contamination added uniformly in the MC leads to an asymetry of IBDs higher than the FN asymetry observed in data, especially beyond the 2 m^3 volume.

The latest proposal of Gd concentration in the ND GC has been obtained by using the integrated asymetry ratio as shown in figure 5.7 where the ratio of FN and IBD asymetries are plotted as a function of the Gd concentration put in the MC. The fit of the curve in figure 5.7, with an exponential plus a

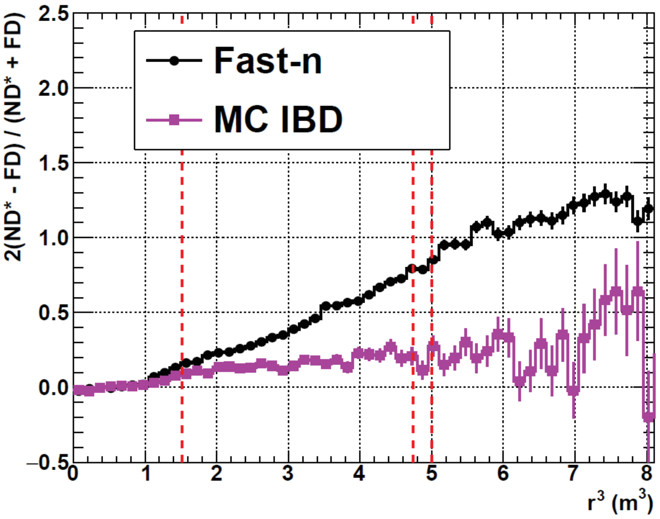

Figure 5.5: *ND-FD Events asymetry as a function of* r^3 *in the default MC data.*

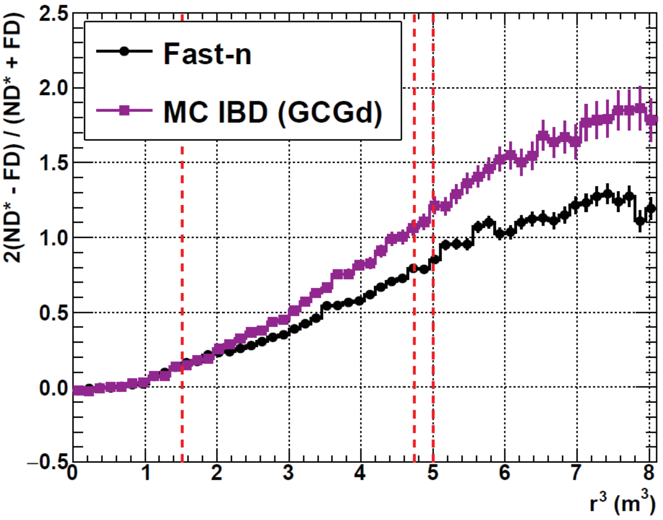

Figure 5.6: *ND-FD Events asymetry as a function of* r^3 *in the MC data doped with* $2.4\mu g/cm^3$ *of Gd in the ND GC.*

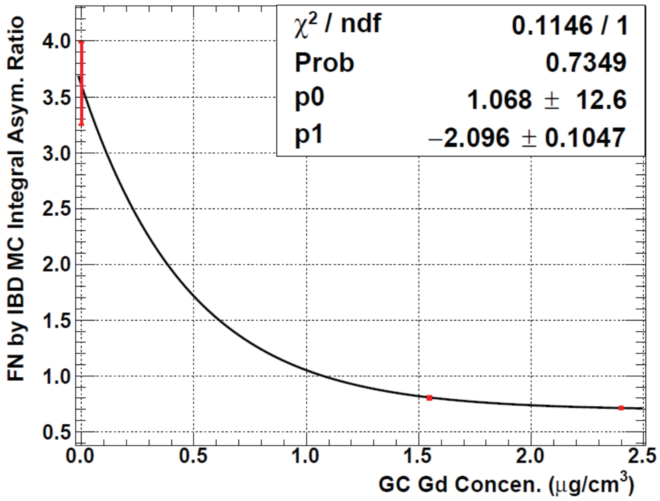

Figure 5.7: *Ratio of FN and IBD asymetries as a function of the Gd concentration of Gd in the ND GC.*

	H-Gamers
MC* (1.1μg/cm^3 Gd-GC)	92.40 ± 0.99
Default MC	93.88 ± 1.00
True data	92.06 ± 0.32

Table 5.5: *Fractions of ND Gamers in the 1.1 μg/cm^3 Gd-GC MC, in the default MC and in the true data after background subtraction.*

logarithmic function, suggests that a ratio equals to 1 can be achieved when Gd-GC $\simeq 1.1\ \mu\text{g/cm}^3$.

We tested the proposal of 1.1μg/cm^3 Gd-GC MC by counting the number of Gamers that we compared to the numbers obtained in the true data (cf. table 7.2). It appears, as it can be seen in table 5.5 that the addition of 1.1 μg/cm^3 Gd-GC in the MC decreases the fraction of H-Gamers observed in the default MC as expected. However, the numbers obtained coincide well within errors with the ones obtained in the true data after background subtraction. Hence, from the point of vue of Gamers too a Gd concentration in the ND GC equivalent to 1.1 μg/cm^3 is coherent.

5.4 Evolution of the leak

The question of stability over time of the leak arose almost as soon as the leak was evidenced. The study of its evolution would allow to know whether the leak has always been present or has occurred at a precise moment of the ND running. As introduced in section 3.2, the 23 Months data analysed in this work can be decomposed in 23 distinct months of well know livetime and run numbers. The overall analysis done above has been reproduced for each of this month.

	H-Gamers	**Gd-Gamers**
ND	87.66 ± 0.31 87.64 ± 0.28	12.34 ± 0.08 12.24 ± 0.08
FD	94.17 ± 0.60 94.16 ± 0.60	05.83 ± 0.11 05.75 ± 0.11

Table 5.6: *Mean fractions of Gamers (in red), prior to background subtraction, as provided by the linear fit of the 23 monthly values. For comparison the values obtained in table 5.4 are repeated here in black.*

Figure 7.6 shows the monthly measured fractions of Gamers in the ND and evidences that these fractions are stable and compatible with a constant function. The mean fractions, prior and after background subtraction, as provided by the fit are listed respectively in table 5.6 and 5.7. Hence, following this analysis the leak has always been constantly present at the ND; one can infer that "leak accident" has happened when the ND was being filled with the scintillator liquids.

	H-Gamers	**Gd-Gamers**
ND	91.85 ± 0.30 91.86 ± 0.30	8.15 ± 0.07 8.14 ± 0.07
FD	95.25 ± 0.66 95.20 ± 0.65	4.75 ± 0.11 4.80 ± 0.11

Table 5.7: *Mean fractions of Gamers, in black, after background subtraction, as provided by the linear fit of the 23 monthly values. For comparison the values of the total fractions are given here in red.*

5.5 Conclusion

An additional proof of the Gd leak into the Gamma Catcher at the ND has been provided by means of statistical analysis of events whose delayed signals are in Gamma Catcher, the so-called Gamers events. The observed relative abundance of Gamers has demonstrated a lower fraction of H-Gamers in ND with respect to the FD in the true data while the MC data have not evidenced such a difference. An analysis of the evolution allows to say that the leak is stable overtime. Moreover, dividing the GC in two parts (top and bottom) reveals that there are more Gd-Gamers in the top part than in the bottom one. This difference with the bottom part is reduced but not

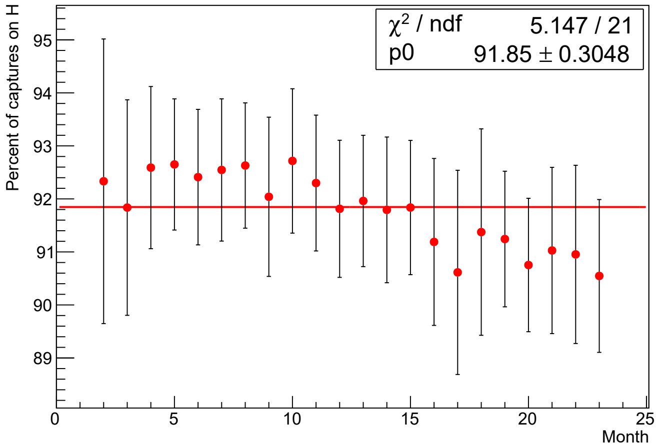

(a) ND

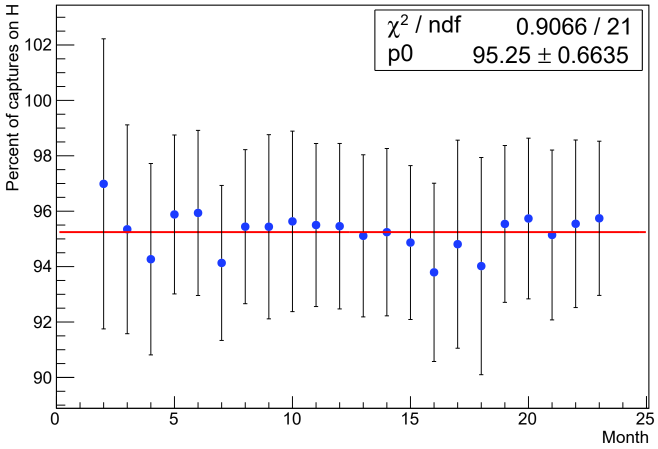

(b) FD-II

Figure 5.8: *Monthly fractions of H-Gamers in the ND (a) and FD (b). After background subtraction.*

cancelled after background subtraction. The Gd++ analysis allows, nevertheless, to overcome the leak issue by collecting all the neutrons captures occurring in the whole detector. However, since unlike in the Target the number of hydrogen nuclei in the GC has not been precisely measured in DC, the Gd++ analysis has the default to increase the uncertainty on the proton number. Indeed, the GC was not thought originally to be the detection volume.

Chapter 6

Final conclusion

> *"Il n'y a qu'un seul salut, c'est la connaissance directe et aucune paresse ne pourra nous dispenser de cet effort. Il faudra absolument acquérir la connaissance directe. A formation égale, la vérité triomphe. Formez-vous, armez-vous de sciences jusqu'aux dents"*
>
> Cheikh Anta Diop

The principal goal of the Double Chooz experiment (DC) is the measurement of the θ_{13} mixing angle value. The robustness and accuracy of this measurement rely on a precise knowledge of the rates and spectral shapes of the backgrounds that contaminate the $\overline{\nu}_e$ selection over the neutrino oscillation expected region. We have studied in the present work the muon induced correlated background in the DC neutrino oscillation experiment. Indeed, cosmic muons crossing the detectors or interacting in the neighborhood constitute, by far, the main source of background events encountered in the DC. Two distinct backgrounds analysis are presented in this thesis; the first is devoted to the fast neutrons (FN) and the second to the double capture of neutrons (DnC).

The physical signatures of the fast neutrons have been identified and the subsequent analysis has settled optimally the vetoes that select efficiently this particular background with an associated inefficiency ($< 0.1\%$) very negligible, beyond the expectations. The sample of events selected by the defined vetoes has provided the spectrum shape of the correlated background. We have been able, thanks to the spectra obtained, to compute the rate of the remaining correlated background in the final sample of IBDs prior to the final fit. These two informations (spectral shapes and background rate) serve as inputs in the final fit whence is determined the θ_{13}

value. The vetoes and the associated rates of background measured in this work are admitted as official by the DC collaboration

Besides the fast neutrons, an analysis of the double capture of neutrons background has been performed in this volume for the first time. The contamination of the final IBD sample, in DC-IV, by the DnC background events have been evidenced by the clear presence of neutrons capture peaks in the prompt energy spectrum of IBD candidates events which have, as preceding event, one or more invalid triggers. Such events are not rejected by the multiplicity cut neither by the Inner Veto veto, based both on valid triggers. Dedicated methods have allowed the measurement of the daily rates of DnC; this contamination of the DnC background is obtained to be respectively of 1.19 ± 0.11 events/day and 0.23 ± 0.02 events/day for the ND and the FD. The question of stability, or not, of DnC events over time has been answered by the affirmative. Moreover, The impact of DnC background on the θ_{13} value has been investigated; it appeared that, at the stage of the current amount of the data collected, including the DnC rates in the final cause a minor shift of the central value of θ_{13}.

In addition to the study of the correlated background, we have investigated the leak of Gadolinium in the ND Gamma Catcher (GC) based on a statistical analysis of events with delayed signals in the Gamma Catcher. Our analysis has provided the proof of the Gd leak into the ND Gamma Catcher by means of statistical analysis of events with delayed signals are in Gamma Catcher. The observed relative abundance of these captures in the GC has demonstrated a lower fraction of captures on Hydrogen in ND with respect to the FD in the true data while the MC data have not evidenced such a difference. An analysis of the evolution allows to say that the leak is stable overtime. Moreover, dividing the GC in two parts (top and bottom) has revealed that the concentration of leak is higher in the top part than in the bottom one. This difference with the bottom part is reduced but not cancelled after background subtraction. The current analysis performed in DC allows to overcome this unbalance that could emerge from the leak since in the particular case of analysis all the captures, both on H and Gd, are collected.

Besides the data analysis undertaken in this work, I have been involved in the different detectors calibration campaigns. Indeed, calibrations are the keystones in the study of the stability of the detectors responses, the evaluation of the vertex and energy reconstructions algorithms developed in DC.

The main results of the analysis described here will be integrated in a paper to be published this summer by the DC collaboration. A part of the work done in this thesis has already been presented in [101] and [102]. Besides, I am contributor author in [103], [104] and [90]. The knowledge of muon induced background and the associated identification techniques that emerge from this work are susceptible to serve in many other neutrino experiments already running or to be built in future years.

Chapter 7

Résumé de la thèse en français

Introduction

Les neutrinos sont les particules les plus intrigantes que l'on rencontre parmi les nombreuses particules qui forment les blocs élémentaires et invisibles qui constituent l'univers visible. On sait maintenant que les neutrinos sont des fermions neutres interagissant faiblement, existant au moins en trois familles ou saveurs leptoniques: les neutrinos électronique, muonique et tauique (ν_e, ν_μ et ν_τ). Postulés en 1930 par le physicien Autrichien W. Pauli comme la solution à la non-conservation de l'énergie observée dans les processus de désintégration bêta, les neutrinos ont depuis mis en évidence de nombreuses propriétés remarquables qui ont été étudiées ou révélées par plusieurs expériences menées dans le monde entier. Ces observations ont notamment permis d'établir que les neutrinos ont une masse faible mais non nulle contrairement à l'hypothèse de masse nulle jusqu'alors admise en modèle standard des particules. Cela suggère qu'une extension du modèle standard, ou un modèle au-delà, est nécessaire pour fournir une description théorique complète des interactions et des propriétés des neutrinos.

Cependant, de nombreuses questions sur les neutrinos demeurent encore sans réponse. En effet, on ne sait pas encore si les neutrinos sont distincts de leurs antiparticules (neutrinos de Dirac) ou de leurs propres antiparticules (neutrinos de Majorana). En outre, on ignore encore quelle est la masse absolue des neutrinos et pourquoi cette masse devrait être, de loin, plus faible que les masses des autres fermions. La liste des questions sans réponse est encore plus longue : on ne sait pas non plus, à l'heure actuelle, si les neutrinos sont liès à la leptogenèse, s'il existe plus de trois saveurs et si la symétrie CP est conservée ou non dans le secteur des leptons. Toutes ces questions fondamentales justifient le grand intérêt de la physique des neutrinos observé au cours des dernières décennies par la multiplication des expériences et des tentatives théoriques visant à trouver des réponses à ces questions cruciales.

Les neutrinos subissent un phénomène particulier directement lié à leur masse, appelé oscillation de neutrinos, selon lequel un neutrino créé avec une saveur leptonique spécifique a une probabilité non nulle d'être ultérieurement détecté avec une saveur différente. La probabilité d'oscillation varie périodiquement en fonction de l'énergie des neutrinos et de la distance parcourue entre la source de production et le point de détection. Les oscillations, résultant de la masse non nulle de neutrinos, sont la conséquence de la non-coincidence des états propres de masse et des états propres de saveur du neutrino. Ces oscillations sont régies par six paramètres indépendants: trois angles de mélange, deux différences des carrés de masses et une phase de violation de CP. A l'heure actuelle, les angles de mélange ont été mesurés avec plus ou moins de précision, tandis que le signe d'une des différence de carré de masse et la phase de violation de CP, malgré quelques avancées récentes, ne sont toujours pas connus.

L'expérience Double Chooz (DC) observe la disparition des antineutrinos électroniques, quand ceux-ci oscillent vers d'autres saveurs, afin de mesurer spécialement le paramètre de mélange θ_{13} qui a longtemps été le dernier angle inconnu de la matrice de mélange des oscillations de neutrinos. Double Chooz utilise à cet effet le flux des antineutrinos électroniques provenant des deux cœurs de réacteur de la centrale nucléaire de Chooz située dans la région des Ardennes, à l'Est de la France. L'expérience consiste en deux détecteurs à scintillateur liquide de conception identique: un détecteur proche (ND) situé à 400 mètres des réacteurs concu pour quantifier le flux initial de neutrinos et un détecteur lointain (FD) situé à 1050 mètres mesurant l'oscillation elle-même. Une analyse dite du "taux et de la forme" est effectuée pour rechercher une distorsion dans le spectre d'énergie mesurée due à la disparition des antineutrinos électroniques. La dernière mesure publiée par la collaboration Double Chooz est $\sin^2 2\theta_{13} = 0.119 \pm 0.016$. La précision et l'exactitude de cette mesure reposent sur une connaissance précise du taux et des formes spectrales des buits de fond contaminant la sélection de neutrinos électroniques sur la région attendue de l'oscillation des neutrinos; ces deux informations, le taux des bruits de fond et leur forme spectrale, constituent les inputs du fit final d'où émerge la valeur de l'angle θ_{13}. Les détecteurs Double Chooz, comme on peut le voir sur la figure 7.1 se composent de trois sous-détecteurs isolés optiquement: le détecteur intérieur (ID), le véto intérieur (IV) et le véto extérieur (OV). L'ID se compose de 3 volumes cylindriques, à savoir de l'intérieur vers l'extérieur, le Target (dopé au Gadolinium), Gamma Catcher (GC) et Buffer. Le IV est un volume cylindrique entourant l'ID ayant pour fonction principale de détecter et d'identifier les muons, source de bruit de fond, entrant dans le détecteur. Le OV installé sur le dessus des détecteurs est indépendant de l'ID et de l'IV, tant du point de vue électronique que de la lecture.

Cette thèse présente, en cinq chapitres, l'étude du bruit de fond induit par les muons cosmiquse dans l'expérience d'oscillation de neutrinos Double Chooz (DC). En effet, les muons cosmiques traversant les détecteurs ou interagissant dans le voisinage proche constituent la source principale du bruit de fond rencontré à DC. Le premier chapitre de ce volume passe brièvement en revue la physique des neutrinos, le phénomène des oscillations, les connaissances actuelles en matière de neutrinos et certaines des questions en suspens. Le deuxième chapitre décrit en détail la conception de l'expérience DC alors que les chapitres suivants sont consacrés au travail d'analyse entrepris dans cette thèse. Le troisième chapitre étudie le bruit de fond corrélé, en particulier les neutrons rapides (FN) de la technique d'identification aux mesures de taux et à la détermination des formes spectrales. Un autre bruit de fond induit par le muon, la double capture des neutrons (DnC), est mis en évidence dans les données et présenté dans le quatrième chapitre. Ici aussi, la technique d'identification développée et les mesures de taux sont décrites en détail. Le dernier chapitre est consacré à un sujet particulier qu'est la fuite accidentelle de gadominium dans le Gamma Catcher observée dans le ND. Les travaux effectués ont permis de mettre en évidence la fuite, de donner une estimation de la fuite et d'étudier son évolution au fil du temps.

L'expérience Double Chooz

Double Chooz vise une mesure de précision de l'angle de mélange θ_{13} de la matrice PMNS. Le concept expérimental de base consiste à utiliser un réacteur nucléaire comme une source intense des antineutrinos électroniques et de placer deux détecteurs à des distances différentes de la source. Le détecteur lointain (FD) , est placé près du maximum d'oscillation, où il surveille le flux des neutrinos du réacteur. Le résultat est comparé au flux de neutrino d'origine attendu à partir des données de la puissance thermique du réacteur, et une valeur pour θ_{13} peut être obtenue à partir du déficit. Le détecteur proche (ND) placé à proximité du coeur du réacteur sert de référence pour le flux de neutrinos d'origine.

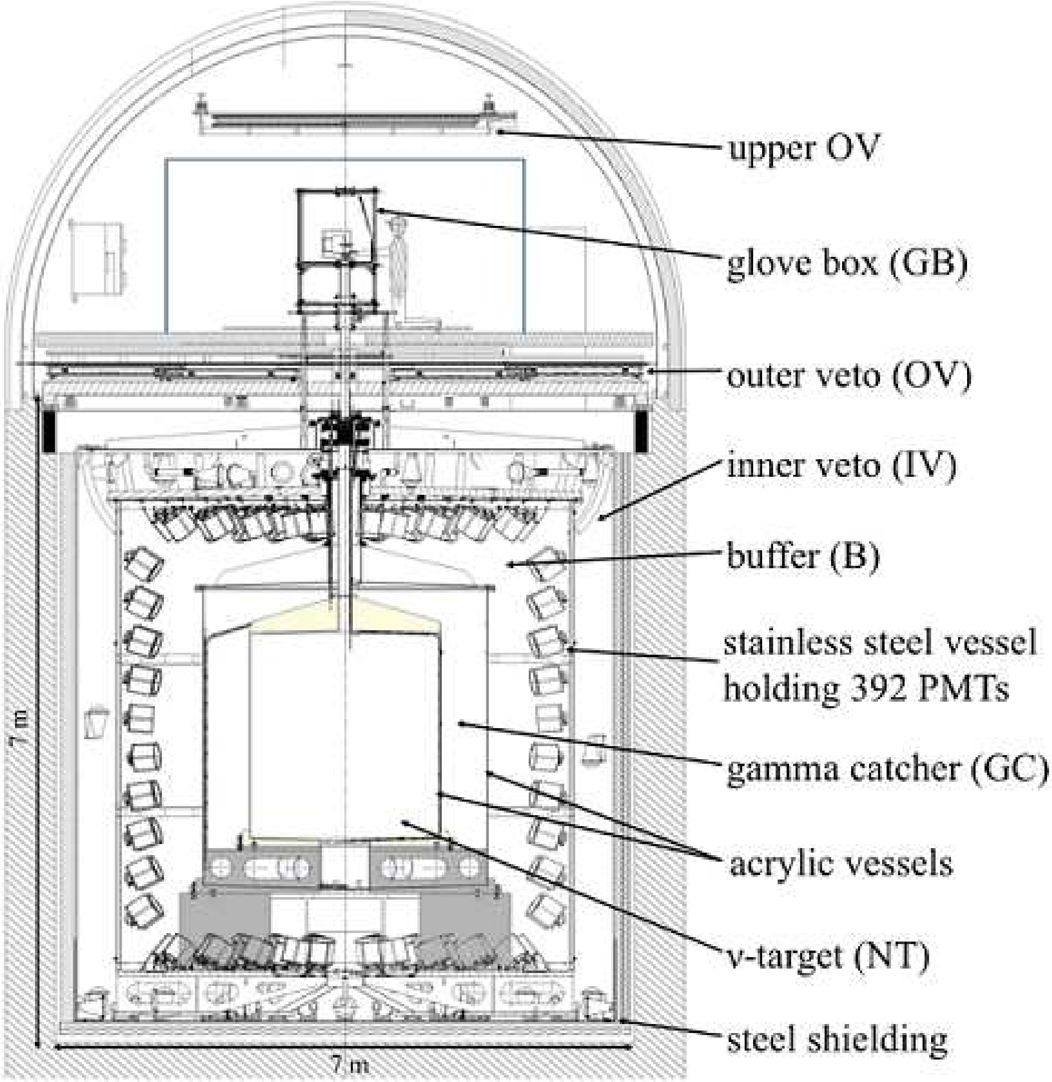

Figure 7.1: *Esquisse du détecteur de Double Chooz .*

Le DC consiste en deux détecteurs identiques: un détecteur de proximité et un détecteur de distance (ND et FD) situés respectivement à une distance moyenne de 400 m et à 1050 m des deux coeurs de réacteur, comme l'illustre la figure 7.2. Les deux détecteurs, ND et FD, ont respectivement des morts-terrains de 300 et 120 mètres d'équivalent eau pour se protéger des muons cosmiques, qui constituent de loin la principale source de bruit de fond de l'expérience.

comme celui-ci. Les deux détecteurs présentent deux topologies différentes: plate pour le ND et une colline pour le FD. Dans cette configuration, le détecteur de proximité surveille le flux d'antineutrinos électroniques avant une oscillation significative, tandis que le flux mesuré dans le détecteur éloigné de 1 km permet en outre la comparaison d'où émerge le paramètre

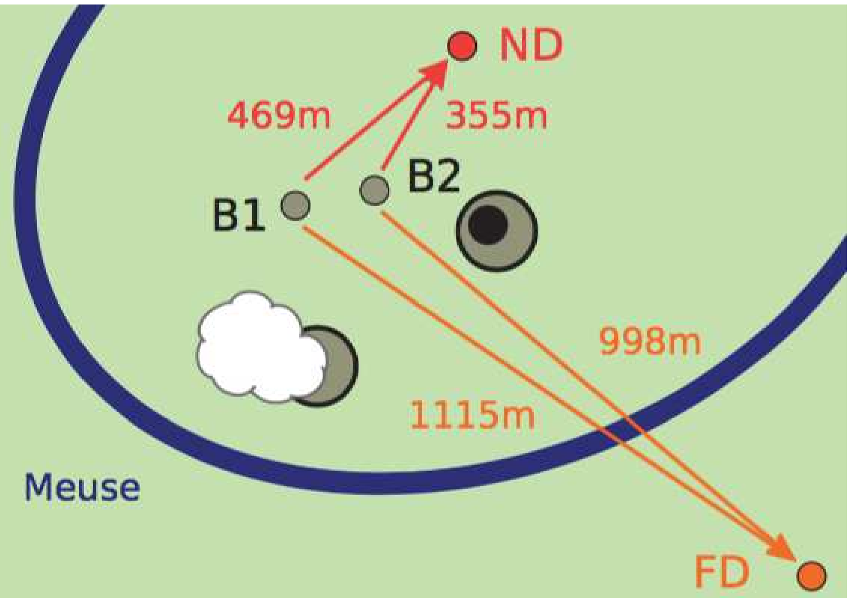

Figure 7.2: *Esquisse de l'expérience Double Chooz. Les cœurs des réacteurs B1 et B2 sont indiqués en noir. Les distances entre les cœurs des réacteurs et les détecteurs sont mentionnées. Image tirée de [73]*

d'oscillation θ_{13}. Cette configuration à double détecteur offre une grande amélioration dans la recherche de la minimisation des incertitudes systématiques en raison de la précision relativement faible avec laquelle on connaît théoriquement à la fois le flux et le spectre d'énergie des antineutrinos du réacteur. Le détecteur lointain (FD) a été construit entre 2009 et 2010 et prend des données depuis avril 2011, tandis que le détecteur proche, construit entre 2011 et 2014, prend des données depuis janvier 2015. Le FD de la période à détecteur unique (2011-2015) est communément désigné en tant que FD-I dans la littérature de DC; FD-2 fait référence à FD dans la période de plusieurs détecteurs (2015-2018) où les données sont prises simultanément dans les ND et FD. Ces deux dénominations de FD sont également utilisées dans le présent texte.

Les neutrinos électroniques détectés dans les DC sont produits dans les deux coeurs de réacteurs de fission de la centrale de Chooz lors de la chaîne de désintégrations bêta de noyaux riches en neutrons. Comme pour Chooz, une centrale électrique typique d'un réacteur à eau pressurisée dégage environ 2×10^{20} neutrinos par seconde.

Le signal d'une interaction d'antineutrino dans DC est le processus de désintégration bêta inverse :

$$\overline{\nu}_e + p \rightarrow e^+ + n$$

Ce processus produit un signal rapide du à l'annihilation du positron et un signal retardé du fait de la capture du neutron. Les deux signaux sont séparés par une différence de temps de l'ordre de quelques dizaines ou centaines de microsecondes. Ces signaux correlés en temps et en espace sont observables à l'aide de détecteurs à scintillateur liquide vus par des tubes photomultiplicateurs (PMT). La coincidence de ces deux signaux peut être utilisée pour supprimer efficacement le bruit de fond.

Analyse du bruit de fond correlé

Trois types de bruits de fond dans DC, à savoir les fast neutrons (FN), les évenements $\gamma - \gamma$ et les stopping muons (SM), peuvent être identifiés grâce à l'énergie qu'ils déposent dans l'Inner Veto.

- les FN sont les neutrons de haute énergie créés par les muons cosmiques qui interagissent à l'extérieur du détecteur, typiquement dans la roche environnante. Comme schématisé dans l'encadré 1 de la figure 7.3, lorsque les FN pénètrent dans le détecteur , ils perdent leur énergie par des collisions sur les protons du milieu. Le recul de ces protons crée alors un signal dans le scintillateur liquide. Une fois le fast neutron thermalisé, ils peut être capturé par un noyau du gadolinium ou d'hydrogène. Par conséquent, le recul du proton et la capture ensuite du neutron qui sont physiquement corrélés, imitent le signal antineutrino de Double Chooz. Puisque les FN sont générés avec une grande multiplicité, certains d'entre eux devraient déposer de l'énergie à la fois dans l'ID et l'IV; les neutrons rapides qui perdent un peu d'énergie au sein de la IV peuvent ensuite être identifiés en utilisant ce dépôt d'énergie dans IV. Le système d'acquisition de données de DC est concu de telle manière que les deux triggers de l'ID et de l'IV se déclenchent quel que soit le détecteur touché. Les neutrons rapides sont donc identifiés et sélectionnés si un dépot d'énergie dans l'ID se produit en coincidence avec un événement dans l'IV.

- Les $\gamma - \gamma$ sont des photons de la radioactivité naturelle ou provenant des neutrons capturés dans les matériaux environnants, qui subissent la diffusion Compton dans le IV et dans l'ID où, en coincidence accidentelle avec une capture d'un neutrons thermique, va imiter le signal. La topologie de ce bruit de fond est schématisée dans l'encadré 2 de la figure 1. Ces $\gamma - \gamma$ peuvent donc être sélectionnés grace à leur dépôt d'énergie dans IV.

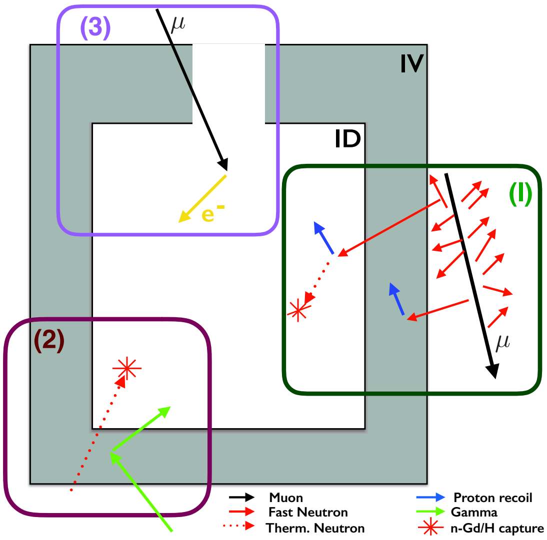

Figure 7.3: *Topologie des événements FN, SM et $\gamma - \gamma$. Box 1 schématise les événements FN visés par les coupures IVV. Box 2 schématise les événements $\gamma - \gamma$ issus de la radioactivité basse énergie: le γ subit une diffusion Compton dans the IV et dans le ID où, en coincidence accidentelle avec un neutron thermique, il imite la signature du $\overline{\nu_e}$. Box 3 schématise le cas particulier des stopping muons (SM) qui traversent les coins de la cheminée et déposent de l'énergie dans l'IV.*

- Le SM vient du fait qu'il y a un trou dans l'IV: la cheminée. L' encadré 3 de la figure 1 montre que les muons peuvent entrer dans l'ID par la cheminée et ne pas déclencher, en principe, l'IV. Néanmoins, certains de ces SM traversent les coins de la cheminée déposant ainsi un peu d'énergie dans le IV. Ce dépot de faible énergie, en dessous du seuil de rejection des muons, peut être utilisé pour identifiér les SM.

Etant donné qu'à Double Chooz, le signal est enregistré pendant une fenetre temporelle de 256 ns, il est attendu qu'une partie de ce bruit de fond, provenant de l'extérieur du détecteur, se produise simultanément avec un dépot d'énergie dans l'IV . Si ce dépôt d'énergie est inférieur au seuil des muons dans l'IV, cet événement ne sera pas étiqueté automatiquement par le système d'acquisition des données comme un muon. "L' Inner Veto Tagging (IVT)" est la technique développée dans DC pour identifier le bruit de fond sur la base des informations dans l'IV.

Nous concluons le présent chapitre par un bref résumé de ce que nous avons fait et appris de l'analyse effectuée. Le veto IV qui utilise des signaux de basse énergie dans le IV pour sélectionner le fond FN a été réglé pour le DC-IV et admis comme officiel par la collaboration du DC. L'inefficacité associée mesurée pour toutes les configurations s'est avérée très négligeable (inférieur à 0.1 pourcent), au-delà des attentes.

L'analyse réalisée avait pour objectif final d'ajuster les conditions de rejet de la VIV sur les candidats IBD afin d'identifier événement par événement celles qui provenaient de l'extérieur du détecteur, en particulier du FN. Le défi consistait à mettre en place l'IVV en minimisant autant que possible l'inefficacité pour éviter le rejet des MICI. Ce défi a été atteint en atteignant des valeurs d'inefficacité très négligeables. L'IVV a été réglé pour tous les détecteurs dans toutes les configurations.

La IVV ainsi ajustée a été officiellement admise comme base de référence par la collaboration Double Chooz dans DC-IV, la campagne de diffusion et d'analyse de données de 15 mois. L' échantillon d' événements sélectionnés par l'IVV a été utilisé pour définir un modèle de forme du fond corrélé et pour mesurer le taux correspondant présenté dans la section suivante.

L'échantillon d'événements IVV a permis des définitions de forme de spectres FN cohérentes. Toutes les configurations de détecteurs (ND, FD-I et FD-II) utilisent une seule forme, un polynome du second ordre, dans la sélection de Gd. Le spectre FN est compatible avec une forme exponentielle se développant à basse énergie pour la sélection Gd ++ pour les trois configurations de détecteurs. Enfin, les taux restants de PN dans l'échantillon final de l'IBD ont été mesurés. Ces deux informations (formes spectrales et fréquence de fond) servent d'intrants dans l'ajustement final, à partir duquel la valeur θ_{13} est déterminée.

Etude de la double capture des neutrons

La double capture de neutrons (DNC) est le dernier bruit de fond étudié dans DC. En effet, en raison de l'absence d'une signature claire, ce bruit de fond a longtemps été ignoré et n'a pas été pris en compte dans les inputs lors du fit final contrairement à tous les autres bruits de fond. Le travail de ma thèse a permis de développer une technique d'identification dédiée et une estimation de la contamination de ce bruit de fond dans les données de DC.

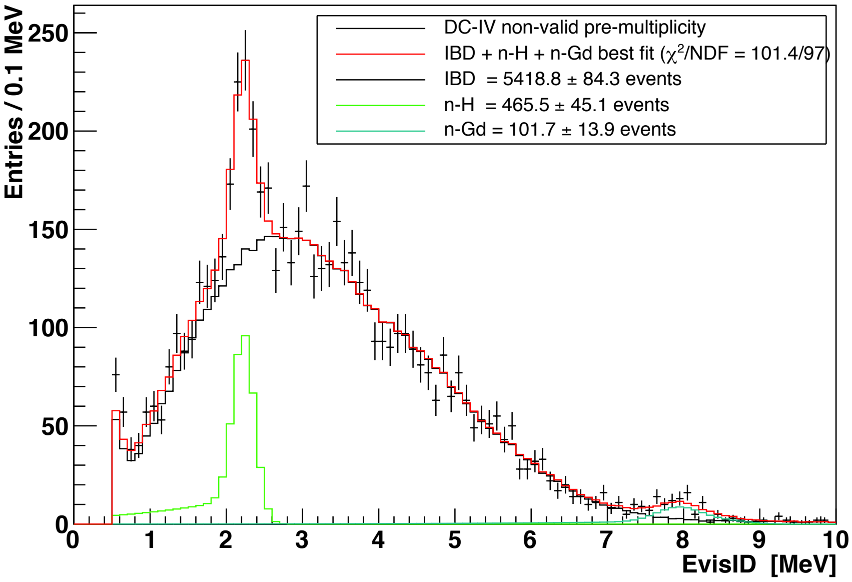

Figure 7.4: *Fit du spectre d'énergie des évenements DnC (en rouge) comme la somme du spectre d'énergie des candidats IBD (en noir) et du spectre d'énergie des captures retardées sur H sur Gd. Le fit, réalisé via la méthode TFractionFitter method, donne comme résultat les histogrammes de capture de neutrons (vert pour H and bleu pour Gd) ainsi que les valeurs associées. ND.*

La contamination de l'échantillon final de l'IBD, dans le DC-IV, par les événements de fond de DnC a été mise en évidence par la présence évidente de pics de capture de neutrons dans le spectre d'énergie rapide des événements candidats d'IBD qui ont, comme événement précédent, un ou plusieurs déclencheurs non valides (cfr. figure 7.4). De tels événements ne sont pas rejetés par la multiplicité réduite ni par le veto Inner Veto, fondé eux sur des déclencheurs valables.

Des méthodes dédiées ont permis de mesurer les taux quotidiens de DnC; on obtient que la contamination du fond de DnC soit respectivement de $1.9 \pm 0,11$ événement par jour et de 0.23 ± 0.02 événements par jour pour le ND et le FD. La question de la stabilité, ou non, des événements de DnC dans le temps a été répondue par affirmative comme on peut le voir sur la figure 7.5. Néanmoins, ces estimations de taux doivent être interprétées comme des limites inférieures, car elles ne tiennent compte que de la fraction de DnC effectivement précédée de déclencheurs non valides; il est en effet possible que certains événements de recul du proton ne soient pas étiquetés comme des déclencheurs non valides, mais ne déclenchent pas du tout (restent non détectés).

	Input	**Fake data without DnC**	**Fake data with DnC**
$\sin^2 2\theta_{13}$	–	0.1000 ± 0.0141	0.0989 ± 0.0141
χ^2	–	–	1.40
Acc ND	3.110 ± 0.004	3.110 ± 0.004	3.110 ± 0.004
Acc FD	4.32 ± 0.02	4.32 ± 0.02	4.32 ± 0.02
Corr ND	20.77 ± 0.43	20.77 ± 0.31	20.75 ± 0.43
Corr FD	2.540 ± 0.070	2.540 ± 0.054	2.540 ± 0.054
Li ND	12.3 ± 2.0	12.3 ± 1.15	13.2 ± 1.6
Li FD	3.01 ± 0.60	3.01 ± 0.30	3.09 ± 0.32

Table 7.1: *Résultats du fit sur les fausses données containnant le bruit de fond DnC.*

Jusqu'à présent, et avant les travaux entrepris dans le présent volume, ce bruit de fond qu'est la double capture des neutrons n'a pas été intégré dans une analyse ou une publication de DC. C'est simplement parce que ce bruit de fond particulier n'avait pas encore été clairement démontré. Par conséquent, à la suite des mesures obtenues dans ce chapitre, l'impact sur la valeur θ_{13} des taux de DnC a été étudié. En fait, comme déjá mentionné, les taux restants estimés de chaque bruit de fond servent d'input pour l'ajustement final qui fournit la valeur de θ_{13}; ces taux ajoutent des contraintes à l'ajustement final et ont donc un impact direct sur la valeur de θ_{13}. Cet impact a été étudié en comparant les résultats des ajustements sur deux ensembles de fausses données, avec et sans DnC inclus.

L'impact du bruit de fond de DnC sur la valeur de θ_{13} a été démontré comme négligeable; l'inclusion des taux de DnC dans l'ajustement final laisse la valeur centrale de θ_{13} quasi inchangée comme on peut le voir dans le tableau 7.1.

Etude de le fuite du Gd dans le Gamma Catcher

L'analyse des 15 mois de données prises au ND a révélé un problème inattendu: la présence du Gd dans le Gamma Catcher, rompant ainsi l'équilibre de la configuration du détecteur décrit ci-haut. Jusqu'à présent, l'origine de cette fuite n'a pas encore été clairement identifiée; cela peut être arrivé très probablement au moment du remplissage du ND. Le travail de ma thèse a présenté une méthode originale pour étudier cette fuite, ce qui a permis une estimation de son ampleur ainsi que sa localisation dans le détecteur.

Une preuve supplémentaire de la fuite de Gd dans le Gamma Catcher au

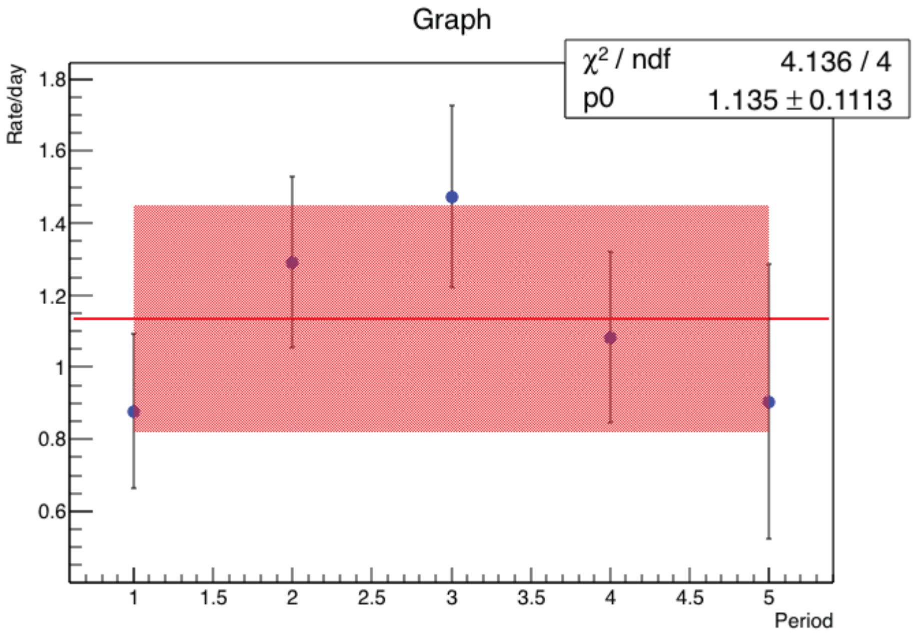

(a)

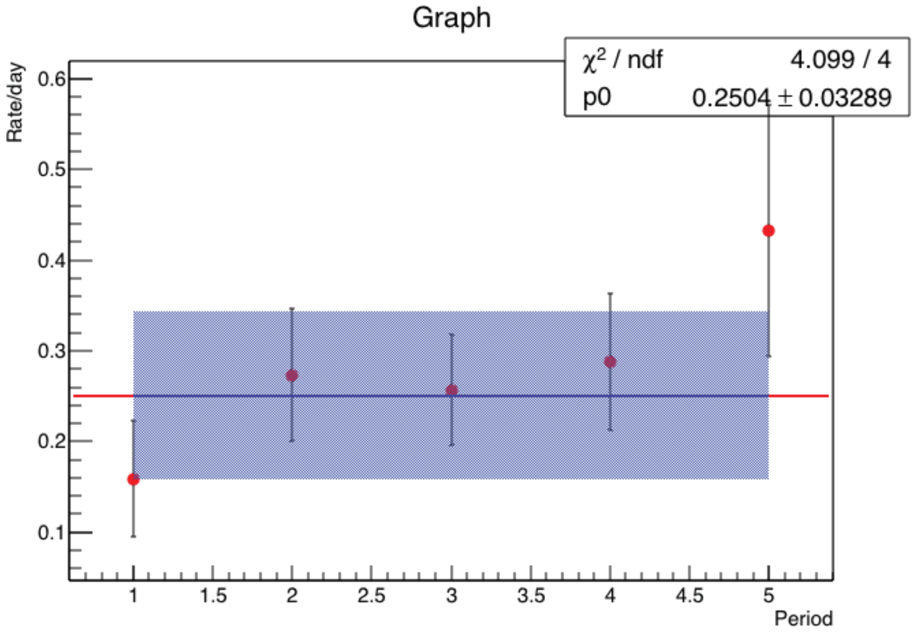

(b)

Figure 7.5: *Evolution du taux des évenements DnC sur cinq périodes. Les captures neutroniques sur l'hydrogène(a) et sur le gadolinium (b) sont compatibles avec des taux stables.*

	H-Gamers	**Gd-Gamers**
All	92.06 ± 0.32 95.51 ± 0.68	8.14 ± 0.07 4.50 ± 0.11
Top	91.07 ± 0.43 95.40 ± 0.94	8.93 ± 0.10 4.59 ± 0.15
Bottom	93.12 ± 0.46 95.61 ± 0.97	6.91 ± 0.09 4.38 ± 0.15

Table 7.2: *Fractions des Gamers dans les vraies données après soustraction du bruit de fond. Les valeurs en noir référent au ND tandis que les valeurs pour le FD, en dessous, sont en rouge.*

niveau du ND a été fournie au moyen d'une analyse statistique des événements dont les signaux retardés se trouvent dans Gamma Catcher, appelés événements Gamers. L'abondance relative observée de Gamers a mis en évidence une fraction inférieure de H-Gamers dans le ND par rapport à FD dans les données vraies, alors que les données MC ne montrent pas une telle différence comme on peut le voir dans la figure 7.2. Une analyse de l'évolution permet de dire que la fuite est stable au cours du temps. De plus, diviser le GC en deux parties (haut et bas) révèle qu'il y a plus de Gd-Gamers dans la partie supérieure que dans la partie inférieure. Cette différence avec la partie inférieure est réduite mais pas annulée après la soustraction du bruit de fond. L'analyse Gd ++ permet néanmoins de résoudre le probléme des fuites en collectant toutes les captures de neutrons se produisant dans l'ensemble du détecteur. Cependant, étant donné que contrairement au Target, le nombre de noyaux d'hydrogène dans la GC n'a pas été mesuré précisément dans les DC, l'analyse Gd ++ a pour défaut d'augmenter l'incertitude sur le nombre de protons. En effet, le GC n'était pas pensé à l'origine comme un volume de détection.

Conclusion

L'objectif principal de l'expérience Double Chooz (DC) est la mesure de la valeur de l'angle de mélange θ_{13}. La robustesse et la précision de cette mesure reposent sur une connaissance précise des taux et des formes spectrales des bruits de fond qui contaminent la sélection des antineutrinos sur la région attendue de l'oscillation des neutrinos. Nous avons étudié dans le présent travail le fond corrélé induit par le muon dans l'expérience d'oscillation de neutrinos de DC. En effet, les muons cosmiques traversant les détecteurs ou interagissant dans le voisinage constituent, de loin, la principale source du bruit de fond rencontrés dans DC. Deux analyses de fond distinctes sont présentées dans cette thèse; le premier est consacré aux neutrons rapides (FN) et le second à la double capture de neutrons (DnC).

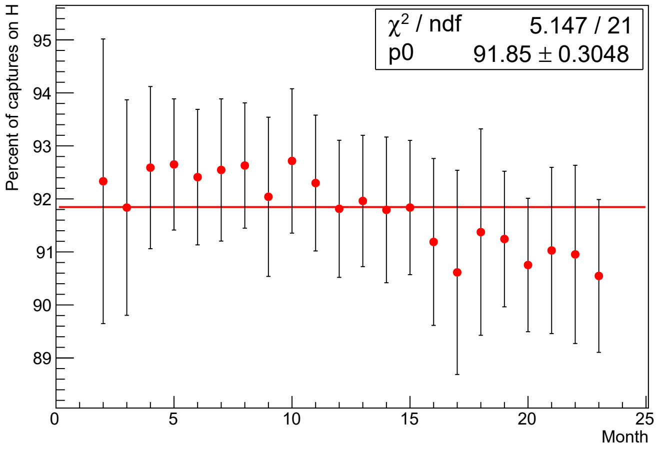

(a) ND

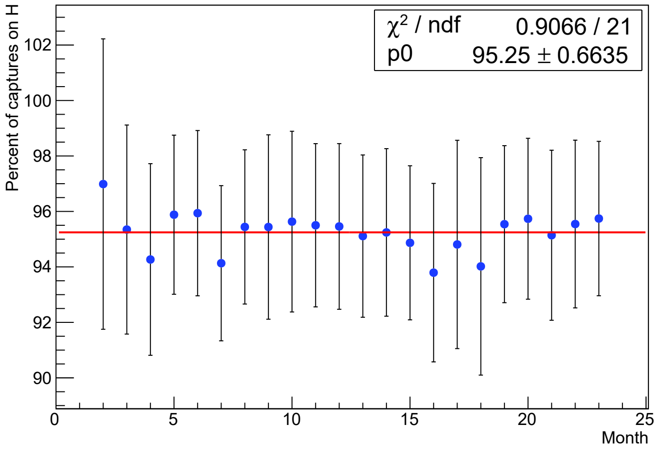

(b) FD-II

Figure 7.6: *Fraction mensuelle des H-Gamers dans the ND (a) et le FD (b). Après soustraction du bruit de fond.*

Les signatures physiques des neutrons rapides ont été identifiées et l'analyse a réglé de manière optimale les vetos qui sélectionnent efficacement ce fond avec une inefficacité associée ($< 0,1\%$) très négligeable, au-delà des attentes. L' échantillon d'événements sélectionnés par les vetos définis a fourni la forme spectrale du fond corrélé. Grâce aux spectres obtenus, nous avons pu calculer le taux du bruit de fond corrélé restant dans l' échantillon final du signal avant le fit final. Ces deux informations (formes spectrales et taux de bruit de fond) servent d'inputs dans le fit final, à partir duquel la valeur θ_{13} est déterminée. Les vetos et les taux associés de bruit de fond mesurés dans ce travail sont reconnus comme officiels par la collaboration de DC

Outre les neutrons rapides, une analyse de la double capture de fond de neutrons a été réalisée dans ce volume pour la première fois. La contamination de l'échantillon final de l'IBD, dans le DC-IV, par les événements de fond de DnC a été mise en évidence par la présence évidente de pics de capture de neutrons dans le spectre d'énergie rapide des événements candidats d'IBD qui ont, comme événement précédent, un ou plusieurs déclencheurs non valides. De tels événements ne sont pas rejetés par la multiplicité ni par le veto Inner Veto, fondé sur des déclencheurs valables. Des méthodes dédiées ont permis de mesurer les taux quotidiens de DnC; on obtient que la contamination du fond de DnC soit respectivement de $1,19 \pm 0,11$ événement / jour et de $0,23 \pm 0,02$ événement / jour pour le ND et le FD. La question de la stabilité, ou non, des événements de DnC dans le temps a été résolue par affirmative. De plus, l'impact du bruit de fond de DnC sur la valeur de θ_{13} a été étudié; il est apparu que, au stade de la quantité actuelle des données collectées, y compris les taux de DnC au final, provoquait une variation mineure de la valeur centrale de θ_{13}.

En plus de l'étude du contexte corrélé, nous avons étudié les facteurs suivants: fuite de Gadolinium dans le ND Gamma Catcher (GC) basée sur une analyse statistique des événements à signaux retardés dans le Gamma Catcher. Notre analyse a fourni la preuve de la fuite de Gd dans le ND Gamma Catcher au moyen d'une analyse statistique des événements avec signaux retardés dans Gamma Catcher. L'abondance relative observée de ces captures dans la GC a mis en évidence une fraction inférieure des captures d'hydrogène dans la ND par rapport à la FD dans les données réelles, alors que les données de MC n'ont pas mis en évidence une telle différence. Une analyse de l'évolution permet de dire que la fuite est stable au cours du temps. De plus, diviser le GC en deux parties (haut et bas) a révélé que la concentration de fuite est plus élevée dans la partie supérieure que dans la partie inférieure. Cette différence avec la partie inférieure est réduite mais pas annulée après la soustraction du bruit de fond. L'analyse en cours réalisée à DC permet de s'affranchir de ce déséquilibre qui pourrait émerger de la fuite puisque dans le cas particulier de l'analyse, toutes les captures, à la fois sur H et sur Gd, sont collectées.

Outre les analyses de données entreprises dans le cadre de ce travail, j'ai également participé aux différentes campagnes d'étalonnage des détecteurs. En effet, les étalonnages sont la clé de voûte de l'étude de la stabilité des réponses des détecteurs, de l'évaluation des algorithmes de reconstruction de vertex et d'énergie développés en DC.

Les principaux résultats des analyses décrites ici seront intégrés dans le dernier article qui sera publié cet été par la collaboration de DC. Une partie du travail effectué dans cette thése a déjà été présentée. La connaissance du bruit de fond induit par lse muons et les techniques d'identification associées qui émergent de ces travaux sont susceptibles de servir à de nombreuses autres expériences sur les neutrinos en cours ou à construire dans les années à venir.

List of Figures

List of Tables

Bibliography

[1] Charles P. Enzi. *Wolfgang Pauli (1900?1958)*. Springer, 1994.

[2] David O. Caldwell. *Current Aspects of Neutrino Physics*. Springer-Verlag Berlin Heidelberg, 2001.

[3] James D Allen. “The Search for the Neutrino through Nuclear Recoil Experiments”. In: *American Journal of Physics* 16 (1948).

[4] F. Reines and C. Cowan. “The Neutrino”. In: *Nature* 176.446 (1956).

[5] G. Danby et al. “Observation of High-Energy Neutrino Reactions and the Existence of Two Kinds of Neutrinos”. In: *Phys. Rev. Lett.* 9 (1 July 1962), pp. 36–44. DOI: `10.1103/PhysRevLett.9.36`. URL: `https://link.aps.org/doi/10.1103/PhysRevLett.9.36`.

[6] Peter Galison. “How the first neutral-current experiments ended”. In: *Rev. Mod. Phys.* 55 (2 Apr. 1983), pp. 477–509. DOI: `10.1103/RevModPhys.55.477`. URL: `https://link.aps.org/doi/10.1103/RevModPhys.55.477`.

[7] K. Kodama et al. “Observation of tau neutrino interactions”. In: *Phys. Lett.* B504 (2001), pp. 218–224. DOI: `10.1016/S0370-2693(01)00307-0`. arXiv: `hep-ex/0012035 [hep-ex]`.

[8] D. Decamp et al. “A Precise Determination of the Number of Families With Light Neutrinos and of the Z Boson Partial Widths”. In: *Phys. Lett.* B235 (1990), pp. 399–411. DOI: `10.1016/0370-2693(90)91984-J`.

[9] C. Patrignani et al. (Particle Data Group). “Neutrino mass, mixing, and oscillations”. In: *Chinese physics C* 40.100001 (2016).

[10] M. Goldhaber, L. Grodzins, and A. W. Sunyar. “Helicity of Neutrinos”. In: *Phys. Rev.* 109 (3 Feb. 1958), pp. 1015–1017. DOI: `10.1103/PhysRev.109.1015`. URL: `https://link.aps.org/doi/10.1103/PhysRev.109.1015`.

[11] David McMahon. *Quantum field theory demystified*. McGraw-Hill Companies, Inc., 2008.

[12] B. Pontecorvo. “Mesonium and antimesonium”. In: *Zhur. Eksptl’. i Teoret. Fiz.* 33 (1957).

[13] B. Pontecorvo. “Inverse beta processes and non-conservation of lepton charge”. In: *Sov. Phys. JETP* 7 (1958). [Zh. Eksp. Teor. Fiz.34,247(1957)], pp. 172–173.

[14] K. Lande et al. “Observation of Long-Lived Neutral V Particles”. In: *Phys. Rev.* 103 (6 Sept. 1956), pp. 1901–1904. DOI: 10.1103/PhysRev.103.1901. URL: https://link.aps.org/doi/10.1103/PhysRev.103.1901.

[15] A. Yu. Smirnov. “The MSW effect and Matter Effects in Neutrino Oscillations”. In: *arXiv:hep-ph/0412391v1* (2004).

[16] S. P. Mikheyev and A. Y. Smirnov. “Resonance enhancement of oscillations in matter and solar neutrino spectroscopy”. In: *Yadernaya Fizika* 42 (1985), pp. 1441–1448.

[17] H. A. Bethe. “Energy Production in Stars”. In: *Phys. Rev.* 55 (5 Mar. 1939), pp. 434–456. DOI: 10.1103/PhysRev.55.434. URL: https://link.aps.org/doi/10.1103/PhysRev.55.434.

[18] Arno A. Penzias. “The origin of the elements”. In: *Rev. Mod. Phys.* 51 (3 July 1979), pp. 425–431. DOI: 10.1103/RevModPhys.51.425. URL: https://link.aps.org/doi/10.1103/RevModPhys.51.425.

[19] John N. Bahcall et al. “Standard solar models and the uncertainties in predicted capture rates of solar neutrinos”. In: *Rev. Mod. Phys.* 54 (3 July 1982), pp. 767–799. DOI: 10.1103/RevModPhys.54.767. URL: https://link.aps.org/doi/10.1103/RevModPhys.54.767.

[20] S. Degl’Innocenti et al. “Helioseismology and standard solar models”. In: *Astropart. Phys.* 7 (1997), pp. 77–95. DOI: 10.1016/S0927-6505(97)00004-2. arXiv: astro-ph/9612053 [astro-ph].

[21] John N. Bahcall et al. “Chlorine and Gallium Solar Neutrino Experiments”. In: *Astrophys. J.* 292 (1985), pp. L79–L82. DOI: 10.1086/184477.

[22] Vladimir N. Gavrin et al. “Solar Neutrino Results From Sage”. In: *Proceedings, 10th Lomonosov Conference on Elementary Particle Physics: Moscow, Russia, August 23-29, 2001*. 2003, pp. 1–12. DOI: 10.1142/9789812704948_0001.

[23] Michael Altmann. “GALLEX Solar Neutrino Observations: Results From The Total Data Set”. In: *Proceedings, 33rd Rencontres de Moriond 98 electrowek interactions and unified theories: Les Arcs, France, Mar 14-21, 1998*. Edition Frontieres. Paris: Edition Frontieres, 1998, pp. 345–352. URL: https://inspirehep.net/record/1631421/files/Pages_from_C98-03-14_345.pdf.

[24] Christopher W. Walter. "The Super-Kamiokande Experiment". In: (2008). DOI: 10.1142/9789812771971_0002. arXiv: 0802.1041 [hep-ex].

[25] Pierce Weatherly. "Super-Kamiokande Solar Neutrino Results and NSI Analysis". In: *J. Phys. Conf. Ser.* 888.1 (2017), p. 012190. DOI: 10.1088/1742-6596/888/1/012190.

[26] Y. Fukuda. "Neutrino Oscillation Measurements at SuperKamiokande". In: *Proceedings, 10th Lomonosov Conference on Elementary Particle Physics: Moscow, Russia, August 23-29, 2001*. 2003, pp. 13–24. DOI: 10.1142/9789812704948_0002.

[27] Q. R. Ahmad et al. "Direct evidence for neutrino flavor transformation from neutral current interactions in the Sudbury Neutrino Observatory". In: *Phys. Rev. Lett.* 89 (2002), p. 011301. DOI: 10.1103/PhysRevLett.89.011301. arXiv: nucl-ex/0204008 [nucl-ex].

[28] A. Bellerive et al. "The Sudbury Neutrino Observatory". In: *Nucl. Phys.* B908 (2016), pp. 30–51. DOI: 10.1016/j.nuclphysb.2016.04.035. arXiv: 1602.02469 [nucl-ex].

[29] Carlo Giunti and Chung W. Kim. *Fundamentals of neutrino physics and astrophysics*. Oxford University Press, 2007.

[30] L. Wolfenstein. "Neutrino oscillations in matter". In: *Phys. Rev. D* 17 (9 1978), pp. 2369–2374. DOI: 10.1103/PhysRevD.17.2369. URL: https://link.aps.org/doi/10.1103/PhysRevD.17.2369.

[31] A. Gando et al. "Constraints on θ_{13} from A Three-Flavor Oscillation Analysis of Reactor Antineutrinos at KamLAND". In: *Phys. Rev.* D83 (2011), p. 052002. DOI: 10.1103/PhysRevD.83.052002. arXiv: 1009.4771 [hep-ex].

[32] Justin Evans. "The MINOS experiment: results and prospects". In: *Adv. High Energy Phys.* 2013 (2013), p. 182537. DOI: 10.1155/2013/182537. arXiv: 1307.0721 [hep-ex].

[33] Jianming Bian. "The NOvA Experiment: Overview and Status". In: *Meeting of the APS Division of Particles and Fields (DPF 2013) Santa Cruz, California, USA, August 13-17, 2013*. 2013. arXiv: 1309.7898 [physics.ins-det]. URL: https://inspirehep.net/record/1256026/files/arXiv:1309.7898.pdf.

[34] K. Abe et al. "Measurement of neutrino and antineutrino oscillations by the T2K experiment including a new additional sample of ν_e interactions at the far detector". In: *Phys. Rev.* D96.9 (2017), p. 092006. DOI: 10.1103/PhysRevD.96.092006. arXiv: 1707.01048 [hep-ex].

[35] M. H. Ahn et al. "Measurement of Neutrino Oscillation by the K2K Experiment". In: *Phys. Rev.* D74 (2006), p. 072003. DOI: 10.1103/PhysRevD.74.072003. arXiv: hep-ex/0606032 [hep-ex].

[36] M. Apollonio et al. "Initial results from the CHOOZ long baseline reactor neutrino oscillation experiment". In: *Phys. Lett.* B420 (1998), pp. 397–404. DOI: `10.1016/S0370-2693(97)01476-7`. arXiv: `hep-ex/9711002 [hep-ex]`.

[37] F. Boehm et al. "Results from the Palo Verde neutrino oscillation experiment". In: *Phys. Rev.* D62 (2000), p. 072002. DOI: `10.1103/PhysRevD.62.072002`. arXiv: `hep-ex/0003022 [hep-ex]`.

[38] Jun Cao and Kam-Biu Luk. "An overview of the Daya Bay Reactor Neutrino Experiment". In: *arXiv:1605.01502v1[hep-ex]* (2016).

[39] J. H. Choi et al. "Observation of Energy and Baseline Dependent Reactor Antineutrino Disappearance in the RENO Experiment". In: *Phys. Rev. Lett.* 116.21 (2016), p. 211801. DOI: `10.1103/PhysRevLett.116.211801`. arXiv: `1511.05849 [hep-ex]`.

[40] Xin Qian and Jen-Chieh Peng. "Physics with Reactor Neutrinos". In: (2018). arXiv: `1801.05386 [hep-ex]`.

[41] Y. Abe and al. (Double Chooz collaboration). "Indication for the disappearance of reactor ??e in the Double Chooz". In: *arXiv:1112.6353v3[hep-ex]* (2012).

[42] F. P. An et al. "Observation of electron-antineutrino disappearance at Daya Bay". In: *Phys. Rev. Lett.* 108 (2012), p. 171803. DOI: `10.1103/PhysRevLett.108.171803`. arXiv: `1203.1669 [hep-ex]`.

[43] J. K. Ahn et al. "Observation of Reactor Electron Antineutrino Disappearance in the RENO Experiment". In: *Phys. Rev. Lett.* 108 (2012), p. 191802. DOI: `10.1103/PhysRevLett.108.191802`. arXiv: `1204.0626 [hep-ex]`.

[44] F. P. An et al. "Improved Measurement of Electron Antineutrino Disappearance at Daya Bay". In: *Chin. Phys.* C37 (2013), p. 011001. DOI: `10.1088/1674-1137/37/1/011001`. arXiv: `1210.6327 [hep-ex]`.

[45] Feng Peng An et al. "Measurement of electron antineutrino oscillation based on 1230 days of operation of the Daya Bay experiment". In: *Phys. Rev.* D95.7 (2017), p. 072006. DOI: `10.1103/PhysRevD.95.072006`. arXiv: `1610.04802 [hep-ex]`.

[46] T2K Collaboration. *T2K presents hint of CP violation by neutrinos*. 2017. URL: `http://www.icrr.u-tokyo.ac.jp/2017/08/04110001.html` (visited on 08/04/2017).

[47] Juno collaboration. "JUNO Conceptual Design Report". In: *arXiv.1508.07166v2[physics.ins-det]* (2015).

[48] F. An and al. "Neutrino Physics with JUNO". In: *arXiv.1507.05613v2[physics.ins-det]* (2015).

[49] Soo-Bong Kim. “New results from RENO and prospects with RENO-50”. In: *Nucl. Part. Phys. Proc.* 265-266 (2015), pp. 93–98. DOI: `10.1016/j.nuclphysbps.2015.06.024`. arXiv: `1412.2199 [hep-ex]`.

[50] Guang Yang. “Neutrino mass hierarchy determination at reactor antineutrino experiments”. In: *Proceedings, 12th Conference on the Intersections of Particle and Nuclear Physics (CIPANP 2015): Vail, Colorado, USA, May 19-24, 2015*. 2015. arXiv: `1509.08747 [physics.ins-det]`. URL: `https://inspirehep.net/record/1395254/files/arXiv:1509.08747.pdf`.

[51] M. G. Aartsen et al. “PINGU: A Vision for Neutrino and Particle Physics at the South Pole”. In: *J. Phys.* G44.5 (2017), p. 054006. DOI: `10.1088/1361-6471/44/5/054006`. arXiv: `1607.02671 [hep-ex]`.

[52] Ulrich F. Katz. “The ORCA Option for KM3NeT”. In: *Proceedings of the 15th International Workshop on Neutrino Telescopes (Neutel 2013): Venice, March 11-15, 2013*. 2014. arXiv: `1402.1022 [astro-ph.IM]`. URL: `https://inspirehep.net/record/1280181/files/arXiv:1402.1022.pdf`.

[53] Jost Migenda. “The Hyper-Kamiokande Experiment: Overview & Status”. In: *Proceedings, Prospects in Neutrino Physics (NuPhys2016): London, UK, December 12-14, 2016*. 2017. arXiv: `1704.05933 [hep-ex]`. URL: `https://inspirehep.net/record/1593759/files/arXiv:1704.05933.pdf`.

[54] Md. Naimuddin et al. “Characterisation of Glass Electrodes and RPC Detectors for $INO-ICAL$ Experiment”. In: *JINST* 9 (2014), p. C10039. DOI: `10.1088/1748-0221/9/10/C10039`. arXiv: `1409.7184 [physics.ins-det]`.

[55] Ernesto Kemp. “The Deep Underground Neutrino Experiment: The precision era of neutrino physics”. In: *Astron. Nachr.* 338.9-10 (2017), pp. 993–999. DOI: `10.1002/asna.201713417`. arXiv: `1709.09385 [hep-ex]`.

[56] R. B. Patterson. “Prospects for Measurement of the Neutrino Mass Hierarchy”. In: *Ann. Rev. Nucl. Part. Sci.* 65 (2015), pp. 177–192. DOI: `10.1146/annurev-nucl-102014-021916`. arXiv: `1506.07917 [hep-ex]`.

[57] Ch. Kraus et al. “Final results from phase II of the Mainz neutrino mass search in tritium beta decay”. In: *Eur. Phys. J.* C40 (2005), pp. 447–468. DOI: `10.1140/epjc/s2005-02139-7`. arXiv: `hep-ex/0412056 [hep-ex]`.

[58] V. N. Aseev et al. “An upper limit on electron antineutrino mass from Troitsk experiment”. In: *Phys. Rev.* D84 (2011), p. 112003. DOI: `10.1103/PhysRevD.84.112003`. arXiv: `1108.5034 [hep-ex]`.

[59] The Katrin collaboration. “KATRIN design report”. In: *Technical report* (2004).

[60] M. Goeppert-Mayer. “Double Beta-Disintegration”. In: *Phys. Rev.* 48 (6 1935), pp. 512–516. DOI: 10.1103/PhysRev.48.512. URL: https://link.aps.org/doi/10.1103/PhysRev.48.512.

[61] G. Mention et al. “Reactor antineutrino anomaly”. In: *Phys. Rev. D* 83 (7 2011), p. 073006. DOI: 10.1103/PhysRevD.83.073006. URL: https://link.aps.org/doi/10.1103/PhysRevD.83.073006.

[62] Victor Helaine. “Sterile neutrino search at the ILL nuclear reactor: the STEREO experiment”. In: *arXiv:1604.08877v2[physics.ins-det]* (2016).

[63] Julia Haser. “Light sterile neutrino searches”. In: *29th Rencontres de Blois on Particle Physics and Cosmology Blois, France, May 28-June 2, 2017*. 2017. arXiv: 1710.06330 [hep-ex]. URL: https://inspirehep.net/record/1631177/files/arXiv:1710.06330.pdf.

[64] C. Athanassopoulos et al. “Evidence for anti-muon-neutrino —> anti-electron-neutrino oscillations from the LSND experiment at LAMPF”. In: *Phys. Rev. Lett.* 77 (1996), pp. 3082–3085. DOI: 10.1103/PhysRevLett.77.3082. arXiv: nucl-ex/9605003 [nucl-ex].

[65] A. A. Aguilar-Arevalo et al. “A Search for electron neutrino appearance at the $\Delta m^2 \sim 1\text{eV}^2$ scale”. In: *Phys. Rev. Lett.* 98 (2007), p. 231801. DOI: 10.1103/PhysRevLett.98.231801. arXiv: 0704.1500 [hep-ex].

[66] C. M. Ignarra. “MicroBooNE”. In: *Particles and fields. Proceedings, Meeting of the Division of the American Physical Society, DPF 2011, Providence, USA, August 9-13, 2011*. 2011. arXiv: 1110.1604 [physics.ins-det]. URL: https://inspirehep.net/record/930970/files/arXiv:1110.1604.pdf.

[67] Y.?J. Ko et al. “Sterile Neutrino Search at the NEOS Experiment”. In: *Phys. Rev. Lett.* 118.12 (2017), p. 121802. DOI: 10.1103/PhysRevLett.118.121802. arXiv: 1610.05134 [hep-ex].

[68] Feng Peng An et al. “Measurement of the Reactor Antineutrino Flux and Spectrum at Daya Bay”. In: *Phys. Rev. Lett.* 116.6 (2016). [Erratum: Phys. Rev. Lett.118,no.9,099902(2017)], p. 061801. DOI: 10.1103/PhysRevLett.116.061801, 10.1103/PhysRevLett.118.099902. arXiv: 1508.04233 [hep-ex].

[69] C. Bemporad. “A long-base search for neutrino oscillations at a reactor: The CHOOZ experiment”. In: *High-energy physics. Proceedings, International Europhysics Conference, Jerusalem, Israel, August 19-25, 1997*. 1997, pp. 834–839.

[70] M. Apollonio et al. “Limits on neutrino oscillations from the CHOOZ experiment”. In: *Phys. Lett.* B466 (1999), pp. 415–430. DOI: `10.1016/S0370-2693(99)01072-2`. arXiv: `hep-ex/9907037 [hep-ex]`.

[71] Y. Abe and al. (Double Chooz collaboration). “Reactor electron antineutrino disappearance in the Double Chooz experiment”. In: *arXiv:1207..6632v4[hep* *ex]* (2012).

[72] Y. Abe and al. “Improved measurements of the neutrino mixing angle ?13 with the Double Chooz detector”. In: *arXiv:1406.7763v4[hep.ex]* (2015).

[73] Valerian Sibille. *Mesure de l’angle de mélange θ_{13} avec les deux détecteurs de Double Chooz*. PhD Thesis, 2016.

[74] EMILY M. CONOVER. *MUON-INDUCED BACKGROUNDS IN THE DOUBLE CHOOZ NEUTRINO OSCILLATION EXPERIMENT*. PhD Thesis, 2014.

[75] Arthur James Franke. *Searching for Reactor Antineutrino Flavor Oscillations with the Double Chooz Far Detector*. PhD Thesis, 2012.

[76] Y. Abe et al. “The Waveform Digitiser of the Double Chooz Experiment: Performance and Quantisation Effects on PhotoMultiplier Tube Signals”. In: *JINST* 8 (2013), P08015. DOI: `10.1088/1748-0221/8/08/P08015`. arXiv: `1307.4917 [physics.ins-det]`.

[77] Guillaume Pronost. *Etudes pour la mesure de l’angle θ_{13} avec l’expérience Double Chooz*. PhD Thesis, 2015.

[78] Y. Declais et al. “Study of reactor antineutrino interaction with proton at Bugey nuclear power plant”. In: *Physics Letters B* 338.2 (1994), pp. 383 –389. ISSN: 0370-2693. DOI: `https://doi.org/10.1016/0370-2693(94)91394-3`. URL: `http://www.sciencedirect.com/science/article/pii/0370269394913943`.

[79] Nuclear Energy Agency. *Mure Framework*. 1999. URL: `http://www.oecd-nea.org/tools/abstract/detail/nea-1845` (visited on 02/17/2017).

[80] J. M. Puzovic, D. Manic, and L. J. Nadderd. “An Improved Method of Lifetime Measurement of Nuclei in Radioactive Decay Chain”. In: *Nucl. Instrum. Meth.* A850 (2017), pp. 68–71. DOI: `10.1016/j.nima.2017.01.004`. arXiv: `1605.05381 [nucl-th]`.

[81] A. Oralbaev, M. Skorokhvatov, and O. Titov. “The inverse beta decay: a study of cross section”. In: *J. Phys. Conf. Ser.* 675.1 (2016), p. 012003. DOI: `10.1088/1742-6596/675/1/012003`.

[82] Th. A. Mueller et al. “Improved Predictions of Reactor Antineutrino Spectra”. In: *Phys. Rev.* C83 (2011), p. 054615. DOI: `10.1103/PhysRevC.83.054615`. arXiv: `1101.2663 [hep-ex]`.

[83] Fumitako Sato and al. “High voltage system for the Double Chooz experiment”. In: *Physics Procedia* 37 (2012), pp. 1164–1170.

[84] W.R. Leo. *Techniques for nuclear and particle physics experiments*. Springer-Verlag, 1987.

[85] Leonidas N. Kalousis. *Calibration of the Double Chooz detector and cosmic background studies*. PhD Thesis, 2012.

[86] Adrien Hourlier. *Background Studies for electron antineutrino oscillations measurement at the Double Chooz Experiment*. PhD Thesis, 2016.

[87] Chang Xu et al. “α-decay width of ^{212}Po from a quartetting wave function approach”. In: *Phys. Rev.* C93.1 (2016), p. 011306. DOI: `10.1103/PhysRevC.93.011306`. arXiv: `1511.07584 [nucl-th]`.

[88] Y. Abe et al. “Precision Muon Reconstruction in Double Chooz”. In: *Nucl. Instrum. Meth.* A764 (2014), pp. 330–339. DOI: `10.1016/j.nima.2014.07.058`. arXiv: `1405.6227 [physics.ins-det]`.

[89] P. Wilkinson. “Book Review: Cosmogenic Radionuclides: Theory and Applications in the Terrestrial and Space Environments”. In: *History of Geo- and Space Sciences* 6.1 (2015), pp. 1–2. DOI: `10.5194/hgss-6-1-2015`. URL: `https://www.hist-geo-space-sci.net/6/1/2015/`.

[90] H. de Kerret et al. “Yields and production rates of ^{9}Li and ^{8}He measured with the Double Chooz near and far detectors”. In: (2018). arXiv: `1802.08048 [hep-ex]`.

[91] Table of Radioactive isotopes. *http://nucleardata.nuclear.lu.se/toi/nuclide.asp?iZA=810208*.

[92] Y. Abe et al. “Characterization of the Spontaneous Light Emission of the PMTs used in the Double Chooz Experiment”. In: *JINST* 11.08 (2016), P08001. DOI: `10.1088/1748-0221/11/08/P08001`. arXiv: `1604.06895 [physics.ins-det]`.

[93] Stefan Wagner. *Energy non-linearity studies and pulse shape analysis of liquid scintillator signals in the Double Chooz experiment*. PhD Thesis, 2003.

[94] A. C. Hayes and Petr Vogel. “Reactor Neutrino Spectra”. In: *Ann. Rev. Nucl. Part. Sci.* 66 (2016), pp. 219–244. DOI: `10.1146/annurev-nucl-102115-044826`. arXiv: `1605.02047 [hep-ph]`.

[95] Y. Abe and al. “Background-independent measurement of θ_{13} in Double Chooz”. In: *arXiv:1401.5981v2[hep.ex]* (2014).

[96] Cristiano Galbiati and John F. Beacom. “Measuring the cosmic ray muon-induced fast neutron spectrum by (n,p) isotope production reactions in underground detectors”. In: *Phys. Rev.* C72 (2005). [Erratum: Phys. Rev.C73,049906(2006)], p. 025807. DOI: `10.1103/PhysRevC.73.049906, 10.1103/PhysRevC.72.025807`. arXiv: `hep-ph/0504227 [hep-ph]`.

[97] TFractionFitter Class Reference. *https://root.cern.ch/doc/v606/classTFractionFitter.html*.

[98] R. Brun and F. Rademakers. “ROOT: An object oriented data analysis framework”. In: *Nucl. Instrum. Meth.* A389 (1997), pp. 81–86. DOI: `10.1016/S0168-9002(97)00048-X`.

[99] X. B. Ma et al. “Antineutrino flux and spectrum calculation for spent nuclear fuel for the Daya Bay antineutrino experiment”. In: *Nucl. Phys.* A966 (2017), pp. 294–305. DOI: `10.1016/j.nuclphysa.2017.06.009`. arXiv: `1512.07353 [physics.ins-det]`.

[100] ZHOU Bin;RUAN Xi-Chao;NIE Yang-Bo;ZHOU Zu-Ying;AN Feng-Peng;CAO Jun. “A study of antineutrino spectra from spent nuclear fuel at Daya Bay”. In: *Chinese physics C* 36.1, 1 (2012), p. 1. DOI: `10.1088/1674-1137/36/1/001`. URL: `http://cpc-hepnp.ihep.ac.cn:8080/Jwk_cpc/EN/abstract/article_2649.shtml`.

[101] K. KALE SAYI. “Study of fast neutrons in the Double Chooz neutrino oscillation experiment”. In: (2017).

[102] Anselmo Meregaglia et al. “IBD background rejection and tagging at the Double Chooz experiment”. In: *PoS* ICHEP2016 (2016), p. 957.

[103] T. Abrahao et al. “Cosmic-muon characterization and annual modulation measurement with Double Chooz detectors”. In: *JCAP* 1702.02 (2017), p. 017. DOI: `10.1088/1475-7516/2017/02/017`. arXiv: `1611.07845 [hep-ex]`.

[104] T. Abrahão et al. “Novel event classification based on spectral analysis of scintillation waveforms in Double Chooz”. In: *JINST* 13.01 (2018), P01031. DOI: `10.1088/1748-0221/13/01/P01031`. arXiv: `1710.04315 [physics.ins-det]`.

Kenny KALE SAYI

Study of the cosmic muon-induced background in the Double Chooz neutrino oscillation experiment

Résumé

L'expérience Double Chooz, située sur le site de la centrale nucléaire de Chooz dans la région des Ardennes en France, étudie la disparition des antineutrinos. Le but principal de l'expérience est de mesurer avec une grande précision l'amplitude d'oscillation $\sin^2 2\theta_{13}$ des antineutrinos émis par les deux réacteurs de la centrale de Chooz. La précision de cette mesure dépend fortement d'une connaissance précise des taux et de la forme des spectres des bruits de fond qui contaminent la sélection finale des antineutrinos en particulier dans la gamme d'énergie où l'oscillation des neutrinos est attendue. Nous avons étudié dans la présente thèse le bruit de fond d'origine cosmique dans l'expérience Double Chooz. En effet, les muons cosmiques traversant les détecteurs ou interagissant dans le voisinage immédiat sont la principale source de bruit de fond observés dans l'expérience Double Chooz. Deux types de bruits de fonds sont analysés et présentes dans cette thèse : les neutrons rapides (FN) et la double capture de neutrons (DnC). Des techniques d'identification dédiées ont été développées pour chacun de ces bruits de fond et, par conséquent, les formes spectrales et les taux associés ont été déterminés. Les valeurs obtenues dans le cadre de ce travail servent de paramètres d'entrée dans le fit final d'où la valeur de θ_{13} est extraite. La dernière mesure publiée par la collaboration Double Chooz est $\sin^2 2\theta_{13} = 0.119 \pm 0.016$.

Mots-clés : Double Chooz, neutrino, bruit de fond corrélé, neutrons rapides, double capture des neutrons, fuite, gamers.

Abstract

The Double Chooz experiment is- a reactor antineutrino disappearance experiment located on the site of the Chooz nuclear power plant in the Ardennes region in France. The principal aim of the experiment is a high precision measurement of the oscillation amplitude $\sin^2 2\theta_{13}$ of the antineutrinos emitted from the two reactor cores of the Chooz power plant. The robustness and accuracy of this measurement depends strongly on a precise knowledge of the rates and spectral shapes of the backgrounds that contaminate the antineutrinos selection over the neutrino oscillation expected region. We have studied in the present thesis the muon induced background in the Double Chooz experiment. Indeed, cosmic muons crossing the detectors or interacting in the neighbourhood constitute the main source of background events encountered in Double Chooz. Two distinct backgrounds analysis are presented in this thesis: fast neutrons (FN) and double capture of neutrons (DnC). Dedicated identification techniques have been developed for each of these backgrounds and, consequently, the associated spectral shapes and rates have been determined. The values obtained in this work serve as inputs in the final fit whence the θ_{13} value is extracted. The latest measurement released by the Double Chooz collaboration is $\sin^2 2\theta_{13} = 0.119 \pm 0.016$.

Key-words: Double Chooz, neutrino, correlated background, fast neutrons, double neutron capture, leak, gamers.